THEORETICAL STUDIES OF CHEMICAL PROCESSES FOR BIOMASS CONVERSION ON METAL CATALYSTS

Rodrigo Antonio García Muelas

Rodrigo Antonio García Muelas

Theoretical Studies of Chemical Processes for Biomass Conversion on Metal Catalysts

DOCTORAL THESIS

Supervised by

Prof. Núria López Alonso

Institute of Chemical Research of Catalonia (ICIQ)
and Rovira i Virgili University (URV)

Tarragona
2017

UNIVERSITAT ROVIRA I VIRGILI
THEORETICAL STUDIES OF CHEMICAL PROCESSES FOR BIOMASS CONVERSION ON METAL CATALYSTS
Rodrigo Antonio García Muelas

Institut Català d'Investigació Química
Av. Països Catalans, 16
43007 Tarragona. Spain

Prof. Núria López Alonso, group leader in the Institute of Chemical Research of Catalonia,

I STATE that the present study, entitled "**Theoretical Studies of Chemical Processes for Biomass Conversion on Metal Catalysts**", presented by Rodrigo Antonio García Muelas for the award of the degree of Doctor in Chemical Science and Technology, has been carried out under my supervision at the Institute of Chemical Research of Catalonia.

Tarragona, June 27th, 2017

Prof. Núria López Alonso

UNIVERSITAT ROVIRA I VIRGILI
THEORETICAL STUDIES OF CHEMICAL PROCESSES FOR BIOMASS CONVERSION ON METAL CATALYSTS
Rodrigo Antonio García Muelas

Sponsors

Dedication and personal acknowledgments

My grandfather, Nicolás García[†], used to say that petroleum was the worst curse of Venezuela. Despite he had no studies, he was clever enough to realize about the "resource curse", many decades before the concept became popular in the 1990's. He was right. As for 2017, the country with highest oil reserves in the world has become a failed state, afflicted by a staggering shortage of food, medicines, and fuels, as well as hyperinflation and violent situations comparable to those in war zones. I would like to dedicate this work to the people that is suffering this obnoxious situation as well as those who joined the Venezuelan diaspora, but specially those that are working actively to change the situation. There are, however, good news: the world's dependence of oil is being reduced everyday thanks to thousands of researchers and business owners, who are dedicating their efforts to develop clean sources for energy and raw materials. As this work presents my two-cents contribution to a more sustainable society, I first would like to thank Prof. Núria López to give me the opportunity I have sought for so many years.

As a part of a great team, I was able to push forward thanks to the feedback of other coworkers besides my supervisor. In particular, I want to thank Martín G and Moisés À for helping me when everything seemed dark (specially my PC monitor). Núria V for her passion against the pigeons, for many hours of proofreading, and also her assistance against the bureaucracy demons. Also Victor F and Ignacio F to share their bureaucracy wisdom with me. Luca B, Max GM, Marçal C, Charles G, Sergey P, and Crisa VF for their useful advices about scripting and programing. Prof. Carles Bo, Prof. Feliú Maseras, Piotr B, Guillem RL, Dr. Neyvis, Adrià GM, María B, WMC Sameera, Jesús J, and Nuno B for, among other things, teaching me important concepts at several stages of my research. Miquel GR for his valuable advices in paper writing and proofreading; also Marcos MK-RP, a tough proofreader for equations and text. Qiang L, for being a good coworker, with whom I shared the crazy 1000-reactions project. Dolores M, Joaquín SL, Giuliano C, Fernando CG, José ALl, Mauro F, Ángel M, Rositha K, Michael H, Albert-the-red, Andrey K, Chunhui L, Damien C, Edvin F, Nathan D, Jacob E, Mikko M, and Benjamin Z, and specially, the long-distance-walker and multifaceted Franziska H, for nice discussions and moments outside the lab. María F for being warm a friendly from the very first day. Stefano S for being an almost-worthy enemy, as every great man needs one. Finally, other lab members like Masoud S,

Contents

Abbreviations

APR	Aqueous phase reforming
ATR	Autothermal reforming
B3LYP	Becke, 3-parameter, Lee-Yang-Parr density functional
BOMD	Born-Oppenheimer molecular dynamics
CI-NEB	Climbing-image nudged-elastic band
DD	Direct decomposition
DFT	Density functional theory
HB	Hydrogen bond
IDM	Improved dimer method
L1O	Leave-one-out
MAE	Mean absolute error
MGCM	Multigrid continuum model
MK	Microkinetic model
NEB	Nudged elastic band
PAW	Projector-augmented wave pseudopotentials
PBE	Perdew-Burke-Ernzerhof density functional
POx	Partial oxidation
SCR	Supercritical reforming
SODE	System of ordinary differential equations
SR	Steam reforming
TPD	Temperature programed desorption
VASP	Vienna *ab-initio* simulation package
vdW	van der Waals
WGS	Water-gas shift reaction

List of publications

1. **Collective descriptors for the adsorption of sugar alcohols on Pt and Pd(111)**. _R. García-Muelas_ and _N. López_, J. Phys. Chem. C, **2014**, 118, 17531-17537.

2. **Generalized models for adsorption of intermediates on transition metals**. _R. García-Muelas_ and _N. López_, Submitted, **2017**.

3. **Density functional theory comparison of methanol decomposition and reverse reactions on metal surfaces**. _R. García-Muelas_, _Q. Li, and N. López_, ACS Catal., **2015**, 5, 1027-1036.

4. **Microkinetics of alcohol reforming for H$_2$ production from a FAIR density functional theory database**. _Q. Li_, _R. García-Muelas_, _and N. López_, Submitted, **2017**.

5. **Diversity at the water-metal interface: Metal, water thickness, and confinement effects**. _L. Bellarosa_, _R. García-Muelas_, _G. Revilla-López_, _and N. López_, ACS Cent. Sci., **2016**, 2, 109-116.

6. **Solvation effects on methanol decomposition on Pd(111), Pt(111), and Ru(0001)**. _M. García-Ratés_, _R. García-Muelas_, _and N. López_, J. Phys. Chem. C, **2017**, 121, 13803-13809.

7. **Glycerol oxidehydration to pyruvaldehyde over silver-based catalysts for improved lactic acid production**. _G. M. Lari_, _R. García-Muelas_, _C. Mondelli, N. López, and J. Pérez-Ramírez_, Green Chem., **2016**, 18, 4682-4692.

R. García-Muelas wrote the first draft and did all the Density Functional Theory calculations of publications 1, 2, and 6. He did part of the calculations and actively participated in writting the rest of the publications.

Furthermore, the author has contributed to the following reviews, which are not included in this thesis:

- **State-of-the-art and challenges in theoretical simulations of heterogeneous catalysis at the microscopic level**. *N. López, N. Almora-Barrios, G. Carchini, P. Błoński, L. Bellarosa, R. García-Muelas, G. Novell-Leruth, and M. García-Mota*, Catal. Sci. Technol., **2012**, 2, 2405-2417.

- **How theoretical simulations can address the structure and activity of nanoparticles**. *G. Carchini, N. Almora-Barrios, G. Revilla-López, L. Bellarosa, R. García-Muelas, M. García-Melchor, S. Pogodin, P. Błoński, and N. López*, Top. Catal., **2013**, 56, 1262-1272.

- **Initial stages in the formation of nickel phosphides**. *R. García-Muelas, Q. Li, and N. López*, Submitted, **2017**.

- **Scaling classes to describe hydrocarbon adsorption energies on transition-metal surfaces**. *D. Kinschel, R, García-Muelas, C. Tsai, L. Vilella, N. López, and F. Abild-Pedersen*, In prep., **2017**.

Abstract

The non-edible fraction of biomass is the most abundant renewable source of poly-alcohols and other oxygenated compounds. These compounds can then be transformed into fuels and platform chemicals that are key for a sustainable chemical industry. This thesis focuses on the study of the adsorption and reactivity of mono- and poly-alcohols derived from non-edible biomass on metal surfaces. The behaviour of the metal-water interface, as well as the effect of solvation and coadsorbed molecules in the reaction paths, are also considered. The thermodynamic and kinetic parameters are obtained from Density Functional Theory (DFT) calculations, and the rationalization of the results is based in microkinetic modeling, linear scaling relationships, and statistical analyses among other tools. The state-of-the-art and the antecedents are introduced in Chapter 1, along with the motivations and the objectives that drove this thesis. In Chapter 2, the main theories and methods used along the manuscript are described. Further methodological details are included in each research Chapter.

The reactivity of alcohols and their molecular fragments was studied in Chapters 3-4. In particular, Chapter 3 presents a scaling relationship to predict the adsorption energy of saturated mono- and poly-alcohols on Pd and Pt(111). The equation, developed with a training set of 14 C_1-C_4 alcohols, states that the main contributors are the oxygen groups in contact with the surface, the number of carbon atoms which interacts via van der Waals, and the number of intramolecular hydrogen bonds which become weaker upon adsorption. The model was succesfully predicting the adsorption energy of eleven C_4-C_7 sugar alcohols commonly found in biomass. In Chapter 4, I presented a database of 71 molecular fragments obtained from the full decomposition network of methanol, ethanol, and ethylene glycol on closed-packed Cu, Ag, Au, Ni, Pd, Pt, Rh, Ir, Ru, Os, Zn, and Cd surfaces. A powerful methodology was developed to predict the thermochemistry of these fragments on any metal surface by taking just three molecules as training set. The main contributions for the adsorption can be traced back to the d-band centre and the oxidation potential of the metal.

Chapter 5 analyzes the reactivity of Cu, Ru, Pd, and Pt for the decomposition and reforming of methanol, ethanol, and ethylene glycol under four reaction conditions: direct decomposition (DD), autothermal, steam, and aqueous-phase reforming (ATR, SR, APR). To this end, linear scaling relationships and microkinetics models were developed to rationalize the activity, selectivity and stability of these surfaces in terms of the most abundant reaction intermediates. The reliability of the microkinetic model holds even when linear-scaling relationships are used to predict the activation energies.

As water is ubiquitous in any stream of biomass-derived compounds, the behaviour of the wetting layers on reactive (Ru) and unreactive (Pd, Pt) metals is discussed in Chapter 6. Then, the effect of solvation, as well as spectator methanol and water molecules on the prefered reaction path of methanol decomposition is quantified in Chapter 7

The reaction path for the conversion of acetol to pyruvaldehyde on a silver catalysts is elucidated in Chapter 8, as part of a promising route to upgrade glycerol into lactic acid. Three surface models were used in this Chapter as silver surfaces may follow a non-ideal behaviour, forming surface oxides under mild oxygen pressures.

Finally, Chapter 9 contains the main conclusions of this thesis. These results pave the way for the rational design of new active, selective, and stable catalysts, needed to develop a sustainable chemical industry based on renewable raw materials. To ensure the FAIR principles of findability, accesibility, interoperability, and reusability of scientific data, all structures generated in this thesis were stored in an open database, ioChem-BD, to promote further discussions and reusability.

Chapter 1

Introduction

The world endeavor towards sustainability began in 1987 with the Brundtland report, which defines sustainable development as balancing our economic, social, and environmental needs without compromising the ability of future generations to meet their owns.[1] In a world threatened by global warming and the depletion of fossil fuels, the development of new technologies is crucial to reach such a future. Therefore, a lot of effort is being made in developing the basis of a green chemical industry, which is based on the use of water as solvent, catalysts, renewable resources as raw materials, and other principles.[2] Among the renewable resource of chemical compounds, the most abundant by far is the non-edible fraction of biomass procedent from agriculture. Biomass-derived molecules are rich in functional groups containing oxygen atoms. A particular focus is done on alcohols, as they can be obtained in large quantities from carbohydrates and be transformed into many platform chemicals by the use of heterogeneous catalysis. Indeed, many alcohols are among the "top 14" biomass-derived compound.[3]

The large-scale obtention of platform chemicals from raw materials is normaly done in industrial processes that use heterogeneous catalysis, as the separation process is much simpler than their homogeneous counterpart. Currently, 75% of industrial chemical processes depend on heterogeneous catalysts.[4,5] Most of the economic development in the 20th century is due to the heterogeneous catalysys. Still, there are many challenges ahead for the years to come. In the beginning, new catalysts were designed by trial-and-error. This practice is grossly inefficient as it consumes lots of material and human resources. However, the development of analytical techniques allowed scientists to relate catalytic properties with composition and structure. More recently, the exponential increase of computational power[6] and the development of theoretical methods such as density functional theory, DFT,[7,8] enabled the prediction of the structure and energetics of many

chemical systems.[9] Indeed, the use of theoretical simulations at several levels can give valuable insights into the activity, selectivity, and stability of most catalyst, Fig. 1.1.[10] Nowadays, the combination of simulations and experiments is the most rational way to design, characterize, and test new catalysts. In this approach, industrial and experimental conditions impose the conditions to numerical simulations, and large-scale simulations imposes contraints to the short-scale ones. Conversely, atomic-scale techniques provide design parameters for larger scale simulations, Fig. 1.1. Additional tools to fill the gaps are scaling relationships[9] and open databases containing the structure and energetics of relevant systems.[11,12]
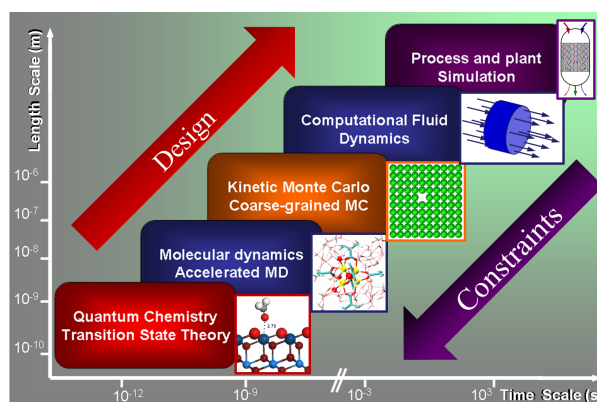
Figure 1.1: Time and length scales for different simulation tools. Taken from Ref. [10].

I concentrated most of my research in developing scaling relationships for thermodynamic and kinetic parameters, as well as the modelling of hydrogen production and glycerol valorization. Hydrogen can be used as energy vector in fuel cells, as well as reactant in many hydrogenation reactions, like the pre-treatment of raw biomass. It can be produced from biomass by decomposition and reforming of alcohols, under the conditions described in Fig. 1.2. To this end, the adsorption and reactivity of poly-alcohols and their fragments is treated in Chapters 3-5, and accurate scaling relationships were developed and validated against experimental data. As water is ubiquitous in biomass, the metal-water interface is modelled in Chapter 6 and the effect of solvation is addressed in Chapter 7. Glycerol is an important commodity chemical[3] that is being overproduced in the manufacture of biodiesel and soap. As the world market cannot absorb the surplus, the retail price of crude glycerol reached zero in 2010.[13] Its reforming into hydrogen is studied in Section 5.4.1 and its upgrade into lactic acid is treated in Chapter 8. Lactic acid is also an important platform chemical[3] whose mar-

ket is expanding 5–8% per year.[14] Finally, to speed-up the discovery of new catalysts, all structures and energetics were made public in ioChem-BD.[12] The development of new technologies for biomass reforming and glycerol upgrade will result in environmental-friendly and profitable processes. This, in turn, will have a positive social impact not to depending on scarce raw materials, thus paving the way towards a sustainable future.

1.1 Antecedents

1.1.1 Surface science studies

Surface science experiments provided the first clues to understand catalytic processes on surfaces. For instance, temperature-programed desorption (TPD) experiments provided the adsorption energy of alcohols and their main decomposition products: CO, H_2 and C,[15–19] even considering the effect of having coadsorbed species.[18,19] Also, the presence of key intermediates can provide insights in the reaction mechanisms. For instance, methoxy has been detected in the decomposition of pure methanol on Ru[20] by high-resolution electron-energy loss spectroscopy (EELS) and on Pd[21] by X-ray photoelectron spectroscopy (XPS), while its potential energy on Pt[22] was obtained recently by microcalorimetry. XPS also provides information about the oxidation state of a particular surface under working conditions, and the experimental core-level shifts can be compared with DFT values.[23] However, polyalcohols derived from biomass have a large and complex reaction network. Even for ethylene glycol, around 250 reactions can occur, Fig. B.1-B.3. The full mapping of all intermediates and transition states is only possible through theoretical methods such as density functional theory. Only few long-lived intermediates have been experimentally detected for ethylene glycol and 1,2-propanediol on Pd(111),[24] while the rest of the reaction path is obscure to current experimental techniques.

Recent improvements in the accuracy of density functional theory for heterogeneous catalysis are the inclusion of van der Waals dispersion[25–27] and solvation[28,29] effects. Dispersion is crucial to reproduce the most stable experimental wetting layer on metals[30] as well as the adsorption of methanol and formaldehyde in aqueous environments.[31] Dispersion also plays an important role for larger poly-alcohols and molecular fragments, Chapters 3-4.[32,33] There are two ways to describe solvation in DFT, either by including explicit solvent molecules or by using a continuum (implicit) model. The influence of explicit water molecules have been scarcely studied in the heterogeneous catalysis of alcohols, besides the pioner works of Okamoto *et al.*[34] and Zope *et al.*[35] The metal-water interface has also been studied by pure DFT,[36–39] molecular dynamics based on force fields,[40–42]

and Born-Oppenheimer molecular dynamics.[43–45] Implicit solvation models has been implemented long ago for homogeneous catalysis.[46] However, their implementation for periodic boundary conditions is quite recent. Currently, only two implicit solvation models are implemented in plane-waves packages, namely the multigrid continuum model, MGCM,[28] and VASPsol.[29]

1.1.2 Rational design toolbox

Large and complex reaction networks can be rationalized using thermo-chemical relations, microkinetic models, and open databases. The first relations from thermochemical data were deduced by Cottrell,[47] Kerr,[48] and Benson.[49, 50] These empirical relations were deduced by different chemical bonds by averaging over the experimental formation energies of many molecules. These relations were recently extended to include the bond energies of molecular adsorbates on heterogeneous catalysts.[51–54] These new relations are based on data from theoretical calculations, and can be linked to the electronic structure of the molecule and the catalyst.[55] Alternatively, the thermochemical relations for adsorbates can be based on building blocks[56–58] Despite building blocks are empirical constructions, their predictions can be more accurate than ones based on chemical bonds.

The potential energies of distorted structures, such as the transition states, can be calculated from thermochemical data of the intermediates by using Shustorovich' bond-order conservation theory (BOC)[59] and unity bond index-quadratic exponential potential (UBI-QEP).[60] Before the development of efficient transition-state search algorithms for DFT,[61–65] transition state energies were nicely estimated with UBI-QEP when experimental data was not available.[66] Another approach was developed by Brønsted, Evans, and Polanyi (BEP)[67] in the 1930's for molecules in solution, and then introduced in heterogeneous catalysys by the groups of Prof. Neurock[68] and Nørskov[69–71] The base of the BEP relationships is that the activation and reaction energies of similar chemical processes are correlated. Two variations, known collectivelly as trantition-state scalings (TSS) correlate the potential energies of transition states of similar reactions with either their initial (ISS) or final states (FSS).[72] BEP and TSS are discussed in Section 5.1.3.

Another useful tool is the microkinetic modeling,[73–75] which gives insights in the activity, selectivity, and stability of reaction networks that are too complex to be represented by energy profiles. The combination of scaling relationships and microkinetic modeling has proveen to be the fastest way to screen large databases of potential catalysts with reduced computational cost.[9, 70, 76, 77] Finally, most of the computed data in literature is scarce, as (i) it has been generated by different groups with differences in

computational setups, (ii) most of the information about structure and energetics is not shared, and (iii) it is insufficient, just covering part of the reaction networks. This prevents the use of data-mining and analysis tools on the available information to speed-up the discovery of new catalysts. In this context, the FAIR[11] initiative is promoting novel ways to treat scientific data, in order to make it findable, accessibe, interoperable, and reusable. Another initiative was the development of the ioChem-BD database,[12] a repository of computational data where all the calculations present in this thesis were uploaded.

1.1.3 Reforming of biomass

Hydrogen is a valuable chemical that can be obtained from oxigen-rich molecules derived from biomass and its efficient productions is key for a sustainable chemical industry.[78–80] Hydrogen can be extracted from biomass by the decomposition of sugar alcohols. This process is prone to poisoning by CO and carbon fragments, thus limiting its industrial applicability.[15, 18, 24, 81] Both poisonings can be avoided by adding water to the reaction mixture, wich undergoes reactions 1.1-1.2 in a family of processes collectivelly known as reforming. Several reforming technologies exists depending on the reaction conditions, Fig. 1.2. In the steam reforming (SR), ethanol, sugar alcohols, and other oxygenated compounds react on metals and oxides with steam at temperatures around 400–1100 K to produce H_2, CO, CO_2, and CH_4.[82] The mechanism of reforming is preserved even if pressure is increased up to supercritical conditions (SCR), although activity and selectivity may change. Moreover, reforming in supercritical conditions (SCR) has been demonstrated to proceed by the same mechanism as steam reforming.[83] Small amounts of oxygen can be added to the steam to reduce the poisoning by CO, generating the conditions for autothermal reforming (ATR). ATR has been tested for ethanol[84] and glycerol[85] on noble metals among other molecules, Table A.2. However, the ATR reactors can have high-temperature spots, which limits its applicability to thermally stable catalysts. Finally, aqueous-phase reforming (APR)[86–88] has the advantage of working at low temperatures, below 650 K, although the process is slow on clean metal surfaces. Only very recently, high turn-over frequencies have been achieved on Pt single-atoms dispersed on α-MoC,[89] but long-term stability might be an issue. An alternative for biomass upgrade is to preserve most of the functionalization of raw biomass, so up to 80% of yield to commercial products can be obtained.[90] This approach was taken on Chapter 8. A review of the most relevant studies on DD, ATR, SR, APR, and SCR can be found in Table A.2 in Appendix A.

$$CH_4 + H_2O \rightleftharpoons CO + 3\,H_2 \tag{1.1}$$

$$CO + H_2O \rightleftharpoons CO_2 + H_2 \tag{1.2}$$
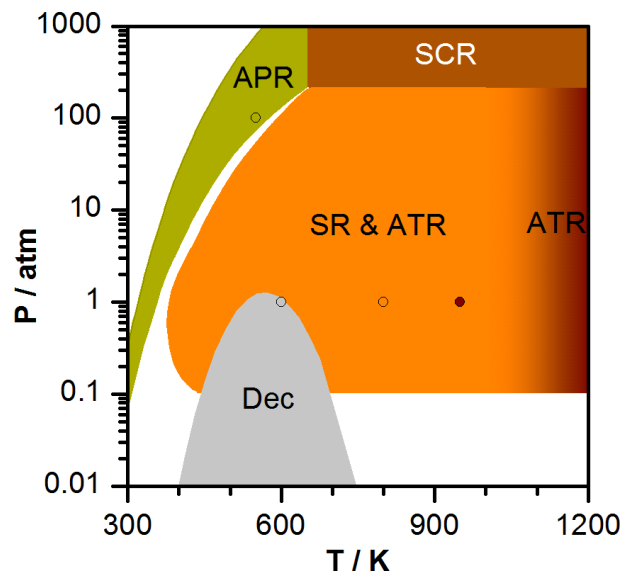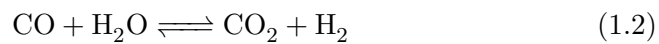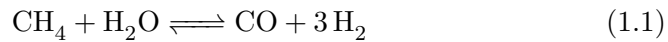
Figure 1.2: Reaction conditions for the obtention of H_2 by direct decomposition (DD), autothermal reforming (ATR), steam reforming (SR), aqueous-phase reforming (APR), and supercritical reforming (SCR) of ethanol. The points show the conditions simulated in Section 5.4. Adapted from Ref. [91].

1.2 Motivation and objectives

The main objective of this thesis is to study chemical processes for biomass conversion on metal catalysts throught theoretical methods. In particular, I focussed on the adsorption and reactivity of oxygenated molecules on group 8-12 metals and the effect of implicit and explicit solvation. The gaps existing in literature are detailed below along the objectives for each chapter:

Chapter 3 Adsorption of mono- and poly-alcohols on Pd and Pt(111)

Despite many scalings for the adsorption of molecules exist in literature, none of them have been developed for large molecules such as those derived from biomass, while the effect of hydrogen bonding on adsorption have been overlooked or oversimplified.

- To obtain the structure and energetics for the conformations of fourteen C_1–C_4 poly-alcohols in gas phase.

- To describe the structural and energetic properties for the adsorption of these alcohols on clean Pd and Pt(111) surfaces.

- To quantify the van der Waals contribution on the adsorption of alcohols on clean Pd and Pt(111).

- To develop a general a scaling relationship to predict the adsorption energy of saturated mono- and poly-alcohols on Pd and Pt(111).

Chapter 4 Adsorption of C_1-C_2 fragments on transition metals

A general model for adsorption of molecular fragments derived from alcohols is missing. In particular, there is a need for reliable methods to predict the thermochemistry of large set of molecular fragments on metal surfaces from a small sample of them.

- To compute the energetics of the most stable conformations for the intermediates procedent from the decomposition network of methanol, ethanol, and ethylene glycol on 12 metal surfaces: Ru, Os, Rh, Ir, Ni, Pd, Pt, Cu, Ag, Au, Zn, and Cd.

- To reduce the dataset dimensionality through a principal component analysis to find a robust set of descriptors.

- To rationalize the descriptors obtained from the principal component analysis in terms of a physical meaning.

- To define a procedure to predict the thermochemistry of the full set of molecular fragments from a small subset of them.

- To validate the reliability of the procedure by comparing their results with experimental and previous theoretical studies.

Chapter 5 Decomposition of C_1-C_2 alcohols on transition metals

To the best of our knowledge, there are not comparative theoretical studies based on DFT and microkinetic modeling on the activity, selectivity, and stability of Cu, Ru, Pd, and Pt for hydrogen production through autothermal, steam, and aqueous-phase reforming of alcohols. Also, the reliability of linear scaling relationships for transition states has not been tested to hold on different metals.

- To obtain the transition states for the decomposition network of C_1-C_2 alcohols on Cu, Ru, Pd, and Pt surfaces.

- To model the kinetics of hydrogen production from direct decomposition, autothermal reforming, steam reforming, and aqueous-phase reforming of ethanol and ethylene glycol on Cu, Ru, Pd, and Pt.

- To generate linear-scaling relationships to correlate kinetic parameters with thermodynamic ones.

- To test the reliability of linear-scaling relationships to predict the hydrogen production rates by reforming of ethanol and ethylene glycol on Cu, Ru, Pd, and Pt.

Chapter 6 Diversity at the metal-water interface

There are limited knowledge about the nature of the interface between metals and liquid water. In particular, previous theoretical studies do not detail which are the minimum box dimensions to reproduce the behaviour of liquid water.

- To characterize the influence of confinement and thickness of the wetting layer on local and non-local ordering parameters.

- To find the most descriptive model for heterogeneous catalytic systems under solvation.

Chapter 7 Solvation effects on reactivity

As implicit solvation models for periodic-boundary conditions are too recent, there are limited data about their reliability when describing reaction

networks of oxygenates, such as the first steps of methanol decomposition. Also, the effect of coadsorbed methanol molecules in the reaction path has not been quantified. Whether linear scaling relationships hold if the reactions occur under solvation.

- To quantify the effect of spectator methanol and water molecules on the preferred methanol dehydrogenation path.

- To comprare the behaviour of a implicit solvation model and a full set of water molecules.

Chapter 8 Role of silver suboxides in the dehydrogenation of acetol to pyruvaldehyde

There are not mechanistic studies on the oxidation of acetol to pyruvaldehyde, which is one of the routes to convert glycerol into lactic acid.

- To describe the reaction mechanism for the oxidehydration of acetol to pyruvaldehyde on a Ag-based catalyst.

- To determine the active phase in the conversion of acetol to pyruvaldehyde on silver under mild oxygen pressures.

The rational design of new catalyst and the understanding of large reaction network can be promoted with the use of FAIR databases for intermediates and transition states. As there are not public data available for the processes studied in this thesis, all structures generated for this thesis were uploaded in a public database, ioChem-BD.

Chapter 2

Theoretical background

2.1   Electronic energy calculations

The time-independent, non-relativistic Schrödinger equation describes any system in stationary state. It has the form of an eigenvalue equation, where $\hat{H}$ is the Hamiltonian operator, which depends on the physical system that is being described. Ψ is a set of solutions (wave functions) of the Hamiltonian. Each of these solutions has an associated eigenvalue, ε , that is a real number.

$$\hat{H}\Psi = \varepsilon\Psi \qquad (2.1)$$

In typical chemical systems, like molecules or periodic solids, the time scale of nuclear motion is much larger than of the electronic motion. Therefore, the nuclei can be consider as fixed entities, which generates a potential $\hat{V}$ in which the electrons are moving. This is known as the Born-Oppenheimer approximation.[92] The term Ψ in Eq. 2.1 then describes the all-electron wave function. Conversely, the Hamiltonian operator decomposes in a kinetic energy term $\hat{T}$, and the potentials generated by the nuclei and other electrons respectively, $\hat{V}$ and $\hat{U}$, as shown in Eq. 2.2. For a system with N electrons with mass m_e, the Schrödinger equation acquires the form of Eq. 2.3.[93]

$$\left[\hat{T} + \hat{V} + \hat{U}\right]\Psi = \varepsilon\Psi \qquad (2.2)$$

$$\left[-\frac{\hbar^2}{2m_e}\sum_{i=1}^{N}\nabla_i^2 + \sum_{i=1}^{N}V(\mathbf{r_i}) + \sum_{i=1}^{N}\sum_{j<i}U(\mathbf{r_i}, \mathbf{r_j})\right]\Psi = \varepsilon\Psi \qquad (2.3)$$

Even with such simplification, Eq. 2.3 still remains as a many-body problem which is too complex to solve for a typical catalytic system. This is because the individual electron wave functions contained in Ψ cannot be found without considering the ones of the other electrons; therefore, the term in the Hamiltonian that defines the electron-electron interaction, needed to define the solution, depends on the same solution.

2.1.1 The density functional theory formalism

In the 1960's decade, Hohenberg, Kohn and Sham provided an alternative way to solve the many-electron Shrödinger equation, known as Density Functional Theory (DFT). It is based on the electronic density, $n(\mathbf{r})$, an universal density functional, F,[7] and the decomposition of Ψ into single-electron wave functions, ψ_i.[8]

Electronic density

The electronic density can be obtained from the single-electron wavefunction from Eq. 2.4. It is expressed as the sum over mono-electronic states, and depends only on the spacial position ($\mathbf{r} = (r_x, r_y, r_z)$) and the spin. As the electronic density is an observable, it presents an advantage over the wave function, which is not.

$$n(\mathbf{r}) = 2 \sum_i \psi_i^*(\mathbf{r})\psi_i(\mathbf{r}) \tag{2.4}$$

The Density Functional

The seminal paper of DFT[7] defines an universal density functional which satisfy two important properties, defined bellow as theorems. The universal density functional is still unknown, but several approximations will be discussed in Section 2.1.2.

Theorem 1 The external potential, $V(\mathbf{r})$, is an unique functional, F, on the electronic density. As the external potential defines the Hamiltonian $\hat{H}$, Eq. 2.1, the full many-electron ground state is an unique functional of the electron density.

Theorem 2 The electron density that minimizes the energy of the functional F is the electron density corresponding to the true solution of the Schrödinger equation.

Single-electron wave functions

Another simplification consist in splitting the all-electron wave function Ψ into single-electron wave functions $\psi_i(\mathbf{r})$. This is equivalent to transform an N-body problem into N single-body equations.[8] For each electron, the Hamiltonian is decomposed in two parts: the kinetic energy, T, and the effective potential felt by each electron, V_{eff}, Eq. 2.5-2.6. The effective potential can be separated in three terms, Eq. 2.7-2.9. The first two are the Coulombic potentials generated by the nuclei and the other electrons, V_N and V_H respectively. V_H is also called Hartree energy. The third term is the exchange and correlation contributions to the single-electron equations, so it can be written as a functional derivative of the exchange and correlation energy, Eq. 2.9.

$$\left[\hat{T} + \hat{V}_{eff}(\mathbf{r})\right]\psi_i(\mathbf{r}) = \varepsilon\,\psi_i(\mathbf{r}) \tag{2.5}$$

$$\hat{T} = -\frac{\hbar^2}{2m_e}\nabla_i^2 \tag{2.6}$$

$$\left[\hat{T} + \hat{V}_N(\mathbf{r}) + \hat{V}_H(\mathbf{r}) + \hat{V}_{XC}(\mathbf{r})\right]\psi_i(\mathbf{r}) = \varepsilon\,\psi_i(\mathbf{r}) \tag{2.7}$$

$$\hat{V}_H(\mathbf{r}) = e^2 \int \frac{n(\mathbf{r}')}{|\mathbf{r} - \mathbf{r}'|} \tag{2.8}$$

$$\hat{V}_{XC}(\mathbf{r}) = \frac{\delta E_{XC}}{\delta n(\mathbf{r})} \tag{2.9}$$

The way of solve those equations is iterative:

1. Define an trial electron density, $n_0(\mathbf{r})$.

2. Solve the Kohn-Sham equations for that density to find the single electron wave functions.

3. Obtain a new electron density from Eq. 2.4.

4. Compare the new density with the initial one. If the two densities have differences higher than a given tolerance, then update the electron density $n(\mathbf{r})$ and continue from step 2. Else, the result of step 3 is the true ground state density.

2.1.2   Approximations

If F were a known and sufficiently simple functional of the electronic density, $F(n(\mathbf{r}))$, we could determine the electronic density and energy in the ground state for any given external potential. This would require the minimization of the functional F in the three-dimensional electronic density function. However, the exact form of the universal density functional F is not known, so several approximations has been developed to deal with the elusive V_{XC} term. The hierarchy of increasing accuracy in the exchange-correlation functionals has been dubbed by John Perdew as "the Jacobs ladder of DFT", and it is shown in Fig. 2.1.[10,94]
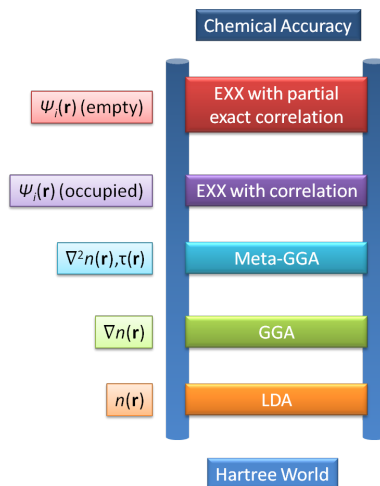
Figure 2.1: Perdew's ladder of DFT functionals. Taken from [10].

The first rung corresponds to the **Local Density Approximation** (LDA), where the exchange and correlation energy is approximated to the one of an homogeneous electron gas of the same density as obtained from stochastic methods, Eq. 2.10.[8,95] The spin-polarized version (LSDA), Eq. 2.11, can be used for magnetic materials.[96] LDA has succeeded in describing the ground state geometries for many molecules, polymers, and extended systems. However, it largely overestimates the bond energies, with error bars as large as 2 eV.[97]

$$E_{XC,LDA}(n) = \int n(\mathbf{r})\varepsilon_{XC,hom}(n)d\mathbf{r} \qquad (2.10)$$

$$E_{XC,LSDA}(n_\uparrow, n_\downarrow) = \int n(\mathbf{r})\varepsilon_{XC}(n_\uparrow, n_\downarrow)d\mathbf{r} \qquad (2.11)$$

The second rung is the **Generalized Gradient Approximation** (GGA). This approach extends the LDA to include electronic density gradient $\nabla n(\mathbf{r})/n(\mathbf{r})$. GGA has a good accuracy and reasonable computational cost, so this approximation normally used to describe many phenomena in homogeneous and heterogeneous catalysis. GGA corrects the overbinding tendency of LDA functionals. For non periodic systems, such as molecules, B3LYP[98–100] is the most used density functional. B3LYP is considered *hybrid* because it takes terms from LDA[101] and GGA.[99, 102] In periodic systems, such as bulk solids and surfaces, the most common density functionals are Perdew-Wang 91 (PW91),[103] Perdew-Burke-Ernzerhof (PBE),[104] and several flavours of the last one such as the reviewed RPBE,,[105] and the optimized version for solids, PBESol.[106] PBE is implemented in all codes and it is used to benchmark them.[107] A novel GGA, the *Bayesian Error Estimation Functional* (BEEF),[108] can estimate the computational error by using Bayesian statistics on different functionals. Pure GGA lacks the terms to account for the London dispersion forces, so it underestimates the physisorption energy of hydrocarbons and aromatics on metal surfaces. Many corrections exist to compensate for the dispersion terms, such as the Grimme's empirical methods,[25, 27, 109, 110] the vdW-DF[111] and vdW-DF2[112] functionals, and the Tkatchenko's method.[113] These corrections improve the accuracy when calculating the adsorption energies of molecules like water and alcohols on metal surfaces,[30, 31] so they were included in all calculations these methods.

$$E_{XC,GGA}(n) = \int n(\mathbf{r})\varepsilon_{XC,hom}(n, \nabla n)d\mathbf{r} \tag{2.12}$$

$$E_{XC,GGA_{\uparrow\downarrow}}(n_\uparrow, n_\downarrow) = \int n(\mathbf{r})\varepsilon_{XC}(n_\uparrow, n_\downarrow, \nabla n_\uparrow, \nabla n_\downarrow)d\mathbf{r} \tag{2.13}$$

Another rung in the Perdew's ladder is the **Meta-GGA**,[114] that includes higher-order derivatives in the calculation of the exchange-correlation energies, Eq. 2.14. Meta-GGA calculations are computationaly demanding, and the improvement of the results from GGA-type functionals is often negligible.

$$E_{XC,GGA}(n) = \int n(\mathbf{r})\varepsilon_{XC,hom}(n, \nabla n, \nabla^2 n)d\mathbf{r} \tag{2.14}$$

2.1.3 Periodic systems

A crystal is a periodic arrangement where the positions of the atoms repeat regularly in three dimensions. These systems can be mathematically

described through Bravais lattices, that are arrays generated by the periodic translation of a primitive cell into a given position in space, $\vec{R}$, Eq. 2.15. The lattice vectors $\vec{a}_i$ are linearly independent. The parametres n_i are integer number, because the translations are discrete.[93, 115]

$$\vec{R} = n_1\vec{a}_1 + n_2\vec{a}_2 + n_3\vec{a}_3 \qquad (2.15)$$

For every Bravais lattice with cell vectors, it is possible to define a reciprocal lattice with cell vectors b_j through the operations described in Eq. 2.16. The reciprocal space is also named *k-space* and its components *wave vectors* The k-space is periodic for translations over $\vec{b}_1$, $\vec{b}_2$, and $\vec{b}_3$. The units of the k-vectors are reciprocal from these of the real space vectors, so if the units of $\vec{a}_j$ are Å, the units of $\vec{b}_j$ will be Å^{-1}. The primitive cell of the k-space is called the first Brillouin zone.

$$\begin{aligned}
\vec{b}_1 &= 2\pi \frac{\vec{a}_2 \times \vec{a}_3}{\langle \vec{a}_1, \vec{a}_2, \vec{a}_3 \rangle} \\
\vec{b}_2 &= 2\pi \frac{\vec{a}_3 \times \vec{a}_1}{\langle \vec{a}_1, \vec{a}_2, \vec{a}_3 \rangle} \\
\vec{b}_3 &= 2\pi \frac{\vec{a}_1 \times \vec{a}_2}{\langle \vec{a}_1, \vec{a}_2, \vec{a}_3 \rangle}
\end{aligned} \qquad (2.16)$$

The orientation of a surface in a crystal is represented by its Miller index. The Miller index is obtained from the points at which the plane intersects the three axes of the material's conventional cell. Then, the reciprocal of these intercepts are multiplied by a scaling factor to convert them into the smaller possible integer, which are the Miller index of that surface. In case there is no intercept in a certain direction, it reciprocal number is set to 0.[115, 116] The metals used in the present work has either a face-centered cubic (fcc) or an hexagonal close packed (hcp) structure, represented in Fig. 2.2 (a)-(b). The most stable surfaces for these packings are normally obtained from the (111) and (0001) cuts respectively, as represented in Fig. 2.2 (c). For hcp crystals, it is common to add a redundant index related with the vector $\vec{a}_3$.

There are at least two types of basis sets that leads to a numerical description of the Kohn-Sham wave functions. The first one consists on localized functions and it is suitable to describe isolated molecules in non-periodic conditions. The second type is the plane-waves basis set, which is the most commonly used for periodic systems, where its mathematical formalism is rooted on the Bloch's theorem, shown in Eq. 2.17. The solutions of the one-electron wave functions can be expresed as a plane wave, $e^{i\vec{k}\cdot\vec{r}}$, multiplied by a function $f_j(\vec{r})$ that has the periodicity of the Bravais lattice,
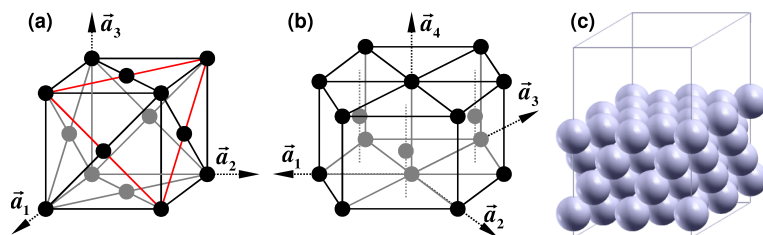
Figure 2.2: (a) Conventional unit cell for fcc metals. The red triangle shows a cut in the (111) direction. (b) Conventional unit cell for hcp metals. (c) Supercell model of an fcc metal surface with an (111) Miller index.

Eq. 2.18 and 2.15.[115, 117] This is a direct consequence of the periodicity of the crystal, where the Hamiltonian of the one-electron wave functions (Eq. 2.3) are periodic, and so are their eigenstates, ψ_j.

$$\psi_j(\vec{r}) = e^{i\vec{k}\cdot\vec{r}} f_j(\vec{r}) \tag{2.17}$$

$$f_j(\vec{r}) = f_j(\vec{r} + \vec{R}) \tag{2.18}$$

The computational cost of solving these equations can be lowered while preserving the quality of the results. I am going to focus on three of them. Firstly, the number of plane-waves can be limited by setting a kinetic energy cutoff. A lower kinetic energy cutoff implies fewer functions when expanding the mono-electronic states of Eq. 2.17. As the eigenvalues in two neighbouring k-points are quite similar, it is only necessary to sample the eigenvalues at a finite number of k-points, reducing drastically the computational effort required to solve the Kohn-Sham equations. Each of those k-points represents a region in the reciprocal space. The k-points define the integration grid in the first Brillouin zone. To decrease the number of k-points, it is possible to take advantage of the lattice symmetry by means of the Monkhorst-Pack method.[118] Finally, the computational cost can be further lowered by using pseudopotentials to describe the core electrons. They will be described in Section 2.1.4.

In heterogeneous catalysis, most of the phenomena occurs at the interface between a crystal and a fluid. As the surfaces are periodic only in two dimensions, there are two ways to describe these surfaces. The first one, largelly used in this dissertation, is the supercell approximation, where few metal layers are interleaved by a vacuum region large enough to avoid interaction between the periodic images, Fig. 2.2 (c).[116] This approximation has the advantage that the electronic structure of the metal is well described, although it can be less efficient if used on isolated molecules, i.e. gas phase. The second way to describe surfaces is the cluster model, used in

some early works, which consist on putting the adsorbates and reactants in a cluster of metal atoms that represent the surface. This approach can be inaccurate if the cluster is very small,[119] as it was used in some early theoretical studies,[120] because the metal eigenstates are described as discrete. In recent years, the rise of available computational power has allowed to compute full nanoparticles instead of small clusters. The electronic structure of nanoparticles will converge to the one of a periodic surface around 16 to 27 Å.[119, 121, 122]

2.1.4 Pseudopotentials

In most chemical problems, the electrons in an atom can be classified into valence and core electrons. While valence electrons are lossely bonded to the atom and are responsible for most of the chemical bonding and other characteristics, the core electrons are tightly bound to the nuclei. To accurately describe core electrons a large kinetic energy cutoff is required, due to the strong oscilations of the wave functions nearby the nuclei, Fig. 2.3 However, the computational burden can be lowered by the use of pseudopotentials. Conceptually, a pseudopotential replaces the nucleus and electron density from the inner electrons with a smooth effective potential, and only valence electrons wave functions are included in further calculations. This approach is known as frozen core approximation.
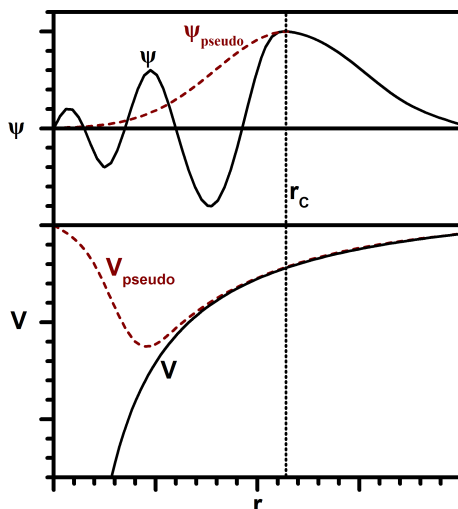
Figure 2.3: All electron (ψ, continuous line) and pseudoelectron (ψ_{pseudo}, dotted line) wave functions and their corresponding potentials. Both wave functions have the same value from a cutoff radius r_C. Adapted from Ref. [117].

Pseudopotentials should be transferable and soft. The transferability

specifies that the pseudopotential should reproduce the properties of the atomic core, independently of the valence states of the atom. The softness means that the number of plane waves required to expand the wave functions of the valence electrons should be as small as possible, i.e., a low kinetic energy cutoff is required. Fig. 2.3 shows the core radius of the pseudopotential, r_c. To increase this radius implies to increase the softness but to lower the transferability, and vice versa: the harder the pseudopotential, the highest the transferability. There most used families of pseudopotentials are the Vanderbilt ultrasoft pseudopotentials (US-PP)[123] and the Projector-Augmented Wave ones (PAW)[124] The results done with the US-PP and PAW approximations are in good agreement with full-electron calculations, but PAW describes better transition metals with strong magnetic moments and also ionic systems.[125]

2.1.5 Modeling of molecules

A molecule in vacuum can be described in either under a plane-waves basis set or under a localized basis set. If plane-waves are being used, the molecule are placed in a box with enought vacuum to avoid spurious interactions between the periodic images of the molecule. Normally 10 to 20 Å will suffice depending on the size of the molecule and the presence of electric dipoles. All molecules in gas phase were described with the plane-waves approximation throughout this dissertation, except for Section 3.2 where localized functions were used as basis set. Despite the good accuracy of describing isolated systems with plane waves, this approximatios is also be computationally inefficient for these systems when compared with the use of localized basis sets. There are many possible basis sets that can be centered on atoms in molecules. To describe organic molecules such as alcohols in gas phase, a very high accuracy at reasonable computational cost can be obtained with the use of a Pople basis set. In this manuscript, I used the 6-311++g(2d,2p) basis set. This means that all the electrons were used to describe C and O atoms, and six gaussian functions were used to describe each one of the core electrons.[126] The valence electrons were splitted in a triple-zeta basis set (311), where the first one has three gaussian functions, and the second and third has one gaussian function each.[126] The ++ stands for the inclusion of two diffuse functions.[127] Finally, g(2d,2p) means that two polarization functions were added on each atom, being d-like for C and O atoms and p-like for H atoms.[128] This setup was considered necessary to correctly describe the polarizations induced by intramolecular hydrogen bonds. A disadvantage of the use of a localized functions is the presence of the basis set superposition error (BSSE). Because in this work the localized functions were only used to compare different conformations of the same

molecule, the BSSE is negligible.

2.2 Microkinetic modeling

Chemical reactions at surfaces are complex processes whose mechanism can be separated in several elementary steps such as the adsorption of one or more reactants, a series of elementary on-surface reactions, and the desorption of one or more products. The microkinetic models are tools that describe the total reaction rate by coupling all these elementary steps provided that all adsorption, reaction, and activation energies are known.[55,73] They are specially useful for large and complex reaction networks, where the analysis of reaction paths becomes impractical. They can also give valuable insights such as the most abundant reaction intermediate and the main desorption products. Instead of indentifying a rate-determining step, the influence of each reaction step on the activity and selectivity is normally quantified with the *Degree of Rate Control*[129] or other frameworks cited herein. Microkinetic models are specific the reactor type and its operating conditions, such as temperature, pressure of reactants and products if any of them is in gas phase, composition in the inlet, catalyst/reactant ratio, and residence time.[74] Each type of reactor has its own design equations and is more suitable for certain applications as described below.

2.2.1 Adsorption kinetics

The adsorption is the first step of heterogeneous catalytic reactions that follow the Langmuir-Hinshelwood mechanism. This process occurs when a gas-phase molecule "C" adsorbs on an empty surface site "*" to form C*, Eq. 2.19. The adsorption energy of "C", E_{ads_C}, can be calculated from the energy of the adsorbate on the surface, E_{C^*}, the energy of "C" in gas phase, E_C, and the energy of the clean empty site, E_*, as shown in Eq. 2.20.[116]

$$C(g) + {}^* \rightleftharpoons C^* \tag{2.19}$$

$$E_{ads_C} = E_{C^*} - E_C - E_* \tag{2.20}$$

In the microkinetic models, the adsorption rates of "C", $r_{ads_{C+}}$, were obtained from the Knudsen equation, Eq. 2.21.[73,75] This equation depends on the density of surface sites per area, N_0, the sticking coefficient, $S_0(T)$, and the molecular mass of species "C", m_C, which are constant during the reaction. Besides, the reaction rate will be dominated during transient conditions by the concentration of empty sites on surface, θ_*, and the partial pressure of "C", P_C. The desorption rate of "C", $r_{ads_{C-}}$, was approximated

to an Arrhenius-like equation, Eq. 2.22,[73] which essentially deppend on the surface concentration of "C*", θ_C. k_B is the Boltzmann constant, h the Plank constant, and "T" the Temperature.

$$r_{ads_{C+}} = \frac{P_C S_0(T)}{N_0 \sqrt{2\pi m_C k_B T}} \theta_* \tag{2.21}$$

$$r_{ads_{C-}} = \frac{k_B T}{h} \exp\left(\frac{E_{ads_C}}{k_B T}\right) \theta_C \tag{2.22}$$

Both equations can be combined to obtain the net adsorption rate of "C", r_{ads_C}. For clarity, all constants are lumped into k_+ and k_-:

$$r_{ads_C} = k_+ P_C \theta_* - k_- \theta_C \tag{2.23}$$

2.2.2 Reaction kinetics

The second step on the Langmuir-Hinshelwood mechanism is the reactions on surface. The rate of the i-th surface reaction 2.24, r_i, can be obtained from Eq. 2.25.[75] That equation depend on the activation energies E_a and E_a' of the direct and inverse reactions respectivelly, and the surface concentrations of species j, θ_j.

$$C^* + {}^* \rightleftharpoons D^* + E^* \tag{2.24}$$

$$r_i = \frac{k_B T}{h} \exp\left(-\frac{E_a}{k_B T}\right) \theta_C \theta_* - \frac{k_B T}{h} \exp\left(-\frac{E_a'}{k_B T}\right) \theta_D \theta_E \tag{2.25}$$

$$r_i = k_{i+} \theta_C \theta_* - k_{i-} \theta_D \theta_E \tag{2.26}$$

2.2.3 Mass balance on common reactor types

Figure 2.4 shows the most common reactor types, starting by the **Batch reactors (BR)**. BR are a closed system, so there is no mass flow into or out the reactor while the reaction is taking place. If the volume of the reaction mixture is constant, the amount of species "j" in the reactor, N_j, depends on the reaction time, t, the volume of the reaction mixture, V, and the rate of formation/consumption of species "j" for reaction "i", r_{ij}, as given by Eq. 2.27.[74, 130] The reactor vessel can include a jacket or a pipe system to cool or heat the reaction mixture and maintain it at a desired temperature. A mixing system is included as well to assure that the composition is constant along all the volume. BR are used to measure kinetic parametres of chemical
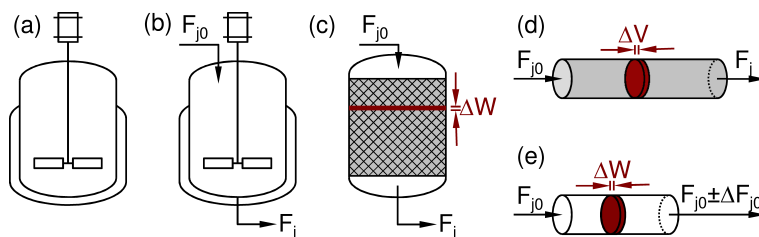
Figure 2.4: (a) Batch reactor (BR). (b) Continuous-stirred tank reactor (CSTR). (c) Packed-bed reactor (PBR). (d) Plug-flow reactor (PFR). (e) Differential reactor (DR). F_{j0} and F_j are the molar flows of species "j" in the inlet and outlet streams respectively.

reactions and on fine chemical applications where small product quantities are required.

$$\textbf{Batch:} \quad \frac{d\,N_j}{d\,t} = V \sum_i \pm r_{ij} \qquad (2.27)$$

In large scale processes, flow reactors are often preferred over batch reactors.[74, 75] In flow reactors, a continuous feed reactants is fed into the reactor while another stream leaves the reactor, Fig. 2.4 (b)-(e). Flow reactors are designed to operate at steady state, meaning that the streams (F_j), concentrations (C_j), reaction rates (r_{ij}), temperatures (T), and other variables are constant over time, Eq. 2.28. However, during the startup and shutdown, flow reactors operate in transient conditions. The flow reactors are classified according to the reaction conditions. For instance, in a **Continuous-stirred tank reactor (CSTR)**, Fig. 2.4 (b), the composition of the whole reaction mixture is constant, so the concentration of species "j" in the outlet stream is the same as into the vessel. In the design equation of a CSTR, Eq. 2.29, the reaction rates r_{ij} depend on the concentrations C_j and viceversa. This leads to a system of non-linear implicit equations that has to be solved for any given volume.[74, 130] Stirred reactors can also operate in semibatch mode. A **Semibatch reactor (SBR)** is essentially a transient reactor with either an input or output steams. SBR are used to enhance the selectivity of certain reaction networks where to have a reactant in high concentrations can lead to unwanted products. SBR also describes the bevaviour of BR and CSTR during startup and shutdown.[74]

$$\textbf{Steady state:} \quad \frac{d\,F_j}{d\,t} = 0; \quad \frac{d\,C_j}{d\,t} = 0; \quad \frac{d\,r_{ij}}{d\,t} = 0, \ \forall i,j; \quad \frac{d\,T}{d\,t} = 0 \quad (2.28)$$

$$\textbf{CSTR:} \quad F_j - F_{j0} = V \sum_i \pm r_{ij} \qquad (2.29)$$

The **Packed-bed Reactor (PBR)**, Fig. 2.4 (c), are flow reactors used for heterogeneous catalytic processes where the catalyst is oin a fixed bed and the reactants and products are in fluid phase. In a PBR the composition of the fluid phase is homogeneous for a given height that encloses a differential amount of catalist, ΔW. The total conversion of the reactor depends only on the total number of active sites, not on the shape of the packed bed. As the number of active sites scales with the mass of catalyst, the design equation and reaction rates are normally written as a function of the weight of catalyst, W, Eq. 2.30.[74, 130] The equations can also be written as a function of the bulk catalyst volume, Eq. 2.31. The latter is also the design equation of a **Plug-flow Reactor (PFR)**, also named tubular reactor, Fig. 2.4 (d). In a PFR, the velocity profile of the fluid phase is considered flat, which is typical for turbulent fluids.[131] Therefore, the fluid is homogeneous in composition for a certain differential of volume ΔV.

$$\textbf{PBR:} \quad \frac{d\,F_j}{d\,W} = \sum_i \pm r'_{ij} \tag{2.30}$$

$$\textbf{PFR:} \quad \frac{d\,F_j}{d\,V} = \sum_i \pm r_{ij} \tag{2.31}$$

Finally, the **Differential reactor (DR)** shown in Fig. 2.4 (e), is particular case of a CSTR with negligible volume, a PBR with negligible mass of catalyst, or a PFR with negligible lenght or volume. As the dimensions of the reactor are made too small compared with the molar flow of reactants, the residence times will be negligible. Therefore, the pressure or concentration of the reactants is almost constant, and just a trace amount of product is present in the outlet, Fig. 2.4 (e). In the microkinetic modeling on heterogeneous catalysys, the use of DR avoids to make a-priori assumptions about reactor volume, mass of catalyst, residence time, or inlet flow. DR are also used experimentally for kinetic measurements on reversible reactions.[74]

2.2.4 Transient differential reactor

The microkinetic model at the present thesis describes the behavior of a differential reactor in transient conditions. The following assumptions were made:

- The reactor is isothermic.

- The residence time in the reactor is negligible compared to the reaction time scales.

- The conversion of the reactants is negligible.

- The pressures of reactants are constant.

- The partial pressures for all products in the outlet stream are negligible and can be set to zero.

- All reaction rates r_{ij} are written per unit of active sites on the surface.

- Each on-surface species occupies one reaction site.

- All the fluid phase is homogeneous. There are not diffusion limitation.

- The sticking coefficients for adsorption were set to 1.

- Adsorbate-adsorbate interactions were ignored.

The mass balance for the surface concentration of a given species "j" can be modeled by Eq. 2.32, which is an ordinary differential equation that deppends on time. s_{ij} are the stoichiometric coefficient of species "j" on each reaction "i". As all surface concentrations are variable upon time and deppend on each other, they are coupled as a system of "n" ordinary differential equations (SODE), corresponding to the "n" species. Because the composition of fluid phase remains essentially constant, the differential equations for all its components (e.g. Eq. 2.31) are eliminated, and only remain the equations related to the surface species, Eq. 2.32. Thus, the SODE of a differential reactor is simpler than for a PFR or a CSTR, which in turns improves the speed of convergence of the solving algorithms. To avoid numerical artifacts, the concentration of empty sites, θ_* must be written as an explicit function from the other adsorbed species, Eq. 2.33, and not in its differential form, Eq. 2.34. The resulting SODEs can be solved by using the Rosenbrock method,[132] where the step size is variable. This algorithm is suitable for SODE that spans on very different time scales, i.e. stiff systems, which is the case of most microkinetic models. Stiff systems require high-precision in floating point operations.[55]

$$\frac{d\theta_j}{dt} = \sum_{i=1}^{n} s_{ij} r_i + r_{ads_j} \tag{2.32}$$

$$\theta_* = 1 - \sum_{j=1}^{n} \theta_j \tag{2.33}$$

$$\frac{d\theta_*}{dt} = -\sum_{j=1}^{n} \frac{d\theta_j}{dt} \tag{2.34}$$

The solutions for the SODEs were computed as follow:

1. Define temperature and pressure of reactants.

2. Calculate the adsorption and reaction constants from equations 2.23 and 2.26.

3. The initial condition is a clean surface: $\theta_{*,t=0} = 1$.

4. Calculate adsorption rates for a given time t, Eq. 2.23.

5. Calculate reaction rates, Eq. 2.26.

6. For each species "j", update the surface concentration after a given timestep, equation 2.32.

7. Calculate the remaining fraction of empty sites, Eq. 2.33.

8. Back to step 4 and proceed until the surface reaches the steady state.

Chapter 3

Adsorption of mono- and poly-alcohols on Pd and Pt(111)

The adsorption of reactants is the first step in heterogeneous catalytic processes. Despite several models exists for the adsorption of small molecules, they do not cover the size and complexity of large sugar polyalcohols derived from biomass. Hence, in this chapter I present a general model for the adsorption of saturated C_1-C_7 alcohols on Pd and Pt(111) surfaces. It starts by the *ab initio* conformational search on 14 mono- and poly-alcohols in gas phase, which comprised the training set: methanol, ethanol, ethylene glycol, 1-propanol, 2-propanol, 1,2-propanediol, 1,3-propanediol, glycerol, 1-butanol, 1,2-butanediol, 1,3-butanediol, 1,4-butanediol, and two diastereomers of 1,2,3-butanetriol (erythro and threo). Then the structure and energetics of these alcohols adsorbed on Pd and Pt was studied. I developed a general model to predict the adsorption energy of any saturated alcohol on these surfaces. Finally, the predictive power of the general model was tested in a validation set composed by eleven sugar alcohols commonly found in biomass: C_4 = erythritol, threitol; C_5 = xylitol, arabitol, ribitol; C_6 = fucitol, sorbitol, mannitol, galactitol, iditol; and C_7 = volemitol. The model also predicts the experimental observations within ± 0.15 eV error bars. The content of this chapter is published in Ref. [32]. The structures can be downloaded from Ref. [133].

3.1   Computational details

The calculations contained in this chapter are divided in two parts. The first one is the *ab initio* conformational analysis of fourteen C_1-C_4 alcohols in gas phase done in the Gaussian 09 package[134] using the 6-311++g(2d,2p) basis set and the B3LYP density functional.[98] Unlike VASP, Gaussian allows inputs in Z-matrix format (this is, specifying bond length, bond angle, and dihedral angles), which allows to automatize the conformational search by using scripts. For each molecule, these steps were followed to find the ground state:

1. The alcohol molecule was generated by specifying the connectivity and bond lengths, which were 1.54, 1.43, 1.07, and 0.98 Å for C-C, C-O, C-H, and O-H respectively.

2. The initial angles were defined as tetrahedral (109.5°).

3. Using a script, different conformations were generated by fixing the dihedral angles to $\pm 60°$ and $180°$, corresponding to gauche($\mp$) and anti dihedrals.

4. All conformations were compared to the ones previously generated to remove those equivalent by symmetry.

5. The conformations were fully relaxed.

6. All vibrational frequencies were checked to be positive, to confirm that they correspond to local minima in the conformational space.

In the second part, the ground state of fourteen alcohols adsorbed on Pd and Pt(111) was obtained using VASP.[135,136] Both surfaces were modelled by a $2\sqrt{3} \times 2\sqrt{3} - R30°$ slab. Each slab has four metal layers, where the two topmost were relaxed while keeping fixed the bottom ones to the bulk distances. I used the PBE density functional,[104] and evaluated the influence of the van der Waals corrections in the adsorption process through the Grimme's DFT-D2 method.[25–27] The plane waves basis set had a kinetic energy cutoff of 450 eV. For the surface calculations, the Brillouin zone was sampled by a $3 \times 3 \times 1$ Γ-centred k-points mesh generated through the Monkhorst-Pack method,[118] and the region occupied with electrons was defined by a Methfessel-Paxton smearing of 0.1 eV.[137] To avoid spurious interactions between the periodic images, a 20 Å vacuum region between slabs was included, and dipole correction along "z".[138] The optimization thresholds were 10^{-5} eV and 0.015 eV/Å for electronic and ionic relaxations, respectively. The ground states of all the alcohols obtained from

the conformational search were relaxed in a $20 \times 20 \times 20$ Å^3 box. Then, their most stable conformations upon adsorption on Pd and Pt(111) were obtained. The adsorption energy was computed using Eq. 2.20 To test that both B3LYP and PBE-D2 yielded qualitatively the same results, the full conformational spectra of glycerol was recalculated with VASP. The results, shown in Fig. 3.1, demonstrate that there is an excellent agreement between both methodologies.
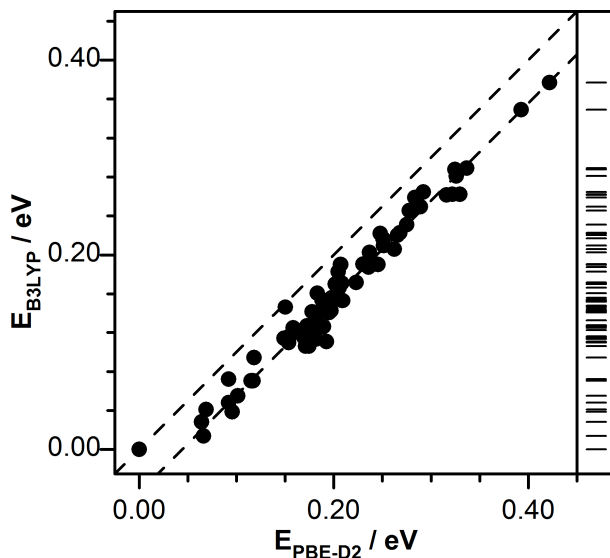
Figure 3.1: Potential energies of glycerol conformations in gas-phase relative to the ground state calculated with B3LYP and PBE-D2. The right side reproduces the corresponding B3LYP glycerol energy spectra from Fig. 3.3. Adapted from Ref. [32].

The structure of alcohols adsorbed on metal surfaces have several local minima besides the true ground state. To obtain structures as close as possible to the true ground state and to reduce the possibility of obtaining only high-energy local minima, an heuristic process was followed, going from the simplest to the most complex molecule. To this end, each molecule was initialized in up to 6 positions, for all molecules in the training and validation sets, as described below:

- **Methanol** binds to the surface through its oxygen atom, and the hydrogen of its hydroxyl group pointing between a top and a bridge position.

- Six different structures of **ethanol** were initialized on Pt(111). Its most stable structure maximize the contact between the carbon tail

and the surface. The rest of the mono-alcohols fulfil that rule.

- **Ethylene glycol** was initialized binding through the oxygen atoms near top positions. The relaxed structures preserve the intramolecular hydrogen bond characteristic of the gas phase. Besides, the the carbon backbone lies on the surface.

- **Glycerol** also adsorbs preserving its three hydrogen bonds. It prefers to adsorb with its hydroxyl groups pointing to the metal, rather than increase the contact between the carbon backbone and the surface.

- The ground state for all alcohols adsorbed on Pd and Pt, roughly preserve the ground state conformation of the gas-phase, or resembles another conformation very close in energy.

- For the poly-alcohols in the validation set, the structures were initialized following these priorities: (1) the alcohol should adsorb through its hydroxyl groups pointing to the surface, (2) the number of hydrogen bonds of the gas-phase structure should be preserved, and (3) if possible, the contact between the carbon tail and the surface should be maximized.

The number of conformations for each alcohol increases exponentially with the size and complexity of the molecule. For instance, erythritol and threitol have 1215 and 1458 conformations in gas phase, respectively.[139] Therefore, it was considered that the ground states for the C_4–C_7 molecules in the validation set followed the rules observed on the smaller C_1–C_4 alcohols. This is, the number of intramolecular hydrogen bonds was maximized while reducing the structural strain. Therefore, between 4 and 10 different conformations were tested for each molecule, taking the structure with lower potential energy as the ground state. In order to avoid on-plane spurious interactions between periodic images, a $3\sqrt{3} \times 3\sqrt{3} - R30°$ slab was used along with a $2 \times 2 \times 1$ Γ-centred k-points mesh for the C_5-C_7 alcohols.

3.2 Alcohols in gas phase

The poly-alcohols under study have several possible conformations with different energetics. Therefore, this study began by a conformational search to find the ground state of these molecules in gas phase, which are shown in Fig. 3.2. The full energy spectra of these conformations is shown in Fig. 3.3. As a general rule, the alcohols tend to minimize strain and to maximize the number of intramolecular hydrogen bonds (HB): 0 for simple alcohols, 1 for diols, 3 for triols, etc. Hydrogen bonds can be classified according to their relative position in a molecule as:

- β, or vicinal, where the OH groups are attached to neighbouring C;

- γ, or conjugated, where the hydroxyls are interleaved by one C atom;

- δ, where the hydroxyls are interleaved by two C atoms; and

- ϵ, where the hydroxyls are interleaved by three C atoms.

Poly-alcohols with two hydroxyl groups attached to the same carbon atom are normally unstable, so the α HB were not considered in this study. After full relaxation, typical bond lengths are around 0.97 Å for O–H, 1.09 Å for C–H, 1.43 Å for C–O, and 1.53 Å for C–C. All angles between two bonds are around the expected value of $109.5 \pm 5.0°$, i.e., the tetrahedral angle. The dihedral angles were also typically in their expected values $180°$ or $\pm 60°$ with deviations of $\pm 9°$. Notable exceptions are the ground states of 1,2-diols and 1,2,3-triols, whose dihedral angle deviates from the expected values $15°$ and $40°$ respectively. This deviation is occurs on O-C-C-O dihedral angles to increase the strength of the β hydrogen bond. In contrast, for the triol conformations containing two-hydrogen bonds, i.e. not the ground states, the maximum dihedral deviations were lower than $25°$. The strongest hydrogen bonds occur in unstrained structures, where the atoms catenate in rings with six or seven members, corresponding to γ and δ the hydrogen bonds.
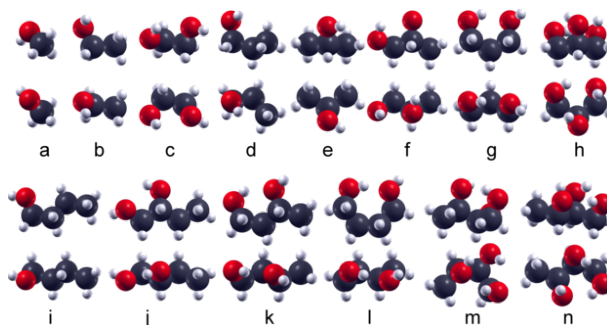
Figure 3.2: Most stable conformations in the gas phase for: a) methanol, b) ethanol, c) ethylene glycol d) 1-propanol, e) 2-propanol, f) 1,2-propanediol, g) 1,3-propanediol, h) glycerol, i) 1-butanol, j) 1,2-butanediol, k) 1,3-butanediol, l) 1,4-butanediol, m and n) erythro- and threo- 1,2,3-butanetriol. Black, red, and white spheres correspond to carbon, oxygen, and hydrogen atoms respectively. Adapted from Ref. [32].

Fig. 3.3 shows the energies for all the possible conformations of the alcohols in gas phase, relative to the ground state for each alcohol. The conformations for the C_1-C_3 monoalcohols are degenerated in energy. For

1-butanol, the presence of strain can make some conformations to rise their energy up to +0.1 eV relative to the ground state. For the poly-alcohols the energy spectra is much broader, and the most important factor that defines the relative energy of the conformations is the number of intramolecular hydrogen bonds. The energy spectra is similar within each one of the poly-alcohol families, namely 1,2-diols, 1,3-diols, and 1,2,3-triols. The energy needed to break one intramolecular hydrogen bond lies in the range between 0.1 and 0.2 eV. The most stable conformation of 1,2,3-triols have three intramolecular hydrogen bonds, but the difference to the conformations with two-hydrogen-bonds is very small. This occurs because the conformations with three hydrogen bonds have strains than rises the potential energy.
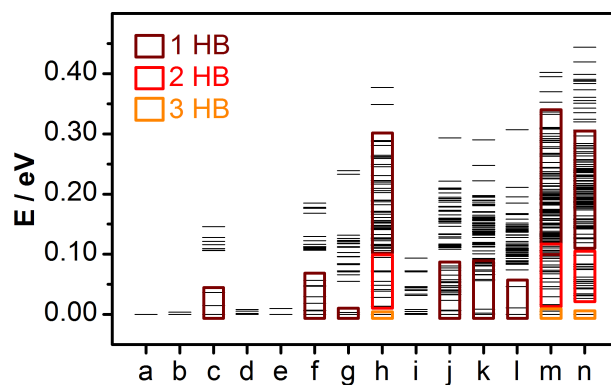
Figure 3.3: Potential energies for all conformations of the considered mono- and polyalcohols relative to the ground state in gas phase: a) methanol, b) ethanol, c) ethylene glycol d) 1-propanol, e) 2-propanol, f) 1,2-propanediol, g) 1,3-propanediol, h) glycerol, i) 1-butanol, j) 1,2-butanediol, k) 1,3-butanediol, l) 1,4-butanediol, m and n) erythro- and threo- 1,2,3-butanetriol. The number of intramolecular hydrogen bonds (HB) is indicated in the boxes. Adapted from Ref. [32].

3.3 Alcohols adsorbed on Pd and Pt(111)

3.3.1 Structural details

Once defined the ground state of the alcohols in gas phase, their adsorption on Pd and Pt(111) was studied. Each molecule was initialized following the heuristic process described in Section 3.1. The most stable molecules obtained upon relaxation are shown in Fig 3.4. For the monoalcohols, the oxygen atom adsorbs on a top position,[140] while the the carbon tail lies parallel to the metal surface to increase the vdW interaction. The contribution of the carbon tail to the adsorption energy was originally proposed by experiments,[141] but early DFT calculations predicted that the carbon tails
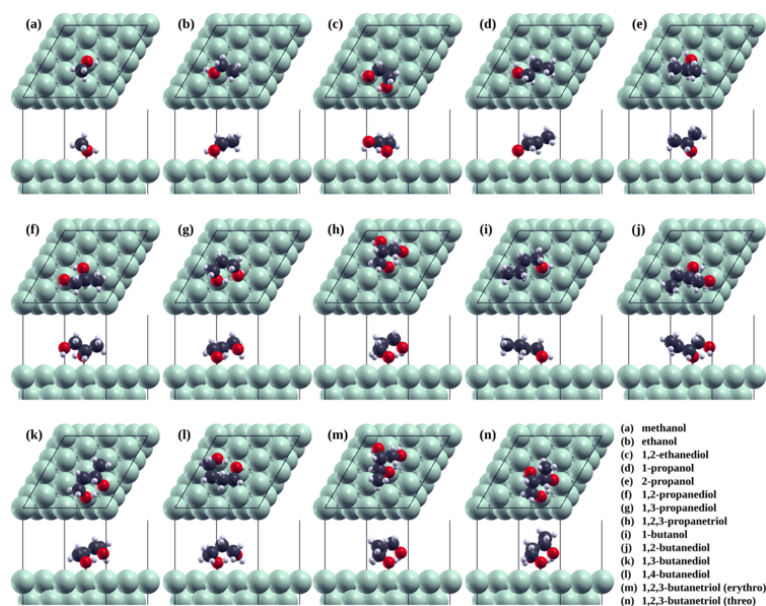
Figure 3.4: Structures of alcohols adsorbed on Pt(111). Green, black, red, and white spheres correspond to metal, carbon, oxygen, and hydrogen atoms respectively. The structures for Pd are very similar and were omitted for simplicity. All structures are publically available on Ref. [133] Taken from Ref. [32].

orient perpendicular to the surface.[142, 143] However, these studies were done on small supercells and neglecting dispersion contributions. Both issues can prevent the carbon tails to interact with the metal surfaces efficiently. Similar to the mono-alcohols, the diols and triols bind strongly through an oxygen atom on a top position. The remaining hydroxyl groups face the surface through their hydrogen atoms. For glycerol, the reported structure is consistent with previous theoretical studies,[144–146] but differs from that in Ref. [147] in which the reported structure lacks two intramolecular hydrogen bonds. The ground-state structure of the alcohols in gas phase is normally preserved upon adsorption. However, some intramolecular hydrogen bonds elongates. The most stable structures were made publicly available in our open database.[133]

3.3.2 Adsorption energies

The DFT and DFT-D2 adsorption energies for all molecules are presented in Fig. 3.5, including the experimental values. For all cases, the DFT-D2 method reproduces much better the experimental values. The interaction energy between an isolated alcohol and a Pd or Pt(111) surface can be defined by three features, namely the number of hydroxyl groups in contact
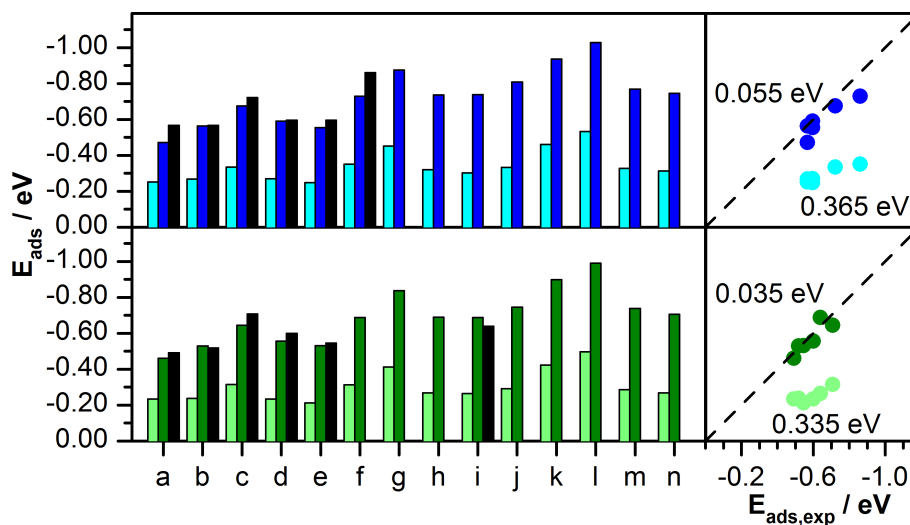
Figure 3.5: Left: Comparison between adsorption energies from temperature-programmed desorption experiments available in literature[17, 24, 141, 148, 149] and those calculated in the present study: a) methanol, b) ethanol, c) ethylene glycol, d) 1-propanol, e) 2-propanol, f) 1,2-propanediol, g) 1,3-propanediol, h) glycerol, i) 1-butanol, j) 1,2-butanediol, k) 1,3-butanediol, l) 1,4-butanediol, m and n) erythro- and threo-1,2,3-butanetriol. Right: Corresponding mean average errors for both DFT and DFT-D2. Adapted from Ref. [32].

with the surface, n_O, the number of carbon atoms in the molecule that are close to the surface, n_C, and the intramolecular hydrogen bonds: n_β, n_γ, and n_δ. In Section 3.3.3, these aspects were considered to deduce an additive model that predicts the adsorption energies for any saturated alcohol. In general, good agreement was found when comaring with structures proposed in the literature.[32]

3.3.3 General equation for the adsorption of alcohols

Following the concepts of functional group additivity and group-group interactions developed in the literature,[50, 58, 59] I developed a model for the adsorption of poly-alcohols on metal surfaces. The main contributions come from the different functional groups, either hydroxyl or CH_x. The second-order interactions comes from the intramolecular hydrogen bonds. The model was first sketched in a way that the contribution for each of the groups was dependent on the "z" position of the atoms with respect to the surface. However, once the results were analyzed, it became clear that a topological model could be drawn by eliminating the explicit dependence of the adsorption energies to the distance of each group to the surface. In the

Table 3.1: Parameters for the model adjusted to the DFT-D2 adsorption data. Mean absolute error and the regression coefficients are shown. All energy parameters (a_X) and MAE in eV.

Metal	a_O	a_C	a_β	a_γ	MAE	R^2
Pd(111)	-0.448	-0.069	$+0.168$	$+0.028$	0.036	0.996
Pt(111)	-0.441	-0.060	$+0.170$	$+0.019$	0.033	0.996

topological model the adsorption energy, E_{ads}, can be expressed as:

$$E_{ads} = a_O\, n_O + a_C\, n_C + a_\beta\, n_\beta + a_\gamma\, n_\gamma \qquad (3.1)$$

Where:

a_O contribution of each hydroxyl group interacting with the metal.

a_C contribution of each CH_x group close to the surface.

a_β energy penalty for weakening the β HB.

a_γ energy penalty for weakening the γ HB.

The weakening for the δ and ε hydrogen bonds is negligible. The $\{n_X\}$ contains the number of effective X=hydroxyl, CH_x, β, or γ hydrogen bonds. The values obtained from the DFT-D2 data are displayed in Table 3.1. Fig. 3.6 shows a remarkable agreement between the adsorption energies obtained by the model with DFT and experimental data.
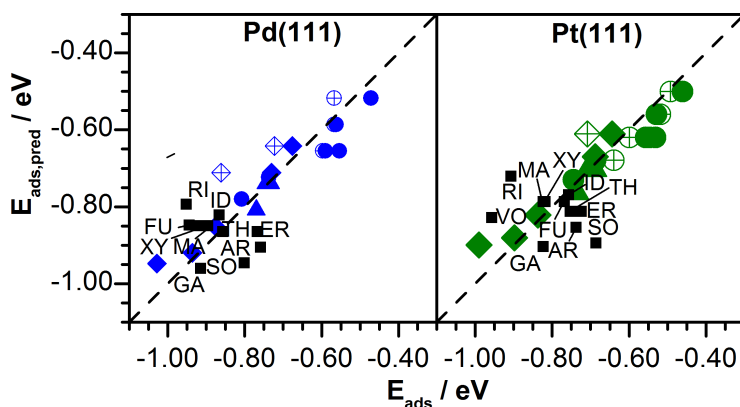
Figure 3.6: Comparison between predicted, $E_{ads,pred}$, and calculated adsorption energies, E_{ads}. Dots, diamonds, and triangles represent monoalcohols, diols, and triols from the training set, respectively. Black squares show the values for the validation set. Experimental data was also included as empty symbols.[17,24,141,148,149] Adapted from Ref. [32].

3.4 Conclusions

I have employed Density Functional Theory with dispersion contributions to analyse the adsorption of 14 mono- and poly-alcohols. These energies were used as the training set for a general model of adsorption energies of alcohols on Pd and Pt(111) surfaces, by analysing the topology of these molecules. In summary, when a polyalcohol adsorbs on Pd or Pt(111) it interacts mainly by its hydroxyl groups, while its intramolecular hydrogen bonds weakens. The carbon tail also contributes to the adsorption energy via van der Waals interactions. I developed a multivariable linear relationship that contains the number of hydroxyl groups that interact with the surface, the number of carbon in the tail, and the energy penalty of loosening the intramolecular hydrogen bonds classified as β or γ. This scaling relationship was validated by predicting the adsorption of larger poly-alcohols with error bars lower than 0.2 eV. For large molecules, their structural complexity can hinder the simultaneous interaction of all the hydroxyl groups with the metal, thus reducing the total adsorption energy. Equation 3.1 can be generalized to include molecular fragments and other functional groups, thus paving the way to study new catalytic routes to transform large oxygenated molecules into chemicals and fuels.[91, 150, 151] As the DFT-D2 methodology succesfully predicted the experimental adsorption energies of a broad set of alcohols, it was used in Chapters 4-7.

Chapter 4

Adsorption of C$_1$-C$_2$ fragments on transition metals

The second step in the study of a reaction network in heterogeneous catalysis, after adsorption, is the description of the molecular fragments that act as intermediates. In particular, this chapter focuses on the intermediates of methanol, ethanol, and ethylene glycol decomposition, whose reactivity is treated in Chapter 5. At the beginning, the formation energies of all intermediates on twelve metals (Ru, Os, Rh, Ir, Ni, Pd, Pt, Cu, Ag, Au, Zn, and Cd) were obtained from DFT taking the most stable conformations for each molecule on each metal. Then, a principal component analysis was applied to reduce the dimensionality of the dataset. Only two principal components are needed to describe the energetics for all intermediates with an astonishing accuracy (MAE=0.08 eV). The principal components correlate with two measurable physical properties, namely the d-band center and the oxidation potential. The structures contained in this chapter were calculated for Ref. [33, 91, 150]. and are available in Ref. [152]. The labels are shown in Fig. B.1-B.3.

4.1 Methodology

4.1.1 Computational details

All electronic calculations were performed in VASP,[135, 136] using the PBE density functional[104] and van der Waals corrections from the Grimme's DFT-D2 method[25, 26] taking the C_6 parameters developed in our group.[27] Spin-polarized DFT was used for all calculations on Ni. The lattice parametres for all metals are listed in Table A.1, along the R_0 and C_6 coefficients derived for the DFT-D2 method.[27] Inner electrons were represented by PAW pseudopotentials,[124, 125] while the valence electrons were described as a linear combination of plane waves with a kinetic energy cutoff of 450 eV. All surfaces were modeled by a four-layers slab and were constructed from the lowest energy cut for the metals: (111) for fcc metals and (0001) for hpc ones. The two topmost layers were fully relaxed while those at the bottom were fixed to bulk distances. Dipole correction were applied along "z" direction to avoid spurious interaction between slabs.[138] The vacuum between the slabs was larger than 12 Å. For surface calculations, the Brillouin zone was sampled by a $3 \times 3 \times 1$ Γ-centered k-points mesh generated through the Monkhorst-Pack method.[118] The molecules in gas phase were relaxed in a box of $20.1 \times 20.0 \times 19.9$ Å^3. All energies included zero-point vibrational energies obtained from the diagonalization of the mass-weighted Hessian matrix. The energy levels were broadened by using a Gaussian smearing with a 0.03 eV width. The optimization thresholds were 10^{-5} eV and 0.02 eV/Å for electronic and ionic relaxations, respectively, and 10^{-7} eV for frequencies calculations.

4.1.2 Energy references

All the energies reported along the manuscript for any given species $C_xH_yO_z{}^*$ adsorbed on the metal surface, $E_{C_xH_yO_z*}$, were computed using Equations 4.1-4.2, taking as reference: the energy of the clean metal surfaces, E_*, and the energy of dihydrogen, E_{H_2}, methane, E_{CH_4}, and water, E_{H_2O} in gas phase The variables on the right side of Eq. 4.2 containing the tag (VASP), are used as obtained from the VASP package and includes the zero-point vibrational energy.

$$x\text{CH}_4 + \left(-2x + \tfrac{3}{2}y - z\right)\text{H}_2 + z\text{H}_2\text{O} + {}^* \longrightarrow \text{C}_x\text{H}_y\text{O}_z{}^* \qquad (4.1)$$
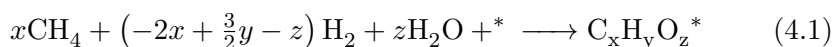
$$E_{\text{C}_x\text{H}_y\text{O}_z*} = E_{\text{C}_x\text{H}_y\text{O}_z*}^{(\text{VASP})} - xE_{\text{CH}_4}^{(\text{VASP})} + \left(2x - \tfrac{3}{2}y + z\right)E_{\text{H}_2}^{(\text{VASP})} - zE_{\text{H}_2\text{O}}^{(\text{VASP})} - E_*^{(\text{VASP})} \qquad (4.2)$$

4.1.3 Algorithm for principal component analysis and regression

1. Generate the unnormalized data matrix $\mathbf{E}$, which contains the formation energy for the molecular fragments on each metal, $E_{C_xH_yO_z*}$, calculated from Eq. 4.2. Each row "i" corresponds to a metal and each column "j" to a molecular fragment. For "m" molecular fragments and "n" metals, $\mathbf{E}$ has size $n \times m$ and its elements are in eV.

2. Calculate the average μ_j and standard deviation σ'_j for each column of $\mathbf{E}$, from Eq. 4.3-4.4. μ_j and σ_j are in eV.

$$\mu_j = \sum_{i=1}^{n} E_{ij} \tag{4.3}$$

$$\sigma'_j = \sqrt{\frac{1}{n}\sum_{i=1}^{n}(E_{ij} - \mu_j)^2} \tag{4.4}$$

3. Generate the deviation data matrix $\mathbf{X}$ from Eq. 4.5. All its components are dimensionless. $\mathbf{X}$ has size $n \times m$ and its elements are in eV.

$$x_{ij} = E_{ij} - \mu_j \tag{4.5}$$

4. Calculate the covariance matrix, $\mathbf{C}$, from Eq. 4.6. The size of $\mathbf{C}$ is $m \times m$ and its elements are in eV^2.

$$\mathbf{C} = \mathbf{X}^t\mathbf{X} \tag{4.6}$$

5. As $\mathbf{C}$ is symmetric, diagonalize it following Eq. 4.7. The matrices $\mathbf{D}$ and $\mathbf{V}$ contain the eigenvalues and eigenvectors of $\mathbf{C}$ in descending order. They have the same size than $\mathbf{C}$, $m \times m$. The elements of $\mathbf{D}$ are in eV^2 and the ones of $\mathbf{V}$ are dimensionless.

$$\mathbf{D} = \mathbf{V}^t\mathbf{C}\mathbf{V} \tag{4.7}$$

6. Select a number of principal components to be used, "l".

7. Generate matrix $\mathbf{W}$ taking the first "l" columns of $\mathbf{V}$. $\mathbf{W}$ has size $m \times l$.

8. Project the deviation data matrix $\mathbf{X}$ onto the basis vectors contained in the columns of matrix $\mathbf{W}$, to get matrix $\mathbf{T}$. $\mathbf{T}$ has size $m \times l$ and its components are in eV.

$$\mathbf{T} = \mathbf{X}\mathbf{W} \tag{4.8}$$

9. The values of $\mathbf{X}$ can be estimated from Eq. 4.9 taking "l" principal components. The formation energy for molecule "j" on metal "i", E_{ij}, can be estimated from Eq. 4.10.

$$\hat{\mathbf{X}} = \mathbf{T}\mathbf{W}^t \tag{4.9}$$

$$\hat{E}_{ij} = t_{i1}w_{1j} + \cdots + t_{il}w_{lj} + \mu_j \tag{4.10}$$

10. The prediction errors ε_j can be obtained from Eq. 4.11 by comparing the predicted and DFT formation energies. The standard error for the predictions, σ_j, can be obtained from Eq. 4.12.

$$\varepsilon_j = \hat{E}_{C_xH_yO_z^*} - E_{C_xH_yO_z^*} \tag{4.11}$$

$$\sigma_j = \sqrt{\frac{1}{m}\sum_{j}^{m}\varepsilon_j^2} \tag{4.12}$$

The formation energy of a molecular fragment on a given metal can be predicted from the remaining set of metals and molecules. To do so, the data matrix $\mathbf{E}$ can be divided in a training and a validation set, for both metals and molecules. As a result, the data matrix divides in four blocks, as shown in Figure 1 in the main text.

1. The principal component analysis is done on the region $\mathbf{I}$ of $\mathbf{X}$, $\mathbf{X}^{\mathbf{I}}$, corresponding to the training set of both metals and molecules. In the present work, this region consisted in 11 metals and only 3 molecular fragments: O*, OH*, and CCHOH*. As a result, the matrices $\mathbf{T}^{\mathbf{I}}$ and $\mathbf{W}^{\mathbf{I}}$ are obtained as descriptors of the metals and molecules of this region. Also, $\mathbf{T}^{\mathbf{III}}=\mathbf{T}^{\mathbf{I}}$ and $\mathbf{W}^{\mathbf{II}}=\mathbf{W}^{\mathbf{I}}$.

2. The metal descriptors for the validation region, $\mathbf{T}^{\mathbf{II}}$, are obtained from Eq. 4.8, using the molecules from the training set of the metal to be predicted, $\mathbf{X}^{\mathbf{II}}$, and inheriting the molecular descriptors already obtained from the PCA, $\mathbf{W}^{\mathbf{I}}$. Also, $\mathbf{T}^{\mathbf{IV}}=\mathbf{T}^{\mathbf{II}}$.
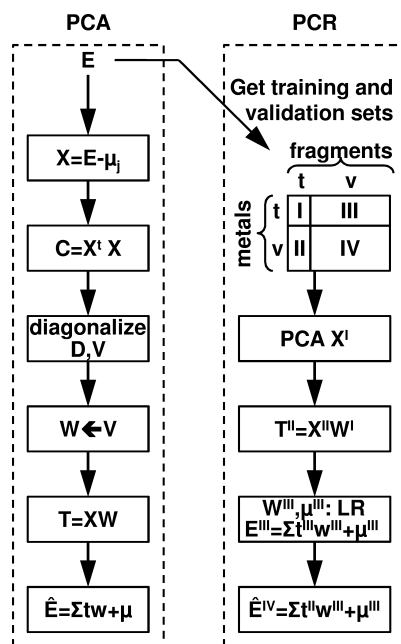
Figure 4.1: Scheme of the principal component analysis and principal component regression procedures. Taken from Ref. [33].

3. The descriptors for the molecular fragments on region **III**, $\mathbf{W^{III}}$, are obtained from a linear regression, using the metal descriptors from $\mathbf{T^I}$. The resulting equation is analogous to Eq. 4.10, and μ_j corresponds to the independent term. Also, $\mathbf{W^{IV}} = \mathbf{W^{III}}$.

4. The energies from the validation set can be obtained from Eq. 4.10.

4.2 Results and discussions

PCA revealed that only two principal components are needed to accurately describe the thermochemistry of the molecular fragments on the metals. Figure 4.2 (a) shows the two metal descriptors for each PC, t_{ik} in Eq. 4.10. The first one expands 16 eV and presents in the endothermic part Au and Ag while Os and Ru stand in the exothermic area. The second component spans a much smaller energy, 5 eV, and the exothermic part contains Os, Ru and Zn while the endothermic section is dominated by Pt and Au. Interestingly, the weights corresponding to the first descriptor of the molecular fragments have all the same sign, Therefore the first PC is directly connected with the metal affinity to form bonds with other species, a characteristic that can be mapped to the d-band centre, Fig. 4.2 (c). The second PC is positive

for species that bind by an oxygen atom, and negative in species that bind through a $-C-OH$ center. Therefore, the second PC can be related to the oxyphilicity of the metal to accept electronic density, i.e., the oxidation potential, Figure 4.2 (d).
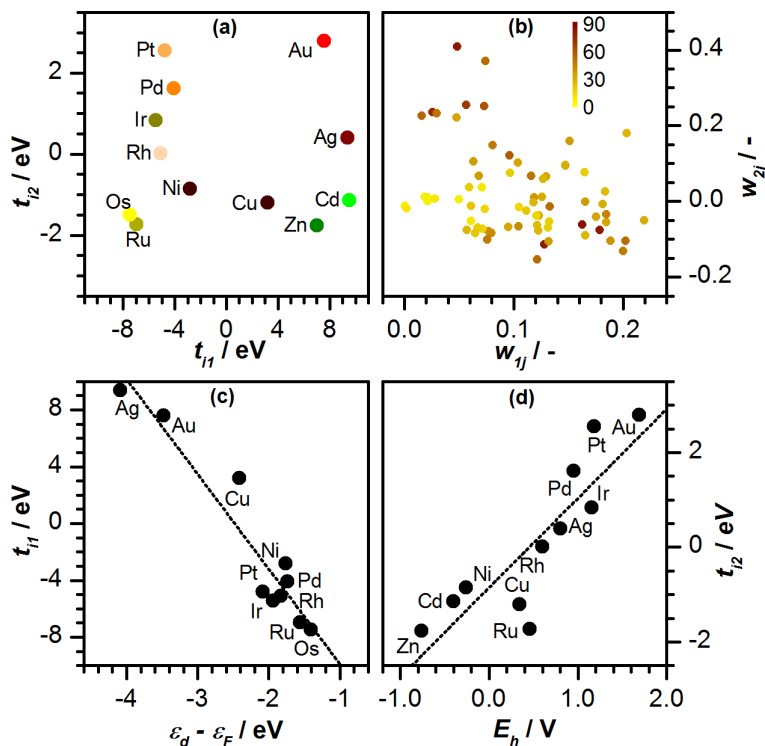
Figure 4.2: (a) PCA descriptors for the metals, t_{ik}, and (b) corresponding weights for the molecules, w_{kj}, according to Eq. 4.10. Correlation maps are included for (c) the d-band centre and the first descriptor and (d) the oxidation potential and the second descriptor. Adapted from Ref. [33].

If we know the formation energies of a small set of molecules on the metal or alloy, we can use the principal component analysis results to predict the formation energies for the full set of on-surface species, $E_{C_x H_y O_z *}$. The number of molecular fragments used as descriptors, "s", should be larger than the number of principal components "l" in order to reduce the noise given by expected inaccuracy of the descriptors' formation energy. In case the number of principal components were equal than the number of descriptors, the results would be analogous to the one reported elsewhere.[153,154] The selection of the molecular fragments should have two criteria. First, they should have a low standard error in the prediction of they own energy within the choosen number of PC; otherwise, they will increase the sys-

tematic error when predicting other molecules. Second, they should have a large weight in at least one of the principal components. Finally, the set of molecules should be as orthogonal as possible. With these criteria, O*, OH*, and CCHOH* were selected as molecular descriptors. Then, by using a leave-one-out (L1O) procedure, the formation energies on one metal was predicted from these three molecular descriptors, following the procedure of items 1-4 on page 58. The prediction errors by using the full dataset and the leave-one-out procedure are compared in Fig. 4.3. While the PCA can predict the formation energies with a MAE=0.08 eV, the use of the L1O procedure yields a MAE=0.12 eV. Further comparisons against previous experimental and theoretical data[155, 156] are done in Ref. [33], showing that the error bars from the L1O procedure are comparable to those from DFT.
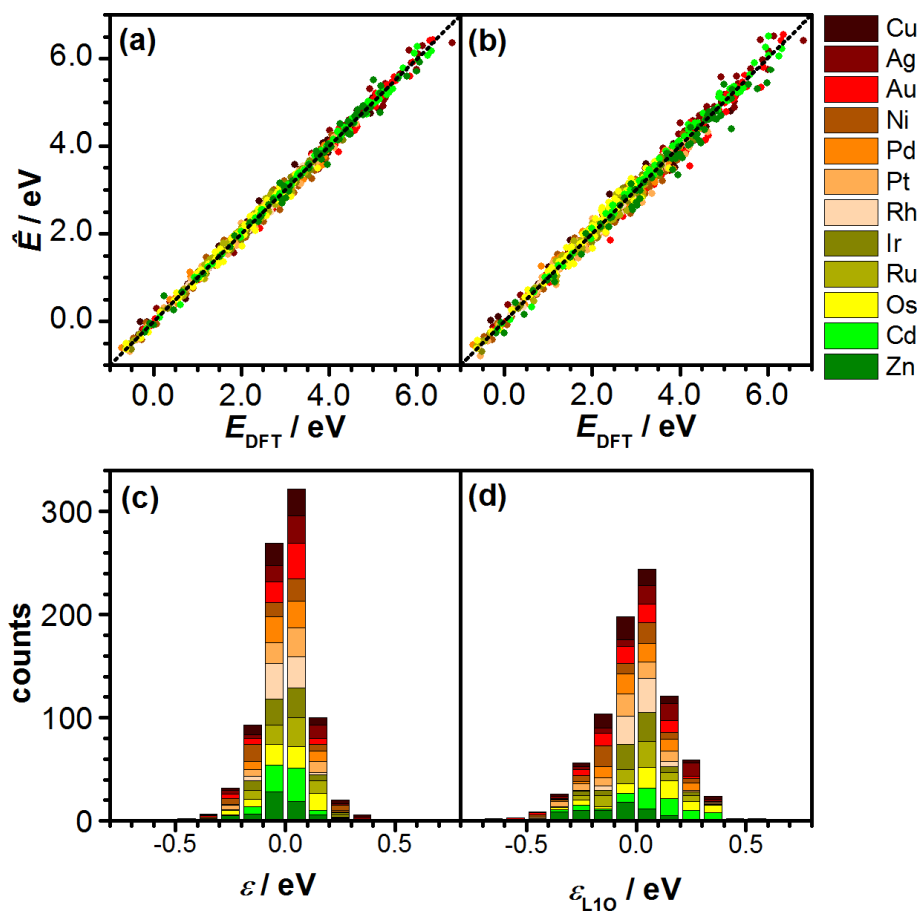
Figure 4.3: Error distribution for the PCA (a) taking all the data, and (b) using the L1O procedure. Cumulative errors are shown on panels (c) and (d). Taken from Ref. [33].

4.3   Conclusions

With the aid of periodic density functional theory, principal component analysis, and linear regressions, I have developed a robust model to predict the thermochemistry of molecular fragments adsorbed on metal surfaces, whose descriptors can be traced back to physically meaningful variables. Firstly, the formation energy of 71 molecular fragments from the C_1-C_2 decomposition network on 12 metal surfaces was computed, taking only the most stable conformations for further analysis. These formation energies can be written as a function of two descriptors within an accuracy of 0.08 eV (MAE), and these descriptors can be mapped as a function of the d-band center and the reduction potential of the metal. A robust methodology based on principal component analysis and regressions was developed to predict the thermochemistry of a large set of intermediates from just three molecules, namely O*, OH*, and CCHOH*. The prediction errors slightly increase to 0.12 eV (MAE), being the major outliers molecular fragments adsorbed on Cd and Ag. The adsorption energies predicted from the methodology based on principal component analysis and regressions are in good agreement with experimental values and previous DFT studies, and are qualitatively equivalent to the use of pure DFT. The molecular fragments on Cu, Ru, Pd, and Pt were used subsequently to the study of reactivity through microkinetic modeling in Chapter 5.

Chapter 5

Decomposition of C_1-C_2 alcohols on transition metals

Hydrogen is an important reactant in many biomass-upgrading processes and can also be used as a clean energy vector. Thus, the future of a sustainable chemical industry depends on the development of new technologies for hydrogen production from renewable resources like non-eddible biomass. This chapter focuses on the full decomposition network of methanol, ethanol, and ethylene glycol on the most stable surfaces of Cu, Ru, Pd, and Pt. The network includes the lateral paths from the decomposition of water, methane and ethane as well as the water-gas shift reaction (WGSR), And extends the database of Chapter 4 to include transition states. This database is complete enough to model the activity of these metals towards H_2 production under industrially-relevant conditions: direct decomposition (DD), autothermal reforming (ATR), steam reforming (SR), and aqueous-phase reforming (APR). The microkinetics of a transient differential reactor was modelled to this end. Linear-scaling relationships were developed for O–H, C–H, C–C, C–O, and C–OH bond cleavages. Further tests indicates that activation energies obtained from the linear scalings are robust enough to predict the catalysts activity within 2 orders of magnitude from DFT results. The content of this chapter is published in Ref. [91, 150]. The structures are available in Ref. [157]. The labels for the intermediates are shown in Fig. B.1-B.3 and the ones for the transition states in Table B.2. This work was done along with Mr. Qiang Li. My contributions were: (i) to obtain the structures of all C_1-C_2 intermediates and transition states on Pd and Pt(111), (ii) to model the microkinetics of DD, ATR, SR, and APR, and (iii) to develop and validate part of the linear-scaling relationships.

5.1 Methodology

5.1.1 Description of the reaction network

The full decomposition network for methanol, ethanol, and ethylene glycol was generated by considering all reactions these alcohols can undergo on metal surfaces For a given on-surface species $C_xH_yO_z$, $x = 0..2$, $y = 0..6$, $z = 0..2$, these reactions can be classified as: dehydrogenations (Eq. 5.1), C–O/C–OH breakings (Eq. 5.2-5.3), and C–C breakings (Eq. 5.4). Each reaction product can experience further cleavages, until the formation of the simplest decomposition fragments, namely C^*, O^*, and H^*. Side reactions were generated from the decomposition networks of methane, ethane, and water, including the water-gas shift reaction mechanism.[158–161] Desorption reactions were included for all species that are stable in gas phase, such as CO, CO_2, H_2, H_2O, aldehydes, alkenols, and others.

$$C_xH_yO_z{}^* + {}^* \rightleftharpoons C_xH_{y-1}O_z{}^* + H^* \tag{5.1}$$

$$C_xH_yO_z{}^* + {}^* \rightleftharpoons C_xH_yO_{z-1}{}^* + O^* \tag{5.2}$$

$$C_xH_yO_z{}^* + {}^* \rightleftharpoons C_xH_{y-1}O_{z-1}{}^* + OH^* \tag{5.3}$$

$$CH_yO_z{-}CH_{y'}O_{z'}{}^* + {}^* \rightleftharpoons CH_yO_z{}^* + CH_{y'}O_{z'}{}^* \tag{5.4}$$
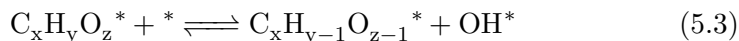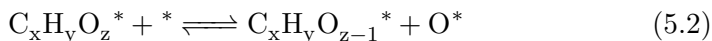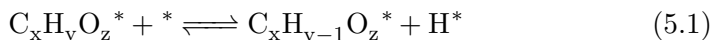
For the C_2 species there are in total 100 dehydrogenations, 55 C–C breakings, and 60 C–O breakings, related with 10, 24, and 21 intermediates in the ethane, ethanol, and ethylene glycol decomposition networks respectively. Besides, there are 23 intermediates and 31 reactions among the species with less that two carbon atoms. The list of intermediates with their corresponding ioChem-BD labels[157] are shown in Fig. B.1-B.3. Moreover, reactions labels are listed in Table B.1-B.2.

5.1.2 Computational details

For all intermediates and transition states, the electronic energies were obtained from VASP[135, 136] following the methodology already described in Section 4.1.1. The transition states were obtained applying the Nudged Elastic Band,[61] the Climbing-Image Nudged Elastic Band,[62] and the Improved Dimer Method.[64, 65] The optimization thresholds were 10^{-5} eV and 0.02 eV/Å for electronic and ionic relaxations, respectively. For IDM and frequencies calculations, the electronic threshold was refined to 10^{-6} eV. All energies reported here included zero-point vibrational energies obtained

from the diagonalization of the mass-weighted Hessian matrix. Besides, the transition states were confirmed to be first-order saddle points of the potential energy surface.

5.1.3 Regressions for the linear-scaling relationships

Based on the reaction database, three types of linear-scaling relationships (LSR) were tested, namely Brønsted-Evans-Polanyi, initial-state scalings and final-state scalings (BEP, ISS, and FSS), Eq. 5.5-5.7. The reactions were classified according to the type of bond breaking, as O–H, C–H, C–C, C–O, and C–OH. The slopes "α" were set to one for ISS and FSS. This leads to a simpler, yet representative, form for the equations, as (i) it eliminates the α regression term avoiding overfitting, (ii) the ISS and FSS equations become independent of the energy reference used. Both conditions are fundamental to use the LSR to predict the activation energies of larger polyalcohols. Then, as Ru, Pd, and Pt followed similar behaviours, the activation energies for each one of these metals was predicted from the energies of the other two, in a Leave-One-Out procedure.

$$\texttt{BEP:} \tilde{E}_a = \alpha \Delta E + \beta \tag{5.5}$$

$$\texttt{ISS:} \tilde{E}_{TS} = \alpha E_{IS} + \beta \tag{5.6}$$

$$\texttt{FSS:} \tilde{E}_{TS} = \alpha E_{FS} + \beta \tag{5.7}$$

5.1.4 Microkinetic model

The activity and selectivity of Cu, Ru, Pd, and Pt were evaluated for four reaction conditions: direct decomposition (DD), autothermal reforming (ATR), steam reforming (SR), and aqueous-phase reforming (APR), Fig. 1.2. Due to the size and complexity of the reaction network, a microkinetic model was used for the analyses, which can be summarized as follows: A stream containing the alcohol, water, and oxygen in variable proportions is fed into an isothermic differential reactor (Section 2.2.4). The reactor operates in transient conditions, with a clean surface as initial conditions. The relative pressures, temperatures, and reaction times resembles those employed experimentally (Fig. 1.2 and Table 5.1. The adsorption rate for the species was modelled from the Knudsen equation (Section 2.2.1). The rate of formation for each surface species is calculated as the sum of the individual rates in which that species participate, Section 2.2.2. In order to do this, the rate coefficients for the elementary steps were evaluated using the

thermodynamic and kinetic parameters from the DFT calculations (MK-DFT). Later on, the activation energies were obtained from linear-scaling relationships (MK-LSR). For Pd, Pt, and Ru, the Leave-One-Out procedure was also used (MK-L1O). The system of differential equations was resolved with Maple 13 using 64 significant digits.[55, 162] A test done using 100 digits converged into the same results. To further the numerical stability of the microkinetic model, a damping function was attached to the reactants pressure, Section A.2. The damping factor τ_P was set to 0.1 s, which assures that the pressure stabilizes in less than 1.0 seconds. The analysis focussed on the H_2 desorption rate, the most common on-surface intermediates, and the preferred desorption products.

Table 5.1: Reaction conditions for the microkinetic model: temperature (T, in K), partial pressures of alcohol, water, and oxygen in the inlet (P_a, P_w, P_{O_2}, in atm).

Process	Alcohol	T	P_a	P_w	P_{O_2}
Direct decomposition	All	600	1.00	0.00	0.00
Autothermal reforming	Ethanol	950	0.30	0.70	0.10
	Ethylene glycol	950	0.30	0.50	0.05
	Glycerol	950	0.25	0.68	0.07
Steam reforming	Ethanol	800	0.20	0.80	0.00
	Ethylene glycol	800	0.25	0.75	0.00
	Glycerol	800	0.10	0.90	0.00
Aqueous phase reforming	Ethanol	550	20.0	80.0	0.00
	Ethylene glycol	550	25.0	75.0	0.00
	Glycerol	550	10.0	90.0	0.00

5.2 Time scales on microkinetic modelling

Microkinetic models are useful tools to study large and complex reaction networks when the analysis of reaction paths become too convoluted. Most MK models in literature are based in flow reactors (CSTR, PFR, or DR) under the steady-state approximation.[159, 163–169] The alternative, known as transient-state formulation, has been scarcely used in literature[170, 171] as it is normally assumed that flow reactors reach their stationary state in few seconds or minutes.[74] In a recent study on the the oxidation of methane on Pd, it was found that the system takes around 10^6 s (12 days) to reach steady state.[171] For complex reaction networks, the ultimate stationary state may not be the same as the pseudo-stationary state observed in experiments and

industrial processes. This idea can be rationalized as follows:
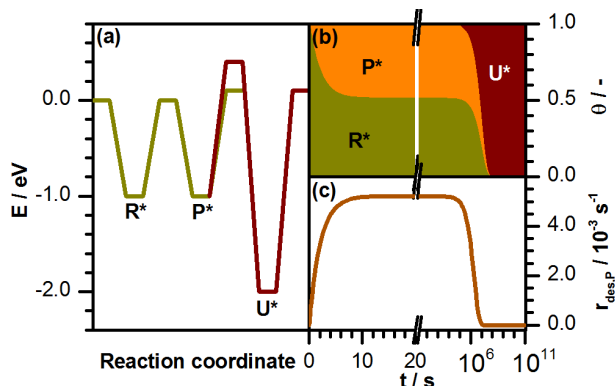
Figure 5.1: (a) Energy profile for the model system Eq. 5.8. (b) Surface coverages of R*, P*, and U* as a function of time. (c) Desorption rate of "P" as a function of time. Reaction conditions: $P_R = 1.0$ atm; $T = 373$ K. Adapted from Supplementary Information of Ref. [91].

Let us consider a system where three isomers interconvert with two consecutive reactions, Eq. 5.8. "R" is the reactant, "P" the desired product, and "U" an undesired by-product. The energy profile is defined by Fig. 5.1 (a). The kinetics of reactions and adsorptions is described by Eq. 2.25 and 2.21. The formation of "U", r_{2d}, is exothermic, but it has an activation barrier is higher than r_{1i} or the desorption of "P". The desorption energy of "U" is larger that "R" and "P", thus "U" will be formed at a rate much lower that "P" and it will poison the surface once formed. Fig. 5.1 (b). When such a system is tested experimentaly, different behaviours will be seen depending on the time scale. Once the reactor is turned on, the desorption rate of "P" will reach a plateau between $t = 10^1 - 10^5$ s. After that, "U" poisoning is not longer negligible and the desorption rate of "P" starts to decrease over time. In four months (aprox. 10^7 s) the production of "P" decreases by two orders of magnitude. Finally, the ultimate stationary state is reached at $t = 10^{10}$ s, or 320 years! In these conditions, the desorption rate of "P" is 9 orders of magnitude lower than during the first day. Under the steady-state approximation, the desorption rate of "P" would describe a poisoned surface instead of the values observed experimentally, considering that a typical catalyst works in the $10^0 - 10^5$ s time range.

$$R^* \underset{r_{1i}}{\overset{r_{1d}}{\rightleftharpoons}} P^* \underset{r_{2i}}{\overset{r_{2d}}{\rightleftharpoons}} U^* \tag{5.8}$$

$$r_1 = k_{1d}\theta_R - k_{1i}\theta_P \tag{5.9}$$

67
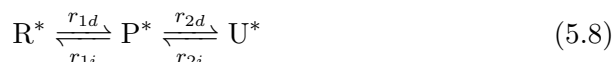
$$r_2 = k_{2d}\theta_P - k_{2i}\theta_U \qquad (5.10)$$
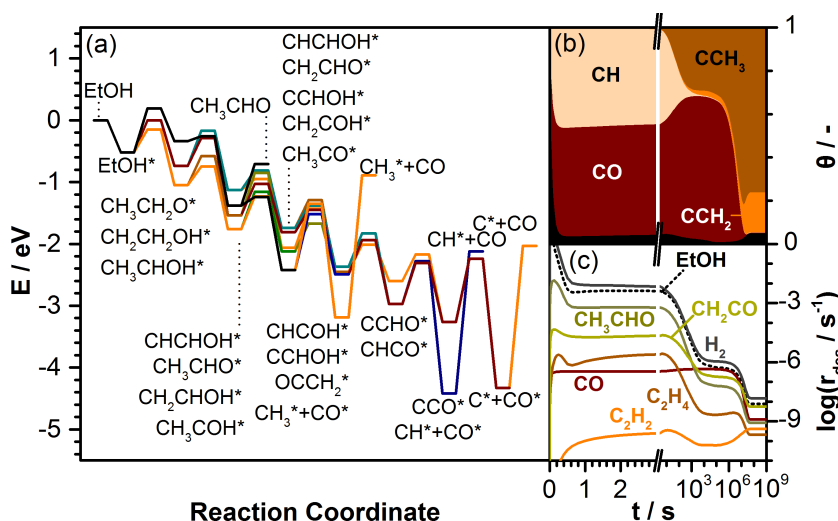
Figure 5.2: (a) DFT energy profile for ethanol decomposition on Pd(111). (b) Surface coverages as a function of time obtained from MK-DFT. (c) Desorption rate of several products as a function of time. Adsorption rate of ethanol is included as reference. Reaction conditions: $T = 600$ K, $P_{ethanol} = 1$ atm. Taken from Ref. [91].

The behaviour described above is unlikely for small reaction networks, in particular when reactions leading to poison formation are excluded. However, large and complex reaction networks, such as the decomposition of ethanol on Pd, Fig 5.2 (a), may include the formation of long-lived intermediates that behave like "U" in Fig. 5.1. Following with the example, in the early stages of ethanol decomposition ($t < 10^0$ s), Pd dehydrogenates the alcohol until a C–C breaking occur, building up a layer of CO and CH poisons, Fig. 5.2 (b). From $t = 10^1 - 10^4$ s, C–O breaking starts to be kinetically relevant, leaving CCH_3 coverages of 30% while the rest is CO (66%). In the meanwhile, most of the CH is consumed. The concentration of CO also increases and reaches a maximum at $t = 10^4$ s (roughly 3 hours), while the desorption rate of H_2 stabilizes in a plateau value around $1.4 * 10^{-6}$ s^{-1}, Fig. 5.2 (c). The surface behavior for $t = 10^4 - 10^6$ s would be the most representative for Pd and can be considered as a pseudo-stationary state. After 60 days, around $5 * 10^6$ s, the desorption rate of hydrogen will still be significant, 30% the initial plateau value. For much longer time scales, CCH_2 and CCH_3 will cover most of the surface and the ultimate steady state will be reached at $t = 6.3 * 10^7$ s (two years) where the desorption rate

of H_2 is just 1% of the previous plateau value. Therefore, in the following analysis, a reaction was considered to enter in a relevant stationary state when the surface concentrations and reaction rates varied less than 0.01%/s, a condition that is fulfilled before 3 hours (t=10800 s) for all processes.

5.3 Linear scaling relationships

The summary of the LSR is presented in Fig. 5.3 and Table B.3. The predictive power of lumped BEP, ISS and FSS were also tested for Ru, Pd, and Pt. Cu follows a different behavior than these three metals, so it was always treated independently, Fig. 5.3. For the O–H bond breaking, the BEP slopes, α, are between 0.18 and 0.39, indicating that the transition states should resemble the initial states.[72] As the ISS had a much higher R^2 and lower mean absoluted error (MAE) than BEP and FSS, the ISS were used to predict the activation energies for O–H breakings for the MK-LSR and MK-L1O models. On the contrary, for C–H, C–C, C–O, and C–OH bond breakings, the BEP slopes, α, were often larger than 0.70, indicating and the transition state for these breakings may resemble the final states.[72] Also, FSS are more suitable for the prediction of the transition states energies as they have much higher R^2 values than BEP and ISS, and lower (or similar) MAE than these scalings. Therefore, the FSS were used to predict the activation energies of C–H, C–C, C–O, and C–OH bond breakings for the MK-LSR and MK-L1O models.

5.4 Catalysts activity

The results from the microkinetic models is shown in Fig. 5.4. In general, there is a good agreement between the DFT results and the ones coming from the LSR and L1O procedures. The differences are within two orders of magnitude, in good agreement with the error bars reported on Ref. [82]. For the direct decomposition, Cu is the most active methal. However, for the reforming technologies, the surface coverage of O and OH on Cu is very high, adding up to 73-99.9% Copper suboxides may appear for oxygen coverages higher than 0.75 ML[172] thus compromising the representability of the metal-only model. For the autothermal reforming, Pt is by far the most active metal, as the CO* poison is efficiently removed by the oxygen stream. However, for the other metals, the oxygen content blocks most of the active sites and also burns most of the hydrogen produced. For the steam reforming of ethanol on Ru, Pd, and Pt, the main surface intermediates are the carbonaceous fragments formed from the C–C breakings as they very stable on surface, thus lowering the overall activity. However, in the steam reform-
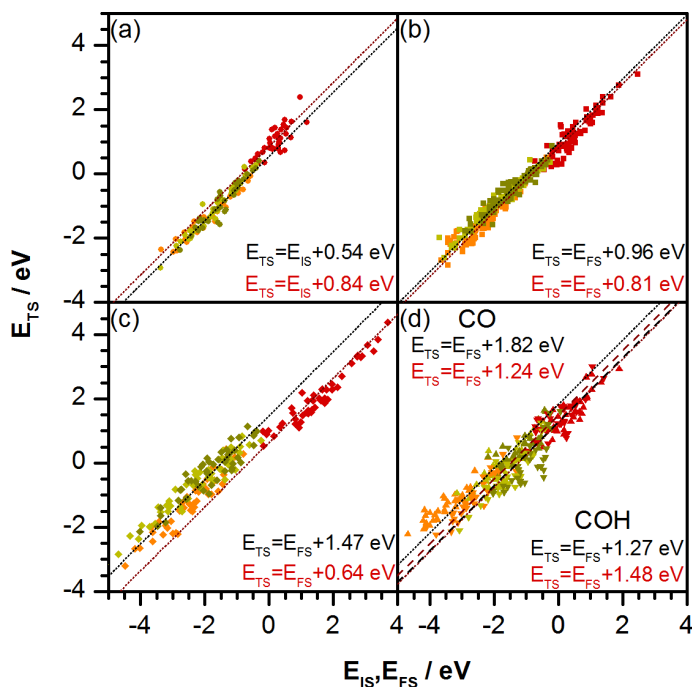
Figure 5.3: Initial-state scaling for (a) O–H bond breaking on Ru, Pd, and Pt (black dotted line) and Cu (red line). Final state scalings for (b) C–H, (c) C–C, and (d) C–O/C–OH bond breakings. The slopes, α, were set to 1.00. Taken from Ref. [91].

ing of ethylene glycol, CO is the most abundant reaction intermediate. As it can be removed from the surface through the water-gas shift reaction, the activity towards hydrogen production is very high on these three metals. Finally, the aqueous-phase reforming is the slowest technology for hydrogen production. For both alcohols, CO is still an important reaction intermediate, showing that the WGS reaction is not efficiently removing the CO poison at these lower temperatures.

This data can be compared to experimental trends. For instance, the activity APR for ethylene glycol on silica-supported metal catalyst follows the order Ru>Pt>Pd.[88] This order is well reproduced for MK-LSR and MK-L1O, while the MK-DFT reports Pt>Ru>Pd. This shows that averaging the data through LSR might avoid some DFT errors. On the other hand, the production rate of CO_2 follows the order Pt>Ru>Pd.[88] This order is obtained from all three microkinetic models considering together the desorption rates of CO and CO_2. All these trends are well reproduced in Fig. 5.4.
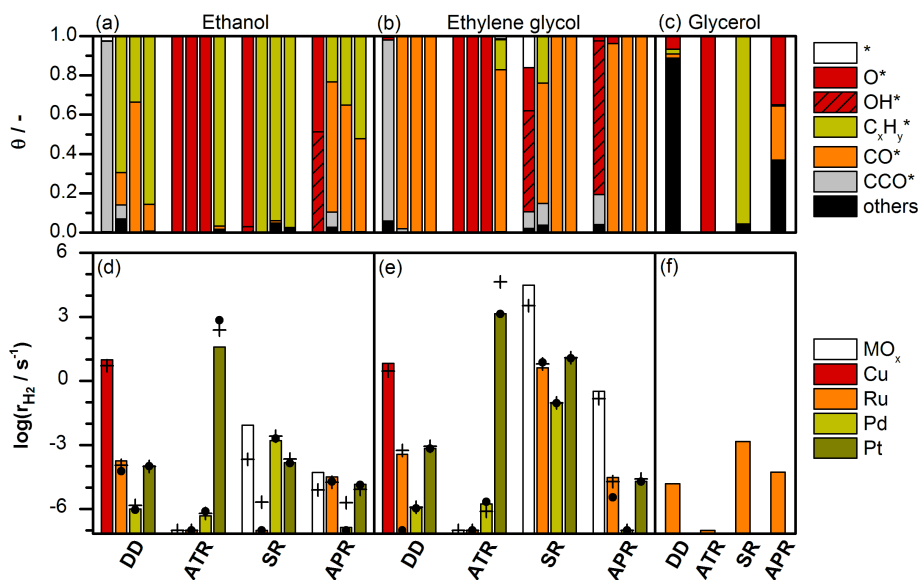
Figure 5.4: Surface coverage obtained with MK-DFT during the direct decomposition, and reforming: ATR, SR, and APR of (a) ethanol and (b) ethylene glycol on Cu, Ru, Pd, and Pt. (c) corresponding values for glycerol on Ru. The hydrogen production rates are shown on panels (d-f). The crosses show the result from MK-DFT, columns from MK-LSR, and dots from the MK-L1O method. White columns stand for configurations where the oxygen content could change the existing catalytic phase. Taken from Ref. [91].

5.4.1 Glycerol decomposition and reforming on Ru(0001)

Finally, the MK-LSR methodology was used to predict the reactivity on Ru(0001) for glycerol, as Ru is expected to produce more hydrogen than Pd and Pt(111) for glycerol steam reforming.[173] The full decomposition network comprises 349 on-surface species and 1944 reaction steps. The MK-LSR was applied as follows: (i) the energies for the C_3 intermediates were obtained by DFT, (ii) with these energies the ISS and FSS from Fig. 5.3 were applied, (iii) the obtained activation energies were employed in the microkinetic model. The coverages and hydrogen production can be seen in Fig. 5.4 (c,f). The most suitable technology to produce hydrogen from glycerol is steam reforming, as aqueous-phase reforming is considerably less active. The activity for glycerol is 4 orders of magnitude smaller than ethylene glycol. This observation agrees with previous experimental results on other catalysts. H_2 production in APR of ethylene glycol is higher than for glycerol on Pt[86] and on Raney catalyst ($Ni_{37}Sn_3$).[87] In addition, the longer the carbon chain of the alcohol (up to C6), the lower the selectivity towards H_2 and the higher to hydrocarbons and other compounds.[86,87,174]

This is well reproduced by the simulations as we obtained 84% of selectivity towards H_2 for ethylene glycol and 72% for glycerol.

5.5   Conclusions

Density functional theory has been employed to to find the intermediates and transition states for the full decomposition network of methanol, ethanol, and ethylene glycol on closed-packed Cu, Ru, Pd, and Pt surfaces. The full network contains 246 reactions, including the water-gas shift and other lateral paths. Linear-scaling relationships were developed to predict the energies from the transition states. For the O–H bond breakings, the transition state structures resemble their corresponding initial states. Also, the energies for transition and initial states scale with each other as an offset. On the other hand, the C–H, C–C, C–O, and C–OH cleavages resemble the final states, and their energies for the transition and final states also scale. Cu behaves different than Ru, Pd, and Pt, so the scalings can be separated in two groups. A microkinetic model was applied using the activation energies obtained from DFT as well as those obtained from linear scaling relationships, and both of them yield qualitatively the same results. There, Cu the most active catalyst for direct decomposition, while Pt is the most active catalyst for autothermal reforming. The remaining metals are not stable for ATR as they have high coverages of oxygen and are prone to oxidation. The activity of Ru is higher for the direct decomposition and steam reforming of ethylene glycol than of glycerol, while both alcohols are comparable in the aqueous-phase reforming. The leave-one-out procedure showed that the linear-scalings on Ru, Pd, and Pt are transferable betveen metals to some extent. However, undesirable deviations may arise when the metal being predicted is not represented on the training set. The influence of spectator molecules and solvation will be discussed of Chapter 7.

Chapter 6

Diversity at the metal-water interface

Despite many green processes in heterogeneous catalysis use water as solvent, there are not complete solvation models for the metal-water interfaces. To sheed light into this phenomenon, ubiquitous in chemical and electrochemical processes, the behaviour of water on Pd(111), Pt(111), and Ru(0001) surfaces was investigated by Born-Oppenheimer Molecular Dynamics (BOMD). The effect of confinement and the thickness of the wetting layers were assessed by measuring the local coordination of the oxygen atoms by means of the tetrahedrality parameter and non-local properties such as density, radial distribution fuctions, and tesselation patterns. This project, done in collaboration with Dr. Luca Bellarosa and Dr. Guillem Revilla-López, is published in Ref. [175]. My main contribution was the analysis of the tetrahedrality parameter in all systems. I also performed part of the *ab initio* molecular dynamics. Snapshots from the BOMD are available in Ref. [176]. Videos of the BOMD are there published as Supporting Information in Ref. [175].

6.1 How ordered is the metal-water interface?

There has been a long-lasting debate about the first wetting layer on transition metal surfaces. The simplest wetting model is a bilayer of hexagonal ice Ih adsorbed on a closed-packed surface, as both structures are commesurate, Fig. 6.2 (h). The resulting water-to-metal ratio is 2:3. This model has two variations, as the hydrogen atoms may point towards the surface (H-down) or opposite to it (H-up).[39, 177] Because of its simplicity, the bilayer model became broadly used within the DFT community.[31, 44, 178–180] In the last two decades, the refinement of experimental techniques such as Scanning-Tunneling Microscopy (STM) allowed the identification of new patterns on the first wetting layer on Pd and Pt(111), with $\sqrt{37} \times \sqrt{37} - R35.3°$, $\sqrt{39} \times \sqrt{39} - R16.1°$, and $p(6 \times 6)$ periodicities. Their water-to-metal ratios are 26:37, 28:39, and 18:36 respectively.[39, 177, 181–185] On Ru(0001), water can also form stripes with a honeycomb pattern.[186] These structures are not commensurate with a stable epitaxial hexagonal ice and may become hydrophobic.[187]

There are few experimental data about the nature of the metal-water interface for coverages much larger than 0.67 ML.[187–189] At 80 K, after the deposition of several bilayers, the characteristics of the water converge into a hexagonal or cubic ice-like structure[189] or a liquid-like one.[190] At higher temperatures, where liquid water is stable, experimental techniques are still unable to characterize the metal-water interface. However, BOMD are able to give valuable insights into this regime, which is fundamental to understand heterogeneus catalytic systems under solvation.[10] In this chapter, BOMD were done in the interface between water and closed-packed metal surfaces: Pd, Pt(111), and Ru(0001). The differentiation between liquid water and ice-like structures was assessed from three properties, namely: the density, the tetrahedrality parameter, and the O–O, O–H, and H–H radial distribution functions.

For hexagonal ice, either Ih or XI, the density is 0.934 g cm^{-1}, the oxygen atoms are tetracoordinated, Fig. 6.3 (a), and the O–O radial distribution functions have well defined peaks in the first and second solvation layers, around r=2.8 and 5.5 Å respectively, Fig. 6.6. However, liquid water is far more complex to be defined. In 1933, Bernal and Fowler concluded that liquid water has (at least) two interpenetrating structures. In the first one, the water molecules are tetracoordinated like in the bulk ice Ih.[191] In the other, the water molecules are tricoordinated and have less restrictions to fit into the available empty spaces. This, in turn, effectively increases the density of the bulk liquid with respect to a regular ice Ih structure to the well-known value of 1.000 g cm^{-1}.[192–194] For this reason, both structures have been named high-density liquid (HDL) and low-density liquid

(LDL) respectively. It has been speculated that both liquid structures may separate in a second, liquid-liquid critical point,[195–197] in the same manner as a supercritical fluid differenciates into vapour and liquid phases below the critical point. This phase separation was proven to occur in recent experiments.[198]
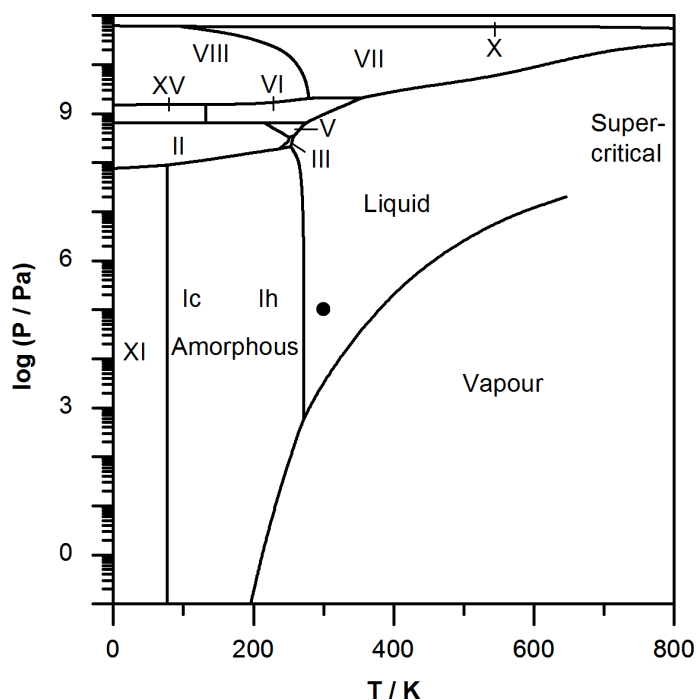
Figure 6.1: Phase diagram of water. The ice phases: IV, IX, XII, XIII, XIV, and XVI are metastable and were omited for clarity. In the absence of a nucleation seed, liquid water can exist in supercooled regime until ~230 K, instead of forming ice Ih.[199] The point represent the conditions at $T = 300$ K and $P = 1$ atm which were used for all the BOMD in Ref. [175]. Adapted from Ref. [200].

The behaviour of the metal-water interface depends on the reactivity of the surface. For instance, the dissociation of water on Ru(0001) is exothermic by –0.54 eV, while for Pd and Pt(111) this process is not so favoured (ΔE =–0.06 and +0.40 eV. Besides, the activation energy is much lower on Ru(0001), +0.57 eV, than for Pd(111) and Pt(111), +0.82 and +0.70 eV. Therefore, Pd(111) and Pt(111) can be considered unreactive surfaces and Ru(0001) a reactive one.

Another factor of debate is the presence of confinement. Early BOMD were done in confined structures and small supercells to make the simulations less computationaly demanding.[34, 35, 45] However, in confined environments, water may develop unusual properties, like the increase of the

viscosity by up to four orders of magnitude.[201] Besides, confinement volume directly affects the water density and therefore the proportion of HDL and LDL. Therefore, the objectives of our study[175] were to quantify the effect of the number of water layers as well as confinement in the behaviour of liquid water.

6.2 Computational details

The metal surfaces were modeled with four metal layers for Pd(111) and Pt(111), and five metal layers for Ru(0001). A multilayered proton-ordered form of ice XI[202] was adsorbed on top of these surfaces. The ice XI structure is hexagonal, similar to ice Ih, but it has a net dipole in "z" direction. The metals and the ice XI were expanded using a $3\sqrt{3} \times 3\sqrt{3} - R30°$ and a 3×3 supercells respectively, as both structures are commensurate within a 3.7-6.3% distortion.[39]
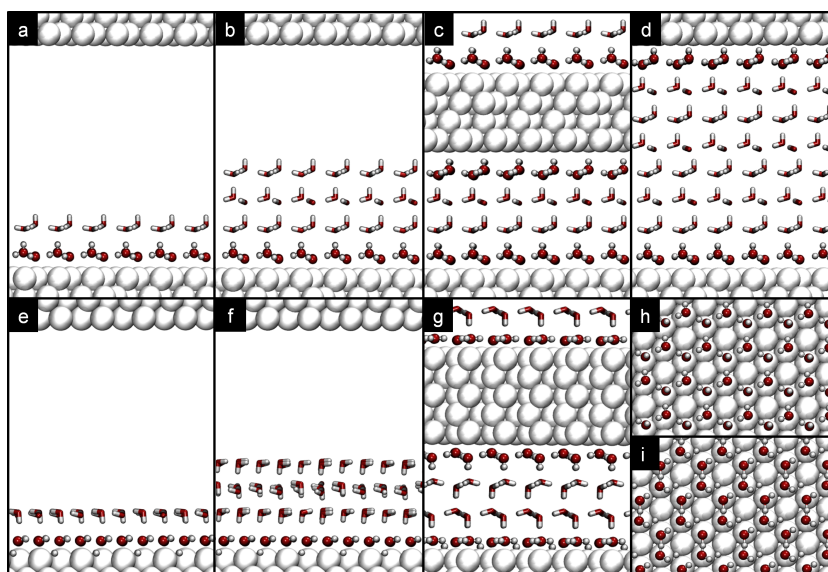
Figure 6.2: Models employed for the adsorption of N-water bilayers on closed packed M=Pd, Pt, and Ru metal surfaces. Longitudinal views of systems for MN systems: Pd and Pt: two (four) free bilayers Pd2, Pt2 in a (Pd4, Pt4 in b), four (eight) confined bilayers Pd4c, Pt4c in c (and Pd8c, Pt8c in d). Equivalent systems are shown for Ru(0001): Ru2 in e, Ru4 in f, and Ru4c in g. Axial views for icelike adsorbed Pd/Pt in h, and Ru in i. Metal, oxygen, and hydrogen atoms are represented by white, red, and black spheres. Bulk water is shown as sticks, respectively. Taken from Ref. [175].

Four water models were used, deppending on the number of bilayers (2,

4, or 8) and the presence of confinement, as shown in Figure 6.2. Herein they are labeled as MN(c), where "M" represents the metal, "N" is the number of water bilayers, and "c" indicates the presence of confinement. The simplest model has two unconfined water bilayers, N=2, Fig 6.2 (a), which contains 36 water molecules adsorbed on 27 metal atoms and 1.67 ML of coverage. By replicating the double bilayer, i.e. N=4, a coverage of 2.67 ML is retrieved. These systems were prepared both unconfined (10 Å vacuum) and confined. Fig 6.2 (b)-(c). The last model consisted on a thicker water slab with 144 confined water molecules, N=8, coverage: 5.33 ML, Fig 6.2 (d).

On Pd and Pt, the first wetting bilayer is more stable in H-down configuration, this is, with the hydrogens atoms pointing towards the surface.[39, 203] However, when growing multiple layers of ice on Pd and Pt in H-down configuration, they turned after 500 fs of simulation time into H-up ones. This agrees with previous theoretical studies showing that the H-up structure is more stable than the H-down for two or more ice bilayers (N≥2).[177, 204] Therefore, all BOMD on Pd and Pt were initialized in H-up configurations. Conversely, all analysis started from the double bilayer model, N=2, while the simple bilayer model, N=1, was not further tested by BOMD. On Ru(0001), half of the molecules on the first wetting layer were put dissociated, Fig. 6.2 (e)-(g), and (i), as that is it most stable configuration.[39, 205]

The DFT calculations were carried on the VASP,[135, 136] using the PBE[104] density functional including dispersion energies from the DFT-D2 formalism.[25–27] Core electrons were described with the PAW formalism.[124, 125] For the relaxations, the plane-wave basis set contained components with energies up to 450 eV. The Brillouin zone was sampled with a $2 \times 2 \times 1$ Γ-centered k-points mesh.[118] With this setup, our tests shown that the density of water is slightly overestimated.[175] The convergence thresholds were set 10^6 eV and 25 meV/Å for electronic and ionic relaxations respectively. The relaxed structures were taken as input for an 11 ps BOMD[206] in the NVT ensemble at 300 K, controlled by a Nosé-Hoover thermostat with 1 fs as time step.[207, 208] The initial 1 ps of the run was taken as equilibration, leaving 10 ps of productive run. For systems comprising four unconfined water bilayers, a larger run was performed. In that case, the equilibration time was 4 ps, and the productive dynamics were extended to 20 ps.

The computational setting of BOMD was simplified to a Γ-only k-point sampling and a cutoff energy of 400 eV. The metal surfaces were kept frozen. Extensive tests done for the structural properties: Radial distribution function (RDF) and tetrahedrality parameter, are maintained after this reduction in computational cost.[175] Besides, a reduction of the time step to 0.5 fs demonstrated no significant difference in these parameters.

6.3   Local coordination and tetrahedrality

To inspect the phase transition between ice and liquid water, we mapped the tetrahedrality parameter "q" of each oxygen atom with respect to its four nearest vicinal hydrogen atoms, Eq. 6.1.[209] The q value is defined between 0.00 and 1.00. Their physical meaning is exemplified in Fig. 6.3. Values close to 1.00 correspond to a perfect tetrahedral configuration. Values lower than 0.88 corresponds to tri-coordinated oxygen atoms, that are acceptors of only one hydrogen bond. Values lower than 0.72 were seldom detected during the BOMDS and correspond to: (i) oxygens that are not acceptors of any hydrogen bond, (ii) short-lived molecular fragments, and (iii) molecules on the topmost layer bordering the vacuum. $\hat{\mathbf{r}}_{\mathbf{j}}$ is the unitary vector whose direction is defined by the central oxygen and the hydrogen "j", in Cartesian coordinates. "$\circ$" is the usual inner product defined in $\Re^3$.

$$q = 1 - \frac{3}{32} \sum_{j=1}^{3} \sum_{k=j+1}^{4} \left(\hat{\mathbf{r}}_{\mathbf{j}} \circ \hat{\mathbf{r}}_{\mathbf{k}} + \frac{1}{3} \right)^2 \tag{6.1}$$
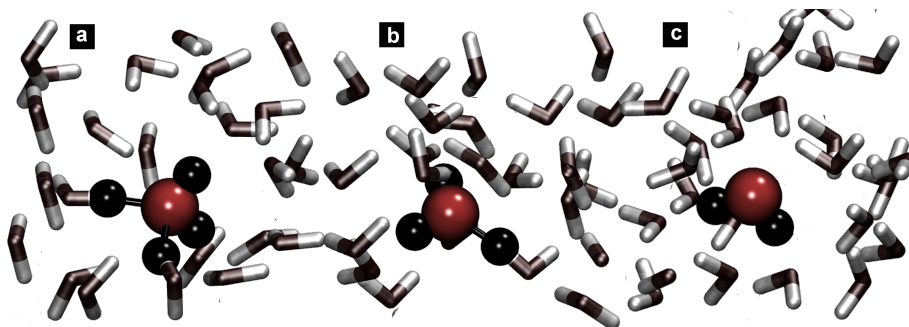
Figure 6.3: Physical meaning of the tetrahedrality parameter. The molecules highlighted on panels (a), (b), and (c) have a tetrahedrality of $q = 0.99$, $q = 0.83$, and $q = 0.69$, being their oxygen atoms tetracoordinated, tricoordinated and dicoordinated respectively. Adapted from Ref. [175].

On the confined systems, the coordination of the oxygen atoms remained essentially constant during the whole simmulation. Besides, all molecules in the bulk conserve their tetrahedrality values close to 1.00. On Pd and Pt, the light-coloured stripes on the first bilayer represent flat-lying water molecules, whose oxygen atoms are coordinated with three hydrogen atoms and a metal atom, $q \approx 0.84$. Then, the first wetting layer on the confined systems conserved their 50% proportion of flat molecules from the initial guess, Fig. 6.2 (c). On the other hand, in the unconfined systems, the water molecules move enough to change their coordination environment,

Fig. 6.4 (a), (b), (e), and (f): While in the bulk some oxygen atoms are tricoordinated, in the first wetting layer few flat molecules rearranges to interact with the bulk liquid.
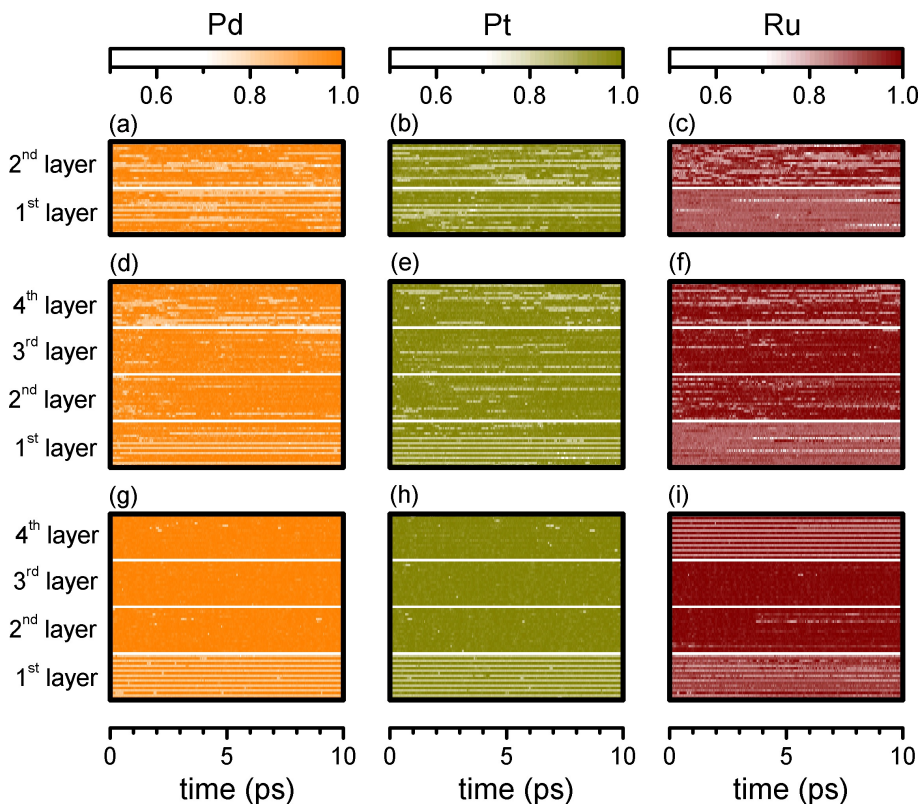
Figure 6.4: Tetrahedrality evolution for each water molecule during 10 ps: M2 systems are on the first row, (a)-(c), M4 on the second row, (d)-(f), while confined M4c are on the third row. M8c systems were omitted for simplicity. The tetrahedrality scale is shown on the top. Darker colors stand for tetrahedral coordination and lighter ones for trihedral or dihedral coordination of the oxygen atom, Fig. 6.3. Adapted from Ref. [175].

For Pd4 (a) and Pt4 (b), most of the non-tetrahedral molecules lies in the metal-water and the vacuum-water layers, but some of them can still be seem in the bulk layers. Globally, 16% of the water molecules are non tetrahedral, in good agreement with a previous study claiming that the water molecules with a non-tetrahedral coordination were 22% in the bulk and 18% in the Au(111)-water interface.[210] On the Ru wetting layer, half of the molecules are dissociated[190] and the distribution of tetrahedralities is different from Pd and Pt(111) surfaces. Instead of a bimodal distribution, most oxigen atoms have a tetrahedrality $q \approx 0.90 \pm 0.04$. Even in the Ru4c

and Ru8c systems, there are sudden changes in the tetrahedrality on the bottom layer. This can be rationalized from the proton transfers between vicinal oxygen atoms, following a Grotthuss-like mechanism.[211]

6.4 Non-local parameters

Density The densities ρ were computed from Eq. 6.2, where N is the number of water molecules in the system; $m_{\text{H}_2\text{O}}$ is the mass of one of them; $\vec{a}_1$ and $\vec{a}_2$ are the two lattice vectors whose component in "z" is zero (i.e. Fig. 2.2 for Ru(0001); and $\Delta\vec{z}$ is computed according to Eq. 6.3. There, z_{max} is the z-coordinate average over all the oxygens belonging to the upper layer; z_{min} is the lowest "z"-coordinate for an oxygen in the system, and 0.60 Å is the ionic radius of the oxygen atom.

$$\rho = \frac{N m_{\text{H}_2\text{O}}}{\langle \vec{a}_1, \vec{a}_2, \Delta\vec{z} \rangle} \tag{6.2}$$

$$\Delta\vec{z} = \left(z_{max} - z_{min} + 2 * 0.60[\text{Å}] \right) \hat{z} \tag{6.3}$$

The water density was 0.95-1.06 g cm^{-3} for unconfined systems and 0.88-1.07 g cm^{-3} for confined ones. Therefore, there was not a significant effect from the use of PBE-D2 or the lack of continuity of the water in the present models. However, some water molecules in the topmost layer displaced from the average z-position to the vacuum.

Tesselation and dissociation patterns Although the lattices employed in the present work, $3\sqrt{3} \times 3\sqrt{3}$, are not commensurate with the ones found experimentally, $\sqrt{37} \times \sqrt{37} - R35.3°$ and $\sqrt{39} \times \sqrt{39} - R16.1°$,[183] the BOMD on the unconfined systems were able to retrieve two characteristics from them. Firstly, during the equilibration, one or two water molecules diffused to the wetting layer, increasing the coverage from 0.667 ML to 0.704–0.741 ML. The experimental coverages are around 0.703–0.718 ML.[183] Secondly, this densification breaks the symmetry from the hexagonal ice, inducing patters with 4-, 5-, 7-, and 8-membered rings.

This is in contrast with previous BOMD studies where these patters were not found due to the small supercell sizes: $p(3 \times 3)$ and $2\sqrt{3} \times 2\sqrt{3} - R30°$.[35, 44] These motifs were also not found on early molecular dynamics studies based on force fields.[40–42] Despite classical molecular dynamics simulations are able to map larger time and length scales than DFT, Fig. 1.1, they depend on rather rigid parametres, such as bond lengths and angles between bonds, thus forcing an hexagonal pattern in the first wetting
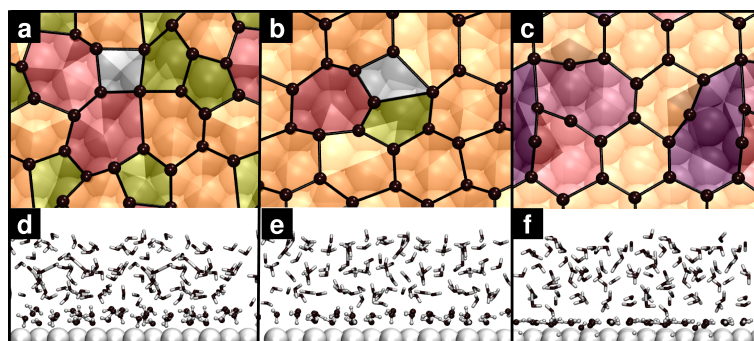
Figure 6.5: Top view of the water layer closest to the metal surfaces in the BOMD simulations for the Pd4 (a), Pt4 (b), and Ru4 (c). The tessellations (Voronoi-like) show local motifs in which water molecules coordinate to each other, following the color code: $4,5,6,7^+$-member cycles in gray; dark yellow, orange, wine, and purple colours. Metal, oxygen, and hydrogen atoms are represented by white spheres and gray sticks in the longitudinal views. Hydrogen atoms are hidden in the axial projection. Adapted from Ref. [175].

layer.[40] Besides, the proportion of dissociated water molecules on Ru(0001) maintained around the 50%.[190]

Radial Distribution Functions   The oxygen–oxygen radial distribution function for oxygen, $g_{O-O(r)}$, averaged over all water molecules for the last 2 ps of simulation, is presented in Fig. 6.6. A comparison with available experimental data on bulk ice and liquid water[212, 213] shows that the M2 and M4 systems have a first peak at 2.80 Å and a broad region centered at 4.5 Å with higher radial distribution. In turn, the second peak for the confined systems is more pronounced, which is characteristic of bulk ice. The case of Ru is peculiar, because it displays a wider peak at 2.8 Å, starting at shorter distances (2.4 Å) than Pd and Pt. This is a consequence of the water dissociation, which produces a plethora of configurations where oxygen atoms accommodate closer to each other.

6.5   Conclusions

Born-Oppenheimer Molecular Dynamics based on Density Functional Theory were used to analyze the behaviour of water on confined and unconfined environments. The liquid-like or ice-like behaviour was assessed from the local coordination through the tetrahedrality besides non-local parameters such as density, radial distribution functions, and tesselation patterns. It was found that surface reactivity has a large impact in the characteristics of the metal-water interface. On Ru(0001) (reactive), 40% to 50% of the
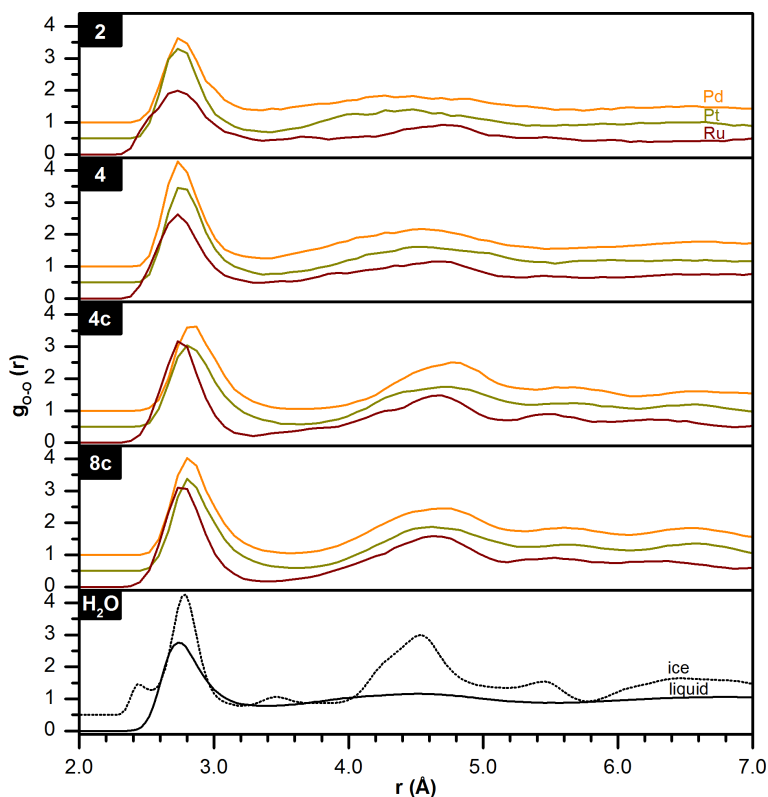
Figure 6.6: Oxygen–oxygen radial distribution function, $g_{O-O(r)}$, for the water molecules adsorbed on Pd (orange), Pt (dark yellow), and Ru (wine) surfaces, for the unconfined (M2, M4) and confined (M4c, M8c) systems. Experimental data for liquid water (298 K and 0.1 MPa, solid black) and ice (122 K, dashed black) are shown for comparison.[212, 213] Taken from Ref. [175].

water molecules remained dissociated during the BOMD. The dissociation products (H_3O^+, OH^-, and others) remains bounded to the surface, so acidification does not occur, as found in experiments. Besides, the wetting layers form a structure that is reminiscent of the electric double layer. On Pd and Pt(111) (unreactive), the BOMD reproduced the irregular 5-, 6-, and 7-membered ring patterns found in experiments, which in turn cannot be obtained from classical molecular dynamics based on force fields. The behavior of liquid water can be reproduced if at least 1.4 nm in each direction is provided to the set of molecules. This is equivalent to a minimum setup of four bilayers on a $3\sqrt{3} \times 3\sqrt{3} - R30°$ supercell for fcc(111)/hcp(0001) surfaces, avoiding the use of confinement. The Pt4 model was used in Chapter 7 to benchmark the behaviour of the implicit solvation model developed in our group, MGCM.[28]

Chapter 7

Solvation effects on reactivity

In complex reaction networks, such the ones of alcohol decomposition, the competition of multiple paths dictates selectivity. This Chapter focuses on the first dehydrogenation step of methanol on Pt, Pd, and Ru, that has been under debate for a long time, and whose preferred reaction path strongly depends on the process. On one hand, during the decomposition of pure methanol, typical of temperature-programed desorption and direct decomposition, the methanol molecules aggregate on the surface. Then, the preferred decomposition pathway is influenced by the molecules coadsorbed with the reactant. This effect is addressed in Section 7.2. On the other hand, under aqueous-phase reforming conditions, the methanol molecules on the surface repel to each other, so other water molecules act as spectator. The effect of water solvation on the reactivity is addressed in Section 7.3. by combining explicit water molecules and the implicit solvation model developed in our group: the Multi-Grid Continuum Model, MGCM.[28] The linear-scaling relationships developed on Chapter 5 were tested on the transition states that include solvation. The content of Section 7.2 is one of the topics discussed in Ref. [150], in which the calculations and analysis were done along with Mr. Qiang Li. The content of Section 7.3 was done with Dr. Miquel García-Ratés and is extensively addressed in Ref. [214] I contributed with all DFT calculations of all intermediates and transition states before aplying the implicit solvent model MGCM.[28] All structures are available in ioChem-BD, Ref. [215].

7.1   Structural models and computational details

For all intermediates and transition states, the electronic energies were obtained from VASP[135,136] using the PBE[104] density functional and vdW[25–27] corrections, following the methodology described in Section 4.1.1.[118,124,125,138]   In Section 7.2, the effect of spectator methanol molecules was addressed by comparing the energy profiles for the first dehydrogenation of methanol with one, two, and three coadsorbed methanol molecules, Fig. 7.1 (CS, S2M, and S3M). In Section 7.3, the decomposition of methanol to formaldehyde on a clean surface (CS) was compared with the same process with two (S2W) and five (S5WR) spectator water molecules, forming a triangle and an hexagonal ring respectively, Fig. 7.1. Also, the implicit solvation model MGCM[28] was used to simulate the effect of a continuum of liquid water as solvent. The systems calculated under the MGCM scheme are identified with the $+\varepsilon$ suffix. Besides, the energy associated to replace an adsorbed water molecule by methanol was benchmarked among all systems, including 71 explicit waters. The full-solvent systems were generated following these steps:

1. A snapshot from the Pt4 system was taken, Chapter 6 and Ref. [175].

2. A flat water was chosen. This molecule was donor of an hydrogen bond and acceptor of another. Its oxygen atom was in contact with the surface.

3. The water molecule was substituted by methanol, preserving the two hydrogen bonds.

4. The adsorbate was relaxed along its vicinal water molecules to get CH_3OH^* (S71W).

5. The methanol was replaced back by a water molecule.

6. Step four was repeated to get H_2O^* (S71W).

7. A snapshot from the BOMD of liquid water was taken from Ref. [175].

8. A water molecule was chosen. It was donor of one hydrogen bond and acceptor of two.

9. The water molecule was substituted by methanol, preserving the hydrogen bonds.

10. The solute was relaxed along its vicinal water molecules to get CH_3OH (71W).
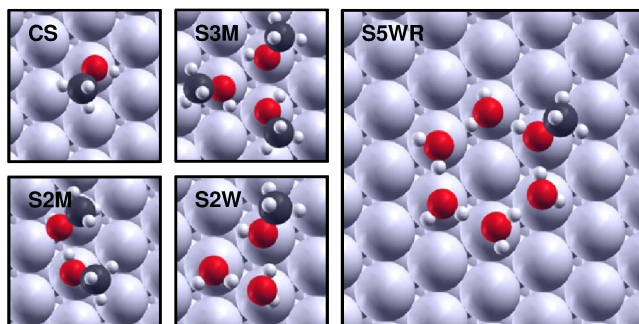
Figure 7.1: Models employed for the adsorption of methanol: Methanol on a clean Pt(111) surface (CS), two and three methanol molecules (S2M, S3M), a methanol molecule with two and five water molecules (S2W, 5WR). The model S2W on Ru(0001) includes a dissociated water molecule.[175,190] Adapted from Ref. [150, 214].

11. The methanol was replaced back by water and the molecule was relaxed again to get H_2O (71W).

12. The replacement energy was obtained from Eq. 7.1.

$$H_2O^*_{(S71W)} + CH_3OH_{(71W)} \longrightarrow CH_3OH^*_{(S71W)} + H_2O_{(71W)} \qquad (7.1)$$

7.2 Effect of spectator methanol molecules on reactivity

The methanol decomposition on Pt(111) may start by the C–H or the O–H bond breaking. However, there is an apparent contradiction between experimental and theoretical results. While TPD experiments on pure methanol indicate that the O–H bond breaks preferentially,[15] well-converged DFT calculations show that the decomposition of a methanol molecule *without any spectator*, Fig. 7.3 (CS), start by a C–H breaking.[140,150] The origin of this discrepancy is that most DFT studies ignore the lateral interactions between methanol molecules, in which the formation of hydrogen bonds compensate the repulsive interactions mediated by the surface, Fig. 7.2. Therefore, on a clean surface without any solvent, the methanol molecules approach each other and a high local coverage takes place even at low pressures and temperatures.[216] However, in the presence of water as solvent, the methanol molecules separate from each other. These models are discussed in Section 7.3.
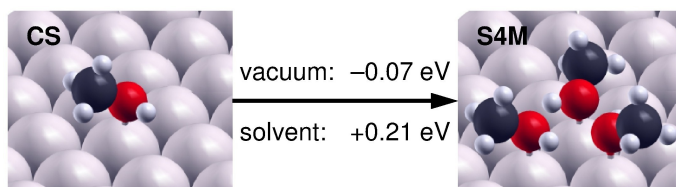
Figure 7.2: Association energies, E_{assoc}, related to the formation of a methanol trimer on a Pt(111) surface. In gas phase E_{assoc} =–0.29 eV and in aqueous solution E_{assoc} =–0.16 eV. Based on data in Ref. [214].

The presence of a spectator methanol molecule can stabilize the transition and final states for the O–H breaking, while slightly destabilizing those for the C–H breaking, Fig. 7.3 (S2M). However, when a second methanol molecule acts as spectator, the transition state for the C–H breaking is strongly destabilized due to structural rigidity, Fig. 7.1 (S3M). Yet, the transition and final states for the O–H breaking are further stabilized, switching the preference to the first dehydrogenation to O–H, just as observed in TPD experiments. This behaviour is also observed on Ru(0001), as discussed in Ref. [150].
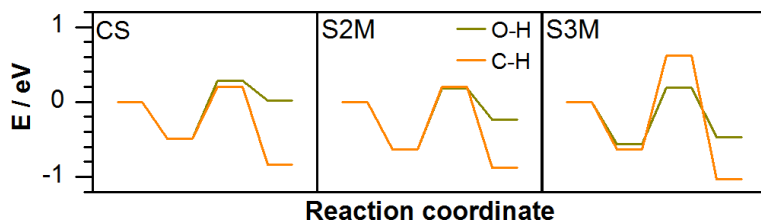
Figure 7.3: Energy profiles for the first dehydrogenation of methanol on a clean Pt surface (CS), and with one and two spectator methanol molecules (S2M, S3M). Adapted from Ref. [150].

7.3 Effect of solvation on reactivity

The energy profiles for methanol decomposition on Pt(111) under different solvation models is shown in Fig. 7.5. These profiles start by the replacement of an adsorbed water molecule by methanol, Eq. 7.1. The replacement energy for all models is benchmarked in Fig. 7.4 against two system with 71 explicit water molecules, with (S71W) and without (71W) a Pt(111) surface. The resulting replacement energy is slighly endothermic (+0.09 eV) if 71 explicit water molecules are used. Among all the models, S2W+ε has the closest match while the remaining models deviate between 0.11 and 0.28 eV.
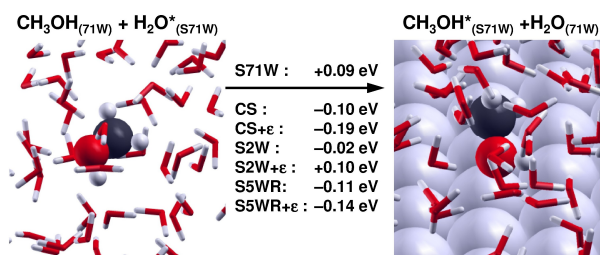
Figure 7.4: Substitution of water molecule adsorbed on Pt(111) by methanol under explicit solvation by 71 water molecules (S71W). The substitution energies for the CS, S2W, and S5WR models, with and without $+\varepsilon$, are shown for comparison. Based on data in Ref. [214].

In the presence of water, theory and experiments agree that methanol decomposition starts by a C–H breaking to produce hydroxymethyl.[217–220] This can be rationalized as, for a methanol molecule in aqueous phase, the hydroxyl group tends to be surrounded by other water molecules, disfavouring its effective interaction with the surface. To account for this, it is fundamental to include explicit water molecules (S2W) near the OH group in order to mimic the first solvation shell. Besides, the inclusion of implicit solvation (S2W$+\varepsilon$) increases the gap between the activation energies and favours C–H breaking, Fig. 7.5, which resuls in a better agreement with experiments.[217] Increasing the number of explicit molecules to form a ring structure (S5WR) does not improve the model, as the gap between the O–H and C–H breaking is just 0.03 eV for vacuum (S5WR) and 0.06 eV under implicit solvation (S5WR$+\varepsilon$), and thus both breakings would be possible in contrast with experiments. This is a consequence of the rigidity of the ring structure. This analysis was extended to Pd(111) and Ru(0001) surfaces in Ref. [214].
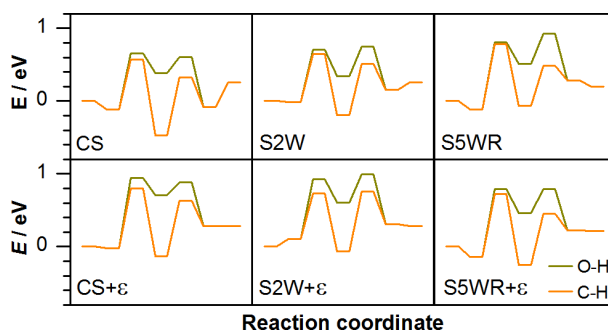
Figure 7.5: Reaction profiles for the dehydrogenation of methanol to CH_2O on Pt(111). ε stands for systems with implicit solvent. Taken from Ref. [214].

Figure 7.6 shows the superposition of the initial- and final state scaling relationships reported in Section 5.3 and the corresponding values calculated in this Chapter. These include the C–H breakings on Pt, Pd, and Ru and the O–H breakings on Pd and Pt, which follow the same mechanism than the reactions in Chapter 5 and Ref. [150]. The O–H breakings on Ru(0001) were excluded, as these reactions are mediated by the coadsorbed OH* and are barrierless, Eq. 7.2-7.3.

$$CH_3OH^* + OH^* \xrightarrow{Ru(0001)} CH_3O^* + H_2O^* \quad E_a = 0.00 \text{ eV} \qquad (7.2)$$

$$CH_2OH^* + OH^* \xrightarrow{Ru(0001)} CH_2O^* + H_2O^* \quad E_a = 0.00 \text{ eV} \qquad (7.3)$$
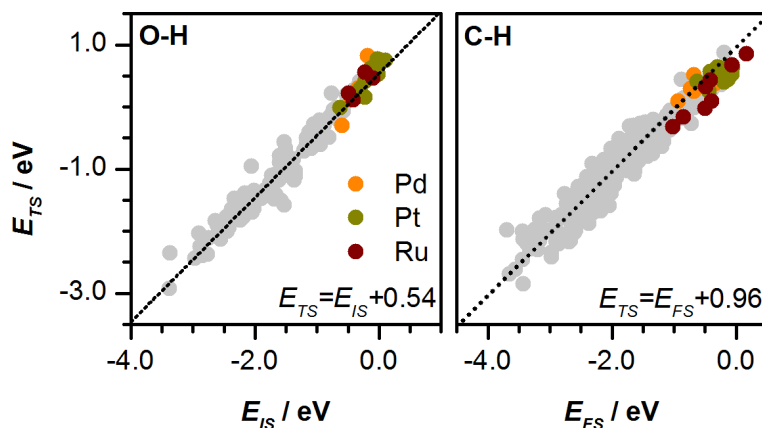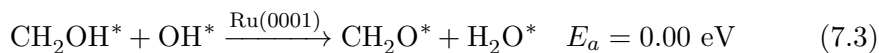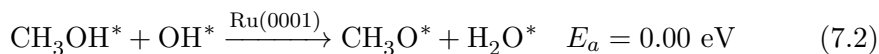
Figure 7.6: Initial-state scaling for O–H and final-state scaling for C–H breaking under all solvation models superposed to the data of Fig. 5.3 (gray) and the scaling line for Pd, Pt, and Ru. Based on data in Ref. [150, 214].

7.4 Conclusions

With the aid of periodic density functional theory and an implicit solvation model, MGCM,[28] we have shed light on the first dehydrogenation steps of methanol on Pt, Pd, and Ru. When pure methanol is present on the surface, methanol molecules aggregate, and the preferred decomposition path starts by the O–H breaking. For aqueous solutions of methanol, which resembles the conditions for aqueous-phase reforming, the methanol molecules on the surface are surrounded by water. The solvent changes the decomposition to start by the C–H breaking. Among all models, the one containing two

explicit water molecules and implicit solvent (S2W+ε) is the most suitable to describe experiments. It is also less computationally demanding than the use of a bulk explicit model. The linear scaling relationships described on Chapter 5 hold when different solvation models are used, thus validating the MK-LSR results for aqueous-phase reforming.

Chapter 8

Role of silver suboxides in the dehydrogenation of acetol to pyruvaldehyde

The content of this chapter is framed in the broader topic of the conversion of glycerol into lactic acid. Glycerol is a low-value chemical currently overproduced as a waste bi-product from the biodiesel production,[13] while lactic acid is among the top-value added chemicals that can be obtained from biomass.[3] This process can be divided in three steps. The first one is the dehydration of glycerol into acetol by means of a Lewis acid, like the alumina from the catalyst support. The second step is the dehydrogenation of acetol to pyruvaldehyde on a metal surface. Finally, the third step is the oxidation of pyruvaldehyde into lactic acid, that proceeds with high yields in Sn-containing zeolites. By using DFT, I rationalized experimental observations on the oxidation of acetol into pyruvaldehyde on a silver catalyst. The experimental part, which was done in the group of Prof. J. Pérez-Ramírez in ETH Zürich,[221] is briefly discussed. The DFT structures are available in Ref [222].

8.1 Glycerol upgrading to lactic acid

Lactic acid is among top value added chemicals obtainable from biomass, according to the US Department of Energy.[3, 223] Currently, lactic acid is mainly produced from glucose as raw material.[14] The first step in this process is the fermentation of a saccharide by Lactobacillus delbrueckii.[14, 224, 225] The optimum pH for this process is between 5 and 7, so along the fermentation, an stoichiometric amount of $Ca(OH)_2$ or $CaCO_3$ should be added to the broth to avoid excesive acidification, Eq 8.1. The lactate solution is then filtered and acidified, producing gypsum $(CaSO_4)$ as a precipitate in stoichiometric amounts, Eq 8.2. The mixture is filtered again to separate the precipitate from the aqueous solution of lactic acid. The main drawback of this process is that gypsum has no further industrial uses and it is considered a waste product.

$$C_6H_{12}O_6 + Ca(OH)_2 \longrightarrow (CH_3CHOHCOO)_2Ca \tag{8.1}$$

$$(CH_3CHOHCOO)_2Ca + H_2SO_4 \longrightarrow 2\,CH_3CHOHCOOH + CaSO_4\downarrow \tag{8.2}$$
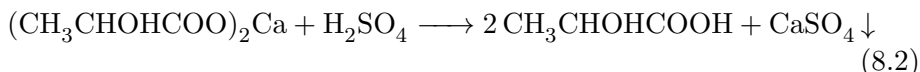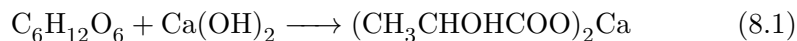
The rise on the demand of lactic acid imposes the development of new, more sustainable ways for its production from renewable resources. Nowadays, glycerol is rising as potential alternative source of lactic acid. Since 2003, the overproduction of glycerol as a by-product from the bio-oil processing has made its price to fall in the recent years. As for 2010, the price of refined glycerol (GLY) was 340 euro, while the unrefined one was sold as a waste product, this is, with a 0 euro value.[13] The reaction steps involved in the catalytic conversion of glycerol into lactic acid are shown in Fig. 8.1, in which several paths can be envisaged.
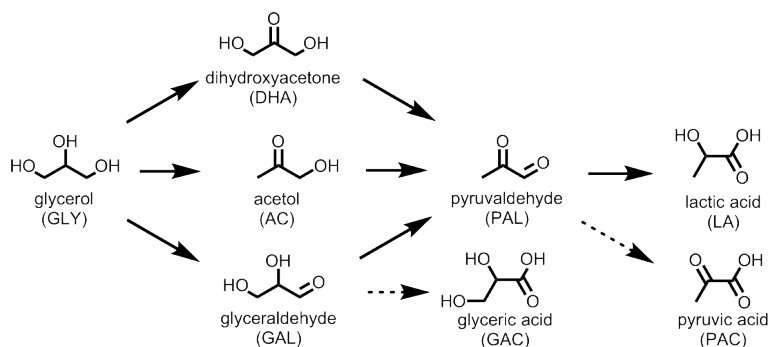
Figure 8.1: Reaction network for the conversion of glycerol to lactic acid. Unwanted lateral reactions are shown as discontinuous lines. Adapted from Ref. [221].

The first path to produce LA starts with the oxidation of the central hydroxyl group of GLY to yield DHA. Among the possible routes to DHA, high yields were obtained from fermentation of GLY by Gluconobacter oxydans, around 90%.[226, 227] GLY oxidation can also be catalyzed by noble metals like Pt-Bi/C[228, 229] and Pd-Ag/C.[230] However, the conversion is lower than 10% while the selectivities range from 75% to 82%. DHA can also be obtained by continuous gas-phase oxidation of GLY in presence of molecular oxygen on iron-containing zeolites.[231] Once optimized, this system has yields and selectivities larger than 90%, and the catalyst also presents good stability. LA can then be obtained from DHA on Sn-containing zeolites, by using either water or methanol as solvents in a continuous process.[232] These zeolites are highly activite due to their Lewis acid sites. Their turnover frequency for the conversion of DHA into LA is 175 h^{-1}. However, a test reported that PAL oxidation to LA is seven times faster on the same conditions.[221]
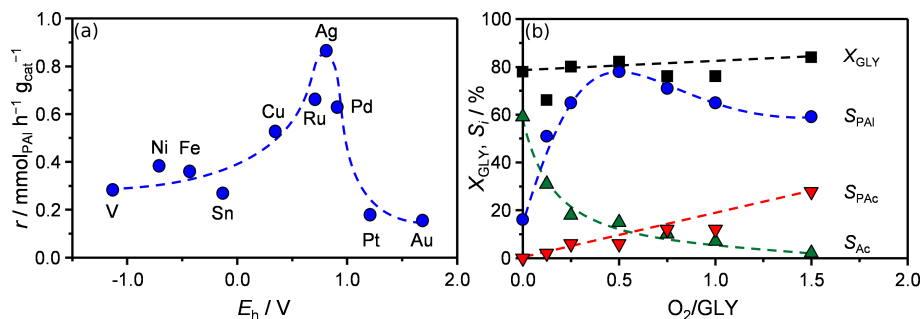
Figure 8.2: (a) Pyruvaldehyde (PAL) formation rate as a function of the metal reduction potential (E_h)[233] for alumina-supported catalyst. (b) Glycerol conversion and product selectivity on alumina-supported Ag as a function of the O_2:GLY ratio. Reaction conditions: Packed-bed reactor, 623 K, 1 bar, 10% wt_{GLY}, LHSV = 6 h^{-1}, O_2:GLY ratio = 0.5 (pannel a). Adapted from Ref. [221].

The conversion of GLY to PAL has been scarcely studied in the recent years. A possible process is the fermentation of GLY to PAL.[224, 234] However, the industrial application of the fermentation is unlikely due to the high toxicity of PAL towards the microorganisms that performs fermentation.[235] An alternative to fermentation was developed by Baltes and Leupold in the 1980s. In this process, GLY is oxidized on an heterogeneous catalyst containing a metal (V, Mo, W, Cu, Ag, S, Pb, Sb, Bi or Fe) in the presence of oxygen.[236, 237] More recently, the group of Prof. Pérez-Ramírez tested this process on ten alumina-supported metal catalysts,[221] and found that Ag has the highest production rate to PAL as shown in Fig. 8.2(a). To improve the selectivity and activity of Ag/Al$_2$O$_3$ and to evaluate its stability for the GLY oxidehydration to PAL, three additional experiments

measured the influence of the temperature, the O_2:GLY ratio at the inlet, and the time on stream on the GLY conversion and PAL selectivity.[221] In the first test, the largest selectivity was achieved at 623 K. In the second one, shown in Fig. 8.2(b), a maximum for PAL selectivity was found for the stoichiometric O_2:GLY ratio of 0.5. In O_2-poor environments, the selectivity to PAL is very low and the major product is AC, which is mainly produced on the support as discussed below. For ratios larger than 0.5, the selectivity to PAL decreases again due to overoxidation to PAC. Finally, in the stability test, the conversion of GLY decreased from 82% to 72% while the selectivity towards PAL was almost constant around 80% after 24h of continuous operation.

The conversion of GLY to PAL occurs in two steps, Fig. 8.4. The first one is the GLY dehydration to AC which catalyzed by the Lewis acid sites on the alumina support.[14] To confirm the role of the support, an experimental test was performed using only the alumina support without any metal on it, resulting in a GLY conversion of 53% with a selectivity to AC as high as 85%.[221] The second step is the AC dehydrogenation to PAL and it is expected to take place on the metal surface. Hence, I focussed all the DFT calculations on the AC conversion to PAL on silver. The aims were to unravel the active phase for this process, to describe the reaction mechanism, and to determine why the process has a high selectivity to PAL.

8.2 Structural models and computational details

Ag surfaces have been studied since the 1970s for their activity in many important reactions, like epoxidation and the obtention of formaldehyde from methanol.[238] In the presence of O_2, Ag can oxidize to form either a bulk oxide, Ag_2O, Eq. 8.3, or a surface oxide.[238–240] In the present chapter, three models were used to describe the silver surface in poor, medium, and oxygen rich conditions, as shown in Fig. 8.3. The first one corresponds to metallic silver, Ag, here represented by 4 layers of a clean 4×4 Ag(111) surface. Although there is debate about the true structure of the surface oxides, the model of Schnadt *et al.*[240] was used herein. This structure, that commensurate with the p(4×4) Ag(111) unit cell, can be generated from metallic Ag(111) by removing 4 metal atoms on the topmost layer while adding 6 oxygen atoms. Model AgO_x/Ag in Fig. 8.3. Finally, for high O_2:GLY ratios, 4 layers of bulk oxide $Ag_2O(111)$ were used. For all structures, two topmost layers were allowed to relax while keeping the other two at bulk distances.

$$2Ag_{(s)} + \frac{1}{2}O_{2\,(g)} \longrightarrow Ag_2O_{(s)} \; ; \; \Delta H = -0.32 \text{ eV} \qquad (8.3)$$
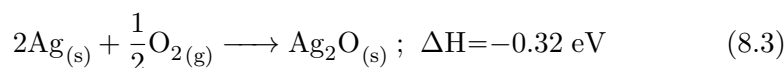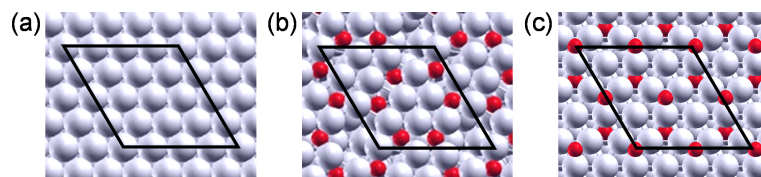
Figure 8.3: Representation of the three surfaces used as models for (a) metallic Ag(111) (b) partially oxidised metal $AgO_x/Ag(111)$, and (c) bulk oxide $Ag_2O(111)$. Taken from Ref. [221].

All the calculations were done WITH VASP,[135, 136] using the RPBE[105] density functional, and PAW pseudopotentials for the core electrons.[124, 125] The valence electrons were described by a kinetic energy cutoff of 450 eV and a Gaussian smearing of 0.1 eV. The Brillouin zone was sampled by a $3 \times 3 \times 1$ Γ-centred k-points mesh generated through the Monkhorst-Pack method.[118] Dipole correction along "z" were included.[138] The transition states were found employing the CI-NEB method.[62] For the calculation of frequencies, the surface atoms were kept frozen, except for the oxygen atoms on AgO_x/Ag or Ag_2O that were participating on the reaction. All of the DFT energies reported include zero-point energies. For electronic and ionic relaxations, the convergence thresholds were set at 10^{-5} and 10^{-3} eV respectively. Finally, an XPS was simulated with spin-polarized DFT. To do this, a *3d* core electron was removed from several probe Ag atoms while the remaining core electrons were relaxed.[23, 241, 242] The dipole correction along "z" was deactivated. All the values are refered to a silver atom on bulk position.

8.3 Acetol dehydrogenation to pyruvaldehyde on Ag

As discussed in Section 8.1, the conversion of glycerol to lactic acid occurs in three steps. The first, the dehydration of GLY to AC, mainly occurs on the catalyst support, Al_2O_3. The second, the oxidation of AC to PAL, occurs on the Ag surface, and the third step, the conversion of PAL to LA, can be catalysed downstream by a Sn-containing zeolite catalyst. I focused the DFT study on the mechanism of acetol to pyruvaldehyde, which occurs as described hereon:

First, AC adsorbs on the surface, Eq. (8.4). Then, the surface abstracts an H atom from the more labile[243] OH bond, Eq. (8.5). This step is performed by an Ag atom on the metallic surface or by an O atom on AgO_x/Ag and Ag_2O. Then, the vicinal C-H bond is broken, forming adsorbed PAL, Eq. (8.6). The reaction proceeds with the desorption of PAL, Eq. (8.7).

When oxygen is present on the surface, the catalyst regeneration starts with the combination of two hydroxyl groups to form a water molecule (8.8), followed by the desorption of the water molecule to create an oxygen vacancy (8.9). Finally, the vacancy is healed by a multiple-steps process related to the adsorption of an oxygen molecule, represented as step (8.10).

$$CH_3COCH_2OH(g) + {}^* \longrightarrow CH_3COCH_2OH^* \tag{8.4}$$

$$CH_3COCH_2OH^* + {}^* \longrightarrow CH_3COCH_2O^* + H^* \tag{8.5}$$

$$CH_3COCH_2O^* + {}^* \longrightarrow CH_3COCHO^* + H^* \tag{8.6}$$

$$CH_3COCHO^* \longrightarrow CH_3COCHO(g) + {}^* \tag{8.7}$$

$$OH^* + H^* \longrightarrow H_2O^* + {}^* \tag{8.8}$$

$$H_2O^* \longrightarrow H_2O(g) + {}^* \tag{8.9}$$

$$\frac{1}{2}O_2(g) + {}^* \longrightarrow O^* \tag{8.10}$$
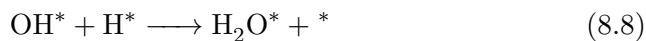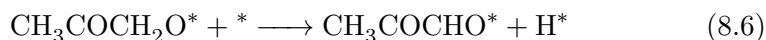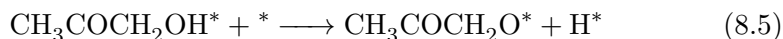
The energy profiles of these reactions are shown in Fig. 8.4. On pure Ag, the adsorption of AC is endothermic and the barrier for reaction 8.5 is higher than on the other two model surfaces, indicating that it proceeds at very low rates. The second dehydrogenation (8.6) occurs simultaneously with PAL desorption (8.7). On Ag_2O, the adsorption of AC is the most exothermic among all systems (8.4), indicating that the bulk oxide traps AC most effectively. The first dehydrogenation (8.5) is less energy-demanding than for pure Ag and the second dehydrogenation (8.6) proceeds rapidly and is followed by the exothermic desorption of the desired product, PAL. However, the regeneration of the catalyst is hindered by the high barrier for water formation (8.8). On AgO_x/Ag, the low reaction and activation energies of step (8.5) suggest that $CH_3COCH_2O^*$ is in equilibrium with adsorbed AC. Reaction (8.6) has a low activation energy and is very exothermic. Since step (8.10) is less energy-demanding, the surface will regenerate faster than in the case of bulk Ag_2O. For the oxidic surface and the bulk oxide, PAL desorption is always exothermic, thus preventing the on-surface over-oxidation to PAC.
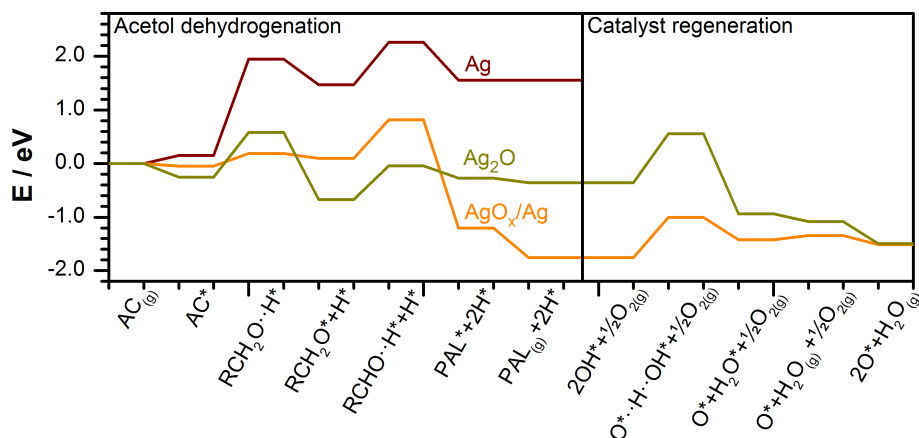
Figure 8.4: Energy profiles for the dehydrogenation of AC to PAL and the regeneration of the AgO_x/Ag and Ag_2O surfaces. Adapted from Ref. [221].

Based on the analysis of the energy diagrams, the high PAL yield found at O_2/GLY=0.5 is explained by its quick desorption from the surface and the easy catalyst regeneration, while the low PAL yields measured for low and high O_2/GLY ratios are due to a very slow CH stripping and a hindered regeneration of the metal, which is in a persistent hydroxyl form, respectively.

8.4 The Ag catalyst is a surface oxide under working conditions

Fig. 8.5 shows the XPS spectra for three catalyst samples. The first sample was prepared by the spray deposition technique, resulting in a layer of deposited Ag_2O nanoparticles of around 5 nm diameter. This catalyst was then reduced in diluted hydrogen to metallic silver, to obtain the second sample. The third sample was obtained from the reactor under the optimal reaction conditions. The *3d* signals for the used catalyst and the as-prepared sample are consistent with the presence of Ag^+ ions, while the signal for the reduced sample is consisted with metallic silver. The XPS peak of the used sample is slightly shifted from the expected Ag_2O. This indicates that the outer layer may not be fully oxidised to Ag(I) and that the oxygen-to-silver ratio at the surface was lower than the expeCted for Ag_2O. To confirm the presence of a surface oxide in the used catalyst, its XPS spectra was measured after successive sputtering with Ar^+. The stepwise shift from 368.0 eV to 367.2 eV after the sputtering implies that an oxidised silver shell formed around a metallic core during the reaction. This 0.8 eV shift is also in good agreement with XPS estimated by DFT, Table

8.1, which predicted that the peak of oxidic silver would appear at binding energy a 0.7 eV higher than that of metallic silver, and that the shift from AgO_x/Ag is smaller than the expected for the bulk oxide Ag_2O.
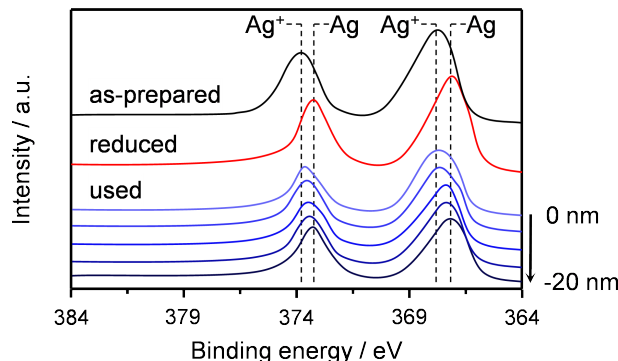
Figure 8.5: XPS characterization of the as-prepared, reduced, and used alumina-supported Ag catalyst. Four additional XPS are included for the used Ag after successive sputtering of the topmost layers with Ar^+. Taken from Ref. [221].

Table 8.1: Calculated core-level shifts for the *3d* transition of an Ag atom on a given atom position with respect to an Ag atom in the bulk in a clean metal slab. Vertex and side indicate the positions of Ag atoms in the 6-atom triangles identified on the AgO_x/Ag surface depicted in Fig. 8.3. Experimental XPS data are reported in Fig. 8.5. Adapted from Ref. [221].

System	Atom position	Shift (eV)
Ag	surface	0.02
AgO_x/Ag	surface-vertex	0.68
	surface-side	0.48
	bulk	0.03
Ag_2O	surface	0.70
	bulk	0.86

8.5   Conclusions

I have employed Density Functional Theory to rationalize the experimental observations on the acetol conversion to pyruvaldehyde on a silver catalyst. The active phase was identified as a surface oxide on silver by means of experimental measures, confirmed by a DFT-simmulated XPS. When the reactor is fed by mixture with low O_2:GLY ratio, the surface is less oxidic

and the dehydrogenation reactions are thermodynamically limited. The most reactive surface was found to be a surface oxide on metallic silver, AgO_x/Ag, which dominates in mild O_2:GLY ratios, around 0.5. In these conditions, the formation of pyruvaldehyde has low energy barriers and the desorption of pyruvaldehyde as product is energically favoured. On oxygen-rich environments, silver tends to overoxidize, adopting a structure similar to a bulk oxide, Ag_2O. This provokes that, at high O_2:GLY ratios, the catalyst regeneration through H_2O formation and desorption becomes hindered, and that further oxidation to pyruvic acid takes place.

Chapter 9

Concluding remarks

The adsorption and reactivity of oxygenated molecules derived from biomass was studied by state-of-the-art multiscale methods based on density functional theory and microkinetics, including novel approaches like dispersion and solvation models. The first research Chapters (3–4) focused on the adsorption of large alcohols and molecular fragments, following with the reactivity of C_1–C_3 alcohols in Chapter 5. The interfaces between liquid water and metal surfaces were studied in Chapter 6, paving the way to study the effect of solvation in reactivity, Chapter 7. As surfaces under working conditions may contain oxides and suboxides, three models were applied for silver on Chapter 8 to account for different oxidation states. In general, the methods applied in this dissertation reproduced accurately experimental trends and semi-quantitative values. All the structures are available in our repository, ioChem-BD, thus satisfying the FAIR data principles: findability, accessibility, interoperability, and reusability. The conclusions specified by Chapter are summarized below.

With respect to the adsorption of mono- and poly-alcohols on Pd and Pt(111):

- The ground-state conformation for a poly-alcohol in gas phase maximize the number of intramolecular hydrogen bonds and minimizes the strain.

- The main energy contributions for the adsorption of polyalcohols on Pd or Pt(111) comes from its hydroxyl groups and the weakening of its intramolecular hydrogen bonds.

- The inclusion of van der Waals interactions is fundamental to reproduce the experimental adsorption energies of alcohols.

- The carbon tail contributes to the adsorption energy via van der Waals interactions, being –0.07 and –0.06 eV/CH_x for Pd and Pt respectively.

- For large molecules, structural complexity may hinder the simultaneous interaction of all the hydroxyl groups with the metal, thus reducing the total adsorption energy.

- The adsorption energy of a C_1-C_7 poly-alcohol can be obtained from its collective descriptor, which contains (i) the number of hydroxyl groups that interact with the surface, (ii) the number of carbon atoms in the tail, and (iii) the energy penalty of loosening β and γ intramolecular hydrogen bonds.

- The model can be generalized to include molecular fragments and other functional groups, thus paving the way to develop new catalytic routes to transform large oxygenated molecules into chemicals and fuels.

With respect to the adsorption of C_1-C_2 fragments on transition metals:

- The energetics for the 71 intermediates from the C_1-C_2 decomposition network on 12 metal surfaces can be written as a function of two descriptors within an accuracy of 0.08 eV (MAE).

- The two metal descriptors can be traced back to the d-band center and the reduction potential.

- With the formation energies of three adsorbates on a given metal, namely O*, OH*, and CCHOH*, the thermochemistry of the remaining intermediates can be predicted within an accuracy of 0.12 eV (MAE), following a robust methodology based on principal component analysis and regressions.

- The adsorption energies predicted from the methodology based on principal component analysis and regressions are in good agreement with experimental and previous DFT studies.

With respect to the decomposition of C_1-C_2 alcohols on transition metals:

- The transition states for the O–H bond breakings resemble their corresponding initial states. Also, the energies for transition and initial states scale with each other as an offset.

- The transition states for the C–H, C–C, C–O, and C–OH cleavages resemble their final states, and the potential energies for their transition and final states also scale as an offset.

- The scaling of Ru, Pd, and Pt can be lumped into one equation while maintaining sufficient accuracy to predict the H_2 production rate.

- During the reforming of C_2 alcohols, several relevant stationary states can be found in the microkinetic models.

- After three hours of reaction, all C_2 reforming processes reached a relevant stationary state within a relative variation threshold of 0.01%/s for all surface concentrations and reaction rates.

- During the autothermal reforming on Ru and Pd, and all reforming technologies on Cu, the surfaces are covered by O* and OH*, compromising the validity of the metal-only model.

- Undesirable deviations in the activity towards H_2 production may arise when linear-scaling relationships are used to predict a metal not represented in the training set (MK-L1O).

With respect to the diversity at the metal-water interface:

- The surface reactivity has a large impact in the characteristics of the metal-water interface.

- Irregular 5-, 6-, and 7-membered rings found in experiments on Pd and Pt were reproduced by Born-Oppenheimer molecular dynamics.

- On Ru, 40% to 50% of the water molecules remained dissociated, in good agreement with the experimental measures.

- On Ru, the wetting layers form a reminiscent of the electric double layer.

- On Ru, the dissociation products (H_3O^+, OH^-, and others) remains bounded to the surface, so acidification does not occur, as found in experiments.

- The behavior of liquid water can be reproduced if at least 1.4 nm in each direction is provided to the set of molecules. This is equivalent to a minimum setup of four bilayers on a $3\sqrt{3} \times 3\sqrt{3} - R30°$ supercell for fcc(111)/hcp(0001) surfaces, avoiding the use of confinement.

With respect to the solvation effects on reactivity:

- When pure methanol is present on the surfaces, methanol molecules aggregate and the preferred decomposition path starts by the O–H breaking.

- For aqueous methanol solutions, which resembles the aqueous-phase reforming conditions, the methanol molecules on the surface are surrounded by water. The solvent changes the decomposition to start by the C–H breaking.

- The model containing two explicit water molecules and implicit solvent (S2W+ε) is the most suitable to describe experiments.

- The linear scaling relationships described on Chapter 5 hold when different solvation models are used, thus validating the MK-LSR results for aqueous-phase reforming.

With respect to the role of silver partial oxides in the dehydrogenation of acetol to pyruvaldehyde:

- Experimental observations found that the O_2:GLY ratio in the feed influences the nature of the active phase. For sub-stoichiometric ratios, $0.0 < O_2$:GLY$ < 0.5$, metallic silver predominates. For oxygen-rich environments, $0.5 < O_2$:GLY, the bulk oxide Ag_2O is formed. For stoichiometric ratios, O_2:GLY$=0.5$, a surface oxide of silver is formed.

- The oxidation potential for each metal also influences the reactivity of the metal.

- When the reactor is fed with a mixture with an sub stoichiometric O_2:GLY ratio, the surface is oxygen-poor and the acetol dehydrogenation is thermodynamically limited, thus lowering the production rate of pyruvaldehyde.

- In oxygen-rich environments, O_2:GLY ratio larger than 0.5, the surface adopts a structure similar to a bulk oxide, Ag_2O. This hinders the catalyst regeneration through H_2O formation and desorption.

- The most reactive surface was the surface oxide on metallic silver, AgO_x/Ag, which dominates in O_2:GLY ratios 0.5. There, both the dehydrogenation of acetol to pyruvaldehyde and the catalyst regeneration are promoted.

Appendices

UNIVERSITAT ROVIRA I VIRGILI
THEORETICAL STUDIES OF CHEMICAL PROCESSES FOR BIOMASS CONVERSION ON METAL CATALYSTS
Rodrigo Antonio García Muelas

Appendix A

Additional methodological details

A.1 Characteristics of the bulk metals

The lattice parametres corresponding to the minimum energy were obtained by regression using the Birch Murnaghan equation. For hcp metals, the c/a ratio was also varied until both parametres were converged to 10^{-5} Å. The C_6 parametres were obtained from[27] or following the methodology detailed therein.

Table A.1: DFT and experimental[233] lattice parameters (a, in Å) for *fcc* and *hcp* metals studied along the dissertation. $[\frac{c}{a}]$ ratio is included for *hcp* metals. R_0 and C_6 (in Å and J nm^6 mol^{-1}) parametres for the Grimme's D2 method[25] were obtained following the procedure on Ref. [27].

Metal	$a_{\mathrm{DFT}}, [\frac{c}{a}]_{\mathrm{DFT}}$	$a_{\mathrm{EXP}}, [\frac{c}{a}]_{\mathrm{EXP}}$	R_0	C_6
Cu	3.634, −	3.615, −	1.562	2.740
Ag	4.147, −	4.086, −	1.819	5.481
Au	4.156, −	4.079, −	1.823	7.308
Ni	3.518, −	3.524, −	1.543	2.383
Pd	3.939, −	3.890, −	1.690	5.510
Pt	3.968, −	3.924, −	1.750	7.000
Rh	3.824, −	3.803, −	1.677	4.364
Ir	3.872, −	3.839, −	1.698	6.163
Ru	2.710, 1.581	2.706, 1.582	1.639	4.168
Os	2.740, 1.601	2.734, 1.606	1.504	5.878
Zn	2.715, 1.734	2.665, 1.856	1.531	3.419
Cd	3.031, 1.907	2.979, 1.886	1.764	5.219

DFT values were obtained from VASP,[135,136] using the PBE functional,[104] PAW pseudopotentials,[124,125] and a $15 \times 15 \times 15$ k-point mesh.

A.2   Damping factor for the pressure
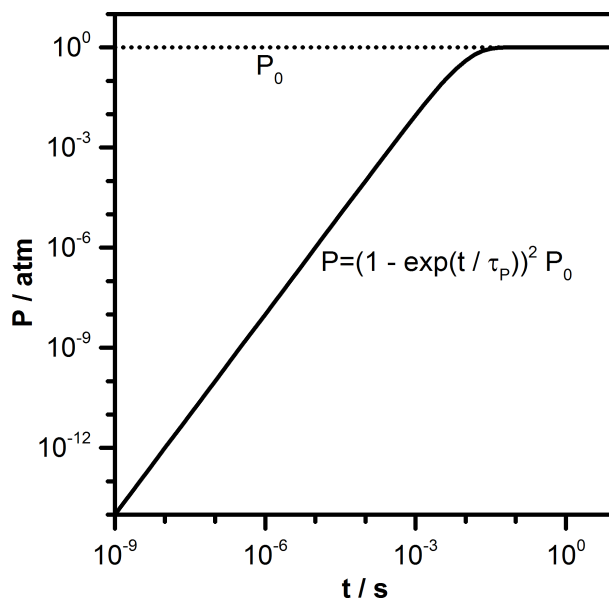
Figure A.1: Total reactant pressure when a damping function (Eq. A.1) is applied.

In the early stages of the microkinetic model, a sudden increase on the reactants pressure induces numerical instabilities. This is a consequence of the iterative nature of the Rosenbrock method. The instabilities manifest when some surface concentrations become negative due to a loose error tolerance. There are two ways to tackle that problem. The first one is to refine the error tolerance by several orders of magnitude, which could make the application of the Rosenbrock method excedingly slow. The second one is to make the pressure for each reactant "j" to increase gently by including a damping function, Eq. A.1. This option is much less expensize, and it assures that the reactant pressures stabilize to the set point values P_{j0} in less than $10\tau_P$, Fig. A.1.

$$P_j = \left(1 - exp\left(-\frac{t}{\tau_P}\right)\right)^2 P_{j0} \tag{A.1}$$

A.3 Literature on Decomposition and Reforming Processes

Table A.2: Reaction conditions for previous studies about alcohol decomposition, ATR, SR, and APR on transition metals: temperature (T, in K), pressure (P, in atm), and composition (as molar ratios).

Ref.	Molec	Metal	T	P	Ratios
		Decomposition			
15	MeOH	Pt	100–600	10^{-12}	–
16	C_1–C_4	Pt	100–600	10^{-12}	–
18	MeOH	Pd	140–300	10^{-13}	–
19	MeOH	Pd	225–800	10^{-13}	–
20	MeOH	Ru	85–400	10^{-13}	–
244	MeOH	Rh	100–600	10^{-13}	–
245	MeOH	Pt	90–350	10^{-13}	–
148	C_1–C_3	Pd	160–700	10^{-12}	–
246	MeOH	Pd	90–500	10^{-12}	–
21	MeOH	Pd	100–550	10^{-12}	–
247	EtOH	Pt	150–850	10^{-13}	–
149	EtOH	Pd	200–600	10^{-12}	–
248	MeOH	Au	77–650	10^{-13}	–
81	MeOH	Ru	80–600	10^{-13}	–
24	EG, 1,2-PG	Pd	100–800	10^{-12}	–
249	EtOH	Pd	150–450	10^{-13}	–
		Authermal reforming			
250	MeOH	Cu, Pd	573–873	1.0	2:0:1
251	MeOH	Cu, Pd	273–900	1.0	10:0:5–10:15:2
252	MeOH	Cu, CuO	283–603	1.0	8:6:1
253	MeOH	Cu	470–590	1.5	1:0:0–1:0.75:0.8
84	EtOH	Rh	873–1096	1.0	3:0:1–3:12:2

Ref.	Molec	Metal	T	P	Ratios
85	MeOH,EtOH,Gly	Pt, Rh	673–1273	3.0	1:0:0–1:9:1.5
254	EtOH	Rh, Pt, RhPt	673–1173	1.0	5:20:1
255	EtOH	M[*]	673–873	1.0	1:0:0.03–1:10:0.3
256	bio-BuOH[†]	CoM[‡]	773	1.0	1:10:1.6
257	BuOH	Rh	773–973	1.0	1:16:0.4
Steam reforming					
258	MeOH	Pd	493	1.0	1:1
259	EtOH	Rh	323–923	1.0	10:84
260	EtOH	Co	573–723	1.0	1:13
261	MeOH	Cu	523	1.0	1:2
262	MeOH	Cu	453–573	1.0	10:13
263	EtOH	CuNi	673–923	394.8	1:3.7
264	EtOH	Co	623–773	1.0	1:10
265	EtOH	Rh	773–1073	1.0	1:3–1:10
266	EtOH	Ru, Pd, Ag	373–873	1.0	1:5
267	EtOH	Ni	773–1023	1.0	1:3
268	EtOH	RhPt	723–923	1.0	1:3.4–1:8.0
269	EtOH	Pt	575–675	1.0	1:3:4
270	BuOH	Rh	773–973	1.0	1:16
Aqueous phase reforming					
271	MeOH, EG	Pt	523	22.1	
272	EG	Pd	498	25.5	
273	Gly	Pt, PtRe	498	29.9	
274	EG	PtM[§]	523	45.0	
275	EG	Pt	548–723	200–250	
Supercritical reforming					
276	EtOH	Ru	873–1073	218–272	1:20–1:5 wt.
277	EG	Ni, Ir, Pt, PtNi	723	247	1:20–6:20 wt.
83	EtOH	Ru	523–643	247	1:20 wt.
278	Gly	M[¶]	648–973	252–266	1:10 wt.
279	MeOH,EtOH	Ru/C	673	247	3:40 wt.
280	Gly	Co	723–848	247	1:20 wt.
281	Gly	Ni	723–848	247	1:20 wt.
282	Gly	Ni, Ru	823–1073	237	1:20–1:5 wt.

---

[*]M: Cu, Ag, Au, Co, Ni, Pd, Pt, Ru, Rh, Ir.
[†]6:3:1 BuOH:acetone:EtOH mass ratio
[‡]M: Ru, Rh, Ir, Pd.
[§]M: Re, Mn, Fe, Cs, Ba, Ga, Ag and Mo
[¶]Pt/CeZrO$_2$, Ni/ZrO$_2$, Ni/CaO6Al$_2$O$_3$, NiCu/CeZrO$_2$, and a CuZn

Appendix B

List of intermediates, reactions, and scalings

B.1   Intermediates

Tables B.1-B.2 list all reactions that were considered.[33,91,150] The label used in the microkinetic model depend on the kind of reaction under study:

001-023	Adsorption/desorptions.
101-141	Reactions for species with less than two carbon atoms.
201-300	Dehydrogenations for C_2 species.
301-355	C–C breaking for C_2 species.
356-415	C–O breaking for C_2 species.
416-417	Keto-enol isomerization for C_2 species.

It was not possible to find the transition state of reactions 301, 311, and 335. In these cases, the saddle points obtained through the NEB and IDM procedures linked two bound states that were not the desired initial and final states. In all attemps, the potential energy surface spawned two transition states: a dehydrogenation and a H^*-assisted C–C breaking. An an example, the saddle points obtained for reaction 301 are shown on Eq. B.1. The IDM either diverged, or converged into one of the spurious saddle points. The activation energies for the second step were above 2.0 eV, much higher than the C–H and O–H dehydrogenation barriers.

$$CH_3CH_3^* + {}^* \rightleftharpoons CH_3CH_2^* + H^* \rightleftharpoons CH_3^* + CH_3^* \qquad (B.1)$$
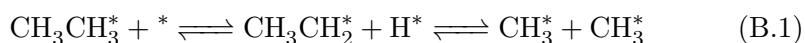
The main reaction path of the water-gas shift reaction mechanism goes through the carboxyl intermediate.[158,159,161] Therefore, all reactions that goes through the formate intermediate were suppresed from further analysis: 130-133 and 137-141,

The full list of intermediates is:

- **Hydrogen decomposition**: H_2^* and H^*.

- **Oxygen decomposition**: O_2^* and O^*.

- **Water decomposition**: OH^* and H_2O^*.

- **Methane decomposition**: C^*, CH^*, CH_2^*, CH_3^*, CH_4^*.

- **Methanol decomposition**: CO^*, CHO^*, COH^*, CH_2O^*, $CHOH^*$, CH_3O^*, CH_2OH^*, CH_3OH^*.

- **Water-gas shift reaction**: CO_2^* and $COOH^*$. Two intermediates were excluded for their negligible influence: $HCOO^*$ and $HCOOH^*$.

- **Ethane decomposition**: C_2^*, C_2H^*, CH_2C^*, $CHCH^*$, CH_3C^*, CH_2CH^*, CH_3CH^*, $CH_2CH_2^*$, $CH_3CH_2^*$, and $CH_3CH_3^*$.

- **Ethanol decomposition**: CCO^*, $CHCO^*$, $CCHO^*$, $CCOH^*$, CH_2CO^*, $CHCHO^*$, CCH_2O^*, $CHCOH^*$, $CCHOH^*$, CH_3CO^*, CH_2CHO^*, $CHCH_2O^*$, CH_2COH^*, $CHCHOH^*$, CCH_2OH^*, CH_3CHO^*, $CH_2CH_2O^*$, CH_3COH^*, CH_2CHOH^*, $CHCH_2OH^*$, $CH_3CH_2O^*$, CH_3CHOH^*, $CH_2CH_2OH^*$, and $CH_3CH_2OH^*$.

- **Ethylene glycol decomposition**: $OCCO^*$, $OCCHO^*$, $OCCOH^*$, $OCHCHO^*$, $OCCH_2O^*$, $HOCCHO^*$, $HOCHCO^*$, $HOCCOH^*$, OCH_2CHO^*, $HOCCH_2O^*$, $HOCHCHO^*$, $OHCH_2CO^*$, $HOCHCOH^*$, $OCH_2CH_2O^*$, $HOCHCH_2O^*$, $HOCH_2CHO^*$, $HOCH_2COH^*$, $HOCHCHOH^*$, $HOCH_2CH_2O^*$, $HOCH_2CHOH^*$, and $HOCH_2CH_2OH^*$.
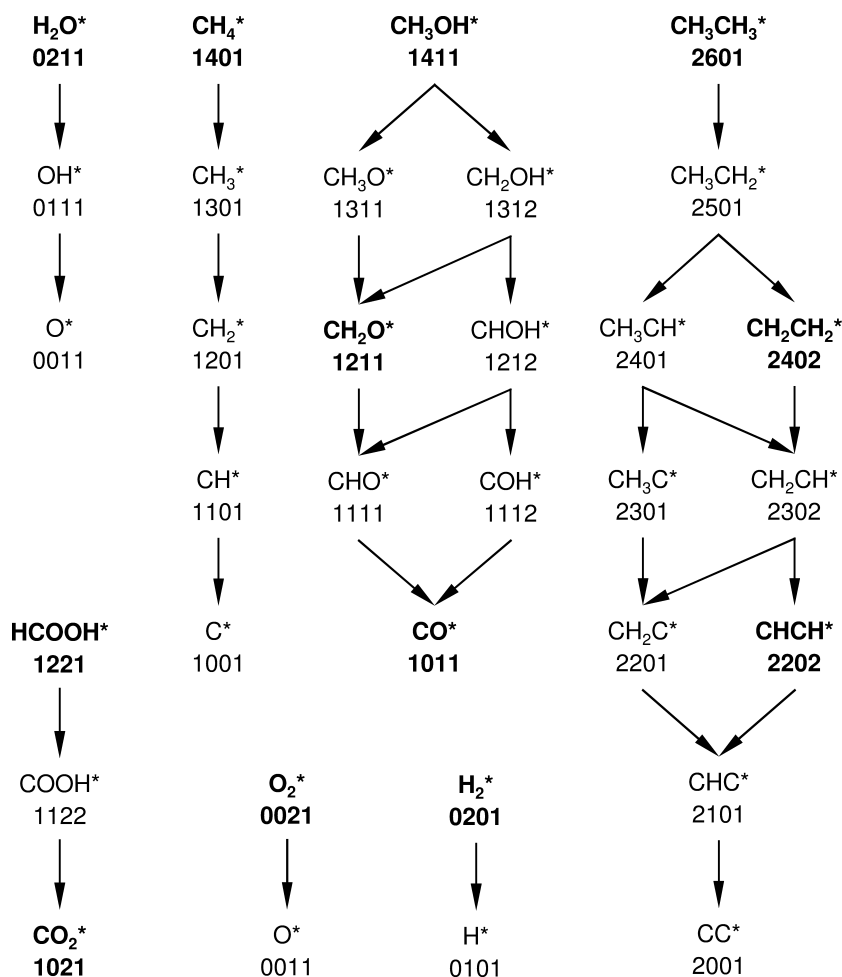
Figure B.1: Reaction network for water, methane, methanol, and ethane dehydrogenation. Additional reactions come from C–O breaking for methanol and its by-products, and C–C bond breaking for ethane and its derivatives. Results for the reaction and activation energies for water, methane, and methanol can be found in our previous study,[150] including 16 dehydrogenations and 8 C–O bond breakings. Ethane decomposition comprises 12 dehydrogenations and 10 C–C bond breakings. Species in bold are stable in gas-phase and may adsorb/desorb.
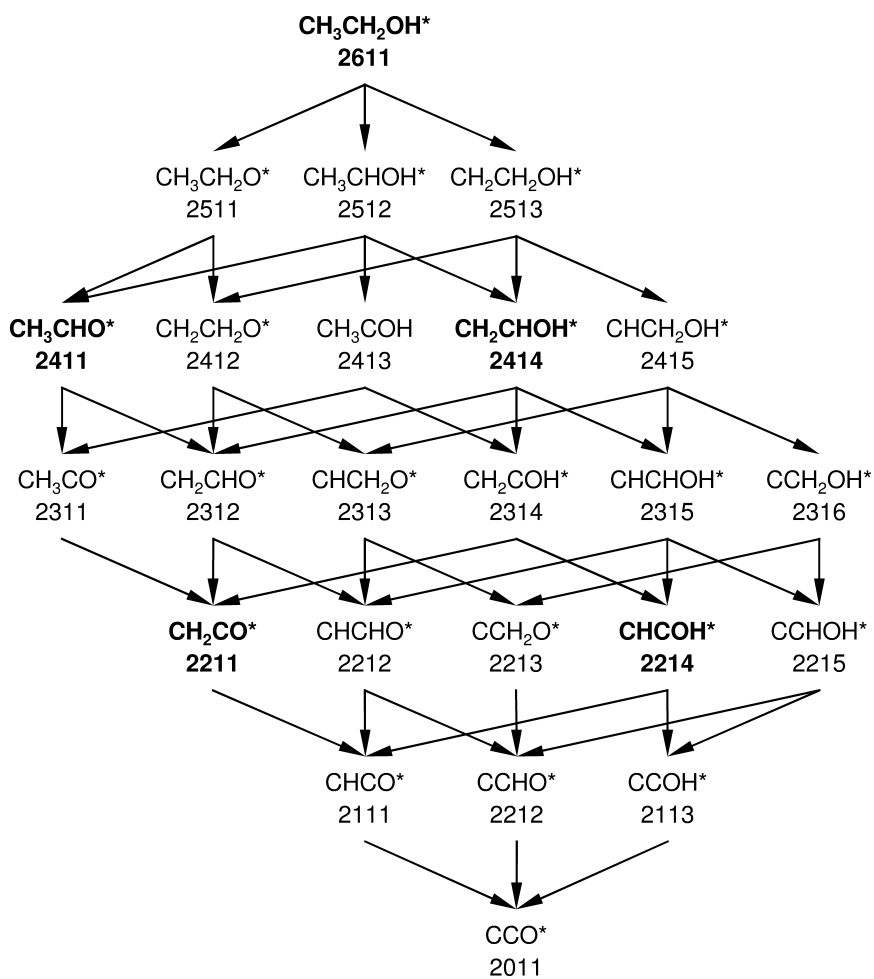
Figure B.2: Reaction network for ethanol dehydrogenation. Additional reactions come from C–O and C–C bond breaking on ethanol and its by-products. The full network comprises 46 dehydrogenations, 24 C–C and 24 C–O bond breakings. Species in bold are stable in gas-phase and may adsorb/desorb.
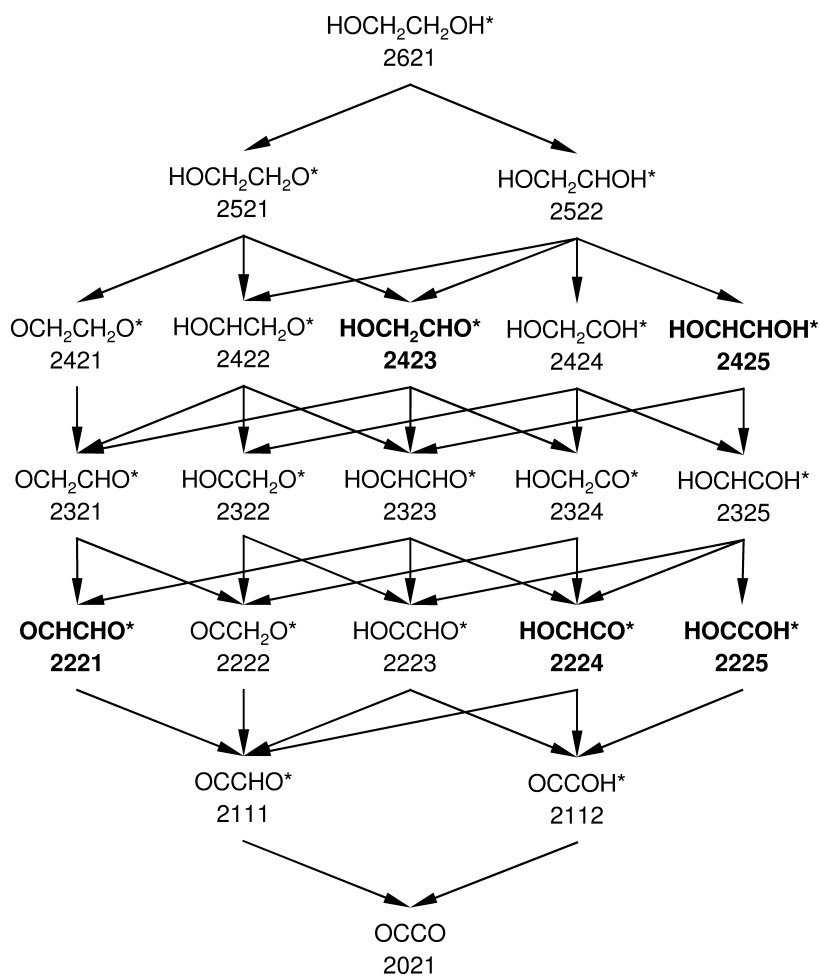
Figure B.3: Reaction network for ethylene glycol dehydrogenation. Additional reactions come from C–O and C–C bond breaking on ethylene glycol and its by-products. The full network comprises 42 dehydrogenations, 21 C–C and 36 C–O bond breakings. Species in bold are stable in gas-phase and may adsorb/desorb.

B.2 Reactions

Table B.1: List of adsorptions/desorptions considered in the microkinetic model.

id.	reaction		
001	$H_2 + {}^*$	$\rightleftharpoons$	H_2^*
002	$O_2 + {}^*$	$\rightleftharpoons$	O_2^*
003	$H_2O + {}^*$	$\rightleftharpoons$	H_2O^*
004	$CH_4 + {}^*$	$\rightleftharpoons$	CH_4^*
005	$CH_3OH + {}^*$	$\rightleftharpoons$	CH_3OH^*
006	$CH_3CH_3 + {}^*$	$\rightleftharpoons$	$CH_3CH_3^*$
007	$CH_3CH_2OH + {}^*$	$\rightleftharpoons$	$CH_3CH_2OH^*$
008	$HOCH_2CH_2OH + {}^*$	$\rightleftharpoons$	$HOCH_2CH_2OH^*$
009	$CO + {}^*$	$\rightleftharpoons$	CO^*
010	$CO_2 + {}^*$	$\rightleftharpoons$	CO_2^*
011	$CH_2O + {}^*$	$\rightleftharpoons$	CH_2O^*
012	$HCOOH + {}^*$	$\rightleftharpoons$	$HCOOH^*$
013	$CH_2CH_2 + {}^*$	$\rightleftharpoons$	$CH_2CH_2^*$
014	$CHCH + {}^*$	$\rightleftharpoons$	$CHCH^*$
015	$CH_3CHO + {}^*$	$\rightleftharpoons$	CH_3CHO^*
016	$CH_2CHOH + {}^*$	$\rightleftharpoons$	CH_2CHOH^*
017	$CH_2CO + {}^*$	$\rightleftharpoons$	CH_2CO^*
018	$CHCOH + {}^*$	$\rightleftharpoons$	$CHCOH^*$
019	$HOCH_2CHO + {}^*$	$\rightleftharpoons$	$HOCH_2CHO^*$
020	$HOCHCHOH + {}^*$	$\rightleftharpoons$	$HOCHCHOH^*$
021	$OCHCHO + {}^*$	$\rightleftharpoons$	$OCHCHO^*$
022	$HOCHCO + {}^*$	$\rightleftharpoons$	$HOCHCO^*$
023	$HOCCOH + {}^*$	$\rightleftharpoons$	$HOCCOH^*$

Table B.2: Full list of reactions considered in the microkinetic model.

id.	reaction		
101	$H_2^* + {}^*$	$\rightleftharpoons$	$H^* + H^*$
102	$O_2^* + {}^*$	$\rightleftharpoons$	$O^* + O^*$
103	$H_2O^* + {}^*$	$\rightleftharpoons$	$OH^* + H^*$
104	$H_2O^* + O^*$	$\rightleftharpoons$	$OH^* + OH^*$
105	$OH^* + {}^*$	$\rightleftharpoons$	$O^* + H^*$
106	$CH_4^* + {}^*$	$\rightleftharpoons$	$CH_3^* + H^*$
107	$CH_3^* + {}^*$	$\rightleftharpoons$	$CH_2^* + H^*$

Continues on next page.

Table B.2: Full list of reactions considered in the microkinetic model. (Continued)

id.	reaction		
108	$CH_2^* + {}^*$	$\rightleftharpoons$	$CH^* + H^*$
109	$CH^* + {}^*$	$\rightleftharpoons$	$C^* + H^*$
110	$CH_3OH^* + {}^*$	$\rightleftharpoons$	$CH_3O^* + H^*$
111	$CH_2OH^* + {}^*$	$\rightleftharpoons$	$CH_2O^* + H^*$
112	$CHOH^* + {}^*$	$\rightleftharpoons$	$CHO^* + H^*$
113	$COH^* + {}^*$	$\rightleftharpoons$	$CO^* + H^*$
114	$CH_3OH^* + {}^*$	$\rightleftharpoons$	$CH_2OH^* + H^*$
115	$CH_3O^* + {}^*$	$\rightleftharpoons$	$CH_2O^* + H^*$
116	$CH_2OH^* + {}^*$	$\rightleftharpoons$	$CHOH^* + H^*$
117	$CH_2O^* + {}^*$	$\rightleftharpoons$	$CHO^* + H^*$
118	$CHOH^* + {}^*$	$\rightleftharpoons$	$COH^* + H^*$
119	$CHO^* + {}^*$	$\rightleftharpoons$	$CO^* + H^*$
120	$CH_3OH^* + {}^*$	$\rightleftharpoons$	$CH_3^* + OH^*$
121	$CH_3O^* + {}^*$	$\rightleftharpoons$	$CH_3^* + O^*$
122	$CH_2OH^* + {}^*$	$\rightleftharpoons$	$CH_2^* + OH^*$
123	$CH_2O^* + {}^*$	$\rightleftharpoons$	$CH_2^* + O^*$
124	$CHOH^* + {}^*$	$\rightleftharpoons$	$CH^* + OH^*$
125	$CHO^* + {}^*$	$\rightleftharpoons$	$CH^* + O^*$
126	$COH^* + {}^*$	$\rightleftharpoons$	$C^* + OH^*$
127	$CO^* + {}^*$	$\rightleftharpoons$	$C^* + O^*$
128	$CO_2^* + {}^*$	$\rightleftharpoons$	$CO^* + O^*$
129	$COOH^* + {}^*$	$\rightleftharpoons$	$CO^* + OH^*$
130	$HCOO^* + {}^*$	$\rightleftharpoons$	$CO_2^* + H^*$
131	$HCOO^* + O^*$	$\rightleftharpoons$	$CO_2^* + OH^*$
132	$HCOO^* + OH^*$	$\rightleftharpoons$	$CO_2^* + H_2O^*$
133	$HCOOH^* + {}^*$	$\rightleftharpoons$	$HCOO^* + H^*$
134	$COOH^* + {}^*$	$\rightleftharpoons$	$CO_2^* + H^*$
135	$COOH^* + O^*$	$\rightleftharpoons$	$CO_2^* + OH^*$
136	$COOH^* + OH^*$	$\rightleftharpoons$	$CO_2^* + H_2O^*$
137	$HCOOH^* + {}^*$	$\rightleftharpoons$	$COOH^* + H^*$
138	$HCOO^* + {}^*$	$\rightleftharpoons$	$CHO^* + O^*$
139	$COOH^* + {}^*$	$\rightleftharpoons$	$COH^* + O^*$
140	$HCOOH^* + {}^*$	$\rightleftharpoons$	$CHO^* + OH^*$
141	$HCOOH^* + {}^*$	$\rightleftharpoons$	$CHOH^* + O^*$
201	$CH_3CH_3^* + {}^*$	$\rightleftharpoons$	$CH_3CH_2^* + H^*$
202	$CH_3CH_2^* + {}^*$	$\rightleftharpoons$	$CH_3CH^* + H^*$

Continues on next page.

Table B.2: Full list of reactions considered in the microkinetic model. (Continued)

id.	reaction		
203	$CH_3CH_2^* + {}^*$	$\rightleftharpoons$	$CH_2CH_2^* + H^*$
204	$CH_3CH^* + {}^*$	$\rightleftharpoons$	$CH_3C^* + H^*$
205	$CH_3CH^* + {}^*$	$\rightleftharpoons$	$CH_2CH^* + H^*$
206	$CH_2CH_2^* + {}^*$	$\rightleftharpoons$	$CH_2CH^* + H^*$
207	$CH_3C^* + {}^*$	$\rightleftharpoons$	$CH_2C^* + H^*$
208	$CH_2CH^* + {}^*$	$\rightleftharpoons$	$CH_2C^* + H^*$
209	$CH_2CH^* + {}^*$	$\rightleftharpoons$	$CHCH^* + H^*$
210	$CH_2C^* + {}^*$	$\rightleftharpoons$	$C_2H^* + H^*$
211	$CHCH^* + {}^*$	$\rightleftharpoons$	$C_2H^* + H^*$
212	$C_2H^* + {}^*$	$\rightleftharpoons$	$C_2^* + H^*$
213	$CH_3CH_2OH^* + {}^*$	$\rightleftharpoons$	$CH_3CH_2O^* + H^*$
214	$CH_3CH_2OH^* + {}^*$	$\rightleftharpoons$	$CH_3CHOH^* + H^*$
215	$CH_3CH_2OH^* + {}^*$	$\rightleftharpoons$	$CH_2CH_2OH^* + H^*$
216	$CH_3CH_2O^* + {}^*$	$\rightleftharpoons$	$CH_3CHO^* + H^*$
217	$CH_3CH_2O^* + {}^*$	$\rightleftharpoons$	$CH_2CH_2O^* + H^*$
218	$CH_3CHOH^* + {}^*$	$\rightleftharpoons$	$CH_3CHO^* + H^*$
219	$CH_3CHOH^* + {}^*$	$\rightleftharpoons$	$CH_3COH^* + H^*$
220	$CH_3CHOH^* + {}^*$	$\rightleftharpoons$	$CH_2CHOH^* + H^*$
221	$CH_2CH_2OH^* + {}^*$	$\rightleftharpoons$	$CH_2CH_2O^* + H^*$
222	$CH_2CH_2OH^* + {}^*$	$\rightleftharpoons$	$CH_2CHOH^* + H^*$
223	$CH_2CH_2OH^* + {}^*$	$\rightleftharpoons$	$CHCH_2OH^* + H^*$
224	$CH_3CHO^* + {}^*$	$\rightleftharpoons$	$CH_3CO^* + H^*$
225	$CH_3CHO^* + {}^*$	$\rightleftharpoons$	$CH_2CHO^* + H^*$
226	$CH_2CH_2O^* + {}^*$	$\rightleftharpoons$	$CH_2CHO^* + H^*$
227	$CH_2CH_2O^* + {}^*$	$\rightleftharpoons$	$CHCH_2O^* + H^*$
228	$CH_3COH^* + {}^*$	$\rightleftharpoons$	$CH_3CO^* + H^*$
229	$CH_3COH^* + {}^*$	$\rightleftharpoons$	$CH_2COH^* + H^*$
230	$CH_2CHOH^* + {}^*$	$\rightleftharpoons$	$CH_2CHO^* + H^*$
231	$CH_2CHOH^* + {}^*$	$\rightleftharpoons$	$CH_2COH^* + H^*$
232	$CH_2CHOH^* + {}^*$	$\rightleftharpoons$	$CHCHOH^* + H^*$
233	$CHCH_2OH^* + {}^*$	$\rightleftharpoons$	$CHCH_2O^* + H^*$
234	$CHCH_2OH^* + {}^*$	$\rightleftharpoons$	$CHCHOH^* + H^*$
235	$CHCH_2OH^* + {}^*$	$\rightleftharpoons$	$CCH_2OH^* + H^*$
236	$CH_3CO^* + {}^*$	$\rightleftharpoons$	$CH_2CO^* + H^*$
237	$CH_2CHO^* + {}^*$	$\rightleftharpoons$	$CH_2CO^* + H^*$
238	$CH_2CHO^* + {}^*$	$\rightleftharpoons$	$CHCHO^* + H^*$

Continues on next page.

Table B.2: Full list of reactions considered in the microkinetic model. (Continued)

id.	reaction		
239	$CHCH_2O^* + {}^*$	$\rightleftharpoons$	$CHCHO^* + H^*$
240	$CHCH_2O^* + {}^*$	$\rightleftharpoons$	$CCH_2O^* + H^*$
241	$CH_2COH^* + {}^*$	$\rightleftharpoons$	$CH_2CO^* + H^*$
242	$CH_2COH^* + {}^*$	$\rightleftharpoons$	$CHCOH^* + H^*$
243	$CHCHOH^* + {}^*$	$\rightleftharpoons$	$CHCHO^* + H^*$
244	$CHCHOH^* + {}^*$	$\rightleftharpoons$	$CHCOH^* + H^*$
245	$CHCHOH^* + {}^*$	$\rightleftharpoons$	$CCHOH^* + H^*$
246	$CCH_2OH^* + {}^*$	$\rightleftharpoons$	$CCH_2O^* + H^*$
247	$CCH_2OH^* + {}^*$	$\rightleftharpoons$	$CCHOH^* + H^*$
248	$CH_2CO^* + {}^*$	$\rightleftharpoons$	$CHCO^* + H^*$
249	$CHCHO^* + {}^*$	$\rightleftharpoons$	$CHCO^* + H^*$
250	$CHCHO^* + {}^*$	$\rightleftharpoons$	$CCHO^* + H^*$
251	$CCH_2O^* + {}^*$	$\rightleftharpoons$	$CCHO^* + H^*$
252	$CHCOH^* + {}^*$	$\rightleftharpoons$	$CHCO^* + H^*$
253	$CHCOH^* + {}^*$	$\rightleftharpoons$	$CCOH^* + H^*$
254	$CCHOH^* + {}^*$	$\rightleftharpoons$	$CCHO^* + H^*$
255	$CCHOH^* + {}^*$	$\rightleftharpoons$	$CCOH^* + H^*$
256	$CHCO^* + {}^*$	$\rightleftharpoons$	$CCO^* + H^*$
257	$CCHO^* + {}^*$	$\rightleftharpoons$	$CCO^* + H^*$
258	$CCOH^* + {}^*$	$\rightleftharpoons$	$CCO^* + H^*$
259	$HOCH_2CH_2OH^* + {}^*$	$\rightleftharpoons$	$HOCH_2CH_2O^* + H^*$
260	$HOCH_2CH_2OH^* + {}^*$	$\rightleftharpoons$	$HOCH_2CHOH^* + H^*$
261	$HOCH_2CH_2O^* + {}^*$	$\rightleftharpoons$	$OCH_2CH_2O^* + H^*$
262	$HOCH_2CH_2O^* + {}^*$	$\rightleftharpoons$	$HOCHCH_2O^* + H^*$
263	$HOCH_2CH_2O^* + {}^*$	$\rightleftharpoons$	$HOCH_2CHO^* + H^*$
264	$HOCH_2CHOH^* + {}^*$	$\rightleftharpoons$	$HOCHCH_2O^* + H^*$
265	$HOCH_2CHOH^* + {}^*$	$\rightleftharpoons$	$HOCH_2CHO^* + H^*$
266	$HOCH_2CHOH^* + {}^*$	$\rightleftharpoons$	$HOCH_2COH^* + H^*$
267	$HOCH_2CHOH^* + {}^*$	$\rightleftharpoons$	$HOCHCHOH^* + H^*$
268	$OCH_2CH_2O^* + {}^*$	$\rightleftharpoons$	$OCH_2CHO^* + H^*$
269	$HOCHCH_2O^* + {}^*$	$\rightleftharpoons$	$OCH_2CHO^* + H^*$
270	$HOCHCH_2O^* + {}^*$	$\rightleftharpoons$	$HOCCH_2O^* + H^*$
271	$HOCHCH_2O^* + {}^*$	$\rightleftharpoons$	$HOCHCHO^* + H^*$
272	$HOCH_2CHO^* + {}^*$	$\rightleftharpoons$	$OCH_2CHO^* + H^*$
273	$HOCH_2CHO^* + {}^*$	$\rightleftharpoons$	$HOCHCHO^* + H^*$
274	$HOCH_2CHO^* + {}^*$	$\rightleftharpoons$	$OHCH_2CO^* + H^*$

Continues on next page.

Table B.2: Full list of reactions considered in the microkinetic model. (Continued)

id.	reaction		
275	$HOCH_2COH^* + {}^*$	$\rightleftharpoons$	$HOCCH_2O^* + H^*$
276	$HOCH_2COH^* + {}^*$	$\rightleftharpoons$	$OHCH_2CO^* + H^*$
277	$HOCH_2COH^* + {}^*$	$\rightleftharpoons$	$HOCHCOH^* + H^*$
278	$HOCHCHOH^* + {}^*$	$\rightleftharpoons$	$HOCHCHO^* + H^*$
279	$HOCHCHOH^* + {}^*$	$\rightleftharpoons$	$HOCHCOH^* + H^*$
280	$OCH_2CHO^* + {}^*$	$\rightleftharpoons$	$OCHCHO^* + H^*$
281	$OCH_2CHO^* + {}^*$	$\rightleftharpoons$	$OCCH_2O^* + H^*$
282	$HOCCH_2O^* + {}^*$	$\rightleftharpoons$	$OCCH_2O^* + H^*$
283	$HOCCH_2O^* + {}^*$	$\rightleftharpoons$	$HOCCHO^* + H^*$
284	$HOCHCHO^* + {}^*$	$\rightleftharpoons$	$OCHCHO^* + H^*$
285	$HOCHCHO^* + {}^*$	$\rightleftharpoons$	$HOCCHO^* + H^*$
286	$HOCHCHO^* + {}^*$	$\rightleftharpoons$	$HOCHCO^* + H^*$
287	$OHCH_2CO^* + {}^*$	$\rightleftharpoons$	$OCCH_2O^* + H^*$
288	$OHCH_2CO^* + {}^*$	$\rightleftharpoons$	$HOCHCO^* + H^*$
289	$HOCHCOH^* + {}^*$	$\rightleftharpoons$	$HOCCHO^* + H^*$
290	$HOCHCOH^* + {}^*$	$\rightleftharpoons$	$HOCHCO^* + H^*$
291	$HOCHCOH^* + {}^*$	$\rightleftharpoons$	$HOCCOH^* + H^*$
292	$OCHCHO^* + {}^*$	$\rightleftharpoons$	$OCCHO^* + H^*$
293	$OCCH_2O^* + {}^*$	$\rightleftharpoons$	$OCCHO^* + H^*$
294	$HOCCHO^* + {}^*$	$\rightleftharpoons$	$OCCHO^* + H^*$
295	$HOCCHO^* + {}^*$	$\rightleftharpoons$	$OCCOH^* + H^*$
296	$HOCHCO^* + {}^*$	$\rightleftharpoons$	$OCCHO^* + H^*$
297	$HOCHCO^* + {}^*$	$\rightleftharpoons$	$OCCOH^* + H^*$
298	$HOCCOH^* + {}^*$	$\rightleftharpoons$	$OCCOH^* + H^*$
299	$OCCHO^* + {}^*$	$\rightleftharpoons$	$OCCO^* + H^*$
300	$OCCOH^* + {}^*$	$\rightleftharpoons$	$OCCO^* + H^*$
301	$CH_3CH_3^* + {}^*$	$\rightleftharpoons$	$CH_3^* + CH_3^*$
302	$CH_3CH_2^* + {}^*$	$\rightleftharpoons$	$CH_3^* + CH_2^*$
303	$CH_3CH^* + {}^*$	$\rightleftharpoons$	$CH_3^* + CH^*$
304	$CH_2CH_2^* + {}^*$	$\rightleftharpoons$	$CH_2^* + CH_2^*$
305	$CH_3C^* + {}^*$	$\rightleftharpoons$	$CH_3^* + C^*$
306	$CH_2CH^* + {}^*$	$\rightleftharpoons$	$CH_2^* + CH^*$
307	$CH_2C^* + {}^*$	$\rightleftharpoons$	$CH_2^* + C^*$
308	$CHCH^* + {}^*$	$\rightleftharpoons$	$CH^* + CH^*$
309	$C_2H^* + {}^*$	$\rightleftharpoons$	$CH^* + C^*$
310	$C_2^* + {}^*$	$\rightleftharpoons$	$C^* + C^*$

Continues on next page.

Table B.2: Full list of reactions considered in the microkinetic model. (Continued)

id.	reaction		
311	$CH_3CH_2OH^* + {}^*$	$\rightleftharpoons$	$CH_2OH^* + CH_3^*$
312	$CH_3CH_2O^* + {}^*$	$\rightleftharpoons$	$CH_2O^* + CH_3^*$
313	$CH_3CHOH^* + {}^*$	$\rightleftharpoons$	$CHOH^* + CH_3^*$
314	$CH_2CH_2OH^* + {}^*$	$\rightleftharpoons$	$CH_2OH^* + CH_2^*$
315	$CH_3CHO^* + {}^*$	$\rightleftharpoons$	$CHO^* + CH_3^*$
316	$CH_2CH_2O^* + {}^*$	$\rightleftharpoons$	$CH_2O^* + CH_2^*$
317	$CH_3COH^* + {}^*$	$\rightleftharpoons$	$COH^* + CH_3^*$
318	$CH_2CHOH^* + {}^*$	$\rightleftharpoons$	$CHOH^* + CH_2^*$
319	$CHCH_2OH^* + {}^*$	$\rightleftharpoons$	$CH_2OH^* + CH^*$
320	$CH_3CO^* + {}^*$	$\rightleftharpoons$	$CO^* + CH_3^*$
321	$CH_2CHO^* + {}^*$	$\rightleftharpoons$	$CHO^* + CH_2^*$
322	$CHCH_2O^* + {}^*$	$\rightleftharpoons$	$CH_2O^* + CH^*$
323	$CH_2COH^* + {}^*$	$\rightleftharpoons$	$COH^* + CH_2^*$
324	$CHCHOH^* + {}^*$	$\rightleftharpoons$	$CHOH^* + CH^*$
325	$CCH_2OH^* + {}^*$	$\rightleftharpoons$	$CH_2OH^* + C^*$
326	$CH_2CO^* + {}^*$	$\rightleftharpoons$	$CO^* + CH_2^*$
327	$CHCHO^* + {}^*$	$\rightleftharpoons$	$CHO^* + CH^*$
328	$CCH_2O^* + {}^*$	$\rightleftharpoons$	$CH_2O^* + C^*$
329	$CHCOH^* + {}^*$	$\rightleftharpoons$	$COH^* + CH^*$
330	$CCHOH^* + {}^*$	$\rightleftharpoons$	$CHOH^* + C^*$
331	$CHCO^* + {}^*$	$\rightleftharpoons$	$CO^* + CH^*$
332	$CCHO^* + {}^*$	$\rightleftharpoons$	$CHO^* + C^*$
333	$CCOH^* + {}^*$	$\rightleftharpoons$	$COH^* + C^*$
334	$CCO^* + {}^*$	$\rightleftharpoons$	$CO^* + C^*$
335	$HOCH_2CH_2OH^* + {}^*$	$\rightleftharpoons$	$CH_2OH^* + CH_2OH^*$
336	$HOCH_2CH_2O^* + {}^*$	$\rightleftharpoons$	$CH_2OH^* + CH_2O^*$
337	$HOCH_2CHOH^* + {}^*$	$\rightleftharpoons$	$CH_2OH^* + CHOH^*$
338	$OCH_2CH_2O^* + {}^*$	$\rightleftharpoons$	$CH_2O^* + CH_2O^*$
339	$HOCHCH_2O^* + {}^*$	$\rightleftharpoons$	$CHOH^* + CH_2O^*$
340	$HOCH_2CHO^* + {}^*$	$\rightleftharpoons$	$CH_2OH^* + CHO^*$
341	$HOCH_2COH^* + {}^*$	$\rightleftharpoons$	$CH_2OH^* + CHO^*$
342	$HOCHCHOH^* + {}^*$	$\rightleftharpoons$	$CHOH^* + CHOH^*$
343	$OCH_2CHO^* + {}^*$	$\rightleftharpoons$	$CH_2O^* + CHO^*$
344	$HOCCH_2O^* + {}^*$	$\rightleftharpoons$	$CH_2O^* + COH^*$
345	$HOCHCHO^* + {}^*$	$\rightleftharpoons$	$CHOH^* + CHO^*$
346	$OHCH_2CO^* + {}^*$	$\rightleftharpoons$	$CH_2OH^* + CO^*$

Continues on next page.

Table B.2: Full list of reactions considered in the microkinetic model. (Continued)

id.	reaction		
347	$HOCHCOH^* + {}^*$	$\rightleftharpoons$	$CHOH^* + COH^*$
348	$OCHCHO^* + {}^*$	$\rightleftharpoons$	$CHO^* + CHO^*$
349	$OCCH_2O^* + {}^*$	$\rightleftharpoons$	$CH_2O^* + CO^*$
350	$HOCCHO^* + {}^*$	$\rightleftharpoons$	$COH^* + CHO^*$
351	$HOCHCO^* + {}^*$	$\rightleftharpoons$	$CHOH^* + CO^*$
352	$HOCCOH^* + {}^*$	$\rightleftharpoons$	$COH^* + COH^*$
353	$OCCHO^* + {}^*$	$\rightleftharpoons$	$CHO^* + CO^*$
354	$OCCOH^* + {}^*$	$\rightleftharpoons$	$COH^* + CO^*$
355	$OCCO^* + {}^*$	$\rightleftharpoons$	$CO^* + CO^*$
356	$CH_3CH_2OH^* + {}^*$	$\rightleftharpoons$	$CH_3CH_2^* + OH^*$
357	$CH_3CH_2O^* + {}^*$	$\rightleftharpoons$	$CH_3CH_2^* + O^*$
358	$CH_3CHOH^* + {}^*$	$\rightleftharpoons$	$CH_3CH^* + OH^*$
359	$CH_2CH_2OH^* + {}^*$	$\rightleftharpoons$	$CH_2CH_2^* + OH^*$
360	$CH_3CHO^* + {}^*$	$\rightleftharpoons$	$CH_3CH^* + O^*$
361	$CH_2CH_2O^* + {}^*$	$\rightleftharpoons$	$CH_2CH_2^* + O^*$
362	$CH_3COH^* + {}^*$	$\rightleftharpoons$	$CH_3C^* + OH^*$
363	$CH_2CHOH^* + {}^*$	$\rightleftharpoons$	$CH_2CH^* + OH^*$
364	$CHCH_2OH^* + {}^*$	$\rightleftharpoons$	$CH_2CH^* + OH^*$
365	$CH_3CO^* + {}^*$	$\rightleftharpoons$	$CH_3C^* + O^*$
366	$CH_2CHO^* + {}^*$	$\rightleftharpoons$	$CH_2CH^* + O^*$
367	$CHCH_2O^* + {}^*$	$\rightleftharpoons$	$CH_2CH^* + O^*$
368	$CH_2COH^* + {}^*$	$\rightleftharpoons$	$CH_2C^* + OH^*$
369	$CHCHOH^* + {}^*$	$\rightleftharpoons$	$CHCH^* + OH^*$
370	$CCH_2OH^* + {}^*$	$\rightleftharpoons$	$CH_2C^* + OH^*$
371	$CH_2CO^* + {}^*$	$\rightleftharpoons$	$CH_2C^* + O^*$
372	$CHCHO^* + {}^*$	$\rightleftharpoons$	$CHCH^* + O^*$
373	$CCH_2O^* + {}^*$	$\rightleftharpoons$	$CH_2C^* + O^*$
374	$CHCOH^* + {}^*$	$\rightleftharpoons$	$C_2H^* + OH^*$
375	$CCHOH^* + {}^*$	$\rightleftharpoons$	$C_2H^* + OH^*$
376	$CHCO^* + {}^*$	$\rightleftharpoons$	$C_2H^* + O^*$
377	$CCHO^* + {}^*$	$\rightleftharpoons$	$C_2H^* + O^*$
378	$CCOH^* + {}^*$	$\rightleftharpoons$	$C_2^* + OH^*$
379	$CCO^* + {}^*$	$\rightleftharpoons$	$C_2^* + O^*$
380	$HOCH_2CH_2OH^* + {}^*$	$\rightleftharpoons$	$CH_2CH_2OH^* + OH^*$
381	$HOCH_2CH_2O^* + {}^*$	$\rightleftharpoons$	$CH_2CH_2O^* + OH^*$
382	$HOCH_2CH_2O^* + {}^*$	$\rightleftharpoons$	$CH_2CH_2OH^* + O^*$

Continues on next page.

Table B.2: Full list of reactions considered in the microkinetic model. (Continued)

id.	reaction		
383	$HOCH_2CHOH^* + {}^*$	$\rightleftharpoons$	$CH_2CHOH^* + OH^*$
384	$HOCH_2CHOH^* + {}^*$	$\rightleftharpoons$	$CHCH_2OH^* + OH^*$
385	$OCH_2CH_2O^* + {}^*$	$\rightleftharpoons$	$CH_2CH_2O^* + O^*$
386	$HOCHCH_2O^* + {}^*$	$\rightleftharpoons$	$CHCH_2O^* + OH^*$
387	$HOCHCH_2O^* + {}^*$	$\rightleftharpoons$	$CH_2CHOH^* + O^*$
388	$HOCH_2CHO^* + {}^*$	$\rightleftharpoons$	$CH_2CHO^* + OH^*$
389	$HOCH_2CHO^* + {}^*$	$\rightleftharpoons$	$CHCH_2OH^* + O^*$
390	$HOCH_2COH^* + {}^*$	$\rightleftharpoons$	$CH_2COH^* + OH^*$
391	$HOCH_2COH^* + {}^*$	$\rightleftharpoons$	$CCH_2OH^* + OH^*$
392	$HOCHCHOH^* + {}^*$	$\rightleftharpoons$	$CHCHOH^* + OH^*$
393	$OCH_2CHO^* + {}^*$	$\rightleftharpoons$	$CH_2CHO^* + O^*$
394	$OCH_2CHO^* + {}^*$	$\rightleftharpoons$	$CHCH_2O^* + O^*$
395	$HOCCH_2O^* + {}^*$	$\rightleftharpoons$	$CCH_2O^* + OH^*$
396	$HOCCH_2O^* + {}^*$	$\rightleftharpoons$	$CH_2COH^* + O^*$
397	$HOCHCHO^* + {}^*$	$\rightleftharpoons$	$CHCHO^* + OH^*$
398	$HOCHCHO^* + {}^*$	$\rightleftharpoons$	$CHCHOH^* + O^*$
399	$OHCH_2CO^* + {}^*$	$\rightleftharpoons$	$CH_2CO^* + OH^*$
400	$OHCH_2CO^* + {}^*$	$\rightleftharpoons$	$CCH_2OH^* + O^*$
401	$HOCHCOH^* + {}^*$	$\rightleftharpoons$	$CHCOH^* + OH^*$
402	$HOCHCOH^* + {}^*$	$\rightleftharpoons$	$CCHOH^* + OH^*$
403	$OCHCHO^* + {}^*$	$\rightleftharpoons$	$CHCHO^* + O^*$
404	$OCCH_2O^* + {}^*$	$\rightleftharpoons$	$CH_2CO^* + O^*$
405	$OCCH_2O^* + {}^*$	$\rightleftharpoons$	$CCH_2O^* + O^*$
406	$HOCCHO^* + {}^*$	$\rightleftharpoons$	$CCHO^* + OH^*$
407	$HOCCHO^* + {}^*$	$\rightleftharpoons$	$CHCOH^* + O^*$
408	$HOCHCO^* + {}^*$	$\rightleftharpoons$	$CHCO^* + OH^*$
409	$HOCHCO^* + {}^*$	$\rightleftharpoons$	$CCHOH^* + O^*$
410	$HOCCOH^* + {}^*$	$\rightleftharpoons$	$CCOH^* + OH^*$
411	$OCCHO^* + {}^*$	$\rightleftharpoons$	$CHCO^* + O^*$
412	$OCCHO^* + {}^*$	$\rightleftharpoons$	$CCHO^* + O^*$
413	$OCCOH^* + {}^*$	$\rightleftharpoons$	$CCO^* + OH^*$
414	$OCCOH^* + {}^*$	$\rightleftharpoons$	$CCOH^* + O^*$
415	$OCCO^* + {}^*$	$\rightleftharpoons$	$CCO^* + O^*$
416	$CH_2CHOH^* + {}^*$	$\rightleftharpoons$	$CH_3CHO^* + {}^*$
417	$CHOHCHOH^* + {}^*$	$\rightleftharpoons$	$CHOCH_2OH^* + {}^*$

B.3 Scalings

Table B.3: Parametres for the Brønsted-Evans-Polanyi, Initial and Final State scaling relationships (BEP, ISS and FSS) for O–H, C–H, C–C, C–O, and C–OH bond breakings on Cu, Ru, Pd, and Pt closed-packed surfaces: α, β, determination coefficient R^2, and the mean average error, MAE. For ISS and FSS, $\alpha = 1$ on Eq. 5.6-5.7. β and MAE are in eV.

Metal	BEP				ISS			FSS		
	α	β	R^2	MAE	β	R^2	MAE	β	R^2	MAE
O–H bonds										
Cu	0.39	0.89	0.27	0.18	0.85	0.89	0.21	1.09	0.82	0.27
Ru	0.23	0.65	0.08	0.12	0.50	0.86	0.15	1.07	0.77	0.19
Pd	0.27	0.65	0.43	0.09	0.58	0.95	0.11	0.90	0.74	0.24
Pt	0.32	0.52	0.21	0.13	0.55	0.89	0.17	0.56	0.82	0.23
Ru, Pd, Pt	0.18	0.60	0.16	0.12	0.54	0.91	0.14	0.85	0.83	0.28
C–H bonds										
Cu	0.63	0.81	0.69	0.14	0.99	0.84	0.25	0.81	0.91	0.19
Ru	0.89	0.77	0.45	0.18	0.35	0.77	0.23	0.80	0.86	0.18
Pd	0.67	0.83	0.78	0.10	0.52	0.83	0.24	1.07	0.93	0.15
Pt	0.77	0.86	0.70	0.15	0.58	0.78	0.29	1.00	0.93	0.17
Ru, Pd, Pt	0.75	0.81	0.62	0.16	0.48	0.82	0.26	0.96	0.93	0.18
C–C bonds										
Cu	0.78	0.88	0.80	0.23	1.77	0.52	0.45	0.64	0.91	0.19
Ru	0.84	1.25	0.46	0.26	0.91	0.28	0.30	1.19	0.56	0.24
Pd	0.69	1.51	0.71	0.24	1.18	0.07	0.38	1.66	0.51	0.26
Pt	0.73	1.50	0.53	0.27	1.17	0.09	0.35	1.58	0.49	0.26
Ru, Pd, Pt	0.70	1.40	0.52	0.29	1.09	0.46	0.36	1.47	0.68	0.30
C–O bonds										
Cu	0.94	1.24	0.80	0.25	1.64	0.41	0.53	1.24	0.89	0.23
Ru	1.13	2.32	0.69	0.18	1.03	0.58	0.29	2.13	0.82	0.19
Pd	1.11	1.68	0.84	0.23	1.73	0.18	0.49	1.71	0.87	0.19
Pt	0.90	1.67	0.80	0.25	1.83	0.27	0.44	1.63	0.80	0.23
Ru, Pd, Pt	0.66	1.52	0.58	0.33	1.53	0.68	0.50	1.82	0.92	0.27
C–OH bonds										
Cu	0.77	1.33	0.42	0.29	1.20	0.68	0.36	1.48	0.80	0.28
Ru	0.92	1.55	0.41	0.21	0.85	0.48	0.30	1.59	0.83	0.22
Pd	0.70	1.27	0.46	0.22	1.44	0.66	0.33	1.26	0.87	0.20
Pt	0.46	1.27	0.22	0.31	1.48	0.61	0.38	0.98	0.64	0.36
Ru, Pd, Pt	0.57	1.27	0.56	0.25	1.26	0.70	0.41	1.27	0.81	0.34

Bibliography

[1] Brundtland, G. H.; Khalid, M. Our common future, *New York,* **1987**.

[2] Anastas, P.; Eghbali, N. Green chemistry: principles and practice, *Chem. Soc. Rev.* **2010,** *39,* 301–312.

[3] Bozell, J. J.; Petersen, G. R. Technology development for the production of biobased products from biorefinery carbohydratesthe US Department of Energys "top 10" revisited, *Green Chem.* **2010,** *12,* 539–554.

[4] Moulijn, J. A.; van Leeuwen, P. W. N. M.; van Santen, R. A. *Catalysis: an integrated approach to homogeneous, heterogeneous and industrial catalysis;* volume 79 Elsevier: 1993.

[5] Bhaduri, S.; Mukesh, D. *Homogeneous catalysis: mechanisms and industrial applications;* Wiley: 2000.

[6] Schaller, R. R. Moore's law: past, present and future, *IEEE Spectr.* **1997,** *34,* 52–59.

[7] Hohenberg, P.; Kohn, W. Inhomogeneous electron gas, *Phys. Rev.* **1964,** *136,* B864.

[8] Kohn, W.; Sham, L. J. Self-consistent equations including exchange and correlation effects, *Phys. Rev.* **1965,** *140,* A1133.

[9] Nørskov, J. K.; Bligaard, T.; Rossmeisl, J.; Christensen, C. H. Towards the computational design of solid catalysts, *Nat. Chem.* **2009,** *1,* 37–46.

[10] López, N.; Almora-Barrios, N.; Carchini, G.; Błoński, P.; Bellarosa, L.; García-Muelas, R.; Novell-Leruth, G.; García-Mota, M. State-of-the-art and challenges in theoretical simulations of heterogeneous catalysis at the microscopic level, *Catal. Sci. Tech.* **2012,** *2,* 2405–2417.

[11] Wilkinson, M. D. *et al.* The FAIR guiding principles for scientific data management and stewardship, *Sci. data* **2016,** *3,* 160018.

[12] Álvarez Moreno, M.; De Graaf, C.; López, N.; Maseras, F.; Poblet, J. M.; Bo, C. Managing the computational chemistry big data problem: The ioChem-BD platform, *J. Chem. Inf. Model.* **2014,** *55,* 95–103.

[13] Ciriminna, R.; Pina, C. D.; Rossi, M.; Pagliaro, M. Understanding the glycerol market, *Eur. J. Lipid Sci. Technol.* **2014,** *116,* 1432–1439.

[14] Dusselier, M.; Van Wouwe, P.; Dewaele, A.; Makshina, E.; Sels, B. F. Lactic acid as a platform chemical in the biobased economy: the role of chemocatalysis, *Energy Environ. Sci.* **2013,** *6,* 1415–1442.

[15] Sexton, B. A. Methanol decomposition on platinum(111), *Surf. Sci.* **1981,** *102,* 271–281.

[16] Sexton, B. A.; Rendulic, K. D.; Huges, A. E. Decomposition pathways of C_1–C_4 alcohols adsorbed on platinum(111), *Surf. Sci.* **1982,** *121,* 181–198.

[17] Rendulic, K. D.; Sexton, B. A. Adsorption and dehydrogenation of alcohols and ethers on platinum(111), *J. Catal.* **1982,** *78,* 126–135.

[18] Gates, J. A.; Kesmodel, L. L. Methanol adsorption and decomposition on clean and oxygen precovered palladium(111), *J. Catal.* **1983,** *83,* 437–445.

[19] Kok, G. A.; Noordermeer, A.; Nieuwenhuys, B. E. Decomposition of methanol and the interaction of coadsorbed hydrogen and carbon monoxide on a Pd(111) surface, *Surf. Sci.* **1983,** *135,* 65–80.

[20] Hrbek, J.; DePaola, R. A.; Hoffmann, F. M. The interaction of methanol with Ru(001), *J. Chem. Phys.* **1984,** *81,* 2818–2827.

[21] Chen, J.; Jiang, Z.; Zhou, Y.; Chakraborty, B. R.; Winograd, N. Spectroscopic studies of methanol decomposition on Pd(111), *Surf. Sci.* **1995,** *328,* 248–262.

[22] Karp, E. M.; Silbaugh, T. L.; Crowe, M. C.; Campbell, C. T. Energetics of adsorbed methanol and methoxy on Pt(111) by microcalorimetry, *J. Am. Chem. Soc.* **2012,** *134,* 20388–20395.

[23] Köhler, L.; Kresse, G. Density functional study of CO on Rh(111), *Phys. Rev. B* **2004,** *70,* 165405.

[24] Griffin, M. B.; Jorgensen, E. L.; Medlin, J. W. The adsorption and reaction of ethylene glycol and 1,2-propanediol on Pd(111): a TPD and HREELS study, *Surf. Sci.* **2010,** *604,* 1558–1564.

[25] Grimme, S. Semiempirical GGA-type density functional constructed with a long-range dispersion correction, *J. Comput. Chem.* **2006,** *27,* 1787–1799.

[26] Bučko, T.; Hafner, J.; Lebegue, S.; Angyán, J. G. Improved description of the structure of molecular and layered crystals: ab initio DFT calculations with van der Waals corrections, *J. Phys. Chem. A* **2010,** *114,* 11814–11824.

[27] Almora-Barrios, N.; Carchini, G.; Błoński, P.; López, N. Costless derivation of dispersion coefficients for metal surfaces, *J. Chem. Theory Comput.* **2014,** *10,* 5002-5009.

[28] García-Ratés, M.; López, N. Multigrid-based methodology for implicit solvation models in periodic DFT, *J. Chem. Theory Comput.* **2016,** *12,* 1331–1341.

[29] Mathew, K.; Sundararaman, R.; Letchworth-Weaver, K.; Arias, T. A.; Hennig, R. G. Implicit solvation model for density-functional study of nanocrystal surfaces and reaction pathways, *J Chem. Phys.* **2014,** *140,* 084106.

[30] Carrasco, J.; Santra, B.; Klimeš, J.; Michaelides, A. To wet or not to wet? Dispersion forces tip the balance for water ice on metals, *Phys. Rev. Lett.* **2011,** *106,* 026101.

[31] Błonski, P.; López, N. On the adsorption of formaldehyde and methanol on a water-covered Pt(111): a DFT-D study, *J. Phys. Chem. C* **2012,** *116,* 15484–15492.

[32] García-Muelas, R.; López, N. Collective descriptors for the adsorption of sugar alcohols on Pt and Pd(111), *J. Phys. Chem. C* **2014,** *118,* 17531–17537.

[33] García-Muelas, R.; López, N. Generalized models for adsorption of intermediates on transition metals, Submitted.

[34] Okamoto, Y.; Sugino, O.; Mochizuki, Y.; Ikeshoji, T.; Morikawa, Y. Comparative study of dehydrogenation of methanol at Pt(111)/water and Pt(111)/vacuum interfaces, *Chem. Phys. Lett.* **2003,** *377,* 236–242.

[35] Zope, B. N.; Hibbitts, D. D.; Neurock, M.; Davis, R. J. Reactivity of the gold/water interface during selective oxidation catalysis, *Science* **2010,** *330,* 74–78.

[36] Desai, S. K.; Neurock, M. First-principles study of the role of solvent in the dissociation of water over a Pt-Ru alloy, *Phys. Rev. B* **2003,** *68,* 075420.

[37] Roudgar, A.; Groß, A. Water bilayer on the Pd/Au(111) overlayer system: Coadsorption and electric field effects, *Chem. Phys. Lett.* **2005,** *409,* 157–162.

[38] Skúlason, E.; Karlberg, G. S.; Rossmeisl, J.; Bligaard, T.; Greeley, J.; Jónsson, H.; Nørskov, J. K. Density functional theory calculations for the hydrogen evolution reaction in an electrochemical double layer on the Pt(111) electrode, *Phys. Chem. Chem. Phys.* **2007,** *9,* 3241–3250.

[39] Hodgson, A.; Haq, S. Water adsorption and the wetting of metal surfaces, *Surf. Sci. Rep.* **2009,** *64,* 381–451.

[40] Raghavan, K.; Foster, K.; Motakabbir, K.; Berkowitz, M. Structure and dynamics of water at the Pt(111) interface: molecular dynamics study, *J. Chem. Phys.* **1991,** *94,* 2110–2117.

[41] Limmer, D. T.; Willard, A. P.; Madden, P.; Chandler, D. Hydration of metal surfaces can be dynamically heterogeneous and hydrophobic, *Proc. Natl. Acad. Sci. U.S.A.* **2013,** *110,* 4200–4205.

[42] Cao, Z.; Kumar, R.; Peng, Y.; Voth, G. A. Hydrated proton structure and diffusion at platinum surfaces, *J. Phys. Chem. C* **2015,** *119,* 14675–14682.

[43] Schnur, S.; Groß, A. Properties of metal–water interfaces studied from first principles, *New J. Phys.* **2009,** *11,* 125003.

[44] Groß, A.; Gossenberger, F.; Lin, X.; Naderian, M.; Sakong, S.; Roman, T. Water structures at metal electrodes studied by ab initio molecular dynamics simulations, *J. Electrochem. Soc.* **2014,** *161,* E3015–E3020.

[45] Pedroza, L. S.; Poissier, A.; Fernández-Serra, M.-V. Local order of liquid water at metallic electrode surfaces, *J. Chem. Phys.* **2015,** *142,* 034706.

[46] Cances, E.; Mennucci, B.; Tomasi, J. A new integral equation formalism for the polarizable continuum model: Theoretical background and applications to isotropic and anisotropic dielectrics, *J. Chem. Phys.* **1997,** *107,* 3032–3041.

[47] Cottrell, T. L. *The strengths of chemical bonds, 2nd edition;* Butterworth: 1958.

[48] Kerr, J. A. Bond dissociation energies by kinetic methods, *Chem. Rev.* **1966,** *66,* 465–500.

[49] Benson, S. W.; Cruickshank, F. R.; Golden, D. M.; Haugen, G. R.; O'neal, H. E.; Rodgers, A. S.; Shaw, R.; Walsh, R. Additivity rules for the estimation of thermochemical properties, *Chem. Rev.* **1969,** *69,* 279–324.

[50] Benson, S. W. *Thermochemical kinetics;* Wiley: 1976.

[51] Abild-Pedersen, F.; Greeley, J.; Studt, F.; Rossmeisl, J.; Munter, T. R.; Moses, P. G.; Skúlason, E.; Bligaard, T.; Nørskov, J. K. Scaling properties of adsorption energies for hydrogen-containing molecules on transition-metal surfaces, *Phys. Rev. Lett.* **2007,** *99,* 016105.

[52] Calle-Vallejo, F.; Martinez, J. I.; García-Lastra, J. M.; Rossmeisl, J.; Koper, M. T. M. Physical and chemical nature of the scaling relations between adsorption energies of atoms on metal surfaces, *Phys. Rev. Lett.* **2012,** *108,* 116103.

[53] Montemore, M. M.; Medlin, J. W. A unified picture of adsorption on transition metals through different atoms, *J. Am. Chem. Soc.* **2014,** *136,* 9272–9275.

[54] Calle-Vallejo, F.; Loffreda, D.; Koper, M. T. M.; Sautet, P. Introducing structural sensitivity into adsorption–energy scaling relations by means of coordination numbers, *Nat. Chem.* **2015,** *7,* 403–410.

[55] Nørskov, J. K.; Studt, F.; Abild-Pedersen, F.; Bligaard, T. *Fundamental concepts in heterogeneous catalysis;* John Wiley & Sons: 2014.

[56] Kua, J.; Faglioni, F.; Goddard III, W. A. Thermochemistry for hydrocarbon intermediates chemisorbed on metal surfaces: $CH_{n-m}(CH_3)_m$ with $n= 1$, 2, 3 and $m \leq n$ on Pt, Ir, Os, Pd, Rh, and Ru, *J. Am. Chem. Soc.* **2000,** *122,* 2309–2321.

[57] Salciccioli, M.; Chen, Y.; Vlachos, D. G. Density functional theory-derived group additivity and linear scaling methods for prediction of oxygenate stability on metal catalysts: adsorption of open-ring alcohol and polyol dehydrogenation intermediates on Pt-based metals, *J. Phys. Chem. C* **2010,** *114,* 20155–20166.

[58] Salciccioli, M.; Edie, S. M.; Vlachos, D. G. Adsorption of acid, ester, and ether functional groups on Pt: fast prediction of thermochemical properties of adsorbed oxygenates via DFT-based group additivity methods, *J. Phys. Chem. C* **2012,** *116,* 1873–1886.

[59] Shustorovich, E. Chemisorption phenomena: analytic modeling based on perturbation theory and bond-order conservation, *Surf. Sci. Rep.* **1986,** *6,* 1–63.

[60] Shustorovich, E.; Sellers, H. The UBI-QEP method: a practical theoretical approach to understanding chemistry on transition metal surfaces, *Surf. Sci. Rep.* **1998,** *31,* 1–119.

[61] Henkelman, G.; Jónsson, H. Improved tangent estimate in the nudged elastic band method for finding minimum energy paths and saddle points, *J. Chem. Phys.* **2000,** *113,* 9978–9985.

[62] Henkelman, G.; Uberuaga, B. P.; Jónsson, H. A climbing image nudged elastic band method for finding saddle points and minimum energy paths, *J. Chem. Phys.* **2000,** *113,* 9901–9904.

[63] Jónsson, H.; Mills, G.; Jacobsen, K. W. Nudged elastic band method for finding minimum energy paths of transitions, **1998,** .

[64] Henkelman, G.; Jónsson, H. A dimer method for finding saddle points on high dimensional potential surfaces using only first derivatives, *J. Chem. Phys.* **1999,** *111,* 7010–7022.

[65] Heyden, A.; Bell, A. T.; Keil, F. J. Efficient methods for finding transition states in chemical reactions: comparison of improved dimer method and partitioned rational function optimization method, *J. Chem. Phys.* **2005,** *123,* 224101(1–14).

[66] Hei, M. J.; Chen, H. B.; Yi, J.; Lin, Y. J.; Lin, Y. Z.; Wei, G.; Liao, D. W. CO_2-reforming of methane on transition metal surfaces, *Surf. Sci.* **1998,** *417,* 82–96.

[67] Evans, M. G.; Polanyi, M. Inertia and driving force of chemical reactions, *T. Faraday Soc.* **1938,** *34,* 11–24.

[68] Pallassana, V.; Neurock, M. Electronic factors governing ethylene hydrogenation and dehydrogenation activity of pseudomorphic PdML/Re(0001), PdML/Ru(0001), Pd(111), and PdML/Au(111) surfaces, *J. Catal.* **2000,** *191,* 301–317.

[69] Logadottir, A.; Rod, T. H.; Nørskov, J. K.; Hammer, B.; Dahl, S.; Jacobsen, C. The Brønsted–Evans–Polanyi relation and the volcano plot for ammonia synthesis over transition metal catalysts, *J. Catal.* **2001,** *197,* 229–231.

[70] Bligaard, T.; Nørskov, J. K.; Dahl, S.; Matthiesen, J.; Christensen, C. H.; Sehested, J. The Brønsted–Evans–Polanyi relation and the volcano curve in heterogeneous catalysis, *J. Catal.* **2004,** *224,* 206–217.

[71] Wang, S. *et al.* Universal transition state scaling relations for (de) hydrogenation over transition metals, *Phys. Chem. Chem. Phys.* **2011,** *13,* 20760–20765.

[72] Zaffran, J.; Michel, C.; Auneau, F.; Delbecq, F.; Sautet, P. Linear energy relations as predictive tools for polyalcohol catalytic reactivity, *ACS Catal.* **2014,** *4,* 464–468.

[73] Dumesic, J. A.; Rudd, D. F.; Aparicio, L. M.; Rekoske, J. E.; Treviño, A. A. *The microkinetics of heterogeneous catalysis;* American Chemical Society: 1993.

[74] Fogler, H. S. *Elements of chemical reaction engineering, 4th ed.;* Prentice-Hall International London;: 2006.

[75] Chorkendorff, I.; Niemantsverdriet, J. W. *Concepts of modern catalysis and kinetics;* John Wiley & Sons: 2006.

[76] Salciccioli, M.; Vlachos, D. G. Kinetic modeling of Pt catalyzed and computation-driven catalyst discovery for ethylene glycol decomposition, *ACS Catal.* **2011,** *1,* 1246–1256.

[77] Wang, S.; Vorotnikov, V.; Sutton, J. E.; Vlachos, D. G. Brønsted–Evans–Polanyi and transition state scaling relations of furan derivatives on Pd(111) and their relation to those of small molecules, *ACS Catal.* **2014,** *4,* 604–612.

[78] Corma, A.; Iborra, S.; Velty, A. Chemical routes for the transformation of biomass into chemicals, *Chem. Rev.* **2007,** *107,* 2411–2502.

[79] Guo, N.; Caratzoulas, S.; Doren, D. J.; Sandler, S. I.; Vlachos, D. G. A perspective on the modeling of biomass processing, *Energy Environ. Sci.* **2012,** *5,* 6703–6716.

[80] Friend, C. M.; Xu, B. Heterogeneous catalysis: a central science for a sustainable future, *Acc. Chem. Res.* **2017,** *50,* 517–521.

[81] Gazdzicki, P.; Jakob, P. Reactions of methanol on Ru(0001), *J. Phys. Chem. C* **2010,** *114,* 2655–2663.

[82] Sutton, J. E.; Guo, W.; Katsoulakis, M. A.; Vlachos, D. G. Effects of correlated parameters and uncertainty in electronic-structure-based chemical kinetic modelling, *Nat. Chem.* **2016,** *8,* 331–337.

[83] Rabe, S.; Nachtegaal, M.; Ulrich, T.; Vogel, F. Towards understanding the catalytic reforming of biomass in supercritical water, *Angew. Chem. Int. Ed.* **2010,** *49,* 6434–6437.

[84] Deluga, G. A.; Salge, J. R.; Schmidt, L. D.; Verykios, X. E. Renewable hydrogen from ethanol by autothermal reforming, *Science* **2004,** *303,* 993–997.

[85] Dauenhauer, P. J.; Salge, J. R.; Schmidt, L. D. Renewable hydrogen by autothermal steam reforming of volatile carbohydrates, *J. Catal.* **2006,** *244,* 238–247.

[86] Cortright, R. D.; Davda, R. R.; Dumesic, J. A. Hydrogen from catalytic reforming of biomass-derived hydrocarbons in liquid water, *Nature* **2002,** *418,* 964–967.

[87] Huber, G. W.; Shabaker, J. W.; Dumesic, J. A. Raney Ni-Sn catalyst for H_2 production from biomass-derived hydrocarbons, *Science* **2003,** *300,* 2075–2077.

[88] Davda, R. R.; Shabaker, J. W.; Huber, G. W.; Cortright, R. D.; Dumesic, J. A. Aqueous-phase reforming of ethylene glycol on silica-supported metal catalysts, *Appl. Catal. B* **2003,** *43,* 13–26.

[89] Lin, L.; Zhou, W.; Gao, R.; Yao, S.; Zhang, X.; Xu, W.; Zheng, S.; Jiang, Z.; Yu, Q.; Li, Y.-W.; Shi, C.; Wen, X.-D.; Ma, D. Low-temperature hydrogen production from water and methanol using Pt/α-MoC catalysts, *Nature* **2017,** *544,* 80–83.

[90] Alonso, D. M. *et al.* Increasing the revenue from lignocellulosic biomass: maximizing feedstock utilization, *Sci. Adv.* **2017,** *3,* e1603301.

[91] Li, Q.; García-Muelas, R.; López, N. Microkinetics of alcohol reforming for H$_2$ production from a FAIR density functional theory database, Submitted.

[92] Born, M.; Oppenheimer, R. Zur quantentheorie der molekeln, *Ann. Phys. (Berlin)* **1927,** *389,* 457–484.

[93] Groß, A. *Theoretical surface science;* Springer: 2014.

[94] Doren, V. E. V.; van Alsenoy, C.; Geerlings, P. Density functional theory and its application to materials, *AIP Conf. Proc.* **2000,** *June,* 8-10.

[95] Ceperley, D. M.; Alder, B. J. Ground state of the electron gas by a stochastic method, *Phys. Rev. Lett.* **1980,** *45,* 566.

[96] Gunnarsson, O.; Lundqvist, B. I.; Wilkins, J. W. Contribution to the cohesive energy of simple metals: spin-dependent effect, *Phys. Rev. B* **1974,** *10,* 1319.

[97] Jones, R. O.; Gunnarsson, O. The density functional formalism, its applications and prospects, *Rev. Mod. Phys.* **1989,** *61,* 689.

[98] Becke, A. D. Density-functional thermochemistry. III. The role of exact exchange, *J. Chem. Phys.* **1993,** *98,* 5648–5652.

[99] Lee, C.; Yang, W.; Parr, R. G. Development of the Colle-Salvetti correlation-energy formula into a functional of the electron density, *Phys. Rev. B* **1988,** *37,* 785.

[100] Stephens, P. J.; Devlin, F. J.; Chabalowski, C. F.; Frisch, M. J. Ab initio calculation of vibrational absorption and circular dichroism spectra using density functional force fields, *J. Phys. Chem.* **1994,** *98,* 11623–11627.

[101] Vosko, S. H.; Wilk, L.; Nusair, M. Accurate spin-dependent electron liquid correlation energies for local spin density calculations: a critical analysis, *Can. J. Phys.* **1980,** *58,* 1200–1211.

[102] Becke, A. D. Density-functional exchange-energy approximation with correct asymptotic behavior, *Phys. Rev. A* **1988,** *38,* 3098.

[103] Perdew, J. P.; Wang, Y. Accurate and simple analytic representation of the electron-gas correlation energy, *Phys. Rev. B* **1992,** *45,* 13244.

[104] Perdew, J. P.; Burke, K.; Ernzerhof, M. Generalized gradient approximation made simple, *Phys. Rev. Lett.* **1996,** *77,* 3865–3868.

[105] Hammer, B.; Hansen, L. B.; Nørskov, J. K. Improved adsorption energetics within density-functional theory using revised Perdew-Burke-Ernzerhof functionals, *Phys. Rev. B* **1999,** *59,* 7413.

[106] Perdew, J. P.; Ruzsinszky, A.; Csonka, G. I.; Vydrov, O. A.; Scuseria, G. E.; Constantin, L. A.; Zhou, X.; Burke, K. Restoring the density-gradient expansion for exchange in solids and surfaces, *Phys. Rev. Lett.* **2008,** *100,* 136406.

[107] Lejaeghere, K. *et al.* Reproducibility in density functional theory calculations of solids, *Science* **2016,** *351,* 1415.

[108] Wellendorff, J.; Lundgaard, K. T.; Møgelhøj, A.; Petzold, V.; Landis, D. D.; Nørskov, J. K.; Bligaard, T.; Jacobsen, K. W. Density functionals for surface science: exchange-correlation model development with Bayesian error estimation, *Phys. Rev. B* **2012,** *85,* 235149.

[109] Grimme, S. Accurate description of van der Waals complexes by density functional theory including empirical corrections, *J. Comput. Chem.* **2004,** *25,* 1463–1473.

[110] Grimme, S.; Antony, J.; Ehrlich, S.; Krieg, H. A consistent and accurate ab initio parametrization of density functional dispersion correction (DFT-D) for the 94 elements H-Pu, *J. Chem. Phys.* **2010,** *132,* 154104.

[111] Dion, M.; Rydberg, H.; Schröder, E.; Langreth, D. C.; Lundqvist, B. I. Van der Waals density functional for general geometries, *Phys. Rev. Lett.* **2004,** *92,* 246401.

[112] Lee, K.; Murray, É. D.; Kong, L.; Lundqvist, B. I.; Langreth, D. C. Higher-accuracy van der Waals density functional, *Phys. Rev. B* **2010,** *82,* 081101.

[113] Tkatchenko, A.; Scheffler, M. Accurate molecular van der Waals interactions from ground-state electron density and free-atom reference data, *Phys. Rev. Lett.* **2009,** *102,* 073005.

[114] Tao, J.; Perdew, J. P.; Staroverov, V. N.; Scuseria, G. E. Climbing the density functional ladder: nonempirical meta–generalized gradient approximation designed for molecules and solids, *Phys. Rev. Lett.* **2003,** *91,* 146401.

[115] Ashcroft, N. W.; Mermin, N. D. *Solid State Physics;* Cengage Learning: India, 1976.

[116] Sholl, D.; Steckel, J. A. *Density functional theory: a practical introduction;* John Wiley & Sons: 2011.

[117] Payne, M. C.; Teter, M. P.; Allan, D. C.; Arias, T. A.; Joannopoulos, J. D. Iterative minimization techniques for ab initio total-energy calculations: molecular dynamics and conjugate gradients, *Rev. Mod. Phys.* **1992,** *64,* 1045.

[118] Monkhorst, H. J.; Pack, J. D. Special points for Brillouin-zone integrations, *Phys. Rev. B* **1976,** *13,* 5188–5192.

[119] Carchini, G.; Almora-Barrios, N.; Revilla-López, G.; Bellarosa, L.; García-Muelas, R.; García-Melchor, M.; Pogodin, S.; Błoński, P.; López, N. How theoretical simulations can address the structure and activity of nanoparticles, *Top. Catal.* **2013,** *56,* 1262–1272.

[120] Kua, J.; Goddard III, W. A. Oxidation of methanol on 2nd and 3rd row group VIII transition metals (Pt, Ir, Os, Pd, Rh, and Ru): application to direct methanol fuel cells, *J. Am. Chem. Soc.* **1999,** *121,* 10928–10941.

[121] Yudanov, I. V.; Genest, A.; Schauermann, S.; Freund, H.-J.; Rösch, N. Size dependence of the adsorption energy of CO on metal nanoparticles: a DFT search for the minimum value, *Nano Lett.* **2012,** *12,* 2134–2139.

[122] Li, L.; Larsen, A. H.; Romero, N. A.; Morozov, V. A.; Glinsvad, C.; Abild-Pedersen, F.; Greeley, J.; Jacobsen, K. W.; Nørskov, J. K. Investigation of catalytic finite-size-effects of platinum metal clusters, *J. Phys. Chem. Lett.* **2012,** *4,* 222–226.

[123] Vanderbilt, D. Soft self-consistent pseudopotentials in a generalized eigenvalue formalism, *Phys. Rev. B* **1990,** *41,* 7892.

[124] Blöchl, P. E. Projector augmented-wave method, *Phys. Rev. B* **1994,** *50,* 17953–17979.

[125] Kresse, G.; Joubert, D. From ultrasoft pseudopotentials to the projector augmented-wave method, *Phys. Rev. B* **1999,** *59,* 1758–1775.

[126] Ditchfield, R.; Hehre, W. J.; Pople, J. A. Self-consistent molecular-orbital methods. IX. An extended Gaussian-type basis for molecular-orbital studies of organic molecules, *J. Chem. Phys.* **1971,** *54,* 724–728.

[127] Clark, T.; Chandrasekhar, J.; Spitznagel, G. W.; Schleyer, P. V. R. Efficient diffuse function-augmented basis sets for anion calculations. III. The 3-21+ G basis set for first-row elements, Li–F, *J. Comput. Chem.* **1983,** *4,* 294–301.

[128] Frisch, M. J.; Pople, J. A.; Binkley, J. S. Self-consistent molecular orbital methods 25. Supplementary functions for Gaussian basis sets, *J. Chem. Phys.* **1984,** *80,* 3265–3269.

[129] Campbell, C. T. Finding the rate-determining step in a mechanism: comparing DeDonder relations with the "Degree of Rate Control", *J. Catal.* **2001,** *204,* 520–524.

[130] Levenspiel, O. *Chemical reaction engineering, 3rd ed.;* Wiley: 1999.

[131] McCabe, W. L.; Smith, J. C.; Harriott, P. *Unit operations of chemical engineering, 7th ed.;* volume 5 McGraw-Hill New York: 2004.

[132] Rosenbrock, H. H. Some general implicit processes for the numerical solution of differential equations, *Comput. J.* **1963,** *5,* 329–330.

[133] García-Muelas, R.; López, N. *Collective descriptors for the adsorption of sugar alcohols on Pt and Pd(111),*
http://dx.doi.org/10.19061/iochem-bd-1-19.

[134] Frisch, M. J. *et al.* Gaussian 09, revision A. 02; Gaussian, *Inc., Wallingford, CT* **2009,** *270,* 271.

[135] Kresse, G.; Furthmüller, J. Efficiency of ab-initio total energy calculations for metals and semiconductors using a plane-wave basis set, *Comput. Mater. Sci.* **1996,** *6,* 15–50.

[136] Kresse, G.; Furthmüller, J. Efficient iterative schemes for ab initio total-energy calculations using a plane-wave basis set, *Phys. Rev. B* **1996,** *54,* 11169–11186.

[137] Methfessel, M.; Paxton, A. T. High-precision sampling for Brillouin-zone integration in metals, *Phys. Rev. B* **1989,** *40,* 3616–3621.

[138] Makov, G.; Payne, M. C. Periodic boundary conditions in ab initio calculations, *Phys. Rev. B* **1995,** *51,* 4014–4022.

[139] Lopes, A. J.; Tomé, L. I. N.; Rosado, M. T. S.; Leitão, M. L. P.; Redinha, J. S. Conformational study of erythritol and threitol in the gas state by density functional theory calculations, *Carbohydr. Res.* **2005,** *340,* 283–291.

[140] Greeley, J.; Mavrikakis, M. Competitive paths for methanol decomposition on Pt(111), *J. Am. Chem. Soc.* **2004,** *126,* 3910–3919.

[141] Sexton, B. A.; Hughes, A. E. A comparison of weak molecular adsorption of organic molecules on clean copper and platinum surfaces, *Surf. Sci.* **1984,** *140,* 227–248.

[142] Alcala, R.; Mavrikakis, M.; Dumesic, J. A. DFT studies for cleavage of C-C and C-O bonds in surface species derived from ethanol on Pt(111), *J. Catal.* **2003,** *218,* 178–190.

[143] Li, M.; Guo, W.; Jiang, R.; Zhao, L.; Shan, H. Decomposition of ethanol on Pd(111): a density functional theory study, *Langmuir* **2010,** *26,* 1879–1888.

[144] Chen, Y.; Salciccioli, M.; Vlachos, D. G. An efficient reaction pathway search method applied to the decomposition of glycerol on platinum, *J. Phys. Chem. C* **2011,** *115,* 18707–18720.

[145] Coll, D.; Delbecq, F.; Aray, Y.; Sautet, P. Stability of intermediates in the glycerol hydrogenolysis on transition metal catalysts from first principles, *Phys. Chem. Chem. Phys.* **2011,** *13,* 1448–1456.

[146] Tereshchuk, P.; Chaves, A. S.; Da Silva, J. L. F. Glycerol Adsorption on Platinum Surfaces: A Density Functional Theory Investigation with van der Waals Corrections, *J. Phys. Chem. C* **2014,** *118,* 15251–15259.

[147] Liu, B.; Greeley, J. Decomposition pathways of glycerol via C–H, O–H, and C–C bond scission on Pt(111): a density functional theory study, *J. Phys. Chem. C* **2011,** *115,* 19702–19709.

[148] Davis, J. L.; Barteau, M. A. Decarbonylation and decomposition pathways of alcohols on Pd(111), *Surf. Sci.* **1987,** *187,* 387–406.

[149] Skoplyak, O.; Barteau, M. A.; Chen, J. G. Reforming of oxygenates for H_2 production: correlating reactivity of ethylene glycol and ethanol on Pt(111) and Ni/Pt(111) with surface d-band center, *J. Phys. Chem. B* **2006,** *110,* 1686–1694.

[150] García-Muelas, R.; Li, Q.; López, N. Density functional theory comparison of methanol decomposition and reverse reactions on metal surfaces, *ACS Catal.* **2015,** *5,* 1027–1036.

[151] Lari, G. M.; Gröninger, O. G.; Li, Q.; Mondelli, C.; López, N.; Pérez-Ramírez, J. Catalyst and process design for the continuous manufacture of rare sugar alcohols by epimerization–hydrogenation of aldoses, *ChemSusChem* **2016,** *9,* 3407–3418.

[152] García-Muelas, R.; López, N. *Generalized models for adsorption of intermediates on transition metals,*
http://dx.doi.org/10.19061/iochem-bd-1-43.

[153] Jones, G.; Jakobsen, J. G.; Shim, S. S.; Kleis, J.; Andersson, M. P.; Rossmeisl, J.; Abild-Pedersen, F.; Bligaard, T.; Helveg, S.; Hinnemann, B.; Rostrup-Nielsen, J. R.; Chorkendorff, I.; Sehested, J.; Nørskov, J. K. First principles calculations and experimental insight into methane steam reforming over transition metal catalysts, *J. Catal.* **2008,** *259,* 147–160.

[154] Lausche, A. C.; Medford, A. J.; Khan, T. S.; Xu, Y.; Bligaard, T.; Abild-Pedersen, F.; Nørskov, J. K.; Studt, F. On the effect of coverage-dependent adsorbate–adsorbate interactions for CO methanation on transition metal surfaces, *J. Catal.* **2013,** *307,* 275–282.

[155] Wellendorff, J.; Silbaugh, T. L.; García-Pintos, D.; Nørskov, J. K.; Bligaard, T.; Studt, F.; Campbell, C. T. A benchmark database for adsorption bond energies to transition metal surfaces and comparison to selected DFT functionals, *Surf. Sci.* **2015,** *640,* 36–44.

[156] Silbaugh, T. L.; Campbell, C. T. Energies of formation reactions measured for adsorbates on late transition metal surfaces, *J. Phys. Chem. C* **2016,** *120,* 25161–25172.

[157] Li, Q.; García-Muelas, R.; López, N. *Microkinetics of alcohol reforming for H_2 production from a FAIR density functional theory database,*
http://dx.doi.org/10.19061/iochem-bd-1-37.

[158] Gokhale, A. A.; Dumesic, J. A.; Mavrikakis, M. On the mechanism of low-temperature water gas shift reaction on copper, *J. Am. Chem. Soc.* **2008,** *130,* 1402–1414.

[159] Grabow, L. C.; Gokhale, A. A.; Evans, S. T.; Dumesic, J. A.; Mavrikakis, M. Mechanism of the water gas shift reaction on Pt: first principles, experiments, and microkinetic modeling, *J. Phys. Chem. C* **2008,** *112,* 4608–4617.

[160] Byron-Smith, R. J.; Loganathan, M.; Shantha, M. S. A review of the water gas shift reaction kinetics, *Int. J. Chem. React. Eng.* **2010,** *8,*.

[161] Prats, H.; Álvarez, L.; Illas, F.; Sayós, R. Kinetic Monte Carlo simulations of the water gas shift reaction on Cu(111) from density functional theory based calculations, *J. Catal.* **2016,** *333,* 217–226.

[162] *Maple 13*, Waterloo Maple Inc. Waterloo, Ontario.

[163] Stegelmann, C.; Schiødt, N. C.; Campbell, C. T.; Stoltze, P. Microkinetic modeling of ethylene oxidation over silver, *J. Catal.* **2004,** *221,* 630–649.

[164] Gokhale, A. A.; Kandoi, S.; Greeley, J. P.; Mavrikakis, M.; Dumesic, J. A. Molecular-level descriptions of surface chemistry in kinetic models using density functional theory, *Chem. Eng. Sci.* **2004,** *59,* 4679–4691.

[165] Kandoi, S.; Greeley, J.; Sanchez-Castillo, M. A.; Evans, S. T.; Gokhale, A. A.; Dumesic, J. A.; Mavrikakis, M. Prediction of experimental methanol decomposition rates on platinum from first principles, *Top. Catal.* **2006,** *37,* 17–28.

[166] Cao, X.-M.; Burch, R.; Hardacre, C.; Hu, P. An understanding of chemoselective hydrogenation on crotonaldehyde over Pt(111) in the free energy landscape: the microkinetics study based on first-principles calculations, *Catal. Today* **2011,** *165,* 71–79.

[167] Sutton, J. E.; Vlachos, D. G. Building large microkinetic models with first-principles' accuracy at reduced computational cost, *Chem. Eng. Sci.* **2015,** *121,* 190–199.

[168] Medford, A. J.; Shi, C.; Hoffmann, M. J.; Lausche, A. C.; Fitzgibbon, S. R.; Bligaard, T.; Nørskov, J. K. CatMAP: a software package for descriptor-based microkinetic mapping of catalytic trends, *Catal. Lett.* **2015,** *145,* 794–807.

[169] Aljama, H.; Yoo, J. S.; Nørskov, J. K.; Abild-Pedersen, F.; Studt, F. Methanol partial oxidation on Ag (1 1 1) from first principles, *ChemCatChem* **2016,** *8,* 3621–3625.

[170] Madon, R. J.; Braden, D.; Kandoi, S.; Nagel, P.; Mavrikakis, M.; Dumesic, J. A. Microkinetic analysis and mechanism of the water gas shift reaction over copper catalysts, *J. Catal.* **2011,** *281,* 1–11.

[171] Jørgensen, M.; Grönbeck, H. First principles micro-kinetic modeling of methane oxidation over Pd(100) and Pd(111), *ACS Catal.* **2016,** .

[172] Gattinoni, C.; Michaelides, A. Atomistic details of oxide surfaces and surface oxidation: the example of copper and its oxides, *Surf. Sci. Rep.* **2015,** *70,* 424–447.

[173] Hirai, T.; Ikenaga, N.-O.; Miyake, T.; Suzuki, T. Production of hydrogen by steam reforming of glycerin on ruthenium catalyst, *Energy & Fuels* **2005,** *19,* 1761–1762.

[174] Huber, G. W.; Cortright, R. D.; Dumesic, J. A. Renewable alkanes by aqueous-phase reforming of biomass-derived oxygenates, *Angew. Chem. Int. Ed.* **2004,** *43,* 1549–1551.

[175] Bellarosa, L.; García-Muelas, R.; Revilla-López, G.; López, N. Diversity at the water–metal interface: metal, water thickness, and confinement effects, *ACS Cent. Sci.* **2016,** *2,* 109–116.

[176] Bellarosa, L.; García-Muelas, R.; Revilla-López, G.; López, N. *Diversity at the water–metal interface: metal, water thickness, and confinement effects*, http://dx.doi.org/10.19061/iochem-bd-1-1.

[177] Carrasco, J.; Hodgson, A.; Michaelides, A. A molecular perspective of water at metal interfaces, *Nat. Mater.* **2012,** *11,* 667–674.

[178] Meng, S.; Xu, L. F.; Wang, E. G.; Gao, S. Vibrational recognition of hydrogen-bonded water networks on a metal surface, *Phys. Rev. Lett.* **2002,** *89,* 176104.

[179] Rossmeisl, J.; Nørskov, J. K.; Taylor, C. D.; Janik, M. J.; Neurock, M. Calculated phase diagrams for the electrochemical oxidation and reduction of water over Pt(111), *J. Phys. Chem. B* **2006,** *110,* 21833–21839.

[180] Shi, C.; O'Grady, C. P.; Peterson, A. A.; Hansen, H. A.; Nørskov, J. K. Modeling CO_2 reduction on Pt(111), *Phys. Chem. Chem. Phys.* **2013,** *15,* 7114–7122.

[181] Haq, S.; Harnett, J.; Hodgson, A. Growth of thin crystalline ice films on Pt(111), *Surf. Sci.* **2002,** *505,* 171–182.

[182] Cerdá, J.; Michaelides, A.; Bocquet, M.-L.; Feibelman, P. J.; Mitsui, T.; Rose, M.; Fomin, E.; Salmeron, M. Novel water overlayer growth on Pd(111) characterized with scanning tunneling microscopy and density functional theory, *Phys. Rev. Lett.* **2004,** *93,* 116101.

[183] Nie, S.; Feibelman, P. J.; Bartelt, N. C.; Thürmer, K. Pentagons and heptagons in the first water layer on Pt(111), *Phys. Rev. Lett.* **2010,** *105,* 026102.

[184] Standop, S.; Redinger, A.; Morgenstern, M.; Michely, T.; Busse, C. Molecular structure of the H_2O wetting layer on Pt(111), *Phys. Rev. B* **2010,** *82,* 161412.

[185] Revilla-López, G.; López, N. A unified study for water adsorption on metals: meaningful models from structural motifs, *Phys. Chem. Chem. Phys.* **2014,** *16,* 18933–18940.

[186] Maier, S.; Stass, I.; Cerdá, J. I.; Salmeron, M. Unveiling the mechanism of water partial dissociation on Ru(0001), *Phys. Rev. Lett.* **2014,** *112,* 126101.

[187] Kimmel, G. A.; Petrik, N. G.; Dohnálek, Z.; Kay, B. D. Crystalline ice growth on Pt(111) and Pd(111): nonwetting growth on a hydrophobic water monolayer, *J. Chem. Phys.* **2007,** *126,* 114702.

[188] Haq, S.; Hodgson, A. Multilayer growth and wetting of Ru (0001), *J. Phys. Chem. C* **2007,** *111,* 5946–5953.

[189] Maier, S.; Lechner, B. A.; Somorjai, G. A.; Salmeron, M. Growth and structure of the first layers of ice on Ru(0001) and Pt(111), *J. Am. Chem. Soc.* **2016,** *138,* 3145–3151.

[190] Liu, F.; Sturm, J. M.; Lee, C. J.; Bijkerk, F. Coexistence of ice clusters and liquid-like water clusters on Ru(0001) surface, *Phys. Chem. Chem. Phys.* **2017,** *19,* 8288–8299.

[191] Bernal, J. D.; Fowler, R. H. A theory of water and ionic solution, with particular reference to hydrogen and hydroxyl ions, *J. Chem. Phys.* **1933,** *1,* 515–548.

[192] Huang, C. *et al.* The inhomogeneous structure of water at ambient conditions, *Proc. Natl. Acad. Sci. U.S.A.* **2009,** *106,* 15214–15218.

[193] Nilsson, A.; Pettersson, L. G. M. Perspective on the structure of liquid water, *Chem. Phys.* **2011,** *389,* 1–34.

[194] Sellberg, J. A. *et al.* Ultrafast X-ray probing of water structure below the homogeneous ice nucleation temperature, *Nature* **2014,** *510,* 381–384.

[195] Limmer, D. T.; Chandler, D. The putative liquid-liquid transition is a liquid-solid transition in atomistic models of water, *J. Chem. Phys.* **2011,** *135,* 134503.

[196] Limmer, D. T.; Chandler, D. The putative liquid-liquid transition is a liquid-solid transition in atomistic models of water. II, *J. Chem. Phys.* **2013,** *138,* 214504.

[197] Palmer, J. C.; Martelli, F.; Liu, Y.; Car, R.; Panagiotopoulos, A. Z.; Debenedetti, P. G. Metastable liquid-liquid transition in a molecular model of water, *Nature* **2014,** *510,* 385–388.

[198] Perakis, F. *et al.* Diffusive dynamics during the high-to-low density transition in amorphous ice, *Proc. Natl. Acad. Sci. U.S.A.* **2017,** www.pnas.org/cgi/doi/10.1073/pnas.1705303114.

[199] Nilsson, A.; Schreck, S.; Perakis, F.; Pettersson, L. G. M. Probing water with X-ray lasers, *Adv. Phys.: X* **2016,** *1,* 226–245.

[200] Lobban, C.; Finney, J. L.; Kuhs, W. F. The structure of a new phase of ice, *Nature* **1998,** *391,* 268–270.

[201] Li, T.-D.; Gao, J.; Szoszkiewicz, R.; Landman, U.; Riedo, E. Structured and viscous water in subnanometer gaps, *Phys. Rev. B 75,* 115415.

[202] Howe, R.; Whitworth, R. A determination of the crystal structure of ice XI, *J. Chem. Phys.* **1989,** *90,* 4450–4453.

[203] Ogasawara, H.; Brena, B.; Nordlund, D.; Nyberg, M.; Pelmenschikov, A.; Pettersson, L.; Nilsson, A. Structure and bonding of water on Pt(111), *Phys. Rev. Lett.* **2002,** *89,* 276102.

[204] Meng, S.; Wang, E. G.; Gao, S. Water adsorption on metal surfaces: a general picture from density functional theory studies, *Phys. Rev. B* **2004,** *69,* 195404.

[205] Feibelman, P. J. Partial dissociation of water on Ru(0001), *Science* **2002,** *295,* 99–102.

[206] Marx, D.; Hutter, J. *Ab initio molecular dynamics: basic theory and advanced methods;* Cambridge University Press: 2009.

[207] Nosé, S. A unified formulation of the constant temperature molecular dynamics methods, *J. Chem. Phys.* **1984,** *81,* 511–519.

[208] Hoover, W. G. Canonical dynamics: equilibrium phase-space distributions, *Phys. Rev. A* **1985,** *31,* 1695.

[209] Chau, P.-L.; Hardwick, A. J. A new order parameter for tetrahedral configurations, *Mol. Phys.* **1998,** *93,* 511–518.

[210] Velasco-Vélez, J.-J.; Wu, C. H.; Pascal, T. A.; Wan, L. F.; Guo, J.; Prendergast, D.; Salmeron, M. The structure of interfacial water on gold electrodes studied by X-ray absorption spectroscopy, *Science* **2014,** *346,* 831–834.

[211] de Grotthuss, C. J. T. Mémoire sur la décomposition de l'eau: et des corps qu'elle tient en dissolution à l'aide de l'électricité galvanique, *Ann. Chim.(Paris)* **1806**, *LVIII,* 54–74. Translated in: *Biochim Biophys Acta-Bioenerg.* **2006**, *1757,* 871–875.

[212] Soper, A. K. The radial distribution functions of water and ice from 220 to 673 K and at pressures up to 400 MPa, *Chem. Phys.* **2000,** *258,* 121–137.

[213] *ISIS Disordered Materials Database*, http://www.isis.stfc.ac.uk/groups/disordered.

[214] García-Ratés, M.; García-Muelas, R.; López, N. Solvation effects on methanol decomposition on Pd(111), Pt(111), and Ru(0001), *J. Phys. Chem. C* **2017,** *121,* 13803-13809.

[215] García-Ratés, M.; García-Muelas, R.; López, N. *Solvation effects on methanol decomposition on Pd(111), Pt(111), and Ru(0001)*, http://dx.doi.org/10.19061/iochem-bd-1-39.

[216] Murphy, C. J.; Carrasco, J.; Lawton, T. J.; Liriano, M. L.; Baber, A. E.; Lewis, E. A.; Michaelides, A.; Sykes, E. C. H. Structure and energetics of hydrogen-bonded networks of methanol on close packed transition metal surfaces, *J. Chem. Phys.* **2014,** *141,* 014701.

[217] Franaszczuk, K.; Herrero, E.; Zelenay, P.; Wieckowski, A.; Wang, J.; Masel, R. I. A comparison of electrochemical and gas-phase decomposition of methanol on platinum surfaces, *J. Phys. Chem.* **1992,** *96,* 8509–8516.

[218] Hartnig, C.; Spohr, E. The role of water in the initial steps of methanol oxidation on Pt(111), *Chem. Phys.* **2005,** *319,* 185–191.

[219] Sakong, S.; Groß, A. The importance of the electrochemical environment in the electro-oxidation of methanol on Pt(111), *ACS Catal.* **2016,** *6,* 5575–5586.

[220] Herron, J. A.; Morikawa, Y.; Mavrikakis, M. Ab initio molecular dynamics of solvation effects on reactivity at electrified interfaces, *Proc. Natl. Acad. Sci. U.S.A.* **2016,** *113,* E4937–E4945.

[221] Lari, G. M.; García-Muelas, R.; Mondelli, C.; López, N.; Pérez-Ramírez, J. Glycerol oxidehydration to pyruvaldehyde over silver-based catalysts for improved lactic acid production, *Green Chem.* **2016,** .

[222] Lari, G. M.; García-Muelas, R.; Mondelli, C.; López, N.; Pérez-Ramírez, J. *Acetol to pyruvaldehyde on Ag, AgO_x/Ag, and Ag_2O*, http://dx.doi.org/10.19061/iochem-bd-1-8.

[223] Werpy, T.; Petersen, G.; Aden, A.; Bozell, J.; Holladay, J.; White, J.; Manheim, A.; Eliot, D.; Lasure, L.; Jones, S. "Top value added chemicals from biomass. Volume 1-Results of screening for potential candidates from sugars and synthesis gas", Technical Report, DTIC Document, 2004.

[224] Bailey, R. B.; Joshi, D. K.; Michaels, S. L.; Wisdom, R. A. *Production of lactic acid by continuous fermentation using an inexpensive raw material and a simplified method of lactic acid purification*, 1988 US Patent 4771001.

[225] Severson, D. K.; Barrett, C. L. Lactobacillus delbrueckii ssp. bulgaricus *strain and fermentation process for producing L-(+)-lactic acid*, 1995 US Patent 5416020.

[226] Hekmat, D.; Bauer, R.; Fricke, J. Optimization of the microbial synthesis of dihydroxyacetone from glycerol with *Gluconobacter oxydans*, *Bioprocess. Biosyst. Eng.* **2003,** *26,* 109–116.

[227] Gätgens, C.; Degner, U.; Bringer-Meyer, S.; Herrmann, U. Biotransformation of glycerol to dihydroxyacetone by recombinant *Gluconobacter oxydans* DSM 2343, *Appl. Microbiol. Biotechnol.* **2007,** *76,* 553–559.

[228] Hu, W.; Knight, D.; Lowry, B.; Varma, A. Selective oxidation of glycerol to dihydroxyacetone over Pt-Bi/C catalyst: optimization of catalyst and reaction conditions, *Ind. Eng. Chem. Res.* **2010,** *49,* 10876–10882.

[229] Kwon, Y.; Birdja, Y.; Spanos, I.; Rodríguez, P.; Koper, M. T. M. Highly selective electro-oxidation of glycerol to dihydroxyacetone on platinum in the presence of bismuth, *ACS Catal.* **2012,** *2,* 759–764.

[230] Hirasawa, S.; Watanabe, H.; Kizuka, T.; Nakagawa, Y.; Tomishige, K. Performance, structure and mechanism of Pd–Ag alloy catalyst for selective oxidation of glycerol to dihydroxyacetone, *J. Catal.* **2013,** *300,* 205–216.

[231] Lari, G. M.; Mondelli, C.; Pérez-Ramírez, J. Gas-Phase Oxidation of Glycerol to Dihydroxyacetone over Tailored Iron Zeolites, *ACS Catal.* **2015,** *5,* 1453–1461.

[232] Morales, M.; Dapsens, P. Y.; Giovinazzo, I.; Witte, J.; Mondelli, C.; Papadokon-stantakis, S.; Hungerbühler, K.; Pérez-Ramírez, J. Environmental and economic assessment of lactic acid production from glycerol using cascade bio-and chemo-catalysis, *Energy Environ. Sci.* **2015,** *8,* 558–567.

[233] Lide, D. *CRC Handbook of Chemistry and Physics;* CRC press LLC: Boca Raton, USA, 84th ed.; 2003–2004.

[234] Dharmadi, Y.; Murarka, A.; Gonzalez, R. Anaerobic fermentation of glycerol by *Escherichia coli*: a new platform for metabolic engineering, *Biotechnol. Bioeng.* **2006,** *94,* 821–829.

[235] Kalapos, M. P. Methylglyoxal in living organisms: chemistry, biochemistry, toxicol-ogy and biological implications, *Toxicol. Lett.* **1999,** *110,* 145–175.

[236] Baltes, H.; Leupold, E. I. *Process for the manufacture of methylglyoxal*, 1981 US Patent 4302609.

[237] Baltes, H.; Leupold, E. I. 2-oxopropanal (methylglyoxal) by oxidation of glycerin in the gas phase, *Angew. Chem. Int. Ed. Engl.* **1982,** *21,* 540–540.

[238] Martin, N.; Klacar, S.; Grönbeck, H.; Knudsen, J.; Schnadt, J.; Blomberg, S.; Gustafson, J.; Lundgren, E. High-Coverage Oxygen-Induced Surface Structures on Ag(111), *J. Phys. Chem. C* **2014,** *118,* 15324–15331.

[239] Schmid, M. *et al.* Structure of Ag(111)-(4 × 4)-O: no silver oxide, *Phys. Rev. Lett.* **2006,** *96,* 146102.

[240] Schnadt, J.; Michaelides, A.; Knudsen, J.; Vang, R. T.; Reuter, K.; Lægsgaard, E.; Scheffler, M.; Besenbacher, F. Revisiting the structure of the p(4 × 4) surface oxide on Ag(111), *Phys. Rev. Lett.* **2006,** *96,* 146101.

[241] *VASP Manual*, http://cms.mpi.univie.ac.at/vasp/vasp/vasp.html, Accessed: Oct 31, **2016**.

[242] This is called "final state approximation" (ICORELEVEL=2, CLZ=1). *3d* electrons has "n" and "l" quantum numbers of 3 and 2 respectively (CLN=3, CLL=2).

[243] Kwon, Y.; Lai, S. C. S.; Rodríguez, P.; Koper, M. T. M. Electrocatalytic oxidation of alcohols on gold in alkaline media: base or gold catalysis?, *J. Am. Chem. Soc.* **2011,** *133,* 6914–6917.

[244] Solymosi, F.; Berkó, A.; Tarnóczi, T. I. Adsorption and decomposition of methanol on Rh(111) studied by electron energy loss and thermal desorption spectroscopy, *Surf. Sci.* **1984,** *141,* 533–548.

[245] Ehlers, D. H.; Spitzer, A.; Lüth, H. The adsorption of methanol on Pt(111), an IR reflection and UV photoemission study, *Surf. Sci.* **1985,** *160,* 57–69.

[246] Rebholz, M.; Kruse, N. Mechanisms of methanol decomposition on Pd(111), *J. Chem. Phys.* **1991,** *95,* 7745–7759.

[247] Lee, A. F.; Gawthrope, D. E.; Hart, N. J.; Wilson, K. A Fast XPS study of the surface chemistry of ethanol over Pt(111), *Surf. Sci.* **2004,** *548,* 200–208.

[248] Gong, J.; Flaherty, D. W.; Ojifinni, R. A.; White, J. M.; Mullins, C. B. Surface chemistry of methanol on clean and atomic oxygen pre-covered Au(111), *J. Phys. Chem. C* **2008,** *112,* 5501–5509.

[249] Williams, R. M.; Pang, S. H.; Medlin, J. W. O–H versus C–H bond scission sequence in ethanol decomposition on Pd(111), *Surf. Sci.* **2014,** *619,* 114–118.

[250] Jenkins, J. W.; Shutt, E. The Hot Spot^{TM}reactor, *Platin. Met. Rev* **1989,** *33,* 118–127.

[251] Edwards, N.; Ellis, S. R.; Frost, J. C.; Golunski, S. E.; van Keulen, A. N. J.; Lindewald, N. G.; Reinkingh, J. G. On-board hydrogen generation for transport applications: the HotSpot^{TM}methanol processor, *J. Power Sources* **1998,** *71,* 123–128.

[252] Geissler, K.; Newson, E.; Vogel, F.; Truong, T.-B.; Hottinger, P.; Wokaun, A. Autothermal methanol reforming for hydrogen production in fuel cell applications, *Phys. Chem. Chem. Phys.* **2001,** *3,* 289–293.

[253] Raimondi, F.; Geissler, K.; Wambach, J.; Wokaun, A. Hydrogen production by methanol reforming: post-reaction characterisation of a $Cu/ZnO/Al_2O_3$ catalyst by XPS and TPD, *Appl. Surf. Sci.* **2002,** *189,* 59–71.

[254] Gutierrez, A.; Karinen, R.; Airaksinen, S.; Kaila, R.; Krause, A. O. I. Autothermal reforming of ethanol on noble metal catalysts, *Int. J. Hydrogen Energy* **2011,** *36,* 8967–8977.

[255] Hung, C.-C.; Chen, S.-L.; Liao, Y.-K.; Chen, C.-H.; Wang, J.-H. Oxidative steam reforming of ethanol for hydrogen production on M/Al_2O_3, *Int. J. Hydrogen Energy* **2012,** *37,* 4955–4966.

[256] Cai, W.; Ramírez de la Piscina, P.; Homs, N. Oxidative steam reforming of bio-butanol for hydrogen production: effects of noble metals on bimetallic CoM/ZnO catalysts (M=Ru,Rh,Ir,Pd), *Appl. Catal., B* **2014,** *145,* 56–62.

[257] Harju, H.; Lehtonen, J.; Lefferts, L. Steam and autothermal reforming of n-butanol over Rh/ZrO_2 catalyst, *Catal. Today* **2015,** *244,* 47–57.

[258] Iwasa, N.; Masuda, S.; Ogawa, N.; Takezawa, N. Steam reforming of methanol over Pd/ZnO: effect of the formation of PdZn alloys upon the reaction, *Appl. Catal., A.* **1995,** *125,* 145–157.

[259] Cavallaro, S. Ethanol steam reforming on Rh/Al_2O_3 catalysts, *Energ. Fuel.* **2000,** *14,* 1195–1199.

[260] Llorca, J.; Homs, N.; Sales, J.; Ramírez de la Piscina, P. Efficient production of hydrogen over supported cobalt catalysts from ethanol steam reforming, *J. Catal.* **2002,** *209,* 306–317.

[261] Shishido, T.; Yamamoto, Y.; Morioka, H.; Takaki, K.; Takehira, K. Active Cu/ZnO and $Cu/ZnO/Al_2O_3$ catalysts prepared by homogeneous precipitation method in steam reforming of methanol, *Appl. Catal., A.* **2004,** *263,* 249–253.

[262] Yao, C.-Z.; Wang, L.-C.; Liu, Y.-M.; Wu, G.-S.; Cao, Y.; Dai, W.-L.; He, H.-Y.; Fan, K.-N. Effect of preparation method on the hydrogen production from methanol steam reforming over binary Cu/ZrO_2 catalysts, *Appl. Catal., A.* **2006,** *297,* 151–158.

[263] Vizcaíno, A. J.; Carrero, A.; Calles, J. A. Hydrogen production by ethanol steam reforming over Cu–Ni supported catalysts, *Int. J. Hydrogen Energy* **2007,** *32,* 1450–1461.

[264] Bayram, B.; Soykal, I. I.; von Deak, D.; Miller, J. T.; Ozkan, U. S. Ethanol steam reforming over Co-based catalysts: investigation of cobalt coordination environment under reaction conditions, *J. Catalysis* **2011,** *284,* 77–89.

[265] Da Silva, A. M.; De Souza, K. R.; Jacobs, G.; Graham, U. M.; Davis, B. H.; Mattos, L. V.; Noronha, F. B. Steam and CO_2 reforming of ethanol over Rh/CeO_2 catalyst, *Appl. Catal., B* **2011,** *102,* 94–109.

[266] Ramos, I. A. C.; Montini, T.; Lorenzut, B.; Troiani, H.; Gennari, F. C.; Graziani, M.; Fornasiero, P. Hydrogen production from ethanol steam reforming on M/CeO$_2$/YSZ M=Ru,Pd,Ag) nanocomposites, *Catal. Today* **2012,** *180,* 96–104.

[267] Rossetti, I.; Biffi, C.; Bianchi, C. L.; Nichele, V.; Signoretto, M.; Menegazzo, F.; Finocchio, E.; Ramis, G.; Di Michele, A. Ni/SiO$_2$ and Ni/ZrO$_2$ catalysts for the steam reforming of ethanol, *Appl. Catal., B* **2012,** *117,* 384–396.

[268] Cobo, M.; Pieruccini, D.; Abello, R.; Ariza, L.; Córdoba, L. F.; Conesa, J. A. Steam reforming of ethanol over bimetallic RhPt/La$_2$O$_3$: long-term stability under favorable reaction conditions, *Int. J. Hydrogen Energy* **2013,** *38,* 5580–5593.

[269] Sutton, J. E.; Panagiotopoulou, P.; Verykios, X. E.; Vlachos, D. G. Combined DFT, microkinetic, and experimental study of ethanol steam reforming on Pt, *J. Phys. Chem. C* **2013,** *117,* 4691–4706.

[270] Harju, H.; Lehtonen, J.; Lefferts, L. Steam reforming of n-butanol over Rh/ZrO$_2$ catalyst: role of 1-butene and butyraldehyde, *Appl. Catal., B* **2016,** *182,* 33–46.

[271] Shabaker, J. W.; Davda, R. R.; Huber, G. W.; Cortright, R. D.; Dumesic, J. A. Aqueous-phase reforming of methanol and ethylene glycol over alumina-supported platinum catalysts, *J. Catal.* **2003,** *215,* 344–352.

[272] Liu, J.; Sun, B.; Hu, J.; Pei, Y.; Li, H.; Qiao, M. Aqueous-phase reforming of ethylene glycol to hydrogen on Pd/Fe$_3$O$_4$ catalyst prepared by co-precipitation: metal–support interaction and excellent intrinsic activity, *J. Catal.* **2010,** *274,* 287–295.

[273] King, D. L.; Zhang, L.; Xia, G.; Karim, A. M.; Heldebrant, D. J.; Wang, X.; Peterson, T.; Wang, Y. Aqueous phase reforming of glycerol for hydrogen production over Pt–Re supported on carbon, *Appl. Catal., B* **2010,** *99,* 206–213.

[274] Kim, H.-D.; Park, H. J.; Kim, T.-W.; Jeong, K.-E.; Chae, H.-J.; Jeong, S.-Y.; Lee, C.-H.; Kim, C.-U. Hydrogen production through the aqueous phase reforming of ethylene glycol over supported Pt-based bimetallic catalysts, *Int. J. Hydrogen Energy* **2012,** *37,* 8310–8317.

[275] De Vlieger, D. J. M.; Mojet, B. L.; Lefferts, L.; Seshan, K. Aqueous phase reforming of ethylene glycol–Role of intermediates in catalyst performance, *J. Catal.* **2012,** *292,* 239–245.

[276] Byrd, A. J.; Pant, K. K.; Gupta, R. B. Hydrogen production from ethanol by reforming in supercritical water using Ru/Al$_2$O$_3$ catalyst, *Energy & Fuels* **2007,** *21,* 3541–3547.

[277] De Vlieger, D. J. M.; Chakinala, A. G.; Lefferts, L.; Kersten, S. R. A.; Seshan, K.; Brilman, D. W. F. Hydrogen from ethylene glycol by supercritical water reforming using noble and base metal catalysts, *Appl. Catal., B* **2012,** *111,* 536–544.

[278] Van Bennekom, J. G.; Kirillov, V. A.; Amosov, Y. I.; Krieger, T.; Venderbosch, R. H.; Assink, D.; Lemmens, K. P. J.; Heeres, H. J. Explorative catalyst screening studies on reforming of glycerol in supercritical water, *J. Supercrit. Fluids* **2012,** *70,* 171–181.

[279] Dreher, M.; Johnson, B.; Peterson, A. A.; Nachtegaal, M.; Wambach, J.; Vogel, F. Catalysis in supercritical water: pathway of the methanation reaction and sulfur poisoning over a Ru/C catalyst during the reforming of biomolecules, *J. Catalysis* **2013,** *301,* 38–45.

[280] Pairojpiriyakul, T.; Croiset, E.; Kiatkittipong, W.; Kiatkittipong, K.; Arporn-wichanop, A.; Assabumrungrat, S. Hydrogen production from catalytic supercritical water reforming of glycerol with cobalt-based catalysts, *Int. J. Hydrogen Energy* **2013,** *38,* 4368–4379.

[281] Pairojpiriyakul, T.; Croiset, E.; Kiatkittipong, K.; Kiatkittipong, W.; Arporn-wichanop, A.; Assabumrungrat, S. Catalytic reforming of glycerol in supercritical water with nickel-based catalysts, *Int. J. Hydrogen Energy* **2014,** *39,* 14739–14750.

[282] Ortiz, F. J. G.; Campanario, F. J.; Ollero, P. Turnover rates for the supercritical water reforming of glycerol on supported Ni and Ru catalysts, *Fuel* **2016,** *180,* 417–423.

Papers

Collective Descriptors for the Adsorption of Sugar Alcohols on Pt and Pd(111)

Rodrigo García-Muelas and Núria López*

Institute of Chemical Research of Catalonia (ICIQ), Avgda. Països Catalans 16, 43007, Tarragona, Catalonia, Spain

Ⓢ *Supporting Information*

ABSTRACT: Linear-scaling relationships are powerful tools in the rational design of new catalysts. Few of these thermodynamic relationships consider multifunctionalized molecules, and none deal with intramolecular interactions such as hydrogen bonds, widely present in polyoxygenated molecules obtained from renewable sources. We have completed an adsorption database with 14 mono- and polyalcohols up to four carbon atoms, on clean Pt and Pd(111) surfaces, using periodic density functional theory, and including van der Waals terms, and we have obtained results that are in good agreement with experimental data. With this data, we propose a robust multifactorial linear-scaling relationship, which is an additive function of the contributions from hydroxyl and CH_x groups and the hydrogen bonds. We have validated the model by comparison with experiments and by the prediction of adsorption energies of C4–C7 sugar alcohols on both surfaces. Our study paves the way for the study of large multifunctionalized molecules, like those derived from biomass.

$$\Delta E_{ads} = \Delta E_{ads}\left[n_O, n_C, n_\beta, n_\gamma \right]$$
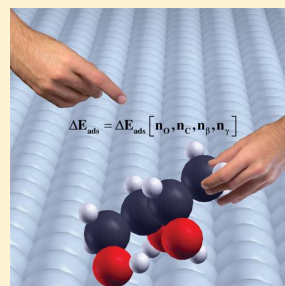
■ INTRODUCTION

Biomass is the most abundant renewable resource and one of the choices to reduce the world's dependence on oil as a source of chemicals.[1] Many emerging technologies in this field focus on a drop-in strategy, also named a platform-molecule approach, where a chemical with multiple end-use derivatives is obtained from nonedible biomass instead of fossil reservoirs.[2,3] Among the ten most promising building blocks, four of them are polyalcohols (glycerol, xylitol, and sorbitol), and another three have a hydroxyl functional group (ethanol, lactic acid, and 3-hydroxypropionic acid).[4] Transforming these alcohols into target molecules cheaply remains a challenge, and new catalysts need to be designed rationally.[5]

The rational design of catalysts has experienced a quantum leap during the past decade. Catalytic materials for the transformation of small molecules have been identified by the combination of density functional theory (DFT), microkinetic modeling, and stability analysis through engineering based on descriptors.[6] However, this rational design becomes exponentially complex with the size of the molecules, which compromises the applicability of these schemes. A way to reduce the computational burden of calculating a myriad of configurations is through the use of linear-scaling relationships, LSRs, that link thermodynamic or kinetic data to other thermodynamic parameters. Several LSRs are available for adsorption and reaction energies of small molecules and molecular fragments.[7−9] These relationships constitute a quantitative way to evaluate the qualitative principles enclosed in the bond-order conservation theory,[10] which states that the density surrounding an atom is rather constant and thus a new interaction (to the metal) occurs at the expense of another. Although LSRs are useful to abridge the technical gap between

theory and complex chemical processes, there are only few examples dealing with multifunctionalized molecules. To the best of our knowledge, only one study[8] gave a preliminary idea of how intramolecular hydrogen bonds might affect the scaling of polyoxygenated molecules like those derived from biomass, stating that the stabilization of hydrogen bonding is around 0.22 eV. Liu and Greeley presented a scheme based on the addition of different C, O, and C−O nearest-neighbors pairs to account for the interaction of molecular fragments coming from glycerol dehydrogenation reactions on different surfaces, including Pt, Pd, Rh, and Cu.[11−13] The procedure is highly modular, but the intramolecular hydrogen bonds are not taken into account explicitly in their description. Therefore, the inclusion of the effect of intramolecular hydrogen bonds in these formulations might reduce the systematic error of such approaches and make them more practical for the rational design of new catalysts to transform biomass into fuels and chemicals.

In the present work, we have studied 14 representative mono- and polyalcohols with up to four carbon atoms and three hydroxyl groups, and their adsorption on Pt and Pd(111) surfaces: methanol; ethanol; 1,2-ethanediol; 1- and 2-propanol; 1,2- and 1,3-propanediol; 1,2,3-propanetriol; 1-butanol; 1,2-, 1,3-, and 1,4-butanediol; and (2*S*,3*R*)- and (2*R*,3*R*)-1,2,3-butanetriol (i.e., erythro and threo diastereomers). With this database, we have developed a model equation, based on the additivity of the contributions of each functional group, to predict the adsorption energy of any saturated mono- or

The Journal of Physical Chemistry C

polyalcohol on these surfaces. We have benchmarked the model against 11 larger polyalcohols (C4−C7) commonly found in biomass: erythritol, threitol, xylitol, arabitol, ribitol, fucitol, sorbitol, mannitol, galactitol, iditol, and volemitol.

METHODS

As a starting point, we performed the extended conformational analysis of the C1−C4 alcohols in the gas phase. We obtained the ground state of each alcohol in the gas phase by (a) specifying the connectivity and bond lengths, which were 1.54, 1.43, 1.07, and 0.98 Å, for C−C, C−O, C−H, and O−H, respectively; (b) defining all initial angles to the tetrahedral (109.5°); (c) fixing the dihedral angles to ±60° and 180° (gauche (∓) and anti); and (d) omitting the conformations equivalent by symmetry to others. We relaxed these conformations with the Gaussian 09 package,[14] using the density functional and basis set B3LYP/6-311++g(2d,2p).[15] We verified that all vibrational frequencies were positive.

The Pt and Pd(111) metallic surfaces were modeled by a four-layer $2\sqrt{3} \times 2\sqrt{3}R30°$ slab. The lattice parameters were 3.968 and 3.939 Å, respectively. The two topmost layers were optimized by keeping the two bottom ones fixed to the bulk distances. Surface relaxations are described and benchmarked against experiments in Table S.I. 1 (Supporting Information). We used the Vienna Ab-initio Simulation Package (VASP),[16,17] the PBE density functional,[18] a kinetic energy cutoff of 450 eV, and a Methfessel−Paxton smearing of 0.1 eV.[19] For the surface calculations, the Brillouin zone was sampled by a $3 \times 3 \times 1$ Γ-centered k-points mesh generated through the Monkhorst−Pack method.[20] To avoid spurious interactions between the periodic images, we included a vacuum region between metal slabs of 20 Å, and dipole correction along z.[21] We relaxed the ground states of all the alcohols obtained from the conformational search in a box of $20 \times 20 \times 20$ Å³. We also evaluated the influence of the van der Waals (vdW), corrections in the adsorption process through the Grimme's DFT-D2 method, using all default parameters for the organic fragments,[22,23] and other parameters derived for the metals: $C_6^{(Pt)}$ = 7.00 J nm⁶ mol⁻¹, $C_6^{(Pd)}$ = 5.50 J nm⁶ mol⁻¹.[24] To prevent artifacts in the relaxation of the metal surface due to the van der Waals terms, the metal slabs were kept frozen during adsorption. The optimization thresholds were 10^{-5} eV and 0.015 eV/Å for electronic and ionic relaxations, respectively. We found the most stable conformation of each training-set alcohol on Pt(111) with the DFT-D2 method, through a rational process described in Section S.I.3 (Structure of the alcohols on Pt and Pd(111)) in the Supporting Information. Then, the same adsorbate structure was inherited for Pd(111), and also the vdW contributions were first removed on both metals, and then totally relaxed again. Because of the size and complexity of the C4−C7 alcohols in the validation set, i.e., 1215 possible conformations for erythritol, 1458 for threitol,[25] and higher for C5−C7 sugar alcohols, we considered that their ground-state conformations are the ones that maximize the number of intramolecular hydrogen bonds. For C5−C7 alcohols, a $3\sqrt{3} \times 3\sqrt{3} R30°$ slab and a $2 \times 2 \times 1$ Γ-centered k-points mesh were used.

RESULTS AND DISCUSSION

Conformational Search. The most stable conformations and the corresponding energy spectra for the different compounds are presented in Figure 1. Polyalcohols tend to
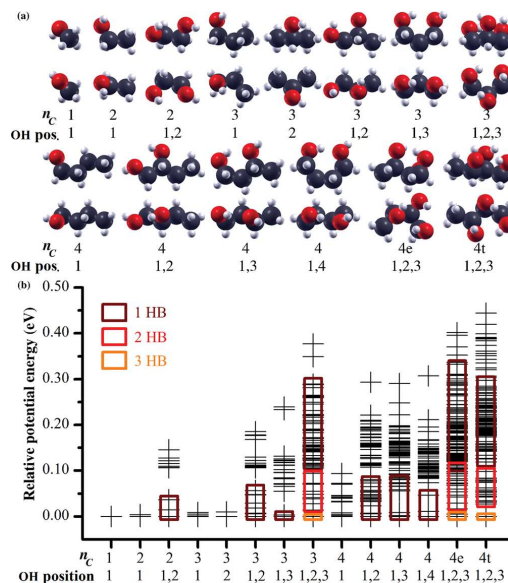
Figure 1. (a) Most stable conformations in the gas phase. Black, red, and white spheres correspond to carbon, oxygen, and hydrogen atoms, respectively. (b) Relative potential energies of all conformations of the considered mono- and polyalcohols. The number of intramolecular hydrogen bonds (HBs) is indicated. n_C is the number of carbon atoms.

maximize the number of intramolecular hydrogen bonds (HBs): 0 for monoalcohols, 1 for diols, 3 for triols, etc. Hydrogen bonds can be classified according to their relative position in a molecule as β vicinal (C nearest neighbors), γ conjugated (C next-nearest neighbors), δ (C second-next-nearest neighbors), and so forth. In all relaxed structures, typical distances are around 0.97 Å for O−H, 1.09 Å for C−H, 1.43 Å for C−O, and 1.53 Å for C−C. All the angles between two C−C bonds lie between the expected value of 109.5° ± 5.0°, and the same occurs for the dihedral ones, i.e., 180° or ±60°, with deviations of ±9°. Notable exceptions are the ground states of 1,2-diols and 1,2,3-triols, which show a larger dihedral angle deviation, up to 15° and 40°, respectively. As a consequence, in the ground state of these triols, some O−C−C−O dihedral angles are almost eclipsed to increase the strength of the β hydrogen bond. For the triol conformations containing two hydrogen bonds, the maximum dihedral deviations were around 25°. In summary, the strongest hydrogen bonds correspond to the formation of six- or seven-membered ring cycles; i.e., the C atoms with the alcohol functionalities are interleaved by one or two C atoms, traditionally assigned as γ and δ positions, respectively.

Figure 1b shows the distribution of the relative energies with respect to the ground state for each alcohol. The number of hydrogen bonds is the key factor controlling the conformational energy spectra of the polyalcohols. For the 1,2,3-triols, the most stable conformations have three intramolecular hydrogen bonds. However, they have a small difference in energy when compared to the two-hydrogen-bond conformations, due to the strains present in the three-hydrogen-bond structures (vide supra). The distribution in energies is similar within each one of the polyalcohol families: 1,2-diols, 1,3-diols,

Article
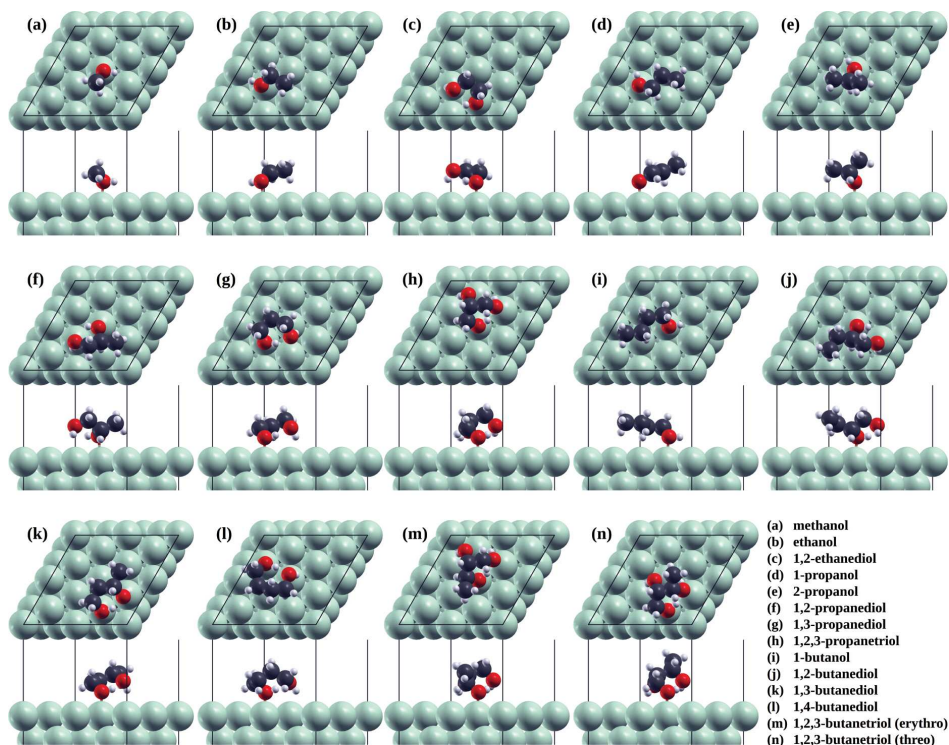
Figure 2. Structures of alcohols adsorbed on Pt and Pd(111) obtained with a DFT-D2 approach. Green, black, red, and white spheres correspond to metal (Pt, Pd), carbon, oxygen, and hydrogen atoms, respectively.

(a) methanol
(b) ethanol
(c) 1,2-ethanediol
(d) 1-propanol
(e) 2-propanol
(f) 1,2-propanediol
(g) 1,3-propanediol
(h) 1,2,3-propanetriol
(i) 1-butanol
(j) 1,2-butanediol
(k) 1,3-butanediol
(l) 1,4-butanediol
(m) 1,2,3-butanetriol (erythro)
(n) 1,2,3-butanetriol (threo)
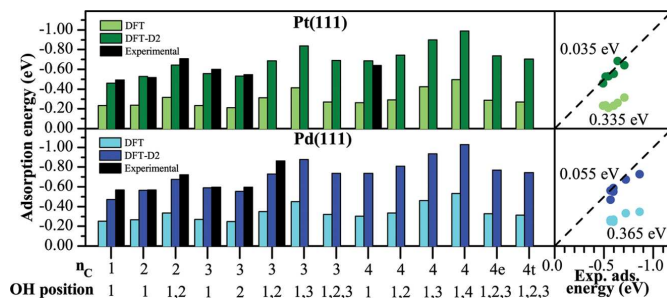
Figure 3. Left: Comparison between temperature-programmed desorption adsorption energies in the literature[27,32−35] and those calculated in the present study. n_C is the number of carbon atoms. Right: Corresponding mean average errors for both DFT and DFT-D2.

and 1,2,3-triols. The energy associated with breaking one intramolecular hydrogen bond is in the range 0.1−0.2 eV. In the Supporting Information, we show how the conformational spectra for the alcohols can be retrieved by DFT-D2 and plane waves; see Figure S.I. 1.

Alcohol Adsorption. Once the gas-phase minima were identified, we studied the adsorption of the polyalcohols on two surfaces: Pt and Pd(111). The structures were initialized from different gas-phase conformers. Figure 2 illustrates the most stable structures for the alcohols adsorbed on Pt(111), considering the van der Waals (vdW) contributions. The

structures for Pd are similar and the qualitative structure is maintained if vdW terms are eliminated. The monoalcohols bind to the metal surface through an oxygen atom near an atop position,[26] while the rest of the carbon tail lies parallel to the metal surface to increase the van der Waals interaction, as suggested by experiments.[27] Previous theoretical studies predicted that the carbon tail points outward to the surface.[28,29] However, these authors employed small supercells and their simulations lack vdW contributions; both issues can prevent the carbon tails to interact with the metal surfaces efficiently. Detailed data can be retrieved in Table S.I. 2 and Figure S.I. 2

(Supporting Information). The diols and triols bind strongly through one oxygen atom near a top position, while the other hydroxyl groups point to the surface by their hydrogen atoms. Our results also suggest that the adsorbates tend to preserve their gas-phase ground-state structures, with elongation in their intramolecular hydrogen bonds. A comparison between our adsorption energies and previous experimental and theoretical values is available in Tables S.I. 3−5 (Supporting Information). In general, we found a good agreement for all the structures proposed in the literature, with the exception of adsorbed glycerol: our final configuration is consistent with previous theoretical studies,[30,31] but differs slightly from that in ref 11 in which the reported structure lacks two intramolecular hydrogen bonds.

In Figure 3, we present the whole set of adsorption energies from DFT and DFT-D2 and compare them with temperature-programmed desorption (TPD) data available in the literature. A close view of these values reveals that the DFT-D2 method reproduces the TPD values best. The interaction between an isolated alcohol on both Pt and Pd(111) is governed by three features: the number of hydroxyl groups in contact with the surface, the intramolecular hydrogen bonds, and the number of carbon atoms in the molecule that are close to the surface. In the next section, we deduce an additive model that predicts the adsorption energies of small C1−C6 alcohols.

Multifactorial Linear-Scaling Relationships. Here, we present the derivation of a multifactorial linear-scaling relationship for the adsorption of alcohols on the metal surface. The DFT-D2 results point out that each hydroxyl group in contact with the surface has a leading contribution to the adsorption energy. It is noticeable that, for both Pt and Pd(111) surfaces, and for a given number of carbon atoms, the least favorable adsorption energy always corresponds to a monoalcohol, irrespective of the vdW terms. An example can be found in ethanol and 1,2-ethanediol, where the latter introduces an extra energy contribution of about 0.10 eV. However, this single rule cannot explain why the adsorption of 1,2,3-propanetriol is weaker than that of 1,3-propanediol on both metals. This discrepancy also appears for 1,3-butanediol and 1,2,3-butanetriol, for either erythro or threo diastereomers.

Second, the intramolecular hydrogen bonds are weaker when the alcohol adsorbs on the metal. This process is endothermic, and the magnitude of the change depends on the local structure of each hydrogen bond. Hydrogen bonds can be classified according to their relative position in a molecule as β vicinal (C nearest neighbors), γ conjugated (C next-nearest neighbors), δ (C second-next-nearest neighbors), and so forth. The larger energy penalty occurs for the β hydrogen bonds, due to the stiffness of this configuration: if the two O atoms are in contact with the metal surface, the backbone has to accommodate the strain.[8,36] As examples, the adsorption of the 1,2-propanediol (1,2-butanediol) is less exothermic than that of 1,3-propanediol (1,3-butanediol). Finally, the CH_x groups physisorb on the metal surfaces through weak vdW interactions; thus, adsorption is more exothermic as the alcohol aliphatic chain grows.

Following the concepts of functional group additivity, and high-order terms (group−group interactions) developed in the literature,[8,10,36] we have put forward an additive model for the adsorption of polyalcohols on metal surfaces. The contributions come from the different functional groups: hydroxyl or methylene groups, and second-order interactions can be mapped to intramolecular hydrogen bonds. The model was first sketched in a way that the contribution for each of the

groups was dependent on the position of the atoms with respect to the surface; see the Supporting Information (Section S.I. 5). However, once the results were analyzed, it became clear that a topologic model that eliminates the explicit dependence of the adsorption energies to the distance to the surface could be drawn. In the topologic model, the adsorption energy, ΔE_{ads}, can be expressed as

$$\Delta E_{ads} = a_O n_O + a_C n_C + a_\beta n_\beta + a_\gamma n_\gamma \tag{1}$$

where a_O is the contribution of each hydroxyl group interacting with the metal, a_C is that of each CH_x group in the molecule close to the surface, and a_β and a_γ are the terms from the distortion of β or γ hydrogen bonds. The contribution from higher-order terms was found negligible. The $\{n_X\}$ is the collective variable that contains the number of effective X = hydroxyl, CH_x, β, or γ hydrogen bonds. For the training set, composed of 14 alcohols, methanol; ethanol; 1,2-ethanediol; 1- and 2-propanol; 1,2- and 1,3-propanediol; 1,2,3-propanetriol; 1-butanol; 1,2-, 1,3-, and 1,4-butanediol; and $(2S,3R)$- and $(2R,3R)$-1,2,3-butanetriol, a detailed counting of the $\{n_X\}$ was performed that allowed the determination of the associated energy parameters $\{a_X\}$.

The easiest way to obtain $\{n_X\}$ is by performing all possible rotations to the target bonds so that (a) the maximum number of hydroxyl groups are on the same side of the molecule, (b) and they can interact with the surface, and (c) the largest number of HBs is maintained. It shall be kept in mind that one of the oxygens atoms shall be in direct contact to a metal atom on the surface. Then, the effectiveness of the bonds can be generalized from the data in Figure 4 as follows: for an interaction between the minimum of the potential well and a
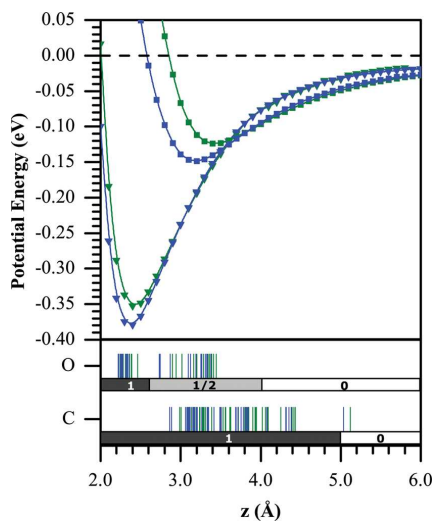
Figure 4. Potential energy surfaces for the interaction of water (triangles) or methane (squares) molecules as a function of the distance from the central atom to the metal surface, z, as obtained with DFT-D2. Blue corresponds to Pd and green to Pt. (b) Distances of the C or O atoms in the molecules of the training set. The strengths of the interactions at different distances are marked by colors: dark, strong; clear, weak. The Cartesian coordinates are displayed in the Supporting Information (Tables S.I. 11−13).

Article

Table 1. Topologic Model Energy Parameters, a_X in eV, Fitted to the DFT-D2 Adsorption Data. The Mean Absolute Error and the Regression Coefficients Are Shown

metal	a_O	a_C	a_β	a_γ	MAE	R^2
Pt(111)	−0.441	−0.060	+0.170	+0.019	0.033	0.996
Pd(111)	−0.448	−0.069	+0.168	+0.028	0.036	0.996

20% extension, the contribution to $\{n_X\}$ accounts for 1; between this expansion and 2/3, it contributes by 1/2; and no contribution is taken into account at longer distances. Then, to obtain the energy contributions of eq 1, $\{a_X\}$, we minimized the mean squared error through multiple linear regressions, using the DFT-D2 adsorption data of the 14 alcohols (C1−C4) in the training set (Table S.I. 3, Supporting Information). The fitted energy parameters are shown in Table 1, and the $\{n_X\}$ are presented in Table S.I. 10 (Supporting Information).

The results of our fitting support the conclusions of an earlier experimental study on the adsorption of short-chain mono-alcohols on Pt(111), which pointed out that the leading contribution for adsorption is that of the hydroxyl group, estimated to be −0.435 eV.[27] Our fitted values are around −0.45 eV for both Pt and Pd(111) surfaces. As for the alkyl contribution, the same set of experiments reports −0.060 eV/CH$_2$ lying on Pt(111),[27] while DFT-D2 leads to −0.060 eV for Pt and is slightly larger for Pd, −0.069 eV. This contribution vanishes when vdW is not considered, see Table S.I. 9 (Supporting Information). In contrast, the hydrogen bonds−surface interaction terms are repulsive. The energy penalties for weakening a β HB are on the order of 0.1−0.2 eV, which corresponds roughly to the energy difference between different conformations discussed in the Conformational Search section. The energy penalties for weakening vicinal β HBs are larger than those of conjugated γ ones. The model above rationalizes why 1,2,3-propanetriol, which has two β and one γ HB, shows a lower binding energy than 1,3-propanediol, as the HBs are loosened on the surface. The destabilization of the intermolecular hydrogen bonds overcompensates the exother-mic contribution of having a third hydroxyl group in the molecule.

With the energy parameters in Table 1 and the $\{n_X\}$ values presented in Table S.I. 10, the energies for the model can be retrieved and compared to the DFT-D2 values; see Figure 5. The training sets, represented by green (Pt) and blue (Pd) points, show that model deviations are smaller than 0.10 eV. The limiting cases in the set are 2-propanol, overestimated by 0.09 eV, and 1,4-butanediol, underestimated by 0.07 eV. The
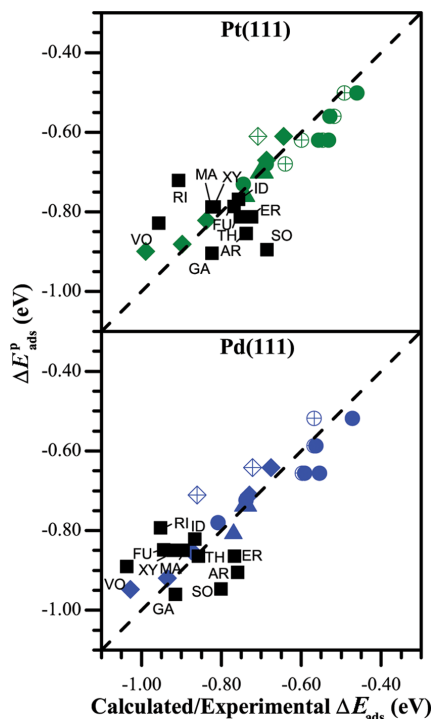
Figure 5. Comparison between predicted, ΔE_{ads}^{MODEL}, and calculated, ΔE_{ads}^{DFT-D2}, adsorption energies. Dots, diamonds, and triangles represent monoalcohols, diols, and triols from the training set, respectively. Black squares show the values for the validation set. Empty symbols stand for the experimental data.[27,32−35]

reason for the small discrepancies found is the ineffective interaction between a carbon group and the metal surfaces in 2-propanol, while 1,4-butanediol has a stronger interaction between the metal surface and the carbon tail, as it lies almost flat.

Then, we tested the predictive power of the model in a validation set, composed of 11 sugar alcohols: C4 = erythritol, threitol; C5 = xylitol, arabitol, ribitol; C6 = fucitol, sorbitol, mannitol, galactitol, iditol; and C7 = volemitol. According to

Table 2. Collective Descriptor n_X and Predicted Adsorption Energies, ΔE_{ads}^p in eV, for Sugar Alcohols on Pt and Pd(111) with the Topologic Model

		n_O	n_C	n_β	n_γ	n_δ	n_ε	ΔE_{ads}^{Pt}	ΔE_{ads}^{Pd}
C4	erythritol	2.5	4	3.0	1.0	0.0	0.0	−0.813	−0.864
	threitol	2.5	4	3.0	1.0	0.0	0.0	−0.813	−0.864
C5	xylitol	2.5	5	3.5	1.0	0.0	0.0	−0.787	−0.849
	arabitol	2.5	5	3.0	2.0	0.0	0.0	−0.854	−0.905
	ribitol	2.5	5	4.0	0.0	1.0	0.0	−0.721	−0.793
C6	fucitol	2.0	6	2.5	1.5	0.0	0.0	−0.787	−0.848
	sorbitol	2.5	6	3.0	3.0	0.0	0.0	−0.895	−0.946
	mannitol	2.5	5	3.5	1.0	1.0	0.0	−0.787	−0.849
	galactitol	2.5	6	3.0	2.5	0.0	0.0	−0.904	−0.960
	iditol	2.5	5	3.5	2.0	0.0	0.0	−0.769	−0.821
C7	volemitol	2.5	6	3.5	2.0	0.0	1.0	−0.828	−0.890

the DFT-D2 data, C4−C7 polyalcohols adsorb exothermically in the range of 0.7−1.1 eV (see Table S.I. 3), which is in the intermediate area of the training set. The collective variables of C4−C7 sugar alcohols are listed in Table 2. The $\{n_X\}$ are obtained by reorganizing the polyalcohol to show as many hydroxyl groups facing the surface as possible. For large molecules, topological constraints due to chirality should be considered because they limit the maximum number of OH groups that can simultaneously interact with the surface. For example, erythritol and threitol are C4 tetraols, which differ in just one chiral center, and thus, their adsorption energies are slightly different. The values obtained through the model are in reasonable agreement with those of the DFT-D2 values, as shown by the black squares in Figure 5. In this case, the errors are slightly larger, up to 0.2 eV, ribitol and sorbitol being the extreme cases. The results above show the predictive nature of the topologic model described in the present work.

CONCLUSIONS

We have employed density functional theory with dispersion contributions to analyze the adsorption of a large group of mono- and polyalcohols. These energies have been used as a training set to a model that can account for the interaction of alcohols with Pt and Pd(111) surfaces by analyzing the topology of these molecules. In summary, when polyalcohols adsorb on Pt or Pd(111) surfaces, they interact mainly by the hydroxyl groups, which weakens their intramolecular hydrogen bonds. The CH_x tails also contribute to the bond via van der Waals interactions. Multifactorial linear relationships, derived from a relatively large database of DFT-D2 energies, allow the definition of a collective variable descriptor that can be used to obtain the adsorption energy of other polyalcohols. This collective variable contains the number of interactions that are present upon adsorption: exothermic contributions from OH and CH_x close to the surface, and the energy penalty of loosening intramolecular hydrogen bonds. The model was then validated to assess the adsorption of larger polyalcohols with positive results. For large molecules, complexity in the form of chirality can hinder the simultaneous interaction of all the hydroxyl groups with the metal, thus reducing the total adsorption energy. The present approach can be extended to include molecular fragments and other functional groups and, thus, paves the way for a simpler study of new catalytic routes to transform complex molecules, like those present in nonedible biomass, into chemicals and fuels.

ASSOCIATED CONTENT

Ⓢ Supporting Information

Comparison between B3LYP and DFT-D2, description of the metal, generation of the adsorbed structures, comparison with the previous studies, details of the model, and coordinates of the metal surfaces and adsorbates. This material is available free of charge via the Internet at http://pubs.acs.org.

AUTHOR INFORMATION

Corresponding Author

*E-mail: nlopez@iciq.es. Phone: +34 977920237. Fax: +34 977920231.

Notes

The authors declare no competing financial interest.

ACKNOWLEDGMENTS

REFERENCES

(1) Ragauskas, A. J.; Williams, C. K.; Davison, B. H.; Britovsek, G.; Cairney, J.; Eckert, C. A.; Frederick, W. J.; Hallett, J. P.; Leak, D. J.; Liotta, C. L.; et al. The path forward for biofuels and biomaterials. *Science* **2006**, *311*, 484−489.

(2) Dapsens, P. Y.; Mondelli, C.; Pérez-Ramírez, J. Biobased chemicals from conception toward industrial reality: Lessons learned and to be learned. *ACS Catal.* **2012**, *2*, 1487−1499.

(3) Ruppert, A. M.; Weinberg, K.; Palkovits, R. Hydrogenolysis goes bio: From carbohydrates and sugar alcohols to platform chemicals. *Angew. Chem., Int. Ed.* **2012**, *51*, 2564−2601.

(4) Bozell, J. J.; Petersen, G. R. Technology development for the production of biobased products from biorefinery carbohydrates − The US Department of Energy's "top 10" revisited. *Green Chem.* **2010**, *12*, 539−554.

(5) Chorkendorff, I; Niemantsverdriet, J. W. *Concepts of Modern Catalysis and Kinetics*; Wiley-VCH: Weinheim, Germany, 2003.

(6) Nørskov, J. K.; Bligaard, T.; Rossmeisl, J.; Christensen, C. H. Towards the computational design of solid catalysts. *Nat. Chem.* **2009**, *1*, 37−46.

(7) Abild-Pedersen, F.; Greeley, J.; Studt, F.; Rossmeisl, J.; Munter, T. R.; Moses, P. G.; Skulason, E.; Bligaard, T.; Nørskov, J. K. Scaling properties of adsorption energies for hydrogen-containing molecules on transition-metal surfaces. *Phys. Rev. Lett.* **2007**, *99*, 016105.

(8) Salciccioli, M.; Chen, Y.; Vlachos, D. G. Density functional theory-derived group additivity and linear scaling methods for prediction of oxygenate stability on metal catalysts: Adsorption of open-ring alcohol and polyol dehydrogenation intermediates on Pt-based metals. *J. Phys. Chem. C* **2010**, *114*, 20155−20166.

(9) Calle-Vallejo, F.; Martínez, J. I.; García-Lastra, J. M.; Rossmeisl, J.; Koper, M. T. M. Physical and chemical nature of the scaling relations between adsorption energies of atoms on metal surfaces. *Phys. Rev. Lett.* **2012**, *108*, 116103.

(10) Shustorovich, E. Chemisorption phenomena: Analytic modeling based on perturbation theory and bond-order conservation. *Surf. Sci. Rep.* **1986**, *6*, 1−63.

(11) Liu, B.; Greeley, J. Decomposition pathways of glycerol via C−H, O−H, and C−C bond scission on Pt(111): A density functional theory study. *J. Phys. Chem. C* **2011**, *115*, 19702−19709.

(12) Liu, B.; Greeley, J. Density functional theory study of selectivity considerations for C−C versus C−O bond scission in glycerol decomposition on Pt(111). *Top. Catal.* **2012**, *55*, 280−289.

(13) Liu, B.; Greeley, J. A density functional theory analysis of trends in glycerol decomposition on close-packed transition metal surfaces. *Phys. Chem. Chem. Phys.* **2013**, *15*, 6475−6485.

(14) Frisch, M. J.; Trucks, G. W.; Schlegel, H. B.; Scuseria, G. E.; Robb, M. A.; Cheeseman, J. R.; Scalmani, G.; Barone, V.; Mennucci, B.; Petersson, G. A.; et al. *Gaussian 09*, revision A.02; Gaussian, Inc.: Wallingford, CT, 2009.

(15) Becke, A. D. Density-functional thermochemistry. III. The role of exact exchange. *J. Chem. Phys.* **1993**, *98*, 5648.

(16) Kresse, G.; Furthmüller, J. Efficiency of ab-initio total energy calculations for metals and semiconductors using a plane-wave basis set. *Comput. Mater. Sci.* **1996**, *6*, 15−50.

(17) Kresse, G.; Furthmüller, J. Efficient iterative schemes for ab initio total-energy calculations using a plane-wave basis set. *Phys. Rev. B* **1996**, *54*, 11169.

(18) Perdew, J. P.; Burke, K.; Ernzerhof, M. Generalized gradient approximation made simple. *Phys. Rev. Lett.* **1996**, *77*, 3865.

(19) Methfessel, M.; Paxton, A. T. High-precision sampling for Brillouin-zone integration in metals. *Phys. Rev. B* **1989**, *40*, 3616.

(20) Monkhorst, H. J.; Pack, J. D. Special points for Brillouin-zone integrations. *Phys. Rev. B* **1976**, *13*, 5188−5192.

The Journal of Physical Chemistry C

(21) Makov, G.; Payne, M. C. Periodic boundary conditions in ab initio calculations. *Phys. Rev. B* **1995**, *51*, 4014−4022.

(22) Grimme, S. Semiempirical GGA-type density functional constructed with a long-range dispersion correction. *J. Comput. Chem.* **2006**, *27*, 1787−1799.

(23) Bučko, T.; Hafner, J.; Lebègue, S.; Ángyán, J. G. Improved description of the structure of molecular and layered crystals: Ab initio DFT calculations with van der Waals corrections. *J. Phys. Chem. A* **2010**, *114*, 11814−11824.

(24) Ruiz, V. G.; Liu, W.; Zojer, E.; Scheffler, M.; Tkatchenko, A. Density-functional theory with screened van der Waals interactions for the modeling of hybrid inorganic-organic systems. *Phys. Rev. Lett.* **2012**, *108*, 146103.

(25) Lopes Jesus, A. J.; Tomé, L. I. N.; Rosado, M. T. S.; Leitão, M. L. P.; Redinha, J. S. Conformational study of erythritol and threitol in the gas state by density functional theory calculations. *Carbohydr. Res.* **2005**, *340*, 283−291.

(26) Greeley, J.; Mavrikakis, M. Competitive paths for methanol decomposition on Pt(111). *J. Am. Chem. Soc.* **2004**, *126*, 3910−3919.

(27) Sexton, B. A.; Hughes, A. E. A comparison of weak molecular adsorption of organic molecules on clean copper and platinum surfaces. *Surf. Sci.* **1984**, *140*, 227−248.

(28) Alcalá, R.; Mavrikakis, M.; Dumesic, J. A. DFT studies for cleavage of C−C and C−O bonds in surface species derived from ethanol on Pt(111). *J. Catal.* **2003**, *218*, 178−190.

(29) Li, M.; Guo, W.; Jiang, R.; Zhao, L.; Shan, H. Decomposition of ethanol on Pd(111): A density functional theory study. *Langmuir* **2010**, *26*, 1879−1888.

(30) Chen, Y.; Salciccioli, M.; Vlachos, D. G. An efficient reaction pathway search method applied to the decomposition of glycerol on platinum. *J. Phys. Chem. C* **2011**, *115*, 18707−18720.

(31) Coll, D.; Delbecq, F.; Aray, Y.; Sautet, P. Stability of intermediates in the glycerol hydrogenolysis on transition metal catalysts from first principles. *Phys. Chem. Chem. Phys.* **2011**, *13*, 1448−1456.

(32) Rendulic, K. D.; Sexton, B. A. Adsorption and dehydrogenation of alcohols and ethers on platinum(111). *J. Catal.* **1982**, *78*, 126−135.

(33) Skoplyak, O.; Barteau, M. A.; Chen, J. G. Reforming of oxygenates for H₂ production: Correlating reactivity of ethylene glycol and ethanol on Pt(111) and Ni/Pt(111) with surface d-band center. *J. Phys. Chem. B* **2006**, *110*, 1686−1694.

(34) Davis, J. L.; Barteau, M. A. Decarbonylation and decomposition pathways of alcohol's on Pd(111). *Surf. Sci.* **1987**, *187*, 387−406.

(35) Griffin, M. B.; Jorgensen, E. L.; Medlin, J. W. The adsorption and reaction of ethylene glycol and 1,2-propanediol on Pd(111): A TPD and HREELS study. *Surf. Sci.* **2010**, *604*, 1558−1564.

(36) Benson, S. W. *Thermochemical Kinetics: Methods for the Estimation of Thermochemical Data and Rate Parameters*; Wiley-Interscience: New York, 1976.

Generalized models for adsorption of intermediates on transition metals

Rodrigo García Muelas* and Núria López*

June 30, 2017

Abstract

The rational design of the new generations of heterogeneous catalysts relies on the efficient survey of reaction networks sampled by Density Functional Theory, DFT. However, massive reaction networks as those involved in the conversion of biomass cannot be sampled efficiently as they involve more than 105 intermediates even for a small C6 sugar. Here we present a statistical principal component analysis of the thermochemical data of 71 C_1-C_2 molecular fragments on 12 metals surfaces. The two main contributions can be traced back to the metal d-band centre and the oxidation potential thus each molecule has a weight on these two parameters. By using a leave-one-out procedure, we found that with a sample containing only three molecules, the full thermochemistry of a metal surface can be retrieved with error bars lower than 0.12 eV MAE. The present methodology is robust enough to be generalized to other systems like alloys, oxides, and the presence of decorations and solvent, thus paving the way for reliable thermochemical models relevant in heterogeneous catalysis.

1   Introduction

Heterogeneous catalysis holds the key to solve fundamental sustainability issues in the 21st century, as introducing new paradigms for energy vectors and the use of renewable raw materials.[1,2] The rational search for the optimal catalysts required for these new transformations can benefit from the extensive use of Density Functional Theory, DFT, and models derived from it.[3,4] This procedure is based on the extensive sampling of the wide web of reaction networks often intertwined that link the adsorbate reactants to the intermediates and final products through transition states for each elementary steps.

However, the use of DFT in biomass transformation has been less successful than for other chemical and electrochemical processes. The intrinsic complexity is inherent to the large number of elementary steps in the reaction network and the ubiquitous presence of multifunctionalized fragments, usually containing different oxygenated functional groups, constitute the main bottlenecks. For instance, the conversion of a C_5-C_6 sugar alcohol encompasses 10^4 intermediates,[5] rendering the computational catalytic screening nonviable unless accurate thermochemical models are developed.

Much before the wide spread use of DFT pioneering work by Benson established the basis for thermochemical scaling relationships both for gas-phase molecules.[6] In this formulation the formation energy for a hydrocarbon or oxygenated molecule, can be obtained as the sum of the energies stored on $C-C$, $C-O$, $C-H$, and $O-H$ bonds, considering also the contribution from closed-rings, unsaturations, and radicals.[6] Despite its simplicity, Benson's model has an impressive accuracy, the associated errors being lower than 0.05 eV for hydrocarbons, alcohols and ethers.[7] For molecules interacting on catalysts the formulation needs to be tuned. The first attempt was the Bond Order Conservation Theory (BOC), that states that the sum of the bond orders in which each atom participate remains constant.[8–10] In spite of the success of BOC theory it is a rather

⁴⁹ simple model as it does not consider additional contributions like electron transfer ⁵⁰ (from or towards the adsorbate), van der Waals interactions or the intramolecular ⁵¹ hydrogen bond weakening in the presence of a surface.[11]

⁵² The massive implementation of DFT provided sufficient thermochemical data ⁵³ to extract representative terms for the adsorption of small molecules. Thus, the ⁵⁴ adsorption energy of a molecule formed by an heteroatom "A" and saturated ⁵⁵ by x hydrogens, E_{ads,AH_x}, can be decomposed into two terms: the coupling of ⁵⁶ the adsorbate orbitals with the metal sp and the hybridization to the d states.[12] ⁵⁷ The sp contribution depends on the particular molecular fragment but is rather ⁵⁸ independent from the metal. The second term varies depends on the metal's d- ⁵⁹ band centre and the slope corresponds to the valence left in the fragment when ⁶⁰ compared to that of the heteroatom "A".[13] The energy of the molecular fragment ⁶¹ AH_x^* can be traced back to the energy of the fully unsaturated central atom ⁶² "A" (A=C, N, O, and S). Site-specific adsorption rules are more precise.[13,14] ⁶³ Further studies found that the adsorption energy of the first and second row ⁶⁴ fragments scale within the group in the periodic table for non-metals, i.e. P* ⁶⁵ scales with N*.[15] This interpretation is in line with the relation to the position of ⁶⁶ the adsorbate HOMO, the lower it is, the more electronic density it takes from the ⁶⁷ metal.[16] Scaling rules spanning the material gap comming from the coordination ⁶⁸ of metal sites have also been proposed for small molecules.[17,18]

⁶⁹ Multifunctionalized molecules, such as the fragments appearing in the de- ⁷⁰ composition of polyalcohols, would require the combination of the heteroatom ⁷¹ scalings described above with the Benson approach. The simplest is an additiv- ⁷² ity rule consisting on the sum of the individual bond energies and has been tested ⁷³ proven on C_1-C_3 oxygenated hydrocarbons on Pt. A slightly more sophisticated ⁷⁴ and accurate approach, introduces a contribution depending on the coordination ⁷⁵ environment for each heteroatom introducing the concept of building blocks.[19,20]

⁷⁶ In the present work, we have devised a new approach based on the use of

statistical analysis tools, Principal Component Analysis, that from a Density Functional Theory well converged set of adsorption energies from fragments (71) derived from C1-C2 alcohols and polyols adsorbed on 12 transition metals the main descriptors are identified. These two descriptors retrieve the well-known d-band model for the main contribution and the redox ability as the second factor. Due to the co-dependence, when the adsorption function is computed the energy of three fragments (O, OH, CCHOH) need to be considered. Once this is done, the error bars in the adsorption with respect to gas-phase reservoirs is reduced to 0.08 eV MAE. Thus getting in the limit of chemical accuracy.

2   Computational Details

We performed Density Functional Theory calculations with the Vienna Ab-initio Simulation Package, VASP,[21,22] for the metal atoms for 71 fragments derived from C_1 and C_2 alcohol decomposition[23,24] on Ru, Os, Rh, Ir, Ni, Pd, Pt, Cu, Ag, Au, Zn, and Cd. This FAIR database is available at ioChem-BD.[25,26] The functional of choice was PBE[27] with the D2 dispersion corrections of Grimme and our reparameterized values.[28,29] The present setup follows the current gold standard in DFT calculations.[30] Core electrons were represented by Projector Augmented Wave pseudopotentials,[31,32] and valence electrons were represented by plane waves with a kinetic energy cutoff of 450 eV. The calculated lattice parameters for the metals show good agreement with experimental values, as detailed in the Supporting Information. Metal surfaces were modeled by a four-layers slab, where the two uppermost layers were fully relaxed and the bottom ones were fixed to the bulk distances. We selected the (111) surfaces for the fcc metals, and the (0001) for the hcp ones. The adsorption was studied in a $2\sqrt{3} \times 2\sqrt{3} - R30°$ supercell. The vacuum between the slabs was set larger than 13 Å, and the dipole correction was applied on "z" direction.[33] The Brillouin

¹⁰³ zone was sampled by a Γ-centered $3 \times 3 \times 1$ k-points mesh generated through

¹⁰⁴ the Monkhorst-Pack method.[34] The most stable conformations were taken for

¹⁰⁵ subsequent analysis. The gas phase molecules were relaxed in a box of $20 \times 20 \times 20$

¹⁰⁶ Å^3.

¹⁰⁷ We included a detailed step-by-step guide of the mathematical treatment we

¹⁰⁸ followed for the PCA and PCR in the Supporting Information. Diagonalizations

¹⁰⁹ were done in Maple using 16 significant digits, increased precision to 96 digits did

¹¹⁰ not change the results.
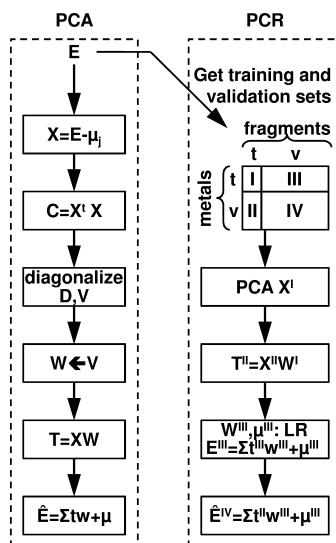
Figure 1: Scheme of the principal component analysis and principal component regression procedures.

¹¹¹ The procedure in PCA is presented schematically in Figure 1. The adsorbate

¹¹² formation energy, $E_{\text{C}_x\text{H}_y\text{O}_z*}$ corresponds to the chemical equation 1 and can be

¹¹³ written in terms of methane, hydrogen, and water reservoirs, Eq. 2.

$$x\text{CH}_4 + \left(-2x + \tfrac{3}{2}y - z\right)\text{H}_2 + z\text{H}_2\text{O} +^* \longrightarrow \text{C}_x\text{H}_y\text{O}_z{}^* \tag{1}$$
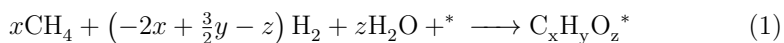
$$E_{C_xH_yO_z*} = E_{C_xH_yO_z*}^{(\text{VASP})} - xE_{CH_4}^{(\text{VASP})} + \left(2x - \tfrac{3}{2}y + z\right)E_{H_2}^{(\text{VASP})} - zE_{H_2O}^{(\text{VASP})} - E_*^{(\text{VASP})} \quad (2)$$

The so-defined matrix spans for the metals "i" in the rows and the fragments "j" in the columns. The average adsorption energy μ_j is employed to center the adsorption matrix. The centered adsorption matrix is multiplyed by its transpose at the left to obtain the covariance matrix, which is subsequentily diagonalized. The eigenvectors of the diagonal matrix should be in decreasing order. The adsorption energy can be retrieved from Eq. 3:

$$\hat{E}_{ij} = t_{i1}w_{1j} + \cdots + t_{il}w_{lj} + \mu_j \quad (3)$$

Where t_{ik} is the metal descriptor (and runs for all metals "i") and w_{kj} that of the molecular fragments ("j") obtained from the first "l" columns from the eigenvector matrix. An error function is then taken to chose the minimum set of components required to predict the energy matrix within a given threshold. From the first to the second component the errors halve, but from the second to the third one the error reduction is insignificant. We used only two principal components on the later analysis, as they suffice to capture most of the variability of the system within a MAE=0.08 eV.

3   Results

PCA revealed that only two principal components are needed to accurately describe the thermochemistry of the molecular fragments on the metals. Figure 2 (a) shows the two metal descriptors for each PC, t_{ik} in Eq. 3. The first one expands 16 eV and presents in the endothermic part Au and Ag while Os and Ru stand in the exothermic area. The second component spans a much smaller energy, 5 eV,
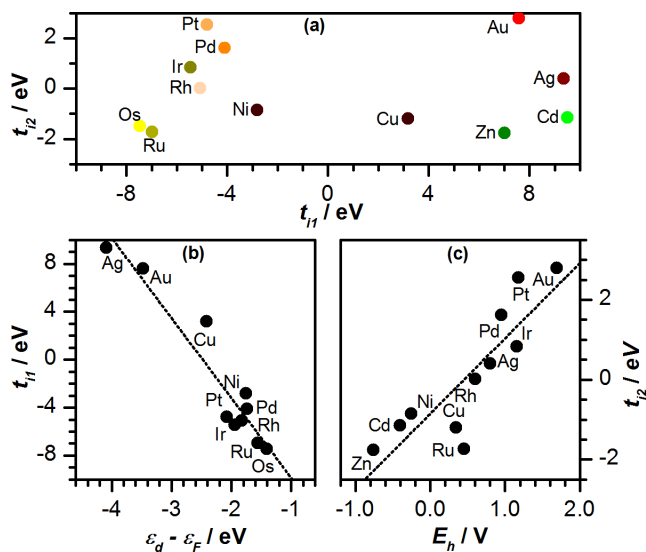
Figure 2: (a) Principal components for the metals. Correlation maps are included for (b) the d-band centre and (c) the oxidation potential as function of the first and second principal components for each metal.

and the exothermic part contains Os, Ru and Zn while the endothermic section is dominated by Pt and Au. Interestingly, the molecular fragments' first descriptor have the same sign, but different magnitudes. Therefore the first PC is directly connected with the metal affinity to form bonds with other species, a characteristic that can be mapped to the d-band centre, Fig. 2 (b). The second PC is positive for species that bind by an oxygen atom, and negative in species that bind through a $-C-OH$ center. Therefore, the second PC can be related to the oxyphilicity of the metal to accept electronic density, i.e., the oxidation potential, Figure 2 (c). To explore the physical meaning of the Principal Components, we checked the cross correlations between them, the d-band centre, and the oxidation potential, as shown in Figure S2 For each metal, the first coordinate scales well with the d-band centre but not with the oxidation potential. Conversely, the second coordinate scales with the oxidation potential but not with the d-band centre (criterion $p < 0.01$). The first Principal Component scales perfectly with the d-band centre of the transition metals, which has been identified as the most

149 important reactivity descriptor.[12] The principal components are thus assign to

150 the covalent contributions PC1 and the PC2 to the redox.

151 In eq. 3, the w_{kj} corresponds to the weight for a given fragment of the

152 two principal components. Therefore, each intermediate is characterized by a

153 covalent contribution and a redox one, and these contributions depend only on

154 the molecular fragment. These characteristics can be found in Figure 3
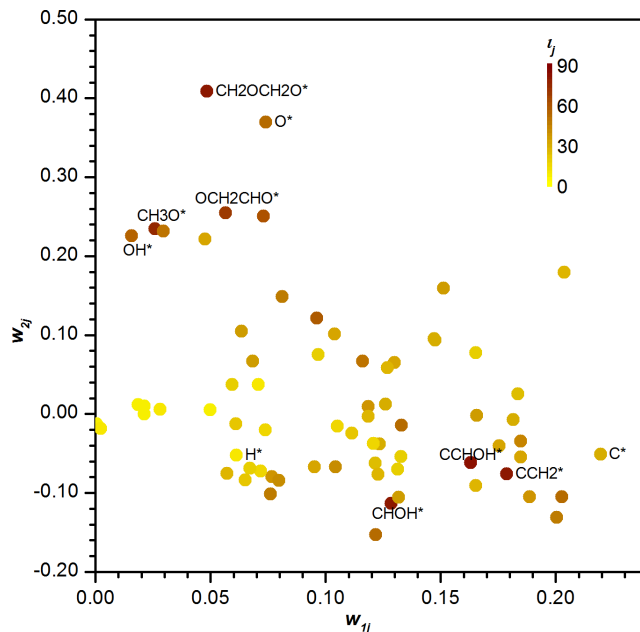
Figure 3: Fragment weights on the orthogonal basis set w. The yellow colors
stand for molecules either close to the origin or with a high prediction error, the
darker the color indicates both a large projection on one of the fragment basis
and a small error in its prediction. Some fragments are identified with labels and
a complete description can be found in the Supporting Information.

155 From the Figure 3 it can be identified that the largest covalent contributions

156 correspond to fragments with C, that present low-values in the redox contribution.

157 This can be linked to the small differences in the electronegativity of C with

158 respect to the metals. The other limit, of low PC1 contributions and large PC2

159 ones we identify O, OH (and other fragments with more than one oxygen atom).

160 The present analysis explains why Ref. [16] needs two different classes for O- and

¹⁶¹ C- containing intermediates. Still, the adsorption energies of E_O and E_C has some

¹⁶² degree of codependence, as shown in Supporting Information and although the

¹⁶³ codependence is weak.[15, 16] it does not allow to employ only these two fragments

¹⁶⁴ as suitable fragment descriptors.

¹⁶⁵ Ideally, a good set of independent molecules used as fragment descriptors

¹⁶⁶ should have adsorption energies that are independent from each other. From

¹⁶⁷ the Figure 3 it becomes clear that to build the w basis set a minimum of three

¹⁶⁸ fragments needs to be computed. To this end we have calculated the error matrix

¹⁶⁹ between the predicted energy with equation 3 and the DFT computed one. The

¹⁷⁰ colors in Figure 3 represent eq. S12, thus yellow colors stand for molecules either

¹⁷¹ close to the origin or with a high prediction error, the darker the color indicates

¹⁷² both a large projection on one of the fragment basis and a small error in its

¹⁷³ prediction.

¹⁷⁴ Three rules have been applied to chose the three fragments: (i) to have the

¹⁷⁵ largest pc contribution in only one of the two directions (while the other is as

¹⁷⁶ close to zero as possible) and both cannot be zero; (ii) that the error in its own

¹⁷⁷ prediction is small (this is denoted by darker colors in the scale); (iii) that the

¹⁷⁸ fragment is bound only through one atom. Once this is done the fragments

¹⁷⁹ identified are: O, OH, and CCHOH.

¹⁸⁰ From the analysis above a predictive tool can be built, see Figure 4. First, we

¹⁸¹ present the error matrix written as the correlation between the predicted energy

¹⁸² values and the full DFT ones, Figure 4 (a). The error distribution function shows

¹⁸³ that all the energies are reproduced within ± 0.5 eV but 98% of them lies within

¹⁸⁴ ± 0.3 eV. Alternatively, a leave one out scheme has been put forward. The results

¹⁸⁵ for all the fragments on all metals except by one can be used to predict all the

¹⁸⁶ energies for the new metal in the following way: Performing a PCA on the DFT

¹⁸⁷ values for 11 metals and three fragments this allow the identification of the metal

¹⁸⁸ characteristic "t" and for the 3 main fragments "w". Then perform DFT for the

¹⁸⁹ training set of metals and only the three most representative fragments, by Eq.
¹⁹⁰ S8 the metal "t_{i1}" components can be identified. Expand the validation metal
¹⁹¹ pool to all the remaining fragments retrieving the remaining "w" through regres-
¹⁹² sion between the DFT data for the 11 metals and the other fragments. Predict
¹⁹³ the values for the validation metal with the so-calculated "t" and "w". Figure
¹⁹⁴ 4(b) shows the outcome of the leave one out procedure described above. The
¹⁹⁵ errors are maintained with respect to the all-DFT auto-validation. In summary,
¹⁹⁶ the dispersion observed is only slightly higher than the DFT only 0.08 vs 0.12
¹⁹⁷ MAE. The distribution in the form of histogram in Figure 4(d) shows that the
¹⁹⁸ population in the central bars, between ±0.10 eV are about 25% less than for
¹⁹⁹ the DFT only but still, a 98% of the estimated energies are within ±0.40 eV.
²⁰⁰ Thus, the present methodology only increases the error span by ±0.10 eV. Rh is
²⁰¹ shows the smallest deviation. The least accurate predictions correspond to highly
²⁰² endothermic fragments, this is a very positive result as we can expect them to be
²⁰³ less relevant in reaction predictions. Thus effectively, reducing the error bars in
²⁰⁴ the prediction.

²⁰⁵ The metals that are better predicted are Rh, Ir, and Cd with 0.05, 0.07 and
²⁰⁶ 0.07 eV MAE (full PCA). The worst predicted metals are Zn and Ag. They
²⁰⁷ correspond to the metals where adsorption averages are more exothermic and en-
²⁰⁸ dothermic respectively. The most problematic fragments are CCH, CHOHCHOH,
²⁰⁹ and CCOH.

²¹⁰ The final benchmark of our approach is the comparison of the computed
²¹¹ values to the state-of-the-art thermochemical data compiled and analyzed by
²¹² Campbell.[35,36] The results in Figure 5 where the estimated $\hat{E}$ are compared
²¹³ against the experimental E_{EXP} values. Our results, shown in orange, lay nicely
²¹⁴ close to the 1:1 line. Moreover, the error bars are comparable to their own DFT
²¹⁵ predictions with two functionals PBE (grey) and BEEF-vdW (light grey).

²¹⁶ The procedures described in this paper are robust enough to be extended to
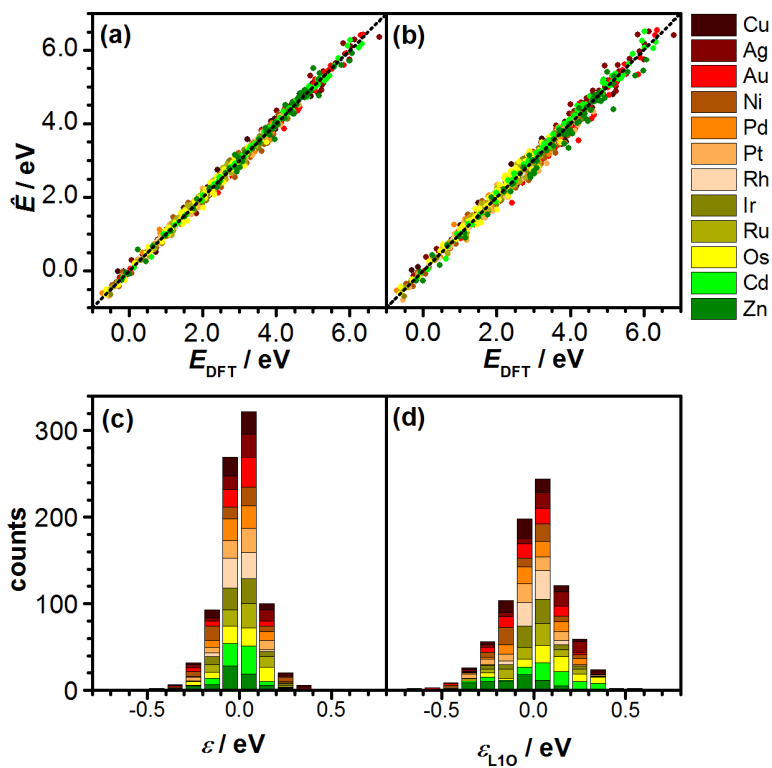
Figure 4: Error distribution for the PCA (a) taking all the data, and (b) using the L1O procedure. Cumulative errors are shown on panels (c) and (d).

217 other methodologies, like other transition metals and their alloys, different metal
218 cuts, including decorations, oxides (material gap), solvation, and other density
219 functionals such as BEEF.

4 Conclusions

221 This work shows a powerful methodology to predic the thermochemistry of molec-
222 ular fragments adsorbed on transition metal surfaces. While the main contribu-
223 tion for adsorption can be traced back to the d-band center, a secondary contri-
224 bution comes from the metal reduction potential. Once only three molecules in
225 the training set are calculated for a given metal or alloy, the thermochemistry of
226 the remaining molecular fragments can be predicted within an accuracy of 0.12
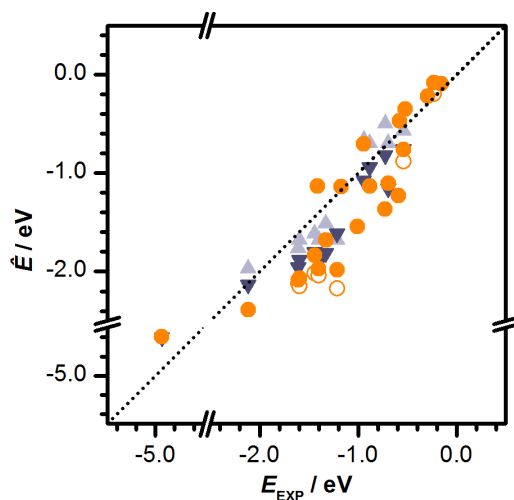
Figure 5: Comparison between experimental adsorption energies from Ref. [36] and the ones obtained from the L1O procedure (orange circles). Open circles stand for the predicted values when coverage effects are not considered. DFT Data from Ref. [35] are provided as benchmark for PBE (grey triangles) and BEEF-vdW density functionals

227 eV MAE, which is much smaller than any of the other previous method, while

228 using only C and O has error 33% larger. The present methodology is robust

229 enough to be generalized to other systems like alloys, oxides, and the presence of

230 decorations and solvent, thus paving the way for reliable thermochemical models

231 relevant in heterogeneous catalysis.

5 Acknowledgments

References

[1] Cortright, R. D.; Davda, R.; Dumesic, J. A. Hydrogen from catalytic reforming of biomass-derived hydrocarbons in liquid water, *Nature* **2002,** *418,* 964–967.

[2] Dapsens, P. Y.; Mondelli, C.; Pérez-Ramírez, J. Biobased chemicals from conception toward industrial reality: lessons learned and to be learned, *ACS Catal.* **2012,** *2,* 1487–1499.

[3] Nørskov, J. K.; Bligaard, T.; Rossmeisl, J.; Christensen, C. H. Towards the computational design of solid catalysts, *Nat. Chem.* **2009,** *1,* 37–46.

[4] Seh, Z. W.; Kibsgaard, J.; Dickens, C. F.; Chorkendorff, I.; Nørskov, J. K.; Jaramillo, T. F. Combining theory and experiment in electrocatalysis: Insights into materials design, *Science* **2017,** *355,* eaad4998.

[5] Sutton, J. E.; Vlachos, D. G. Building large microkinetic models with first-principles' accuracy at reduced computational cost, *Chem. Eng. Sci.* **2015,** *121,* 190–199.

[6] Benson, S. W. *Thermochemical kinetics;* Wiley: 1976.

[7] Benson, S. W.; Cruickshank, F.; Golden, D.; Haugen, G. R.; O'neal, H.; Rodgers, A.; Shaw, R.; Walsh, R. Additivity rules for the estimation of thermochemical properties, *Chem. Rev.* **1969,** *69,* 279–324.

[8] Shustorovich, E. Chemisorption phenomena: analytic modeling based on perturbation theory and bond-order conservation, *Surf. Sci. Rep.* **1986,** *6,* 1–63.

[9] Shustorovich, E.; Bell, A. T. The thermochemistry of C2 hydrocarbons on transition metal surfaces: The bond-order-conservation approach, *Surf. Sci.* **1988,** *205,* 492–512.

[10] Shustorovich, E.; Bell, A. T. Analysis of CO hydrogenation pathways using the bond-order-conservation method, *J. Catal.* **1988,** *113,* 341–352.

[11] García-Muelas, R.; López, N. Collective descriptors for the adsorption of sugar alcohols on Pt and Pd(111), *J. Phys. Chem. C* **2014,** *118,* 17531–17537.

[12] Hammer, B. *et al.* Why gold is the noblest of all the metals, *Nature* **1995,** *376,* 238–240.

[13] Abild-Pedersen, F.; Greeley, J.; Studt, F.; Rossmeisl, J.; Munter, T.; Moses, P. G.; Skulason, E.; Bligaard, T.; Nørskov, J. K. Scaling properties of adsorption energies for hydrogen-containing molecules on transition-metal surfaces, *Phys. Rev. Lett.* **2007,** *99,* 016105.

[14] Montemore, M. M.; Medlin, J. W. Site-specific scaling relations for hydrocarbon adsorption on hexagonal transition metal surfaces, *J. Phys. Chem. C* **2013,** *117,* 20078–20088.

[15] Calle-Vallejo, F.; Martinez, J.; García-Lastra, J. M.; Rossmeisl, J.; Koper, M. Physical and chemical nature of the scaling relations between

281   adsorption energies of atoms on metal surfaces, *Phys. Rev. Lett.* **2012**, *108*,
282   116103.

283 [16] Montemore, M. M.; Medlin, J. W. A unified picture of adsorption on tran-
284   sition metals through different atoms, *J. Am. Chem. Soc.* **2014**, *136*, 9272–
285   9275.

286 [17] Calle-Vallejo, F.; Loffreda, D.; Koper, M. T.; Sautet, P. Introducing struc-
287   tural sensitivity into adsorption–energy scaling relations by means of coor-
288   dination numbers, *Nat. Chem.* **2015**, *7*, 403–410.

289 [18] Calle-Vallejo, F.; Tymoczko, J.; Colic, V.; Vu, Q. H.; Pohl, M. D.; Mor-
290   genstern, K.; Loffreda, D.; Sautet, P.; Schuhmann, W.; Bandarenka, A. S.
291   Finding optimal surface sites on heterogeneous catalysts by counting nearest
292   neighbors, *Science* **2015**, *350*, 185–189.

293 [19] Salciccioli, M.; Chen, Y.; Vlachos, D. G. Density functional theory-derived
294   group additivity and linear scaling methods for prediction of oxygenate sta-
295   bility on metal catalysts: adsorption of open-ring alcohol and polyol dehy-
296   drogenation intermediates on Pt-based metals, *J. Phys. Chem. C* **2010**, *114*,
297   20155–20166.

298 [20] Salciccioli, M.; Edie, S.; Vlachos, D. Adsorption of acid, ester, and ether
299   functional groups on Pt: fast prediction of thermochemical properties of ad-
300   sorbed oxygenates via DFT-based group additivity methods, *J. Phys. Chem.*
301   *C* **2012**, *116*, 1873–1886.

302 [21] Kresse, G.; Furthmüller, J. Efficiency of ab-initio total energy calculations
303   for metals and semiconductors using a plane-wave basis set, *Comput. Mater.*
304   *Sci.* **1996**, *6*, 15–50.

[22] Kresse, G.; Furthmüller, J. Efficient iterative schemes for ab initio total-energy calculations using a plane-wave basis set, *Phys. Rev. B* **1996,** *54,* 11169–11186.

[23] García-Muelas, R.; Li, Q.; López, N. Density functional theory comparison of methanol decomposition and reverse reactions on metal surfaces, *ACS Catal.* **2015,** *5,* 1027–1036.

[24] Li, Q.; García-Muelas, Rodrigo López, N. Microkinetics of alcohol reforming for H$_2$ production from a FAIR density functional theory database, *Submitted* **2017,** .

[25] Álvarez Moreno, M.; De Graaf, C.; López, N.; Maseras, F.; Poblet, J. M.; Bo, C. Managing the computational chemistry big data problem: The ioChem-BD platform, *J. Chem. Inf. Model.* **2014,** *55,* 95–103.

[26] García-Muelas, R.; López, N. *Generalized models for adsorption of interme-diates on transition metals,*
https://doi.org/10.19061/iochem-bd-1-43
Reviewers link:
https://iochem-bd.iciq.es/browse/review-collection/100/4212/c9732214fefbd10218ef1e4c.

[27] Perdew, J. P.; Burke, K.; Ernzerhof, M. Generalized gradient approximation made simple, *Phys. Rev. Lett.* **1996,** *77,* 3865–3868.

[28] Grimme, S. Semiempirical GGA-type density functional constructed with a long-range dispersion correction, *J. Comput. Chem.* **2006,** *27,* 1787–1799.

[29] Almora-Barrios, N.; Carchini, G.; Błoński, P.; López, N. Costless derivation of dispersion coefficients for metal surfaces, *J. Chem. Theory Comput.* **2014,** *10,* 5002-5009.

[30] Lejaeghere, K. *et al.* Reproducibility in density functional theory calculations of solids, *Science* **2016,** *351,*.

[31] Blöchl, P. E. Projector augmented-wave method, *Phys. Rev. B* **1994,** *50,* 17953–17979.

[32] Kresse, G.; Joubert, D. From ultrasoft pseudopotentials to the projector augmented-wave method, *Phys. Rev. B* **1999,** *59,* 1758–1775.

[33] Makov, G.; Payne, M. C. Periodic boundary conditions in ab initio calculations, *Phys. Rev. B* **1995,** *51,* 4014–4022.

[34] Monkhorst, H. J.; Pack, J. D. Special points for Brillouin-zone integrations, *Phys. Rev. B* **1976,** *13,* 5188–5192.

[35] Wellendorff, J.; Silbaugh, T. L.; García-Pintos, D.; Nørskov, J. K.; Bligaard, T.; Studt, F.; Campbell, C. T. A benchmark database for adsorption bond energies to transition metal surfaces and comparison to selected DFT functionals, *Surf. Sci.* **2015,** *640,* 36–44.

[36] Silbaugh, T. L.; Campbell, C. T. Energies of formation reactions measured for adsorbates on late transition metal surfaces, *J. Phys. Chem. C* **2016,** *120,* 25161–25172.

Density Functional Theory Comparison of Methanol Decomposition and Reverse Reactions on Metal Surfaces

Rodrigo García-Muelas, Qiang Li, and Núria López*

Institute of Chemical Research of Catalonia (ICIQ), Avgda. Països Catalans 16, 43007 Tarragona, Catalonia, Spain

S *Supporting Information*

ABSTRACT: Methanol decomposition on metals has been subject of several theoretical studies, usually concentrating on a particular set of reactions in the main reaction path. In this work, we present an extensive study that considers all potential elementary steps for four close-packed surfaces including Cu, Ru, Pt, and Pd that shows the different behaviors and alternative routes through which the decomposition can take place by theoretical methods, including dispersion contributions. Decomposition follows different paths on these metals; while Cu would produce CH_2O, CO is the major product for the other metals. In addition, coverage effects might change the first step in Pt and Ru from methylenic to alcohol H activation. Alternatively the reaction network can be inspected for the formation of methanol from CO and hydrogen. Under these conditions, Cu generates CH_2O and only at very high H coverages is methanol likely to appear. On Pd, methanol formation and CHOH dissociation compete, thus leading to an inefficient process. A similar path takes place for Pt. For Ru the lateral paths leading to C−O breaking can occur at several points in the reaction network, never reaching CH_3OH. A compilation of the results with comparable computational setups presents a detailed database that can be added to the thermodynamics and kinetics for other reactions, such as methanation, with which they share a common list of reactions, or employed when analyzing larger alcohols such as those derived from biomass.
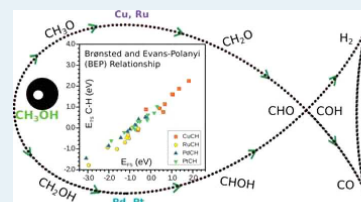
KEYWORDS: methanol, density functional theory, Brønsted and Evans−Polanyi (BEP) relationships, Pt, Pd, Ru, Cu

INTRODUCTION

Methanol is the smallest of all alcohols and, as it is a liquid and is easy to store, it has been presented as a potential energy vector that can be employed in new energy approaches. Indeed, the methanol economy concept was coined in the 1990s to account for this possibility.[1] The use of methanol in mobile applications seemed to be the most promising, as it can be directly used as fuel in combustion engines, directly converted to energy in electrochemical cells, or converted into another energy vector such as hydrogen.[2] Several of those approaches are based on its electrochemical transformation and the corresponding energy release, but the problem of direct methanol fuel cells comes from the strong adsorption of one of the subproducts, namely CO. Although methanol is currently produced by hydrogenation of a mixture of CO and CO_2 in a Cu/ZnO catalyst,[3,4] it is also possible to produce it from agricultural products and municipal waste, making it a recycled product. Methanol is also employed as a surrogate for larger biomass-derived alcohols,[5] even if this approach might be overly simple.

Methanol decomposition and synthesis on metal surfaces has been extensively investigated by several authors during the past decade. Greeley and Mavrikakis also investigated methanol decomposition on Cu(111),[6] where the preferred path would start by the dehydrogenation of the hydroxyl group. In the decomposition route on Pt(111),[7,8] the same authors studied a reaction network either starting with the dissociation of the alcohol hydrogen or starting from the methylenic H atoms.

According to them, carbon dehydrogenation would be a preferred step, in contrast with the preferential O−H bond breaking found in experimental studies.[9] A recent study by the group of Campbell showed that the methoxy radical adsorbed on Pt(111) is rather unstable, as was predicted by DFT studies.[10] For the same system Neurock and co-workers[11] found that, under ultra-high vacuum conditions, methanol would desorb rather than react, as the activation barriers for the first dehydrogenation are higher than the desorption energy. In the study, two intermediates were discarded due to complexity, CHOH and COH; as we will show, both might belong to the minimum energy path. To rationalize the results for Pt, several attempts have been made. According to the d-band model, the activity of a metal is a function of the d-band center.[12−14] This analysis was employed by Park and co-workers[15] to study the methanol electrooxidation activity of Pt. In parallel, Ferrin and co-workers demonstrated that the catalyst performance for methanol electrooxidation can be described as a function of the free energy of adsorption of CO and OH radicals.[16] However, the adsorption energies and d-band positions are correlated, as the energies are a function of the d-band positions.[14] Yudanov and co-workers focused on C−O bond breaking on Pd nanoparticles, identifying it as a slow side process in the decomposition reaction.[17] On Pd and other metals, the

decomposition or dehydrogenation steps have been compiled for a large range of molecules and fragments containing the same heteroatom.[18,19] As for Ru(0001), experiments have shown the coexistence of two paths, one leading to CO and the other one leading to C and O separate fragments, where the second path was identified as responsible for surface poisoning.[20] The reason is that H-assisted reactions have been found to lower the barriers to difficult decompositions such as that of CO.[21]

Completeness at any stage is thus crucial to understand intricate reaction networks that can be intercrossed. As the reaction set becomes quite large, there is a need to describe the fragments to generate a database that can be employed to predict the activation energies of each particular step. Furthermore, the database can be modified to include the particular cases of lateral interactions and/or solvents for a more adequate representation of complex electrocatalytic systems.

This is precisely the aim of the present work. For methanol, we have built a consistent complete reaction network that accounts for crossings between different paths at any time in a way similar to that which we reported for HCN synthesis.[22] The reactions considered in our network are presented in Scheme 1. For this set of reactions we have investigated the

Scheme 1. Reaction Network for the Decomposition of Methanol on the Different Surfaces Considered in This Work
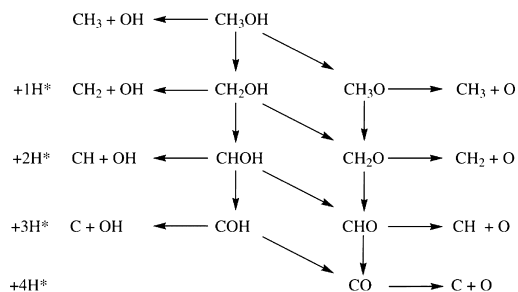
following items: (i) we have stablished a common connectivity matrix notation that allows extrapolation to more complex substrates; (ii) we have analyzed the role of different kinetic–thermodynamic relationships to ensure the best form to predict the energies for other metals; (iii) we have described the potential hysteresis in the decomposition/synthesis paths by inspecting the direct and reverse reactions; and (iv) we have analyzed lateral effects for key competitive routes.

◼ COMPUTATIONAL DETAILS

Slab calculations were performed using the Vienna ab initio simulation package (VASP),[23,24] the PBE density functional,[25] and a kinetic energy cutoff of 450 eV. The inner electrons were represented by projector augmented wave (PAW) pseudopotentials.[26,27] The calculated lattice parameters for Ru, Cu, Pd, and Pt are 2.712, 3.629, 3.939, and 3.968 Å, respectively, and $[c/a]_{Ru} = 1.581$, in good agreement with experimental values of 2.706, 3.615, 3.893, and 3.924 Å and $[c/a]_{Ru} = 1.582$.[28–31] The cells were built in a p (3×3) configuration for Ru and Cu, with a $2\sqrt{3} \times 2\sqrt{3} - R30°$ supercell. Therefore, the coverages are low and comparable, between 0.08 and 0.11 ML. To inspect

lateral interactions in reaction and activation energies, we included one or two additional methanol molecules in the $2\sqrt{3} \times 2\sqrt{3} - R30°$ supercell. All metallic surfaces were modeled by a four-layer slab. The two topmost layers were fully relaxed, and the two bottom layers were fixed to the bulk distances. For surface calculations, the Brillouin zone was sampled by a Γ-centered k-point mesh generated through the Monkhorst–Pack method,[32] and the samplings were denser than 0.3 Å^{-1}. We included a vacuum region larger than 12 Å and a dipole correction along the z direction.[33] We also included the van der Waals (vdW) corrections by applying Grimme's DFT-D2 method,[34,35] with the C_6 parameters developed in our group.[36,37] The van der Waals contributions to adsorption can be found in Table S1 of the Supporting Information. The molecules in the gas phase were relaxed in a box of $20 \times 20 \times 20$ Å^3. We employed both the nudged elastic band (CI-NEB) and the improved dimer method, (IDM) to find the transition states.[38–40] The optimization thresholds were 10^{-5} eV and 0.015 eV/Å for electronic and ionic relaxations, respectively. In all cases the saddle point nature of the transition states was assessed by the calculation of the numeric Hessian with a step of 0.02 Å and its diagonalization that rendered a unique imaginary frequency. In the following, all discussed energies correspond to dispersion-containing values including zero-point energy unless stated otherwise.

◼ RESULTS

Description of the Reaction Network. The data for adsorption of key intermediates can be found in Table S1 in the Supporting Information. The contribution of van der Waals dispersion terms has been evaluated for reactants and products. Inclusion of vdW interactions raises (more exothermic) the adsorption values between 0.01 and 0.20 eV. Tests of different adsorption sites and comparison to previous results in the literature are provided in Tables S2–S4 in the Supporting Information. In order to simplify and order all of the intermediates, an identification vector that defines them has been developed (see Table S5 in the Supporting Information) which can be extended to more complex compounds. The vector defines the stoichiometry with the first three numbers (carbon, hydrogen, oxygen), and isomerism is given as a fourth number; thus, methanol corresponds to 1411 and CO to 1011.

In this section we describe all of the potential reaction steps described in Scheme 1 for all four metals in the present study: Cu(111), Ru(0001), Pt(111), and Pd(111). In Figures 1–3, we present top and side perspectives for all of the reaction steps in the paths for the particular case of copper. A complete version of these figures for all metals considered can be found in the final section of the Supporting Information.

The first group of reactions corresponds to the O–H bond breaking and contains four elementary steps starting from methanol (CH$_3$OH), hydroxymethyl (CH$_2$OH), hydroxymethylidene (CHOH), and hydroxymethylidyne (COH) (Figure 1). For adsorbed molecules, the initial configuration presents the OH fragment close to the surface and thus bond activation easily occurs. In the case of CH$_2$OH, both O and C atoms are bonded to the surface but the hydrogen on the OH group is closer to the surface in comparison to the methylenic H; thus, it seems rather straighforward that the OH is more activated at this stage. On the other hand, the CHOH and COH fragments are bonded to the surface by the carbon center (Figure 1), and thus the alcoholic hydrogens are farther away from the surface. Such kinds of configurations would be better activated by
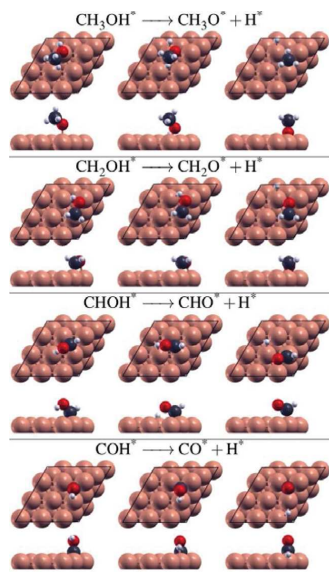
Figure 1. Schematic representation of the reaction steps considered for the decomposition on Cu(111), regarding O–H bond breaking. Large spheres correspond to metal atoms and red, gray, and white spheres to O, C, and H, respectively.

nearby structural defects on the metal surface.[41] Indeed, coordinative unsaturated atoms, such as those present on step sites, could be more effective to catalyze the perpendicularly adsorbed fragments, as they not only are more reactive but also prevent the rotation needed to activate the O–H fragment. In the final positions of methanol and COH decomposition the fragments stand up perpedicular to the surface. In comparison, the fragments with partially dehydrogenated C moieties (CH_2OH and CHOH) either lie on the surface or are just bonded through the C atom. For CH_3OH and CH_2OH, O–H activation implies a change in the coordination of the O atoms from top to fcc sites, Pt being the only exception. For CHOH or COH dehydrogenation, C moves from the bridge to the top site or keeps the fcc site, respectively.

Figure 2 illustrates the dehydrogenation of the carbon atom in six different molecules: CH_3OH, CH_3O, CH_2OH, CH_2O, CHOH, and formyl (CHO). In all cases a change in the coordination of the carbon atom to fulfill the empty valence is found.[42] In some cases, such as the dehydrogenation of CH_2OH, this is accompanied by a reorientation of the final carbon fragment CHOH which leads to O atoms no longer adsorbed to the surface. The rotation is induced by the larger empty valence of C atoms in comparison to O atoms.

The eight elementary steps for the C–O bond breaking are presented in Figure 3, corresponding to CH_3OH, CH_3O, CH_2OH, CH_2O, CHOH, CHO, COH, and CO. It is well-known that the CO decomposition is much easier at steps due to the stand-up nature of the adsorbed CO molecules and the fact that step atoms are more reactive; however, the rest can be analyzed for planar surfaces with a sufficiently high confidence. As we will see later, the obtained barriers are low enough to ensure that the remaining reactions can occur under mild experimental conditions.

Figure 2. Schematic representation of the reaction steps considered for the decomposition on Cu(111), regarding C–H bond breaking. Large spheres correspond to metal atoms and red, gray, and white spheres to O, C, and H, respectively.

Energy Profiles for Dehydrogenation. The lowest energy paths for methanol decomposition on the different surfaces are shown in Figure 4. Reaction and activation energies are given in Tables S6 and S7 in the Supporting Information, and the structures are depicted in Table S13 in the Supporting Information. On Cu(111), the methanol decomposition pathway follows as $CH_3OH \rightarrow CH_3O \rightarrow CH_2O \rightarrow CHO \rightarrow CO + H_2$. It is the simplest pathway among all of the metals and is also supported by previous theoretical studies.[6,43–45] The first step consists of O–H bond breaking, which is slightly exothermic (−0.22 eV). However, this step presents a rather large energy barrier of 0.98 eV, which is 0.61 eV higher than the desorption energy. CH_3O is acknowledged as the most stable intermediate among all of the species during the decomposition process on Cu(111).[6,44–46] From CH_3O on, all subsequent reactions correspond to C–H breaking. The bond lengths of C–H in sequential TS structures are 1.86, 1.57, and 1.14 Å, respectively, which demonstrates that the C–H bond breaking occurs more easily with further dehydrogenations. In correspondence, the activation energy barriers are 1.04, 0.55,
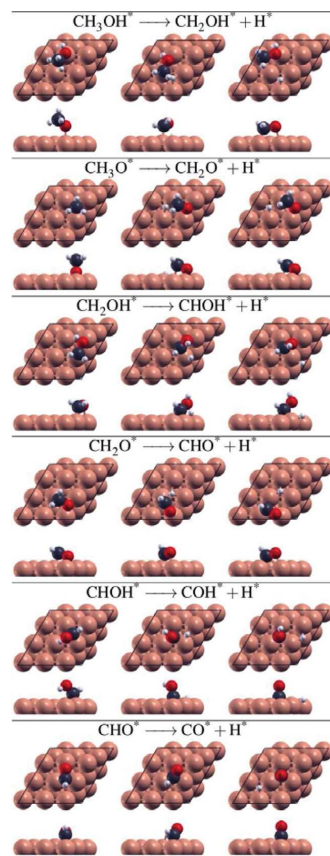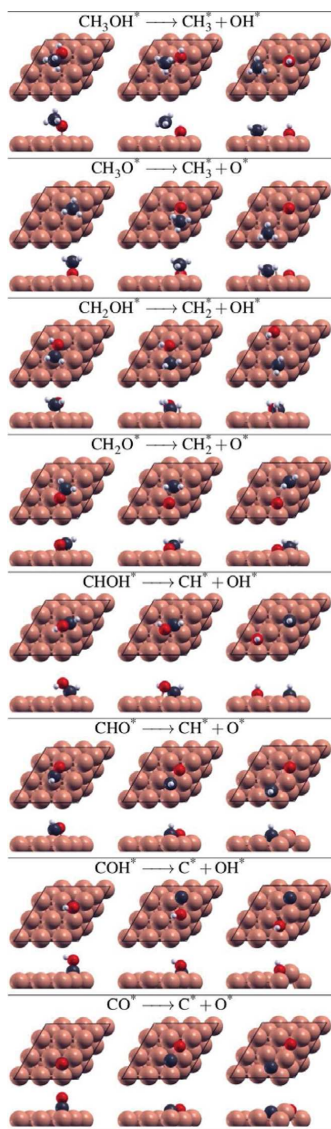
Figure 3. Schematic representation of the reaction steps considered for the decomposition on Cu(111), regarding C–O bond breaking. Large spheres correspond to metal atoms and red, gray, and white spheres to O, C, and H, respectively.

can easily desorb from Cu(111) because its binding energy of 0.31 eV is less than the energy barrier for the dehydrogenation, 0.55 eV. When dehydrogenation continues from formaldehyde, then the C–H bond breaks directly or spontaneously from CHO with a lower energy barrier (0.19 eV) and a highly exothermic path (−0.99 eV). Similar results were obtained by Lim[43] (−0.89 eV) and Zuo[44] (−0.93 eV).

C–O bond breaking could only occur for the CHOH intermediate, but in the direct methanol decomposition path this intermediate is never observed. It has been suggested that in the presence of water the reaction network could continue through the condensation of CH_2O with an adsorbed OH and further oxidation to CO_2.[46]

On Ru(0001) surfaces, there are two competing pathways for methanol decomposition: on one side, $CH_3OH \rightarrow CH_3O \rightarrow CH_2O \rightarrow CHO \rightarrow CO + H_2$, and on the other, $CH_3OH \rightarrow CH_2OH \rightarrow CHOH \rightarrow COH \rightarrow CO + H_2$. The first path is the same as that on Cu(111); the O–H bond breaks first, and then the reaction proceeds for the C–H bonds. However, in the alternative pathway only C–H bond breaking occurs and the O–H bond is retained during the whole process until the final step, which leads to CO and H_2. Starting from methanol, both O–H and C–H bond breakages are exothermic with reaction energies of −0.74 and −0.39 eV and the required bond-breaking energies are 0.60 and 0.48 eV, respectively. Thus, C–H bond splitting is more kinetically preferable, while the O–H bond breaking which leads to the CH_3O is more favored thermodynamically. However, on the basis of experimental studies,[47] only methoxy species were observed in the temperature range from 180 to 340 K. In the first pathway, the dehydrogenation of methoxy to formaldehyde is the step with the highest energy demand, with an energy barrier of 0.90 eV. Unlike the formaldehyde desorption on Cu(111), formaldehyde binds strongly on Ru(0001) with a desorption energy of 1.09 eV, in good agreement with the study by Chiu (1.06 eV).[48] Moreover, the dehydrogenation from CH_2O to CHO occurs easily through a negligible barrier of 0.06 eV. The dehydrogenation of CHO is also almost barrierless (0.04 eV) and is highly exothermic (−0.90 eV). Our results are in good agreement with recent experiments for high methanol coverages, which report that O–H bonds break to form methoxy, which subsequently evolves to CO and hydrogen with no significant C–O bond breaking.[47] In the next section, we will analyze the effect of spectator methanol molecules for the first dehydrogenation reactions on Ru(0001) and Pt(111). Significatively, along the $CH_3OH \rightarrow CH_2OH \rightarrow CHOH \rightarrow COH \rightarrow CO + H_2$ path the three barriers are quite low, although two intermediates are higher in energy than those of the methoxy path. From a thermodynamic perspective, the elementary steps are not as favored as the first path and the first two reactions are only weakly exothermic: −0.39 and −0.43 eV, respectively. Moreover, the last H abstraction from COH to CO, although being exothermic (−0.76 eV), is hindered by a sizable energy barrier of 0.77 eV.

Carbon monoxide binds strongly on Ru(0001), Pd(111), and Pt(111) surfaces, with desorption energies of +1.93, +2.29, and +1.95 eV, respectively. At high methanol pressures, the reaction will proceed until all of these surfaces become covered by carbon monoxide, and further reactions will take place only after carbon monoxide desorbs. This is one of the most common problems for the direct methanol fuel cells that are usually described for Pt. In turn, methanol adsorption on such

and 0.19 eV. Considering the required energy for O–H scission (0.98 eV), the dehydrogenation from CH_3O to CH_2O, which is also highly endothermic by 0.73 eV, is the most energy-demanding step in the decomposition pathway. The reported reaction (activation) energies for this step in previous theoretical studies are 0.97 (1.42),[6] 0.92 (1.27),[45] 0.85 (1.85),[44] and 1.00 (1.16)[43] eV, respectively. To enhance decomposition, any basic center on the carrier could thus be more adequate than the metal surface itself. Moreover, CH_2O
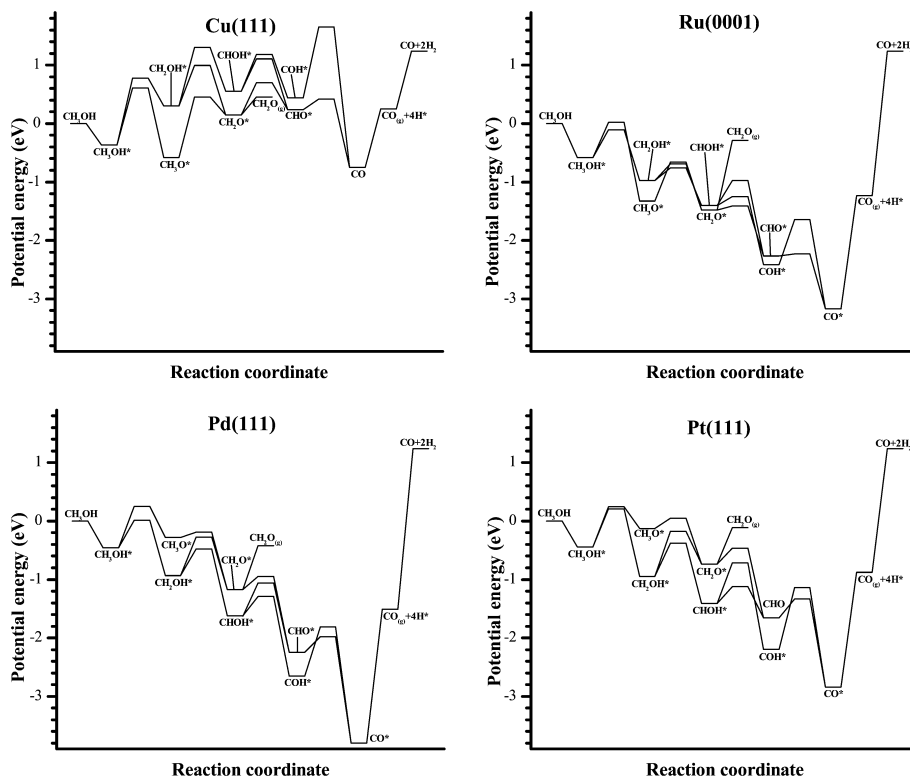
Figure 4. Reaction profiles for the decomposition of methanol to CO and H_2 on different metal surfaces. The minimum energy paths are considered in each particular case.

poisoned surfaces might end up being the observed rate-determining step.

For Pd(111), the lowest energy barrier corresponds to the methylinic dehydrogenation, where the activation energy, 0.47 eV, is on the order of the desorption energy, 0.46 eV. The O−H dehydrogenation has a rather high activation barrier of 0.71 eV and it is thus not feasible. These results are in qualitative agreement with reported values.[49] The main pathway is $CH_3OH \rightarrow CH_2OH \rightarrow CHOH \rightarrow COH \rightarrow CO + H_2$, the subsequent activation barriers being 0.45, 0.34, and 0.84 eV, respectively. Because the last step has a relatively high activation energy, the reaction can also follow the alternative path CHOH $\rightarrow$ CHO $\rightarrow$ CO + H_2, with activation energies of 0.56 and 0.26 eV. The energy profile shows the largest energy span[50] among the four surfaces and thus it is the worst to decompose methanol. The experimental decomposition to CO and H_2 was experimentally reported to occur around 250 K.[51] The C−O breaking of methanol was found to be not likely, with a high energy barrier of 1.57 eV, in good agreement with a previous theoretical study (not ZPE corrected 1.78 eV).[52]

For Pt we discuss two routes. The loss of the methylenic hydrogen drives the reaction according to the following elementary steps: $CH_3OH \rightarrow CH_2OH \rightarrow CHOH \rightarrow COH \rightarrow CO + H_2$. Once the first barrier (0.65 eV) is overcome, the reaction will proceed to CO with low energy barriers of 0.57, 0.69, and 1.06 eV. Alternatively, the route CHOH $\rightarrow$ CHO $\rightarrow$

CO + H_2 has energy barriers of just 0.28 and 0.32 eV. After full dehydrogenation, CO removal is likely to be the bottleneck, as it can accumulate and poison the surface. Our results are in good agreement with experiments, which determined that the methanol dehydrogenation on Pt(111) occurs at temperatures as low as 140 K,[9] significantly lower than the previously reported 250 K Pd value. Yet, another possible route is $CH_3OH \rightarrow CH_3O \rightarrow CH_2O \rightarrow CHO \rightarrow CO + H_2$. In this route, the first reaction is O−H bond scission, which is also the most demanding energy step with an energy barrier of 0.69 eV, followed by moderate barriers of 0.18, 0.28, and 0.32 eV, which facilates the decomposition reactions. According to these results, an isolated methanol molecule will desorb rather than react on Pt(111),[11] and if any reaction takes place, the C−H dehydrogenation would be preferred to the O−H breaking,[8] given that CH_3O is rather unstable on Pt(111), a fact that has been confirmed by experiments.[10] Nevertheless, experimental observations on the dehydrogenation of methanol and other monoalcohols on Pt(111) detected the methoxy radical as an intermediate, but not CH_2OH.[9,53] The source of this apparent discrepancy is that the former analysis does not consider the effect of neighboring methanol molecules, which might play a significant role in O−H bond breaking (see below).

Role of Lateral Interactions. As we have indicated earlier, there are some apparent contradictions between experimental and theoretical results corresponding to the first stage of

dehydrogenation. Lateral interactions based on hydrogen bonds could be responsible for most of the phenomena regarding O–H groups on metal surfaces.[5,54] Methanol adsorption energy on Cu, Ru, Pd, and Pt is −0.37, −0.59, −0.46, and −0.44 eV, respectively. The hydrogen bond is one of the main lateral interactions between adsorbed methanol molecules, being exothermic by around −0.20 eV. Therefore, under the initial conditions on the clean surfaces, the methanol molecules will approach each other and thus a relatively high coverage even at medium pressures and low temperatures can take place.

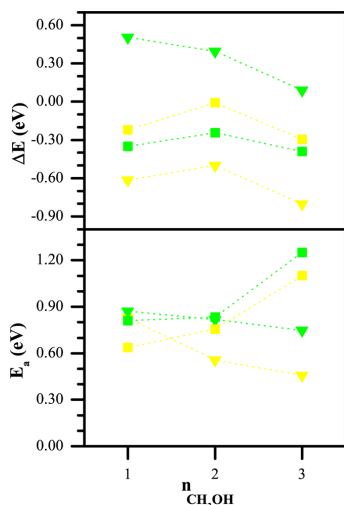In Figure 5 we show that the inclusion of neighboring methanol molecules changes the reaction and activation

Figure 5. Reaction energies and activation barriers for the dissociation of methanol through the competing O–H (triangles) and C–H (circles) bond breaking, as a function of methanol coverage for Pt(111) (green) and Ru(0001) (yellow).

energies for both O–H and C–H decomposition as follows. On one hand, the nearby OH groups stabilize the methoxy intermediate via hydrogen bonding by around 0.20 eV for each group. They also stabilize the transition state of the O–H decomposition and lower the activation energy by around 0.10−0.20 eV/spectator molecule. On the other hand, the activation barrier for the C–H decomposition increases around 0.10 eV if one spectator methanol molecule is included and then additionally increases by 0.40 eV if a second molecule is incorporated, due to strains in the transition state. The barriers for the competitive reactions at low coverage on Ru favor C–H bond breaking with ΔE_a = 0.19 eV, but at high coverage this value is −0.64 eV, and the values are +0.05 to −0.50 eV for Pt. Therefore, the surrounding methanol molecules will induce a change in the reaction pathway. This is not so clear for Pd, for which the energy difference between both paths is still within the energy change of the lateral hydrogen interactions.

Other intermediates or products can be affected by lateral interactions. For instance, for CO adsorption in dense layers a significant reduction of the average binding energy has been found.[55]

Energy Profiles for the Inverse Reaction: CO Hydrogenation. Over the paths for methanol decomposition, those

for synthesis from CO and H_2 without considering the role of CO_2 and/or the water−gas shift reaction can be superimposed to clarify some aspects of methanol synthesis (see Figure 6).

As for the CO hydrogenation, the profiles show that the CHO formation is much more preferable than COH, as the required energies for CHO (COH) formation are 0.17 (2.41) on Cu(111), 0.94 (1.53) on Ru(0001), 1.82 (1.99) on Pd(111), and 1.51 (1.70) eV on Pt(111), respectively. Because of the upright CO adsorption on the four surfaces with C atoms, the interactions between carbon and H atoms are much stronger than those between oxygen and H atoms, which eventually leads to the formation of C–H bonds instead of O–H bonds. For Cu(111) the reaction goes through the adsorption of CO and H_2, forming CHO, which further evolves toward formaldehyde (CH_2O). This formaldehyde preferentially desorbs from the surface. Only if there is a trap for formaldehyde (such as an oxide as in Cu/ZnO[4]) or the amount of H is extremely high could the reaction end up in the formation of methanol. In the modeling of CO_2 electroreduction also some selectivity issues were found on the copper case compatible with our analysis.[56]

The reactions on Ru(0001) are rich, as there are abundant intermediate species and close energy barriers (0.65−0.95 eV) for C–H, C–O, and O–H bond breaking and formation. It should be pointed out here that formaldehyde is the crucial intermediate in the reaction network. The three elementary reactions starting from formaldehyde are $CH_2O \rightarrow CH_3O$, $CH_2O \rightarrow CH_2OH$, and $CH_2O \rightarrow CH_2 + O$. It is interesting to find that they have extremely close barriers of 0.73, 0.70, and 0.72 eV, respectively. Hence, all three reactions can take place in the system. However, the methanol formation from CH_3O is hindered by the largest barrier, 1.34 eV. On the other side, the energy barriers for decomposition from CH_2OH to CHOH (0.21 eV) or CH_2+OH (0.68 eV) are lower than that for methanol formation (0.87 eV). Furthermore, the decomposition from CHOH to CH and OH requires only 0.44 eV and is very exothermic (−1.17 eV). From the above analysis, it is clear to demonstrate that the C–O bond activation reactions are favored on the Ru(0001) surface and, to some extent, methanol formation is unlikely on Ru(0001), as C and O species poison the reactive sites.

On Pd(111), there are two competing reactions from CHOH: CHOH $\rightarrow$ CH_2OH and CHOH $\rightarrow$ CO + OH. The barriers (and reaction energies) are 1.14 (0.69) and 1.18 (−0.06) eV, respectively. Therefore, C–O bond scission from CHOH is most favorable thermodynamically despite similar kinetics. In addition to the CHOH formation, as shown in Figure 6, formaldehyde can also be formed, but it is not as favored as CHOH. There are also two ways for formaldehyde to react on the surface, desorption or hydrogenation to CH_2OH, with energy barriers of 0.75 and 0.90 eV. From CH_2OH, the hydrogenation to methanol is favored, as its energy barrier is 0.95 eV, which is lower than that of C–O bond breaking, 1.31 eV. This reaction barrier is in very good agreement with a previous theoretical study (1.30 eV).[57] Hence, although it seems possible to achieve the methanol synthesis from CO and H_2 on Pd(111), the large barrier for the first hydrogenation step would render the process difficult.

On Pt(111), the first likely intermediate for hydrogenation is CHO followed by CHOH upon the second hydrogenation. Then, the reaction goes as CHOH $\rightarrow$ $CH_2OH \rightarrow CH_3OH$ with activation (reaction) energies of 1.03 (0.46) and 1.16 (0.51) eV. Thus, the network is similar to that of Pd(111); CHOH
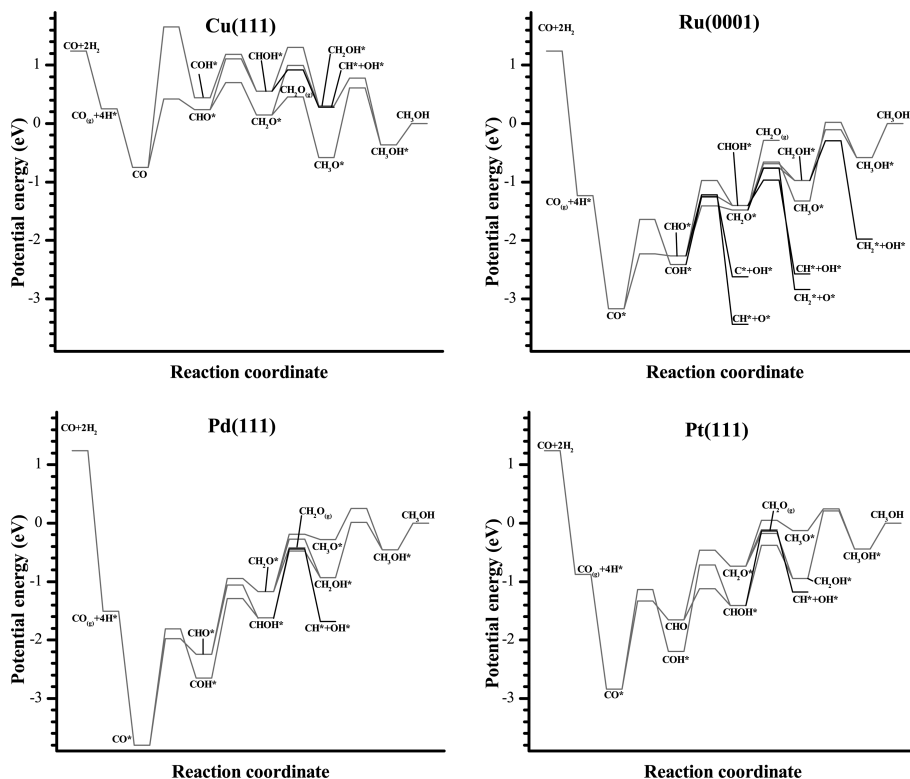
Figure 6. Reaction profiles for the reaction of CO and H_2 on the different surfaces considered here. The minimum energy paths are considered in each particular case.

and CH_2OH are important intermediate species for methanol synthesis. However, it has to be mentioned here that the energy barriers on Pd(111) and Pt(111) are higher than those on other surfaces, and thus these surfaces are less prone to hydrogenate CO.

Kinetic–Thermodynamic Relationships. The relationship between kinetic and thermodynamic parameters was put forward by Brønsted[59] generalized by Evans and Polanyi (BEP),[60] and reintroduced in the density functional theory framework more recently by the groups of Neurock and Nørskov.[61,62] The theory states that the target molecules belonging to a family have similar transition states in nature and thus a change in the thermodynamics of the reaction, i.e. toward more exothermic, is accompanied by a lower activation energy of the direct reaction. If the stability of the intermediates on the surfaces is linked to a single parameter through linear energy scalings,[42] then the BEP relationship directly gives a volcano plot.[63] However, we and others have found that in many cases the BEP relationships represent the dissociation paths better than the associative paths and this behavior has been linked to the early or late-like character of the transition states. An explanation put forward by Hammer[64] indicates that in dissociative paths the interaction between fragments in the transition state resembles that of the final state, provided that this structure corresponds to the fragments sharing some metal atoms in the site ensemble. An alternative formulation of the

BEP that allows the systematization for different compounds was presented by Sautet and co-workers.[58,65] These authors employed a general reference and placed the energy of the transition state as a function of either the initial (IS) or the final states (FS). In our case we have employed the two methodologies with the three possible variations (ΔE, IS, FS), to analyze the different classes and deduce the potential relevance of the wide set of data gathered in the present work. The corresponding results are summarized in Figure 7, where all energies contain the ZPE term; to compare only the potential energy values the reader is addressed to Tables S8–S12 and Figures S1–S3 in the Supporting Information.

For the BEP relationships (first column) in Figure 7 it is clear to see that a proper linear dependence is only observed for CH and especially for CO dissociation. In both cases the dispersion is significant in the low energy regime ($\Delta E \leq -1$ eV). In the case of C–H dissociation it seems that the ΔE value is saturated and thus a plateau appears. Indeed, in an understanding of BEP relationships through a Marcus-like approach[66] it becomes clear that for reactions with high endo(exo)thermic energies the values of the activation barrier should be limited by flat areas. The C–H dissociation energies were already reported extensively to show a BEP relationship in the case of the alkyne–alkene–alkane series for a single metal.[18,67] For CO the discrepancy comes from Ru(0001) points that lie at the lowest part of the energy span; in this case the large influence might be
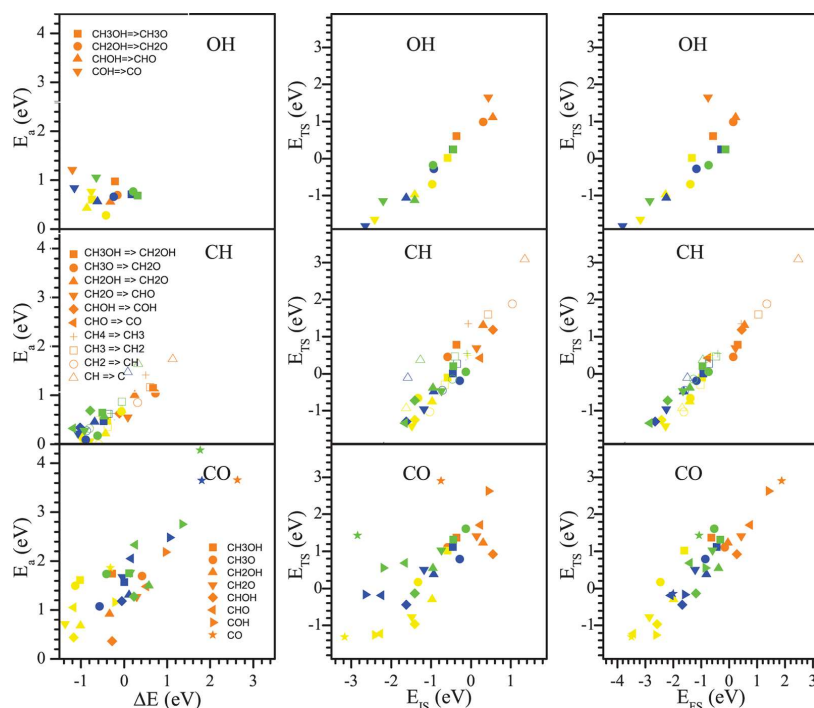
Figure 7. Brønsted−Evans−Polanyi and initial and final state[58] relationships for the different bond breaking reactions: (a) O−H; (b) C−H; (c) C−O. The results of the linear fits are presented in Tables S8−S12 in the Supporting Information.

brought by the strong affinity of Ru toward O atoms (see Table S1 in the Supporting Information).

The situation improves significantly for the dependence on the energy of the initial state, at least for O−H and C−H bond breaking. For O−H a clear line appears with little scattering of around 0.20 eV, the larger being that of Pt (see Figure 7). The values for all metals are distributed quite evenly. The reason for such a good relationship can be traced back to the simple nature of the transition state in this case (Figure 1). A similar, not yet well-defined dependence is found for C−H bonds. In this case the energy span is again large and the points are aligned preferentially on a single line with no semblance of the saturation observed in the BEP plot. However, the point distribution significantly broadens in the central part, where displacements of the individual points to the line can amount up to 0.30 eV. The C−O dissociation class is completely different in this perspective. The list of points is largely scattered, and not even the distribution by individual metals (shown by colors) can illustrate the differences other than from a very qualitative analysis.

Finally, we have considered the dependence of the transition state on the final state energies (third column in Figure 7). For O−H the distribution is no better than that of the initial state. The main reason is the smaller energy span and the appearance of a couple of outliers. When these configurations are analyzed independently, they correspond to Pt and Cu, as in the final state the fragments do not share any metal atoms. In these metals, the FS has no "geometric memory" of the TS, and as described by Hammer[64] the correlation observed for the other

points breaks here. For C−H the correlation is excellent and all points show the lowest dispersion from the reference line. The discrepancies are below the 0.20 eV error of DFT, and thus the line can be accepted as presenting an excellent predictive power for this class of reactions. For C−O the final-like transition state nature is nicely captured in the correlation between the transition and final state energies, which gives a good representative character to the BEP line (except for Ru). Since the final states considered here have the fragments sharing same atoms, an even better predicting nature is given to the TS−FS correlation. Discrepancies, for instance the green star at about 0 eV, might be relevant though even on the central part of the point distribution, highlighting that this kind of dissociation, between two heteroatoms that do not differ much in adsorption strength, are the most prone to errors when interpolated.

We note that for several reactions where cooperative, lateral interactions are important, for instance when a web of H bonds is formed, the modification induced by coverage might be much larger than the error made by employing the most suitable kinetic−thermodynamic scaling. Coverage effects in hydroxylic systems might add up an extra 0.15 eV/H bond to the dissociated forms, while the errors of the best prediction curve are around 0.2 eV.

■ **CONCLUSIONS**

By means of density functional theory we have investigated the complex networks arising from the decomposition of methanol on four metal surfaces: Cu, Ru, Pd, and Pt. The product

ACS Catalysis

distributions are different on these metals, where Cu preferentially renders CH_2O, while Pt, Pd, and Ru initially generate large amounts of CO that could potentially poison the surface. The initial decomposition state on Pt and Ru has been a subject of discrepancies between experiments and theory, but coverage effects can fine-tune the relative competing routes. On one hand O–H bond breaking is improved at high coverages while the alternative activation of the methylenic H ends up with an intermediate that requires a larger ensemble and thus is more repulsive. The same set of reactions can be employed to understand the reverse reaction of CO hydrogenation. Again differences in the product distribution appear, Cu being quite unique and the reaction leading to CH_2O. For Pt and Pd the routes to form methanol are affected by CO blocking and the large barriers to transfer the first hydrogen. On Ru, the selectivity problem is more acute, as several routes inducing C–O bond breaking appear at different stages of the hydrogenation. For the kinetic–thermodynamic relationships we have explored different routes to obtain the best-predicting representations. C–H bond breaking is the easiest set of reactions to represent, with almost no error in the TS to FS plot. For O–H the initial state representation seems more adequate, the reason being that the H bond is not as different on the metal surfaces. Activation energies for C–O bond breaking are by far the most difficult to be retrieved. In summary, for complex substrates it would be operative to obtain from the kinetic–thermodynamic scalings the first values for C–H and O–H dissociations and evaluate in detail the more complex C–O dissociations. There is a final point regarding the concept of mechanism in heterogeneous catalysis. According to the IUPAC definition, a mechanism is the list of elementary reactions that lead from reactants to products. However, in line with the complexity of the networks that we observe, the total list of reactions involved might contain a richer information indicating that the set of potential steps is common, although due to the energy differences they are manifested in different "mechanisms".

■ ASSOCIATED CONTENT

ⓢ Supporting Information

The following file is available free of charge on the ACS Publications website at DOI: 10.1021/cs501698w.

> Computed adsorption (with van der Waals contribution analysis), reaction, and activation energies, comparison with previous theoretical and experimental studies, Brønsted–Evans–Polanyi, initial state, and final state scalings, and structures of initial, transition, and final states for all of the reactions in the study (PDF)

■ AUTHOR INFORMATION

Corresponding Author

*N.L.: e-mail, nlopez@iciq.es; tel, +34 977920237; fax, +34 977920231.

Notes

The authors declare no competing financial interest.

■ ACKNOWLEDGMENTS

■ REFERENCES

(1) Olah, G. A. *Angew. Chem. Int. Ed.* **2005**, *44*, 2636−2639.
(2) Nielsen, M.; Alberico, E.; Baumann, W.; Drexler, H.-J.; Junge, H.; Gladiali, S.; Beller, M. *Nature* **2013**, *495*, 85−89.
(3) Gallagher, J. T.; Kidd, J. M. Patent UK1159035, 1966.
(4) Behrens, M.; Studt, F.; Kasatkin, I.; Kühl, S.; Hävecker, M.; Abild-Pedersen, F.; Zander, S.; Girgsdies, F.; Kurr, P.; Kniep, B.-L.; Tovar, M.; Fischer, R.; Norskov, J.; Schlögl, R. *Science* **2012**, *336*, 893−897.
(5) García-Muelas, R.; López, N. *J. Phys. Chem. C* **2014**, *118*, 17531−17537.
(6) Greeley, J.; Mavrikakis, M. *J. Catal.* **2002**, *208*, 291−300.
(7) Greeley, J.; Mavrikakis, M. *J. Am. Chem. Soc.* **2002**, *124*, 7193−7201.
(8) Greeley, J.; Mavrikakis, M. *J. Am. Chem. Soc.* **2004**, *126*, 3910−3919.
(9) Sexton, B. A. *Surf. Sci.* **1981**, *102*, 271−281.
(10) Karp, E. M.; Silbaugh, T. L.; Crowe, M. C.; Campbell, C. T. *J. Am. Chem. Soc.* **2012**, *134*, 20388−20395.
(11) Desai, S. K.; Neurock, M.; Kourtakis, K. *J. Phys. Chem. B* **2002**, *106*, 2559−2568.
(12) Hammer, B.; Nørskov, J. *Surf. Sci.* **1995**, *343*, 211−220.
(13) Greeley, J.; Nørskov, J. K.; Mavrikakis, M. *Annu. Rev. Phys. Chem.* **2002**, *53*, 319−348.
(14) Nørskov, J. K.; Bligaard, T.; Rossmeisl, J.; Christensen, C. H. *Nat. Chem.* **2009**, *1*, 37−46.
(15) Kang, J.; Nam, S.; Oh, Y.; Choi, H.; Wi, S.; Lee, B.; Hwang, T.; Hong, S.; Park, B. *J. Phys. Chem. Lett.* **2013**, *4*, 2931−2936.
(16) Ferrin, P.; Nilekar, A. U.; Greeley, J.; Mavrikakis, M.; Rossmeisl, J. *Surf. Sci.* **2008**, *602*, 3424−3431.
(17) Yudanov, I; Matveev, A.; Neyman, K.; Rösch, N. *J. Am. Chem. Soc.* **2008**, *130*, 9342−9352.
(18) Andersin, J.; López, N.; Honkala, K. *J. Phys. Chem. C* **2009**, *113*, 8278−8286.
(19) Wang, S.; Petzold, V.; Tripkovic, V.; Kleis, J.; Howalt, J. G.; Skulason, E.; Fernández, E.; Hvolbæk, B.; Jones, G.; Toftelund, A.; Falsig, H.; Björketun, M.; Studt, F.; Abild-Pedersen, F.; J, R.; Nørskov, J.; Bligaard, T. *Phys. Chem. Chem. Phys.* **2011**, *13*, 20760−20765.
(20) Deckert, A.; Brand, J.; Mak, C.; Koehler, B.; George, S. *J. Chem. Phys.* **1987**, *87*, 1936−1947.
(21) Loveless, B. T.; Buda, C.; Neurock, M.; Iglesia, E. *J. Am. Chem. Soc.* **2013**, *135*, 6107−6121.
(22) Gómez-Díaz, J.; López, N. *J. Phys. Chem. C* **2011**, *115*, 5667−5674.
(23) Kresse, G.; Furthmüller, J. *Comput. Mater. Sci.* **1996**, *6*, 15−50.
(24) Kresse, G.; Furthmüller, J. *Phys. Rev. B* **1996**, *54*, 11169−11186.
(25) Perdew, J. P.; Burke, K.; Ernzerhof, M. *Phys. Rev. Lett.* **1996**, *77*, 3865−3868.
(26) Blöchl, P. E. *Phys. Rev. B* **1994**, *50*, 17953−17979.
(27) Kresse, G.; Joubert, D. *Phys. Rev. B* **1999**, *59*, 1758−1775.
(28) Lide, D. *CRC Handbook of Chemistry and Physics*, 84th ed.; CRC Press: Boca Raton, FL, 2003−2004; pp 12(19−21).
(29) Clendenen, R.; Drickamer, H. *J. Phys. Chem. Solids* **1964**, *25*, 865−868.
(30) King, H.; Manchester, F. *J. Phys. F: Metal Phys.* **1978**, *8*, 15−26.
(31) Arblaster, J. *Platinum Met. Rev.* **1997**, *41*, 12−21.
(32) Monkhorst, H. J.; Pack, J. D. *Phys. Rev. B* **1976**, *13*, 5188−5192.
(33) Makov, G.; Payne, M. C. *Phys. Rev. B* **1995**, *51*, 4014−4022.
(34) Grimme, S. *J. Comput. Chem.* **2006**, *27*, 1787−1799.
(35) Bučko, T.; Hafner, J.; Lebegue, S.; Angyán, J. G. *J. Phys. Chem. A* **2010**, *114*, 11814−11824.
(36) Błoński, P.; López, N. *J. Phys. Chem. C* **2012**, *116*, 15484−15492.
(37) Almora-Barrios, N.; Carchini, G.; Błoński, P.; López, N. *J. Chem. Theory Comput.* **2014**, *10*, 5002−5009.
(38) Henkelman, G.; Jónsson, H. *J. Chem. Phys.* **2000**, *113*, 9978−9985.
(39) Henkelman, G.; Uberuaga, B. P.; Jónsson, H. *J. Chem. Phys.* **2000**, *113*, 9901−9904.

(40) Heyden, A.; Bell, A. T.; Keil, F. J. *J. Chem. Phys.* **2005**, *123*, 224101(1−14).

(41) Lin, S.; Ma, J.; Zhou, L.; Huang, C.; Xie, D.; Guo, H. *J. Phys. Chem. C* **2012**, *117*, 451−459.

(42) Abild-Pedersen, F.; Greeley, J.; Studt, F.; Rossmeisl, J.; Munter, T.; Moses, P. G.; Skulason, E.; Bligaard, T.; Nørskov, J. K. *Phys. Rev. Lett.* **2007**, *99*, 016105(1-4).

(43) Lim, K. H.; Chen, Z.-X.; Neyman, K. M.; Rösch, N. *J. Phys. Chem. B* **2006**, *110*, 14890−14897.

(44) Zuo, Z.-J.; Wang, L.; Han, P.-D.; Huang, W. *Int. J. Hydrogen Energy* **2014**, *39*, 1664−1679.

(45) Gu, X.-K.; Li, W.-X. *J. Phys. Chem. C* **2010**, *114*, 21539−21547.

(46) Lin, S.; Johnson, R. S.; Smith, G. K.; Xie, D.; Guo, H. *Phys. Chem. Chem. Phys.* **2011**, *13*, 9622−9631.

(47) Gazdzicki, P.; Jakob, P. *J. Phys. Chem. C* **2010**, *114*, 2655−2663.

(48) Chiu, C.-C.; Genest, A.; Rösch, N. *Top. Catal.* **2013**, *56*, 874−884.

(49) Jiang, R.; Guo, W.; Li, M.; Fu, D.; Shan, H. *J. Phys. Chem. C* **2009**, *113*, 4188−4197.

(50) Kozuch, S.; Shaik, S. *Acc. Chem. Res.* **2011**, *44*, 101−110.

(51) Davis, J.; Barteau, M. *Surf. Sci.* **1987**, *187*, 387−406.

(52) Zhang, C.; Hu, P. *J. Chem. Phys.* **2001**, *115*, 7182−7186.

(53) Rendulic, K. D.; Sexton, B. A. *J. Catal.* **1982**, *78*, 126−135.

(54) Revilla-Lopez, G.; Lopez, N. *Phys. Chem. Chem. Phys.* **2014**, *16*, 18933−18940.

(55) Loffreda, D.; Simon, D.; Sautet, P. *Surf. Sci.* **1999**, *425*, 68−80.

(56) Peterson, A. A.; Abild-Pedersen, F.; Studt, F.; Rossmeisl, J.; Nørskov, J. K. *Energy Environ. Sci.* **2010**, *3*, 1311−1315.

(57) Lin, S.; Ma, J.; Ye, X.; Xie, D.; Guo, H. *J. Phys. Chem. C* **2013**, *117*, 14667−14676.

(58) Zaffran, J.; Michel, C.; Auneau, F.; Delbecq, F.; Sautet, P. *ACS Catal.* **2014**, *4*, 464−468.

(59) Brönsted, J. *Chem. Rev.* **1928**, *5*, 231−338.

(60) Evans, M.; Polanyi, M. *Trans. Faraday Soc.* **1938**, *34*, 11−24.

(61) Pallassana, V.; Neurock, M. *J. Catal.* **2000**, *191*, 301−317.

(62) Nørskov, J.; Bligaard, T.; Logadottir, A.; Bahn, S.; Hansen, L. B.; Bollinger, M.; Bengaard, H.; Hammer, B.; Sljivancanin, Z.; Mavrikakis, M.; Xu, S. Y.; Dahl; Jacobsen, C. *J. Catal.* **2002**, *209*, 275−278.

(63) Bligaard, T.; Nørskov, J. K.; Dahl, S.; Matthiesen, J.; Christensen, C. H.; Sehested, J. *J. Catal.* **2004**, *224*, 206−217.

(64) Hammer, B. *Phys. Rev. Lett.* **1999**, *83*, 3681−3684.

(65) Loffreda, D.; Delbecq, F.; Vigné, F.; Sautet, P. *Angew. Chem. Int. Ed.* **2009**, *48*, 8978−8980.

(66) Marcus, R. A. *Angew. Chem. Int. Ed.* **1993**, *32*, 1111−1121.

(67) García-Mota, M.; Bridier, B.; Pérez-Ramírez, J.; López, N. *J. Catal.* **2010**, *273*, 92−102.

Microkinetics of alcohol reforming for H_2 production from a FAIR density functional theory database

Qiang Li[1], Rodrigo García-Muelas[1], and Núria López[*][1]

[1]Institute of Chemical Research of Catalonia (ICIQ), The Barcelona Institute of Science and Technology, Avgda. Països Catalans 16, 43007, Tarragona, Catalonia, Spain.

Abstract

The production of hydrogen from biomass under technologically relevant conditions is fundamental for a sustainable future. Here, we present a multiscale study of the available technologies based on a Density Functional Theory open database that allows the formulation of linear-scaling relationships and microkinetics. The database fulfills the FAIR criteria: findability, accessibility, interoperability and reusability. Moreover, it contains *ca.* 1000 transition states for the decomposition of C_2 alcohols on closed-packed Cu, Ru, Pd, and Pt surfaces. The microkinetic results for activity, selectivity towards H_2 and stability can be directly mapped to experiments, and the catalytic performance is controlled by various types of poisoning. Linear-scaling relationships provide valid quantitative results that allow the extrapolation to larger compounds like glycerol. Our database presents a robust roadmap to investigate the complexity of biomass transformations through the use of small fragments as surrogates when investigated under different reaction conditions.

[*]nlopez@iciq.es

The conversion of biomass to provide chemicals and energy vectors like H_2 is a fundamental challenge for a sustainable chemical industry based on renewable sources.[1,2] Particularly, to extract hydrogen from biomass, three reforming methodologies as well as direct decomposition (DD) have been put forward, Fig. 1 and Table S1. In the Steam Reforming (SR) process ethanol, sugars, and other oxygenated compounds react on metals and oxides with steam at temperatures around 400–1100 K to produce H_2, CO, CO_2, and CH_4.[3] Autothermal Reforming (ATR) constitutes an improvement over this process as small amounts of oxygen are added along with steam to produce raw syngas. ATR has been tested for ethanol[4] and glycerol[5] on noble metals. However, the high temperatures reached impose limitations to thermal stability related to poisoning. Compared with the former processes, Aqueous Phase Reforming (APR),[6–8] has the advantage of working at temperatures below 650 K, although the process is slow on clean metal surfaces. Only very recently, high turn-over frequencies have been achieved on single-atom catalysts Pt dispersed on α-MoC,[9] but long-term stability of this catalyst might be an issue.
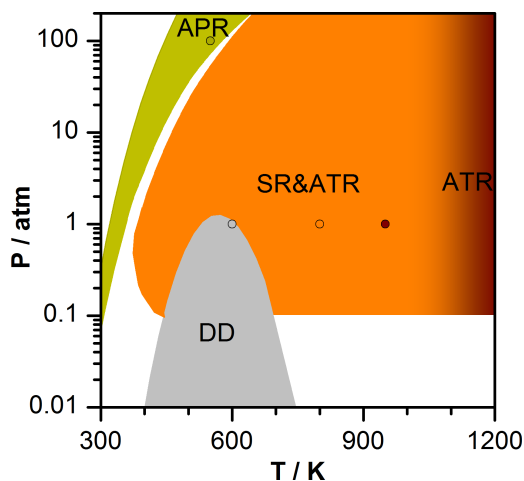
Figure 1: Phase diagram for the engineering conditions of hydrogen production by biomass reforming. Shaded areas correspond to Direct Decomposition (DD), Steam (SR), Autothermal (ATR), and Aqueous-Phase (APR) Reforming. The points correspond to the experimental conditions employed in the simulations and reported in Table S1.

A large number of potential catalysts have been experimentally screened for these reactions, a detailed summary can be found in Table S2, however large scale H_2 pro-

duction is still costly. A better understanding of the reaction mechanisms and their role when searching a high performance catalyst is needed. Theoretical simulations based on Density Functional Theory (DFT) and micro-kinetic modeling (MK) hold the key for a rational design.[10] The most complete kinetic model on alcohol decomposition analyzed 50 species for ethanol on Pt and about 100 reactions in a correlative global sensitivity analysis.[3] There, the errors inherent to DFT are correlated due to the similar nature of the oxygenated fragments on the metal surface, thus keeping the predictive value of MK based on DFT data. The complexity of the compounds derived from biomass has prevented an extensive study of full reaction mechanisms (C_6 sugar alcohol decomposition encompasses 10^5 reactions).[11]

As full mechanistic studies by DFT are impractical for large alcohols, divide-and-conquer strategies have been put forward, although their representativity has not been fully assessed. The decomposition of small alcohols including methanol, ethanol, ethylene glycol, glycerol, and other oxygenates has been extensively studied. Thermodynamics for the adsorption of intermediates can be obtained from multivariable scaling based on group additivity rules[12–14] inferred by taking the small molecules as surrogates. The rate coefficients are then extracted from kinetic-thermodynamic relationships[15–21] derived from key (calculated) decomposition steps either on a single metal, or a small group of alcohols. A summary of previous DFT calculations including up to C_3 alcohol decomposition on different metal surfaces is provided in Table S3.

However, the computed data is scarce (only partial networks have been mostly considered), has been generated with differences in the computational setups and thus the FAIR (findability, accessibility, interoperability and reusability) nature of the data is not ensured. This prevents the use of large analysis tools to systematize the available information. To diminish the errors, sparsity, and asymmetries in the computational data, we have developed a full open database that contains all the decomposition steps of C_1–C_2 alcohols: methanol, ethanol, ethylene glycol, together with the complementary steps from the water-gas shift reaction (WGSR) and oxygen adsorption. Initially, the database contains the results for the close packed surfaces, as they are most exposed in the catalytic preparations,[22] but can be extended to include lateral interactions, side reactions, other metals, alloys, undercoordinated sites and supports.[12,23,24] In that

70 case, the linear-scaling relationships previously reported in the literature can also be
71 incorporated.[12,23,24] The database has then been interrogated through microkinetic
72 models to unravel whether the same reaction set is able to reproduce the different ex-
73 perimental behavior on the generation of hydrogen under different reaction conditions,
74 and to predict the best conditions in the reforming of glycerol for one of the metals.

Results and Discussion

76 We have generated a database that can be retrieved from ioChem-BD,[25] where we
77 have uploaded the computed 55 reaction intermediates and 215 reactions for the C_2
78 species on each metal.[26] They correspond to 100 dehydrogenations, 55 C–C, and 60
79 C–O breakings, related to 10, 24, and 21 intermediates in the ethane, ethanol, and
80 ethylene glycol decomposition networks, respectively. Besides, we included 7 reactions
81 to account for the water-gas shift, the O_2 decomposition, and our previous results
82 on methanol.[27] The procedure to generate the full decomposition network of a given
83 species is presented in Figure 2. The species can undergo C–C, C–H, O–H, and C–O
84 bond breakings, and each of these reaction products can further experience these four
85 bond cleavages until the formation of the simplest decomposition products: C*, H*,
86 and O*. The network expanded in Figures S2–S4, and includes lateral paths. The
87 equations used to calculate the energies are shown in Section S1.1, and the computed
88 data are summarized in Table S5-S6.

89 Based on the reaction database, we tested the predictive power of three types of
90 linear-scaling relationships (LSR): Brønsted-Evans-Polanyi (BEP), Initial-State and
91 Final-State Scalings (ISS, FSS). The reactions were classified according to the type
92 of bond breaking, as O–H, C–H, C–C, C–O, and C–OH. For the O–H bond breaking,
93 the BEP slopes, α, are between 0.07 and 0.24 (Section S3.1 and Table S7). This
94 indicates that the transition states should resemble the initial states.[19] Indeed, the ISS
95 have much better statistics (R^2 and MAE) than the BEP or FSS. For C–H, C–C, C–O,
96 and C–OH bond breakings, the BEP slopes, α, are larger than 0.50, and the FSS are
97 more suitable for the prediction of the transition states energies. The best LSR are
98 presented in Fig. 3 (see Table S8 for the statistics). In the ISS or FSS-relationships
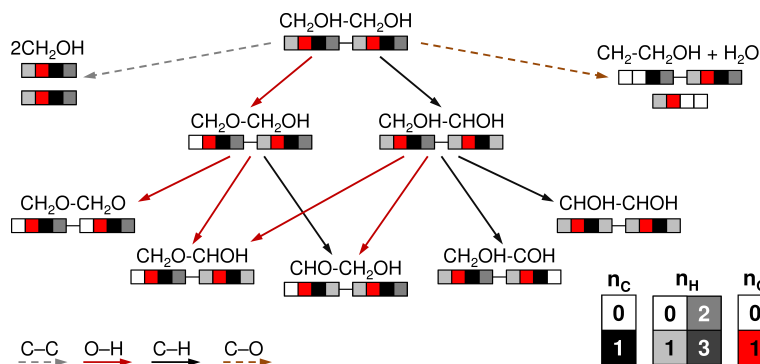
Figure 2: Reaction network for the decomposition of ethylene glycol. Each CH_xOH moiety is shown as a quadruplet whose colours are representative of the stoichiometry. The two central boxes are red (O) and black (C) while the first and last boxes indicate the number of hydrogen atoms attached to them, darker grey stands for higher H content. C–C, O–H, C–H, and C–O bond breakings are displayed as grey, red, black, and brown arrows respectively. C–C breakings lead to the lateral path of methanol decomposition, while C–O breakings lead to the lateral path of ethanol and water dehydrogenation. The full set of reactions is shown in Fig. S2-S4, the same labels have been used in the database.

99 the slope, α, was forced to be one. This leads to a simpler yet representative form for

100 the equations, as (i) it eliminates the α regression term avoiding overfitting, (ii) the

101 LSR equations are independent of the energy reference used, see Section S3.1.1. Both

102 conditions are fundamental to use the LSR to predict the activation energies of larger

103 polyalcohols. Cu follows a different behavior than Ru, Pd, and Pt, and therefore it was

104 treated independently in Fig. 3.

105   The complexity of the reaction network can only be described by combining the

106 energy profile with a microkinetic analysis. In Fig. 4 (a) the decomposition of ethanol

107 on Pd is taken as example. To generate this energy profile the transition state with

108 lowest barrier is selected for each intermediate. The rest are only plotted in the figure

109 if their barriers are up to 0.30 eV higher than this reference state. However, in the

110 microkinetic modeling all 246 steps are considered simultaneously. The interpretation

111 of such a complex profile is not straightforward. Microkinetics on the DFT results show

112 that a complex reaction network, as the one shown in Fig. 4 (a), may exhibit several

113 pseudo-stationary states,[29] Fig. 4 (b)-(c) (Supplementary Information Section S3.2).

114 These pseudo-stationary states were identified to obtain the coverages and hydrogen
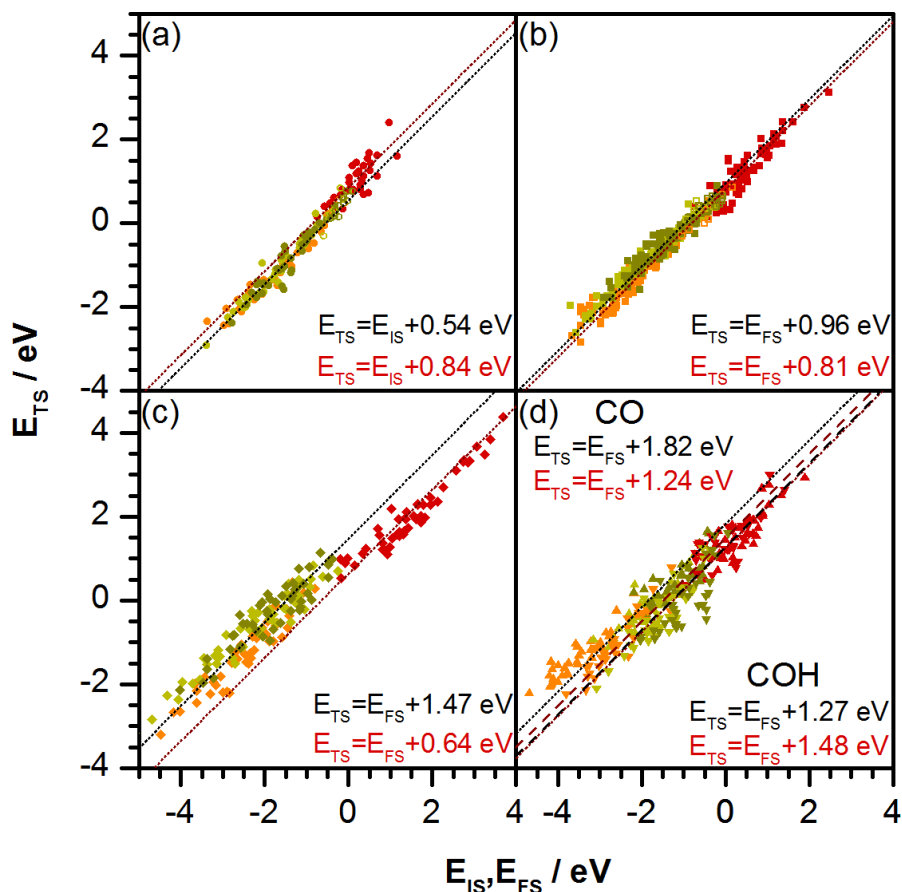
Figure 3: Best Linear Scaling Relationships (LSR) (a) Initial state scaling relationships for O–H bond breaking on Ru, Pd, and Pt (black dotted line) and Cu (red line). Final state scalings for (b) C–H, (c) C–C, and (d) C–O/C–OH bond breakings. The α (slope) values in the LSRs were set to 1.00. Transition states calculated with explicit water molecules and/or the implicit solvation model for methanol are taken from ref. [28] and included as empty symbols showing that the LSRs also hold when solvation is considered.

115   production reported as crosses in Fig. 5 (a-b) and (d-e). Following with the example,

116   in the early stages ($t < 10^0$ s) of ethanol decomposition, Pd dehydrogenates the alcohol

117   moiety, building up a layer of CO and CH poisons, Fig 4 (b). From $t = 10^1 - 10^4$ s, C–O

118   breaking starts to be kinetically relevant, leaving CCH_3 coverages of 30% while the rest

119   is CO (66%). In the meanwhile, most of the CH is consumed. The concentration of

120   CO also increases and reaches a maximum at $t = 10^4$ s (roughly 3 hours), while the

121   desorption rate of H_2 stabilizes in a plateau value around $1.4 * 10^{-6}$ s^{-1}. The surface

behavior for $t = 10^4..10^6$ s would be the most representative pseudo-stationary state. After 60 days, the desorption rate of hydrogen will still be significant (30% the initial plateau value) and CCH_2 and CCH_3 will cover most of the surface. The ultimate steady state will be reached at $t = 6.3 * 10^7$ s (two years) where the desorption rate of H_2 is 1% of the previous plateau value. The observed times are only qualitatively meaningful as they have been obtained in a model with no lateral interactions. When those are included, the pseudo-stationary states are the same, both in terms of main products and poisons, but they are reached at shorter reaction times, an example is shown in Figure S9. The expandable nature of our database would allow the incorporation of this type of effects, although this discussion is beyond the scope of the present work. Long equilibration times (in the order of hours) have experimentally been reported for APR of ethylene glycol on Pt.[8] The analysis can then be extended to all metals under all the technical conditions of the reforming. The H_2 production can be found in Fig. 5 (a-b) marked with crosses, along the main surface species, (d-e). The analysis is based on the relevant stationary state reached before 3 h.

The decomposition of ethanol and ethylene glycol on Cu leaves CCO^* as the most abundant intermediate, which covers 97% and 92% of the surface and leave a small fraction of empty sites, 2.4% and 0.6%. For the reforming technologies, the surface coverage of O and OH is very high, adding up to 73-99.9%, thus lowering the productivity of the surface towards H_2. Special care should be taken as for oxygen coverages higher than 0.75 ML suboxides might appear,[30] thus compromising the representability of the metal-only model. Acetaldehyde is the main product of ethanol reforming, while ethylene glycol yields a mixture of CH_2O, CO, and glyoxal. In ATR, the high oxygen coverage strips the hydrogen to generate water and, therefore, no H_2 is produced.

In the ethanol direct decomposition on Ru (the main on-surface species are CCH (68%), CO (16%), and CCO (7%). The main desorption products are CO and H_2, close to the stoichiometric ratio of 2:3. For ethylene glycol C–C bonds can easily break and the surface is strongly poisoned by CO (98%) with minor CCO species. ATR is a very inefficient process on Ru and shows the lowest hydrogen production rate: less than 10^{-10} s^{-1}, as the high O* coverage consumes all hydrogen. Oxygen is also the most abundant on-surface species for the SR and APR of ethanol on Ru. In the
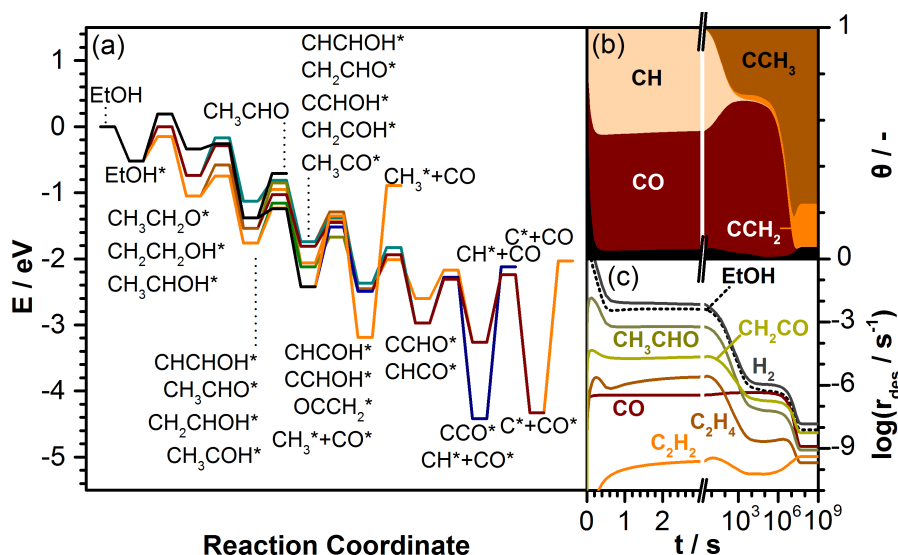
Figure 4: (a) Simplified DFT-Reaction profile for ethanol decomposition on Pd(111) only considering transition states within 0.30 eV energy windows for each TS. MK-DFT: (b) Surface coverages during the decomposition of ethanol on Pd(111) as a function of time at the reaction conditions: $T = 600$ K, $P_{ethanol} = 1$ atm. Main intermediates are labelled, while the black area stands for the small intermediate fractions together with the empty sites. (c) Desorption rate of ethanol and several products as a function of time.

steam reforming of ethanol, CO and CH_3CHO are produced at a 2.3 ratio, but the decomposition proceeds slowly and the desorption rate of H_2 is very low. In contrast, CO is the most abundant intermediate for ethylene glycol in SR and APR and the main product along with traces of CO_2. The desorption rate of hydrogen is relatively high for SR.

The direct decomposition of ethylene glycol on Pd produces CO and traces of $HOCH_2CHO$ and other oxygenates. The activity of Pd is low for ATR as the surface is highly covered by O*, which reacts with most of the hydrogen to form water, leading to almost no hydrogen production. The main products from the ATR of ethanol are CO_2 and CH_3CHO in a 8:5 proportion, while ethylene glycol produces glycolaldehyde. In the SR of ethanol and ethylene glycol, the main product is CO, with small traces of C_2H_2 and CH_3CHO. CO accumulates since the high dissociation barrier of water limits the efficiency of the WGSR. On the ethanol steam reforming, three stable carbonaceous species are formed as poisons: CCH_3 (27%), CCH_2 (32%), and CCH

167 (28%), while CO is the main poison for ethylene glycol. In APR, the main on-surface
168 species are CO (65%) and CCH_3 (28%) for ethanol and CO for ethylene glycol. The
169 carbonaceous fragments tend to accumulate rather than desorb.

170   In the direct decomposition of ethanol on Pt(111), CO is the main desorption prod-
171 uct and it is also present on the surface (14%) along CH (42%), CCH_2 (6%), and CCH_3
172 (37%). CO is the only poison for ethylene glycol, and it is produced along $HOCH_2CHO$
173 in a 2:1 proportion. The ATR has the highest H_2 productivity on Pt compared with any
174 other metal, as the CO poisoning is efficiently removed by oxidation. The H_2:alcohol
175 ratios are 2.8 and 2.9, respectively. The main surface species are all carbonaceous: C
176 (10%), CH (38%), CCH_2 (29%), and CCH_3 (20%), for ethanol and only CH (23%) and
177 CO (66%) for ethylene glycol. The fraction of empty sites is moderate 0.06% and high
178 3.80% for the mono and di-alcohol. In the SR, the main desorption products are CO
179 and traces of C_2H_4 for ethanol, and glyoxal for ethylene glycol. For ethanol, most of
180 the on-surface species are carbonaceous: CCH_2 (80%), CH (4%), and C (5%), while
181 for ethylene glycol, CO is the main poison. Without CO oxidation, the H_2 production
182 is slower for SR and APR than for ATR (up to 7 orders of magnitude). Nonetheless, a
183 small fraction of water undergoes the WGSR and reduces the CO poisoning. The H_2
184 productivity is much lower for the APR than for SR of ethanol. For ethanol, CO is the
185 main desorption product, and it is present on the surface along with CH, roughly in
186 1:1 amounts. Finally, $HOCH_2CHO$ is produced along with CO in the APR of ethylene
187 glycol, but CO is still the main surface intermediate.

188   To assess the robustness of the linear-scaling relationships in reproducing the full
189 MK-DFT data, we built two different microkinetic models, which differ in the method-
190 ology followed to obtain the energies: (i) MK-LSR: The intermediates are taken from
191 DFT, while the activation energies were obtained from the optimum LSR. (ii) MK-
192 L1O: The activation energies were obtained from LSR but employing a Leave-One-Out
193 procedure for the Ru, Pd and Pt triad. These results are shown as bars and dots in
194 Fig. 5 (a-c), respectively.

195   The general performance of the different models can be found in Fig. 5 (a-b).
196 The agreement between the simplified methodologies and the full DFT results is thus
197 remarkable, particularly as the relative ordering between the different metals is kept
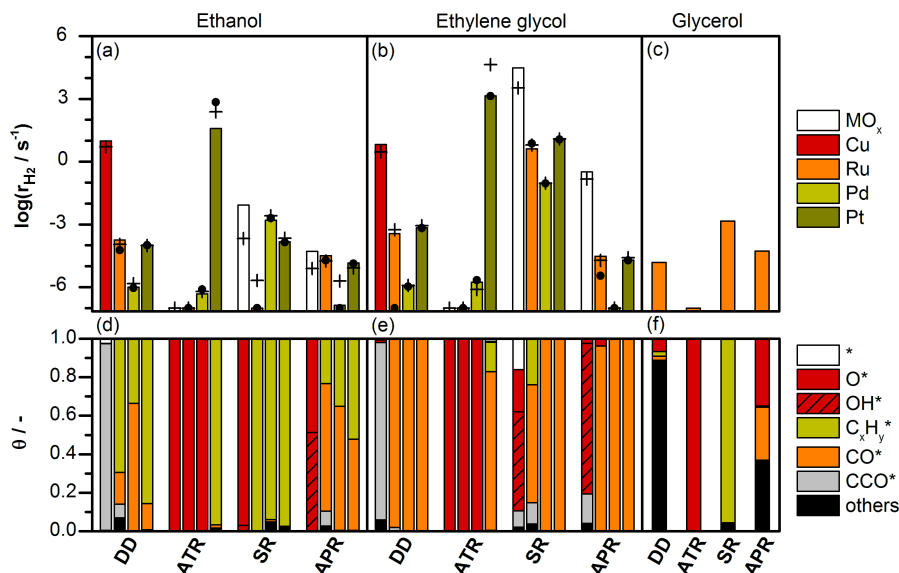
Figure 5: Hydrogen production rate during the direct decomposition, and reforming: ATR, SR, and APR of (a) ethanol and (b) ethylene glycol on Cu, Ru, Pd, and Pt. (c) corresponding values for glycerol on Ru. The crosses show the result from MK-DFT, columns from MK-LSR, and dots from the MK-L1O method. White columns stand for configurations where the oxygen content could change the existing catalytic phase. The surface coverages obtained with MK-DFT are shown on panels (d-f).

and semi-quantitative values can be retrieved. The deviations are within one-two orders of magnitude (similar to the limits identified by Vlachos)[3] for three situations: ATR on Pt and the ethanol SR-Ru and APR-Ru for which higher activities for which the real value is higher than the one obtained from MK-LSR and MK-L1O. Deviations towards higher activities in the MK-LSR model are found only for Cu in the SR of both ethanol and ethylene glycol and to a lesser extent for APR. The production rate of hydrogen is also well reproduced with the MK-L1O methodology, showing differences lower than two orders of magnitude with respect to the MK-DFT results. The direct decomposition of ethylene glycol on Ru is the only process where MK-L1O deviates. The origin of this behavior is that the average activation energies for C–C breakings on Pd and Pt are 0.43 eV higher than the ones from Ru, so the MK-L1O procedure represents a Ru surface that is much less active than for MK-DFT and MK-LSR. This deviation does not appear when taking Pt and Ru or Pd and Ru as sources for the models.

²¹² The microkinetic data can be then compared to experimental trends. For instance,
the activity for ethylene glycol APR on silica-supported metal catalyst follows the order
Ru>Pt>Pd.[8] This order is well reproduced for MK-LSR and MK-L1O, while the MK-
DFT reports Pt>Ru>Pd. This shows that the rules obtained through LSR might
avoid accurate convergence issues in transition state searching, thus providing a slightly
more robust framework. Still, intrisic DFT errors would require the improvement of
the functionals. On the other hand, the production rate of CO_2 follows the order
Pt>Ru>Pd.[8] This order is obtained from all three microkinetic models considering
together the desorption rates of CO and CO_2.

A detailed comparison to the available literature regarding kinetic parameters (rates,
apparent activation energies and reaction orders) has been attempted. Unfortunately
the set of experiments is sparse and thus particularly, there is no clear experimental set
comparing those similar particle sizes, supports and external conditions for the different
materials. In addition, when the catalytic tests are presented together with detailed
kinetic analysis, the characterization of the samples before and after reaction is lacking.
This is a major handicap when attempting to formulate a robust framework for com-
parison. However, Table /reft.exp2 shows a summary of the results in the literature.
The microkinetic model has been rerun with the experimental conditions reported in
Ref. [22, 31–33] The systems have been equilibrated to the pseudo-stationary point at
t=3h, then a perturbation, either in the temperature or the pressure, has been ap-
plied.[34] The results show that the reaction orders and activation energies are properly
reproduced except for when a relevant role of the support can be anticipated, CeO_2.
The activation barriers show a larger deviation but are qualitative in the same range.

Table 1: Experimental apparent activation energies, E_a^{app} (in eV), and reaction orders with respect to ethanol and water, n_a and n_w (dimensionless), for the steam reforming of ethanol. The experimental results (indicated by "exp") and the calculations are performed under the same conditions. The conditions for temperature, T (in K), and partial pressures of ethanol and water, P_a and P_w (in atm), are also shown.

Ref.	Metal	T	P_a	P_w	n_a^{exp}	n_a	n_w^{exp}	n_w	$E_a^{app,exp}$	E_a^{app}
31	Ru/γ-Al$_2$O$_3$	923	0.042	0.420	1.0	1.0	0.0	0.0	0.99	0.66
22	Pd/γ-Al$_2$O$_3$	575	0.125	0.375	-	0.9	-	0.0	0.49	0.54
22	Pt/γ-Al$_2$O$_3$	575	0.125	0.375	-	1.1	-	0.0	0.59	0.71
32	Pt/γ-Al$_2$O$_3$	575	0.125	0.375	0.8	1.1	-	0.0	0.48	0.71
33	Pt/CeO$_2$	575	0.005	0.015	0.5	1.0	0.0	0.0	0.19	0.69

Finally, the MK-LSR methodology was used to predict the reactivity for glycerol on Ru as, experimentally, it has been a better catalyst in steam reforming than Pd or Pt.[35] The full decomposition network comprises 349 on-surface species and 1944 reaction steps. The MK-LSR was applied as follows: (i) the energies for the C_3 intermediates were obtained by DFT, (ii) with these energies the ISS and FSS from Fig. 3 were applied (Table S12) and employed in the MK setup. The coverages and hydrogen production can be seen in Fig. 5. The results show that most suitable technology to produce hydrogen from glycerol is SR, as APR is considerably less active. The activity for the glycerol steam reforming is 3.5 orders of magnitude smaller than that of ethylene glycol. This observation agrees with previous experimental results on other catalysts. H_2 production in the APR of ethylene glycol is higher than for glycerol on Pt[6] and on Raney catalyst ($Ni_{37}Sn_3$).[7] The longer the alcohol carbon chain (up to C_6), the lower the selectivity towards H_2 and the higher to hydrocarbons and other compounds.[6,7,36] This is correctly reproduced by the simulations as we obtained 84% of selectivity towards H_2 for ethylene glycol and 72% for glycerol with the MK-LSR scheme.

We would like to summarize our present results to highlight their importance in further catalytic design. First of all, setting up a FAIR database accessible to other researchers, allowing its extension to consider lateral interactions, low-coordinated sites, other metals, and supports within the same computational framework. Second, the common nature of many elementary steps that can then easily be transferred, inherited, and expanded to investigate other reactions in the same metals, thus preventing repetitive computations. Third, the completeness in the decomposition path ensures that no intermediates/products are discarded as has been done in the literature, where many times only the selective path was identified, this would allow effective machine learning implementations as those in Ref. [37]. We hope that the standard set by the present approach is adopted by other practitioners in the field and accelerates the comparison of the catalytic properties of different materials and provides robust design guidelines from a accumulated databases.

Conclusions

We have investigated the complex reaction networks arising from the decomposition of ethanol and ethylene glycol on Cu, Ru, Pd, and Pt, through a multiscale method encompassing microkinetic modelling on the energies obtained through Density Functional Theory. To this end an open database has been set up to provide the most robust sets of Linear Scaling Relationships that allow the evaluation of different catalysts. With this scheme, activity, selectivity towards H_2 and stability under a variety of technical reforming conditions have been derived and compared to experiments. The present work paves the way towards an open, accessible, interoperable, and reusable database for simulations of catalytic properties that can speed up the identification of better performing catalysts in the transformation of biomass compounds.

Methods

The Density Functional Theory calculations were performed with the Vienna Ab-initio Simulation Package (VASP).[38,39] The functional of choice was PBE[40] and the van der Waals (vdW) contributions were obtained through the DFT-D2 method,[41,42] with our reparameterization of C_6 coefficients.[43] This setup has been proven to predict the experimental adsorption energies of several mono- and poly-alcohols accurately.[14] The inner electrons were represented by Projector-Augmented Wave pseudopotentials (PAW)[44,45] and the monoelectronic states were expanded in plane waves with a kinetic energy cutoff of 450 eV. Metal surfaces were modeled by a four-layers slab and at least $p(3 \times 3)$ supercells, where the two uppermost layers were fully relaxed and the rest fixed to the bulk distances. In the surface calculations, the Brillouin zone was sampled by a Γ-centred k-points mesh from the Monkhorst-Pack method,[46] and the k-point samplings were denser than 30 Å^{-1}. The vacuum between the slabs was at least 13 Å, and the adsorbates were placed only on one side of the slab and thus a dipole correction was applied to remove spurious contributions arising from this asymmetry.[47] The molecules were placed in a cubic box of 20 Å sides. Transition states were located by a combination of the Nudged Elastic Band and the Improved Dimer Methods.[48–50] In all cases, the nature of the saddle points was assessed by the diagonalization of

the numerical Hessian generated by 0.02 Å displacements for each coordinate. All TS structures have a single imaginary frequency. In all cases the optimization thresholds were 10^{-5} eV and 0.02 eV/Å for electronic and ionic relaxations, respectively. The decomposition reactions can be used to explore all the experimental conditions including water and oxygen effects as: (i) Water gas-shift related reactions are explicitly included in the reaction pool; (ii) O-assisted breaking C-H require higher energies than the C-H counterparts by 0.60-1.00 eV as shown in Table S6; (iii) Proton abstraction in alcohols by oxygen molecules is barrierless[28] on metals. In addition, the formulations of the catalyst are typically supported on carriers with acid/base characteristics[8] thus, when compared to experiments with active supports (Table 1), these reactions have been considered to occur on the support and to be barrierless. Finally, as for the water-assisted reactions two groups can be made: on unreactive metals the LSR are kept as shown by explicit/implicit continuum models,[28] Supplementary Information Figure S7; for reactive metals (Ru) hydroxyl groups are present render proton abstraction from the alcohols barrierless.[28, 51]

The microkinetic model explores hydrogen production on the closed packed surfaces of Cu, Ru, Pd, and Pt under four reaction conditions: DD at constant temperature, ATR, SR, and APR, which are presented in Fig. 1 and Table S1. The reason to chose the (111) surface ((0001) in the case of Ru) is because it presents the lowest energy surface and thus is more represented in the equilibrium structure of the active metal nanoparticles. Moreover, most of the catalyst preparation results in active nanoparticles larger than 5 nm in diameter.[22] In addition, choosing (111) presents the advantage that the cells are smaller than for other open surfaces, are easier to compare to previous computational data. Since our database is expandable, adding the results from low-coordinated sites, alloys, lateral effects, and carriers would be possible.[23, 24] The procedure, detailed in the Supplementary Information Section S1.2, can be summarized as follows: A stream containing the alcohol, water, and oxygen in variable proportions was fed into an isothermal differential reactor. The reactor operates in transient state and the initial coverages correspond to a clean surface, while the temperatures and pressures resemble typical experimental conditions. The adsorption rates were obtained from the Knudsen equation,[34] the rate coefficients from Transition

324   State Theory,[34] and the activation energies from DFT calculations. The mass balance

325   for each species "i" comes from the sum of rates "j" in which species "i" participates.

326   Site balance equation was also included. The system of ordinary differential equations

327   was solved in Maple.[52] A reaction was considered to reach a relevant stationary state

328   when the surface concentrations and reaction rates varied less than 0.01%/s.

References

[1] Corma, A., Iborra, S., and Velty, A. *Chem. Rev.* **107**(6), 2411–2502 (2007).

[2] Guo, N., Caratzoulas, S., Doren, D. J., Sandler, S. I., and Vlachos, D. G. *Energy Environ. Sci.* **5**(5), 6703–6716 (2012).

[3] Sutton, J. E., Guo, W., Katsoulakis, M. A., and Vlachos, D. G. *Nat. Chem.* **8**, 331–337 (2016).

[4] Deluga, G. A., Salge, J. R., Schmidt, L. D., and Verykios, X. E. *Science* **303**(5660), 993–997 (2004).

[5] Dauenhauer, P. J., Salge, J. R., and Schmidt, L. D. *J. Catal.* **244**(2), 238–247 (2006).

[6] Cortright, R. D., Davda, R. R., and Dumesic, J. A. *Nature* **418**(6901), 964–967 (2002).

[7] Huber, G. W., Shabaker, J. W., and Dumesic, J. A. *Science* **300**(5628), 2075–2077 (2003).

[8] Davda, R. R., Shabaker, J. W., Huber, G. W., Cortright, R. D., and Dumesic, J. A. *Appl. Catal. B* **43**(1), 13–26 (2003).

[9] Lin, L., Zhou, W., Gao, R., Yao, S., Zhang, X., Xu, W., Zheng, S., Jiang, Z., Yu, Q., Li, Y.-W., Shi, C., Wen, X.-D., and Ma, D. *Nature* **544**(7648), 80–83 (2017).

[10] Nørskov, J. K., Bligaard, T., Rossmeisl, J., and Christensen, C. H. *Nat. Chem.* **1**(1), 37–46 (2009).

[11] Sutton, J. E. and Vlachos, D. G. *Chem. Eng. Sci.* **121**, 190–199 (2015).

[12] Abild-Pedersen, F., Greeley, J., Studt, F., Rossmeisl, J., Munter, T. R., Moses, P. G., Skúlason, E., Bligaard, T., and Nørskov, J. K. *Phys. Rev. Lett.* **99**(1), 016105 (2007).

[13] Salciccioli, M., Chen, Y., and Vlachos, D. G. *J. Phys. Chem. C* **114**(47), 20155–20166 (2010).

355 [14] García-Muelas, R. and López, N. *J. Phys. Chem. C* **118**(31), 17531–17537 (2014).

356 [15] Ferrin, P., Simonetti, D., Kandoi, S., Kunkes, E., Dumesic, J. A., Nørskov, J. K.,
357   and Mavrikakis, M. *J. Am. Chem. Soc.* **131**(16), 5809–5815 (2009).

358 [16] Wang, S., Petzold, V., Tripkovic, V., Kleis, J., Howalt, J. G., Skúlason, E.,
359   Fernández, E. M., Hvolbæk, B., Jones, G., Toftelund, A., Falsig H, B. M., Studt,
360   F., Abild-Pedersen, F., Rossmeisl, J., Nørskov, J. K., and Bligaard, T. *Phys.*
361   *Chem. Chem. Phys.* **13**(46), 20760–20765 (2011).

362 [17] Wang, S., Temel, B., Shen, J., Jones, G., Grabow, L. C., Studt, F., Bligaard, T.,
363   Abild-Pedersen, F., Christensen, C. H., and Nørskov, J. K. *Catal. Lett.* **141**(3),
364   370–373 (2011).

365 [18] Wang, S., Vorotnikov, V., Sutton, J. E., and Vlachos, D. G. *ACS Catal.* **4**(2),
366   604–612 (2014).

367 [19] Zaffran, J., Michel, C., Auneau, F., Delbecq, F., and Sautet, P. *ACS Catal.* **4**(2),
368   464–468 (2014).

369 [20] Rangarajan, S., Brydon, R. R. O., Bhan, A., and Daoutidis, P. *Green Chem.*
370   **16**(2), 813–823 (2014).

371 [21] Zaffran, J., Michel, C., Delbecq, F., and Sautet, P. *J. Phys. Chem. C* **119**(23),
372   12988–12998 (2015).

373 [22] Basagiannis, A. C., Panagiotopoulou, P., and Verykios, X. E. *Top. Catal.* **51**(1-4),
374   2–12 (2008).

375 [23] Calle-Vallejo, F., Loffreda, D., Koper, M. T. M., and Sautet, P. *Nat. Chem.* **7**(5),
376   403–410 (2015).

377 [24] Calle-Vallejo, F., Tymoczko, J., Colic, V., Vu, Q. H., Pohl, M. D., Morgenstern,
378   K., Loffreda, D., Sautet, P., Schuhmann, W., and Bandarenka, A. S. *Science*
379   **350**(6257), 185–189 (2015).

380 [25] Álvarez-Moreno, M., De Graaf, C., López, N., Maseras, F., Poblet, J. M., and Bo,
381   C. *J. Chem. Inf. Model.* **55**(1), 95–103 (2014).

382   [26] Li, Q., García-Muelas, R., and López, N.

383   *http://dx.doi.org/10.19061/iochem-bd-1-37*

384   Embargoed link for rewievers:

385   *https://iochem-bd.iciq.es/browse/review-collection/100/2347/50e1ec03e8af71571cd3f664*.

386   [27] García-Muelas, R., Li, Q., and López, N. *ACS Catal.* **5**(2), 1027–1036 (2015).

387   [28] Garcia-Ratés, M., García-Muelas, R., and López, N. *J. Phys. Chem. C* **121**,
388   13803–13809 (2017).

389   [29] Jørgensen, M. and Grönbeck, H. *ACS Catal.* **6**(10), 6730–6738 (2016).

390   [30] Gattinoni, C. and Michaelides, A. *Surf. Sci. Rep.* **70**(3), 424–447 (2015).

391   [31] Vaidya, P. D. and Rodrigues, A. E. *Ind. Eng. Chem. Res.* **45**(19), 6614–6618
392   (2006).

393   [32] Sutton, J. E., Panagiotopoulou, P., Verykios, X. E., and Vlachos, D. G. *J. Phys.*
394   *Chem. C* **117**(9), 4691–4706 (2013).

395   [33] Ciambelli, P., Palma, V., and Ruggiero, A. *Appl. Catal., B* **96**(1), 190–197 (2010).

396   [34] Chorkendorff, I. and Niemantsverdriet, J. W. *Concepts of modern catalysis and*
397   *kinetics.* John Wiley & Sons, (2006).

398   [35] Hirai, T., Ikenaga, N.-o., Miyake, T., and Suzuki, T. *Energy & Fuels* **19**(4), 1761–
399   1762 (2005).

400   [36] Huber, G. W., Cortright, R. D., and Dumesic, J. A. *Angew. Chem. Int. Ed.*
401   **43**(12), 1549–1551 (2004).

402   [37] Ulissi, Z. W., Medford, A. J., Bligaard, T., and Nørskov, J. K. *Nat. Comm.* **8**,
403   14621 (2017).

404   [38] Kresse, G. and Furthmüller, J. *Comput. Mater. Sci.* **6**(1), 15–50 (1996).

405   [39] Kresse, G. and Furthmüller, J. *Phys. Rev. B* **54**(16), 11169–11186 (1996).

406   [40] Perdew, J. P., Burke, K., and Ernzerhof, M. *Phys. Rev. Lett.* **77**(18), 3865–3868
407   (1996).

408 [41] Grimme, S. *J. Comput. Chem.* **27**(15), 1787–1799 (2006).

409 [42] Bučko, T., Hafner, J., Lebegue, S., and Angyán, J. G. *J. Phys. Chem. A* **114**(43),
410   11814–11824 (2010).

411 [43] Almora-Barrios, N., Carchini, G., Błoński, P., and López, N. *J. Chem. Theory*
412   *Comput.* **10**(11), 5002–5009 (2014).

413 [44] Blöchl, P. E. *Phys. Rev. B* **50**(24), 17953–17979 (1994).

414 [45] Kresse, G. and Joubert, D. *Phys. Rev. B* **59**(3), 1758–1775 (1999).

415 [46] Monkhorst, H. J. and Pack, J. D. *Phys. Rev. B* **13**(12), 5188–5192 (1976).

416 [47] Makov, G. and Payne, M. C. *Phys. Rev. B* **51**, 4014–4022 (1995).

417 [48] Henkelman, G. and Jónsson, H. *J. Chem. Phys.* **113**(22), 9978–9985 (2000).

418 [49] Henkelman, G., Uberuaga, B. P., and Jónsson, H. *J. Chem. Phys.* **113**(22), 9901–
419   9904 (2000).

420 [50] Heyden, A., Bell, A. T., and Keil, F. J. *J. Chem. Phys.* **123**(22), 224101(1–14)
421   (2005).

422 [51] Bellarosa, L., García-Muelas, R., Revilla-López, G., and Lopez, N. *ACS Cent. Sci.*
423   **2**(2), 109–116 (2016).

424 [52] Waterloo Maple Inc. Waterloo, Ontario.

Acknowledgements

Author contributions

Q.L. and R.G.-M. performed the numerical calculations and contributed equaly to this work. N.L. supervised the project. All authors contributed to analyze the data and to write the manuscript.

Competing financial interest

The authors declare no competing financial interests.

Corresponding author

Correspondence to: Núria López. `nlopez@iciq.es`

Supplementary Information

Derivation of the equations, review of previous theoretical and experimental studies, detailed reaction networks, adsorption energies for all intermediates on Cu, Ru, Pd, and Pt, reaction and activation energies for all reactions, analysis of the energy profiles, scalings and analysis of stationary states. The structures of all intermediates and transition states can be downloaded from DOI: 10.19061/iochem-bd-1-37.[26]

Diversity at the Water−Metal Interface: Metal, Water Thickness, and Confinement Effects

Luca Bellarosa, Rodrigo García-Muelas, Guillem Revilla-López, and Núria López*

Institute of Chemical Research of Catalonia (ICIQ), The Barcelona Institute of Science and Technology, Av. Països Catalans 16, 43007 Tarragona, Spain

S Supporting Information

ABSTRACT: The structure and properties of water films in contact with metal surfaces are crucial to understand the chemical and electrochemical processes involved in energy-related technologies. The nature of thin water films on Pd, Pt, and Ru has been investigated by first-principles molecular dynamics to assess how the chemistry at the water−metal surface is responsible for the diversity in the behavior of the water layers closer to the metal. The characteristics of liquid water: the radial distribution functions, coordination, and fragment speciation appear only for unconfined water layers of a minimum of 1.4 nm thick. In addition, the water layer is denser in the region closest to the metal for Pd and Pt, where seven- and five-membered ring motifs appear. These patterns are identical to those identified by scanning tunneling microscopy for isolated water bilayers. On Ru densification at the interface is not observed, water dissociates, and protons and hydroxyl groups are locked at the surface. Therefore, the acid−base properties in the area close to the metal are not perturbed, in agreement with experiments, and the bulk water resembles an electric double layer. Confinement affects water making it closer to ice for both structural and dynamic properties, thus being responsible for the higher viscosity experimentally found at the nanoscale. All these contributions modify the solvation of reactants and products at the water−metal interface and will affect the catalytic and electrocatalytic properties of the surface.
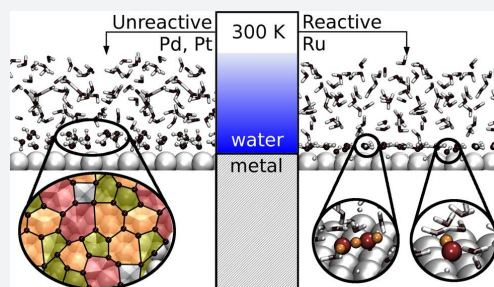
INTRODUCTION

Water surface interactions are ubiquitous in chemistry, physics, materials, and planetary sciences and for the development of life itself. A better knowledge of the water−metal structure will enable us to tackle the energy challenges that lie ahead of us,[1] as this interface is key to control the electrochemical[2] and chemical[3] processes that will generate the future energy vectors by transforming inactive molecules into fuels and back to energy with the lowest possible losses. The description of the water−metal interface relies mainly on the classical models describing electric double layer that goes back to the studies by Helmholtz. Only recently have molecular studies reached enough accuracy to present an increasingly detailed analysis of low-coverage structures formed at the interface between water and the metal by scanning tunneling microscopy (STM) and density functional theory (DFT).[1,4] Still, the nature, structure, and dynamics of water on metal surfaces and the emergence of liquid-like behavior are far from being understood.

Water is among the most studied and yet most complex compounds as both solid and liquid states present multiple phases. Three main features differentiate water phases: the density, the atom−pair radial distribution function, and the oxygen coordination shell.[5] Rearrangements in the water coordination shell and the topological ring structure have been taken as suitable descriptors for the liquid to ice

transition.[6] The ice density at 273 K is 0.934 g cm^{-3}, the X-ray diffraction gives peaks in oxygen−oxygen radial distribution function at 2.8, 3.5, and 4.5 Å,[7] and each oxygen is characterized by an ideal tetrahedrality. Both I$_h$ and XI forms of ice, the common ones at atmospheric pressure, share these features. In contrast, the structure of liquid water still faces important challenges.[6,8−10] The most popular interpretation of the macroscopic state of liquid water is that it is constituted by a complex mixture[11] of two microscopic domains in variable proportions.[12,13] At room temperature the minor domain, low density liquid (LDL), corresponds to an enthalpy-favored tetrahedral arrangement where water molecules are four-fold coordinated. The LDL arrangement is fairly similar to hexagonal I$_h$ both regarding the atomic coordination and the presence of two different distances: the direct chemical O−H bond at 1.0 Å and the hydrogen bond at 1.8 Å. This structure is very rigid resulting in a small entropic contribution. In turn, the major domain, high density liquid (HDL) is characterized by a lower number of hydrogen bonds with weakened strength.[5] The thermodynamic penalties of lesser H-bonds are counterbalanced by the higher entropy associated with a larger fraction of free librational modes. Therefore, in the HDL microstructure
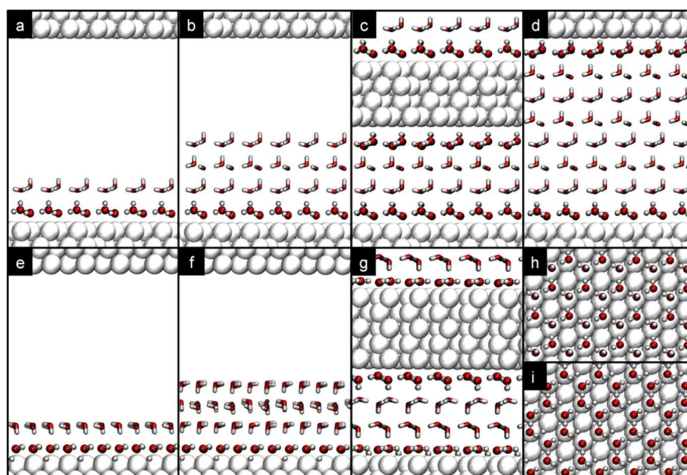
Research Article

Figure 1. Models employed for the adsorption of *N*-water bilayers on closed packed M = Pd, Pt, and Ru metal surfaces. Longitudinal views of systems for MN systems: Pd and Pt: two (four) free bilayers Pd2, Pt2 in a (Pd4, Pt4 in b), four (eight) confined bilayers Pd4c, Pt4c in c (and Pd8c, Pt8c in d). Equivalent systems are shown for Ru(0001): Ru2 in e, Ru4 in f, and Ru4c in g. Axial views for ice-like adsorbed Pd/Pt in h, and Ru in i. Metal, oxygen, and hydrogen atoms are represented by white, red, and black spheres; bulk water is shown as sticks, respectively.

water molecules present a fraction of trihedral, instead of tetrahedral, arrangements. The experimental detection of density fluctuations in the bulk liquid is limited to around 1 nm.[13] The macroscopic features of liquid water at around room temperature are (i) the presence of a peak in O–O radial distribution function (RDF) around 2.8–2.9 and a plateau at 4.5 Å, corresponding to first and second coordination spheres in LDL; (ii) and only a single peak between 2.8 and 2.9 for HDL.[7,14,15] LDL has been claimed to be responsible for ice nucleation due to slow dynamics[6] and strong bond directionality.[16] The tetrahedrality (*q*) of oxygen in water is between the limiting values of the ideal LDL 1.00 and that of the isolated water value 0.75.

The water–metal interface, at room temperature, is expected to show intermediate features between those of the ordered bilayer or ice structures[1] and the labile bulk water.[7,15,17] STM experiments and complementary DFT-based simulations have provided accurate descriptions for the first wetting layer,[1] but extensions to multiple layers exist.[18,19] Notice that several of these studies are devoted to the study of ice and its nucleation,[15] and many of the experiments were performed at low temperatures. These studies have shown different degrees of wettability on metals[1,18] and the ability of some of them, like Ru, to split water into hydroxides and protons.[20] This feature adds more structural complexity to the interface. Theoretical simulations hold the key to understand the nature of the boundary between water and metals. For extended water–metal systems early molecular dynamics (MD) simulations have highlighted the need for dispersion interactions in the simulations,[21,22] and when those are included then it is possible to explain subtle details such as the structural changes for water adsorbed on gold associated with the decrease in the fraction of flat and planar molecules at the interface.[23] In addition, classical simulations, have identified the hydrophobic character of water on Pt,[24] and the role of extended time and size dynamics in water exchange close to Pt.[25−27] Unfortunately, such long time and length scales are not accessible by ab initio simulations, and

classical MD cannot address the properties on reactive surfaces like Ru. Thus, only with ab initio MD it is possible to understand how the chemistry at the surface induces different interfacial water–metal structures.

In the present work, we have employed first-principles Born–Oppenheimer molecular dynamics (BOMD) to unravel the intimate structure of the interface between water and different metals typically employed as electrodes or catalyst (Pd, Pt, and Ru) driven by the water reactivity at the interface in their most common surface and identify the differences between confined and free-standing water layers of different thickness, ranging from 4 to 16 water layers (6−24 Å width). The ultimate goal is to (i) define the minimum amount of water on a metal surface for which liquid-like features appear, (ii) illustrate the differences between metals, (iii) highlight how the interfaces will affect the catalytic properties of the metals, and (iv) identify the differences induced by confinement of the water structures.

RESULTS AND DISCUSSION

BOMD simulations for adsorption of water on metals were carried out for at least 11 ps at 300 K with 1 fs as the time step. The model systems investigated present a $3\sqrt{3} \times 3\sqrt{3} - R30°$ metal surface slabs where different water slabs following the ice structure with an H-down configuration are added. The structures were labeled as MN(c) where M states for the metal surface, N is the number of water bilayers and (c) indicates that the water slab is confined. For Ru(0001) dissociation of 50% of the water molecules adsorbed on the surface was taken as the initial configuration.[20] A schematic representation of the models can be found in Figure 1. Movies for the trajectories (Pd4, Ru4, and Pt4) are available as Supporting Information.

We start by analyzing the most general features, like density and radial distribution function, and then move to more atomistically detailed terms as the local coordination of the

oxygen atoms described by the tetrahedrality (q) and speciation of fragments for the reactive Ru(0001) surface. Notice that these parameters taken one by one are not conclusive, but instead the full toolbox presented here is complementary and describes the landscape in a detailed manner, as already discussed in refs 28 and 29. The final aim is to assess when these properties start to correspond to those of the liquid water, described in terms of both HDL and LDL contributions. In all simulations, no evaporation is observed; i.e., no molecule stays freely in the vacuum region. The water density (see Supporting Information for the definition) in our models is 0.95−1.06 g cm^{-3} for unconfined systems and 0.88−1.07 g cm^{-3} for the confined ones. This demonstrates that there is not a significant effect from the use of PBE-D or the lack of continuity of water in the MN models. However, we have observed that some water molecules might displace from the average z-position in the vacuum configurations. This agrees with the displacements observed by Michaelides and van de Vondele for the outermost water molecules in an ice slab.[30]

As for the analysis, we start from the most general patterns, like the radial distribution functions and then evaluate more microscopic features. The radial distribution function for oxygen, $g_{O-O}(r)$, averaged for the last 2 ps of simulation is presented together with available experiments of bulk ice, 122 K, and water, 298 K, at 0.1 MPa,[7,31] in Figure 2. All the water molecules were considered, and although the frontier (with the surface or the vacuum) might present a different behavior, we consider that this is meaningful when trying to establish the perturbations induced by the interfaces. Complementary g_{O-H}
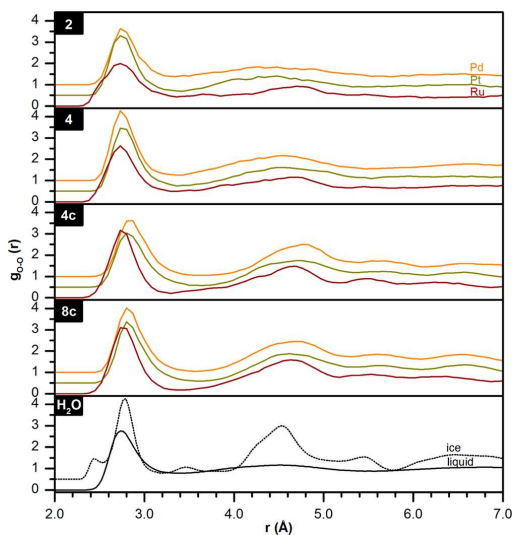

Figure 2. Radial oxygen−oxygen distribution function, $g_{O-O}(r)$, for the water molecules in the multilayers adsorbed on Pd (orange), Pt (dark yellow), and Ru (wine) metal (M) surfaces, for the confined M4c, M8c and unconfined M2, M4 unconfined water slabs. Experimental data for liquid (water 298 K and 0.1 MPa solid black)[31] and ice (122 K dashed black)[7] are shown for comparison (g_{O-H} and g_{H-H} can be found in Figure S.I. 9−10). The comparison between the computed and the experimental liquid results can be found in the Supporting Information Figure S.I. 11.

and g_{H-H} are presented and compared to a slab of ice following that in ref 30 in Figure S.I. 9−10. The results for Pd and Pt parallel each other provided that the same N-bilayer is compared. For both the 2-bilayer does not present the characteristic long-distance peak due to the small size of the model. In turn, M4 shows a first peak around 2.80 Å and a wide region at about 4.5 Å with a higher radial distribution value but very broad. The lack of clear signals at high distances hints to only one defined coordination sphere, typical of HDL structures. On the other side, the confined systems M4c and M8c show a second broader but clear peak at 4.8 Å, as well as weaker coordination spheres at 5.8 and 6.6 Å. The case of Ru(0001) is peculiar, because it displays a wide peak at 2.8 Å, starting at rather short distances. This shape is an indicator of a plethora of configurations where oxygen atoms accommodate around each other in different ways as a consequence of water dissociation on Ru. Again the Ru4 model is closer to the g_{O-O} liquid water pattern than the confined ones.

From the differences between the experimentally retrieved values[31] and the results we obtained with the different models it is possible to identify that a minimum water thickness of four bilayers, 1.4 nm, is needed to retrieve the complex interplay between high and low density liquid features characteristic of liquid water. This agrees with the correlation regime of 1 nm reported in the experiments.[12] Instead confined water slabs even if much thicker show a low density structure LDL domain after 11 ps. As a consequence in the following we will mainly center on the analysis of the M4 models, retrieving the results from the other models when required only and reporting in the Supporting Information the rest of the results.

The second step is to characterize the coordination sphere of each water molecule in the slab along the BOMD trajectories. To inspect the HDL−LDL water domains we have mapped the H-related tetrahedrality (q) for each oxygen with respect to its four nearest neighboring hydrogen atoms, following the equation by Chau and Hardwick,[32]

$$q = 1 - \frac{3}{32} \sum_{j=1}^{3} \sum_{k=j+1}^{4} \left(\hat{r}_j \circ \hat{r}_k + \frac{1}{3} \right)^2 \tag{1}$$

where r_j is the positions of the oxygen atoms in the j-molecule; see Supporting Information, Section 1.2 for further details and tests. With this definition $q = 1$ corresponds to a fully tetrahedral oxygen environment (LDL-like), while lower values, close to 0.84 and lower indicate less ordered structures (see right column in Figure 3). The time evolution of the tetrahedrality index for each molecule in M4 models along the simulation time is shown in Figure 3a−c. The molecules were assigned to a layer according to their initial ($t = 0$ ps) z-positions. Darker colors indicate higher coordination. The accumulated values for all molecules during the entire simulation are presented in Figure 3d−f. The layer decomposition can be found in the Supporting Information, Figure S.I. 15. In these panels the results from the equivalent four bilayer confined slab are presented for comparison (black line). Additional values for all the other systems are reported in Figure S.I. 12−13.

We start the analysis by the water−vacuum termination (fourth layer) and then go deep into the water layers down to the interface (top block in each panel). Because of the presence of the vacuum roughly 1:3 on the top bilayer has a trihedral configuration. The central second and third layers present subtle changes indicative of a fast and more labile environment.
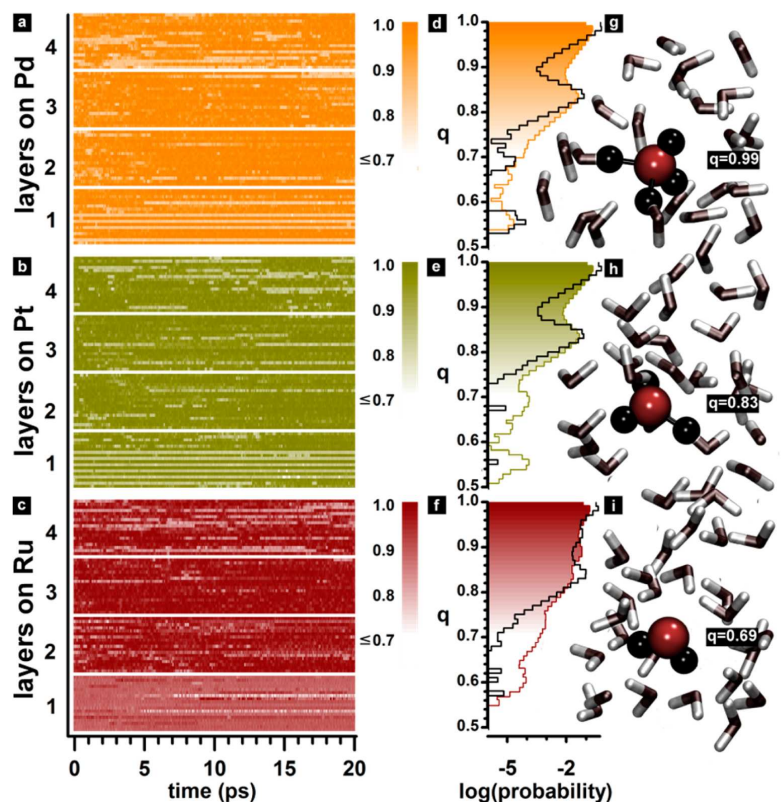
Research Article

Figure 3. Left panel: tetrahedrality evolution for each of the water molecules in the slab as a function of time: (a) Pd4, (b) Pt4, and (c) Ru4 models. Darker colors stand for tetrahedral coordination. Central panel: cumulative tetrahedrality index (all simulation time and all molecules) shown as normalized histogram for the unconfined (color) referenced to the corresponding confined (black). Right panel, local water configuration environments: tetrahedral (top), trihedral (middle), and dicoordinated (bottom). Complementary figures can be found in the Supporting Information Figure S.I. 12−14.

After the dynamics, a large fraction of the water molecules still preserve the full tetrahedrality, thus pointing toward an LDL-like behavior. However, the accumulated index in Figure 3d−f indicates that a significant amount have reduced their tetrahedrality to ca. 0.84. Indeed, the fraction of trihedral oxygens remained 14% in the bulk layers. Regarding the Pd- or Pt-water interfacial bilayer the light-colored areas forming long stripes of low tetrahedrality along the simulation time correspond to flat water molecules where the oxygen atoms were originally coordinated to the surface that reorient to be more in contact with the bulk water molecules. This agrees with the recent work that indicates that 49% of the water molecules on the interface with Au(111) lie flat.[23]

In comparison, the accumulated q index for the confined system, marked by the black line in Figure 3d−f, shows that confinement induces a much higher amount of tetrahedral molecules. The scarcity of trihedral oxygens in confined configurations is confirmed with the 8c models, Figure S.I. 12. The few trihedral molecules that appear in the confined mode revert to their tetrahedral environments in less than 0.5 ps. Therefore, all these four structures, Pd4c, Pd8c, Pt4c, Pt8c, keep their high-ordered ice-like structures during the whole

trajectory. This discards confined systems for the theoretical modeling of a bulk water−metal (electrode-like) interface since they show induced rigidity and absence of HDL-like features. In addition, previous studies have assigned larger water viscosity[33,34] to an increase of the average tetrahedrality index. Our results would indicate that confined systems are more rigid and viscous in agreement with experimental results on confined water layers that have reported a more viscous liquid at the nanoscale[35] and proposed to exhibit improved electrocatalytic properties from static theoretical methods[36] (only ligand effects without dynamics were taken into account).

For Ru, the bulk layers are slightly more compact than their Pd and Pt counterparts in agreement with the observation that the first bilayer on Ru is hydrophobic.[18] From our simulations, the main reason is that water dissociation at the interface perturbs the layers on top of it. This is very clearly seen in Figure 3a−c; the interface layer is mainly formed by alternate dark/light colors for Pd and Pt, while the structure at the Ru interface is more homogeneous and the coordination pattern darker, which are indicative of values closer to 1. For instance, the second bilayer shows an average coordination shell smaller than the ideal liquid value. Indeed, around 35% of the water
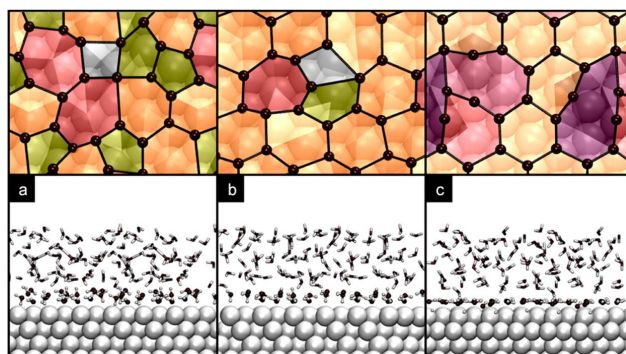
Figure 4. Longitudinal views of water layer closest to the metal surface in the BOMD simulations for the Pd4 (a), Pt4 (b), and Ru4 (c). The axial projection shown in the top indicates the local motifs in which the first layer water molecules coordinate to each other as tessellations (Voronoi-like) following the color code: 4,5,6,7-member cycles in gray; dark yellow, orange, wine, and larger in purple darker colors. Metal, oxygen, and hydrogen atoms are represented by white spheres and gray sticks in the longitudinal views. Hydrogen atoms are hidden in the axial projection.
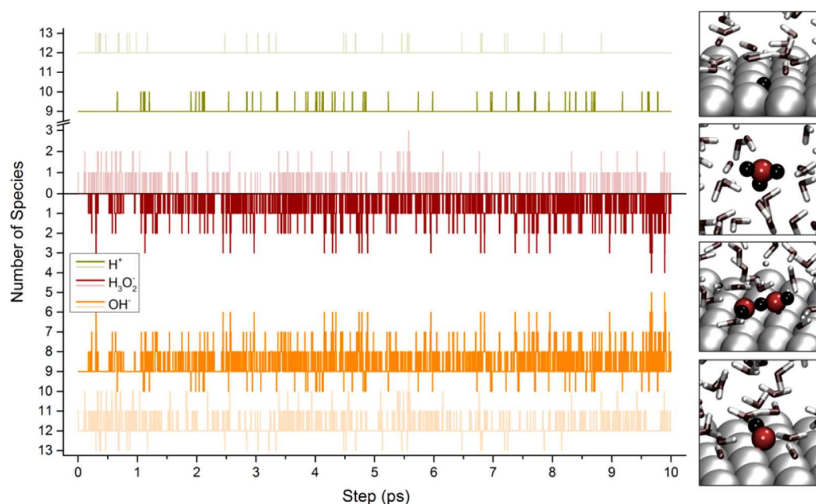

Figure 5. Most common ionic species resulting from the interaction of water with Ru(0001) surfaces found during the 10 ps of the MD. Free standing Ru4 (bright colors) and confined Ru4c (pale colors) are shown for comparison. Isolated protons H^+ are reported in dark yellow, whereas anions are in shown in wine (OH^-) and orange ($H_3O_2^-$). H_3O^+ species are seldom observed during the simulation. The local configurations for each of these ions are shown on the right.

molecules present a non-tetrahedral arrangement, q values closer to HDL. In turn, the third bilayer is slightly more rigid showing higher q and LDL-like features. This structure of alternated regions with different characteristics is reminiscent of the electrical double layer.

To further understand the nature of the interface we have inspected the interfacial bilayer that is in contact with the surface by analyzing the topology of the water rings. Once the initial hexagonal symmetry is thermally relaxed the structures at the interface might display unusual water motifs. These rings have been identified through the visual inspection of the last 2 ps of the dynamics on Pd4, Pt4, and Ru4, and are exemplified by the last configuration analyzed in Figure 4. Pd and Pt effectively increase the water interfacial coverage to 0.74 and 0.70 ML; this is 20 (two more molecules) and 19 (one more), respectively. This densification occurs in the very early stages of the simulation, during equilibration, and once it occurs the z-displacement of these molecules is within 2 Å; see Supporting Information Figure S.I. 14. Note that although the lattice employed in the present work, $3\sqrt{3} \times 3\sqrt{3} - R30°$ and that reported in experiments, $\sqrt{37} \times \sqrt{37} - R29.5°$, are not commensurate, our simulations are able to retrieve both (i) the higher water coverage at the interface and (ii) the multiple motifs present. For Pd and Pt the interface water layer breaks the hexagonal lattice yielding a tessellation that includes five-, six-, and seven-membered rings. Some kind of smaller, severely distorted, arrangements appear as well. Similar structures, in particular the 6−5−7 linked patterns, have been experimentally identified when increasing coverage from ice,[37] or in water bilayers[38] on Pt, and they are theoretically predicted for Pd.[39]

ACS Central Science

This is in contrast with previous first-principles dynamics simulations due to the geometry constraints (very small lateral size) employed.[22]

The situation is completely different for Ru(0001) where the hexagonal lattice is less disrupted. In Figure 4c the surface hydroxyls attract one of the water molecules belonging to the adlayer bending the hexagonal pattern. The ultimate consequence is that large pseudo-rings with missing units appear. For instance in Figure 4c an open water hexagon (one monomer missing) and an open nine-membered cycle are identified. This patch is surrounded by mostly regular hexagonal cycles thanks to the higher binding strength of the half-dissociated water layer.

In summary, the local structure at the water−metal interface, i.e., within 5 Å, is denser and contains unusual coordination patterns for metals like Pt and Pd. In contrast, for Ru the structure at the interface keeps the hexagonal arrangement without showing any density fluctuations in the vicinity of the metal. These terms will affect the solvation sphere and how the solvent surrounding reactants and products will need to rearrange to reach the surface active site. According to Marcus theories these solvent redistributions are crucial to explain the rates of electron transfer processes.

Compared to recent results in the literature we have found some differences. For instance, the coordination patterns for water molecules at the interfaces do not retrieve five- or seven-membered rings, and mainly on-top adsorption is observed for all water molecules on Pt(111) with classical MD.[24] A similar effect together with a large fraction of flat water molecules at the interface was reported by Cao et al. when illustrating proton diffusion by reactive force fields.[25] Both effects can be caused by a too strong directionality and the strength of the water−metal bond interaction in the force fields. Extrapolation of the classical MD behavior of Pt(111) to other surfaces was suggested,[24] but our results for Ru show that for reactive surfaces the chemistry at the interface dominates. Our results are also in line with recent first-principles MD simulations,[22] performed for Pd(111) that illustrated the need for dispersion and large unit cells with a large number of water molecules. Moreover, we reinforce the need for large lateral cells to retrieve the interfacial water patterns.

A final aspect that requires attention is the study of the fragments that appear in the simulations for the water interface on Ru(0001). In static simulations and for STM images at low coverages it is normally found that at the first bilayer the number of dissociated water molecules is close to 50%.[20] Recent simulations have described the water/Ru(0001) phase diagram showing a wide range of configurations that include hydroxyl/water and hydride domains.[40] However, in larger water thicknesses the question regarding the number of ions and their mobility once formed at the interface has not been addressed. Results are reported in Figure 5 for the systems Ru4 and Ru4c. Ru2 shows similar patterns to Ru4, and thus it is only presented in Figure S.I. 8 together with more details on the computational settings.

The species identified during the simulations are isolated adsorbed protons, hydronia in the liquid, adsorbed hydroxides, and $H_3O_2^-$. Others, like the water clusters H_4O_2 and H_6O_3, have been observed, but their lifetime is very short (below 4 fs behave as transient species) and represent less than 0.01% of the total simulation time. Therefore, they have not been further considered. All the isolated H atoms (dark yellow lines in Figure 5) are adsorbed on the metal surface; they do not sink

into the metal or are released to the surrounding bulk of water, and the total number was constant during the run. This agrees with the tritration experiments showing that the solvent pH is preserved in the close contact of Ru electrodes.[41] Thus, they are uncorrelated to H_3O^+ species which only have been observed in the bulk and for very short periods of 3 fs (that actually do not enable us to fully identify them as nontransient species). In turn, the hydroxides left on the surface interact with the closest water molecule, forming $H_3O_2^-$ species via a shared H that shuttles to and from the two oxygen atoms. Thus, these structures oscillate from a pure $H_3O_2^-$ with one H exactly in the middle between the two oxygens, to polarized H_2O and OH^- fragments. This interconversion is reflected in Figure 5 by the trend of the $H_3O_2^-$ species (orange) that almost perfectly mirror the OH^- lines (wine). The $H_3O_2^-$ species is quite common, counting around 350 times over 1 ps.

The same fragments have also been identified in the confined Ru4c model. The presence of two surfaces in contact with the water slab increases the number of ionic species as three more water molecules were split on the upper surface. Whereas unconfined systems confirm the stability of the half dissociated layer configuration (0.50 dissociated water/Ru), in confined ones this ratio is sensibly decreased (0.33 dissociated water counting both surfaces/Ru). However, Ru4c is less dynamic than Ru4: the frequency of water splitting and reforming is much smaller than for Ru4 (13.3 ps^{-1} for the protons in Ru4 versus 7.9 ps^{-1} for Ru4c). This is due to the more ice-like structure of confined systems that let a minor number of rearrangements occur. Therefore, confined systems present differences regarding the number and dynamics of the ions at the interface and thus can be explored in an alternative way to benefit from these results of impeded mobility and transport again adding an extra contribution to the impeded mobility responsible for high viscosity.[35]

In summary, the species formed at the surface stay there and are not transferred to the bulk liquid. Thus, reactants need to reach the surface to interact with acid or basic species anchored there.

CONCLUSIONS

Simulations hold the key for the understanding of the water structure at the interface with metals, and the complex behavior including different time and length scale phenomena requires different computational approaches. The reactivity of water molecules on the surface has a large impact on the structure of the region in close contact with the metal. This phenomenon can only be observed through ab initio MD simulations. With this computational tool and analyzing the radial distribution function, tetrahedrality, interfacial configuration, and relevant fragments we have shown that the water−metal interface is different for reactive and more noble metals. At the interface between water and Pd and Pt structural patterns of five- and seven-membered rings are identified resulting in the densification of the water interface layer close to the surface. The patterns that were identified in surface science studies' for the first wetting layer are thus also present under water-thick conditions. Dissociation only occurs on Ru as a consequence of the electronic structure of this reactive surface; we have found the fraction of dissociated molecules and again this is in good agreement with the values reported from dissociation of the bilayer.[20] Water dissociation on Ru does not imply the acidification of the surrounding interfacial water layer as protons and hydroxyls are bound to the surface, in agreement

ACS Central Science

with experimental observations.[41] These differences will severely affect the transport of active species from the bulk solvent to the surface where chemical and electrochemical reactions take place. Finally, we have observed that in order to retrieve the main characteristics of liquid water a minimum of four water bilayers (1.4 nm) interleaved by vacuum are required. The confinement induced by sandwiched configurations reduces the mobility of the layer, and this has important implications in the viscosity.[35] The present results identify new key contributions that are fundamental to reach an atomistic understanding and control of chemical, electrochemical, and photoelectrochemical processes.

METHODS

The metal surfaces were modeled with slabs of four (Pd and Pt(111)) and five metal layers for Ru(0001) and a $3\sqrt{3} \times 3\sqrt{3} - R30°$ supercell. A multilayered proton-ordered form of hexagonal ice, ice XI,[42] was adsorbed on top. The different models systems were labeled in terms of the metal, M, number of water bilayers, N, and confinement, c, MN(c) shown in Figure 1. The single water bilayer corresponding to 18 water molecules (0.67 ML) is found to be more stable in H-down configurations. However, when growing multiple layers the H-down configurations for Pd and Pt turn in 500 ps of simulation to H-up ones. This agrees with the experimental observation that water layers reorient to form the water-tetrahedral structure. Thus, the simplest model considered in the present work, is the N = 2 double bilayer (coverage 1.33 ML), 36 water molecules in H-up configurations for Pd and Pt and the H-down for Ru, with a vacuum larger than 10 Å, Figure 1a,e. By replicating the double bilayer, larger coverages of 2.67 ML (N = 4) can be retrieved (72 water molecules) and were prepared both free (10 Å vacuum) and confined, Figure 1b,f and 1c,g. For Pt and Pd a thicker water slab with 144 water molecules (5.33 ML, (8)) in the confined mode was studied, Figure 1d.

DFT calculations were carried out with the Vienna Ab initio Simulation Package VASP.[43,44] Core electrons were described using the projector-augmented-wave PAW formalism.[45] The plane-wave set contained components with energies up to 450 eV. The Perdew, Burke, and Ernzerhof (PBE) functional was used.[46] Dispersion energies were accounted for by the semiempirical DFT-D2 potential with modified coefficients for the surface.[47,48] With this setup the density of water is slightly overestimated. For the unconfined systems we have investigated whether the presence of the vacuum boundary induces a tetragonal distortion to relax the density, and we have found that this is not the case; see Supporting Information. The threshold for electronic convergence was set to 10^{-6} eV. All initial configurations were relaxed until the forces acting on water atoms were lower than 25 meV/Å. These relaxed structures were taken as input for 11 ps BOMD in the NVT ensemble at 300 K controlled by a Nosé–Hoover thermostat.[49,50] The computational setting of BOMD was simplified to a gamma-only k-point sampling and a cutoff energy of 400 eV. The initial 1 ps of the run was taken as equilibration, leaving 10 ps of productive run with 1 ps as time step. Test with shorter time steps demonstrate no difference in the parameters investigated Supporting Information Section 2.2. For systems comprising four unconfined water bilayers a larger run was performed. In that case, the equilibration time was 4 ps, and productive dynamics were extended up to 20 ps. Extensive tests done for the structural properties: radial distribution function

plotted similarly to ref 51 and tetrahedrality show that the features obtained with the present simulations are maintained if improving the k-point sampling; see Supporting Information Section 2.1.

ASSOCIATED CONTENT

Ⓢ Supporting Information

The Supporting Information is available free of charge on the ACS Publications website at DOI: 10.1021/acscentsci.5b00349. The xyz files after 1 ps can be inspected in DOI: 10.19061/iochem-bd-1-1.

> The mathematical definitions, convergence test, and results for all the water–metal models (PDF)
> Movies for BOMD trajectories are also available as separate files (Pd4, Ru4, and Pt4)

AUTHOR INFORMATION

Corresponding Author
*E-mail: nlopez@iciq.es.

Notes
The authors declare no competing financial interest.

ACKNOWLEDGMENTS

REFERENCES

(1) Carrasco, J.; Hodgson, A.; Michaelides, A. A molecular perspective of water at metal interfaces. *Nat. Mater.* **2012**, *11*, 667–674.

(2) Nørskov, J. K.; Bligaard, T.; Rossmeisl, J.; Christensen, C. H. Towards the computational design of solid catalysts. *Nat. Chem.* **2009**, *1*, 37–46.

(3) Zope, B. N.; Hibbitts, D. D.; Neurock, M.; Davis, R. J. Reactivity of the Gold/Water Interface During Selective Oxidation Catalysis. *Science* **2010**, *330*, 74–78.

(4) Tatarkhanov, M.; Ogletree, D. F.; Rose, F.; Mitsui, T.; Fomin, E.; Maier, S.; Rose, M.; Cerdá, J. I.; Salmeron, M. Metal– and hydrogen–bonding competition during water adsorption on Pd(111) and Ru(0001). *J. Am. Chem. Soc.* **2009**, *131*, 18425–18434.

(5) Soper, A. K.; Ricci, M. A. Structures of high–density and low–density water. *Phys. Rev. Lett.* **2000**, *84*, 2881.

(6) Palmer, J. C.; Martelli, F.; Liu, Y.; Car, R.; Panagiotopoulos, A. Z.; Debenedetti, P. G. Metastable liquid–liquid transition in a molecular model of water. *Nature* **2014**, *510*, 385–388.

(7) Soper, A. K. The radial distribution functions of water and ice from 220 to 673 K and at pressures up to 400 MPa. *Chem. Phys.* **2000**, *258*, 121–137.

(8) Nilsson, A.; Pettersson, L. G. M. The structural origin of anomalous properties of liquid water. *Nat. Commun.* **2015**, *6*, 8998.

(9) Chandler, D. *Illusions of phase coexistence.* arXiv:1407.6854.

(10) Johari, G. P.; Teixeira, J. Thermodynamic analysis of the two–liquid model for anomalies of water, HDL–LDL fluctuations, and liquid–liquid transition. *J. Phys. Chem. B* **2015**, *119*, 14210–14220.

(11) Bernal, J. D.; Fowler, R. H. A Theory of Water and Ionic Solution, with Particular Reference to Hydrogen and Hydroxyl Ions. *J. Chem. Phys.* **1933**, *1*, 515.

(12) Nilsson, A.; Pettersson, L. G. M. Perspective on the structure of liquid water. *Chem. Phys.* **2011**, *389*, 1–34.

(13) Huang, C.; Wikfeldt, K. T.; Tokushima, T.; Nordlund, D.; Harada, Y.; Bergmann, U.; Niebuhr, M.; Weiss, T. M.; Horikawa, Y.; Leetmaa, M.; Ljungberg, M. P.; Takahashi, O.; Lenz, A.; Ojamäe, L.;

ACS Central Science

Lyubartsev, A. P.; Shin, S.; Pettersson, L. G. M.; Nilsson, A. The inhomogeneous structure of water at ambient conditions. *Proc. Natl. Acad. Sci. U. S. A.* **2009**, *106*, 15214−15218.

(14) Venkatesh, C. G.; Rice, S. A.; Narten, A. H. Amorphous Solid Water: An X−ray Diffraction Study. *Science* **1974**, *186*, 927−928.

(15) Sellberg, J. A.; Huang, C.; McQueen, T. A.; Loh, N. D.; Laksmono, H.; Schlesinger, D.; Sierra, R. G.; Nordlund, D.; Hampton, C. Y.; Starodub, D.; DePonte, D. P.; Beye, M.; Chen, C.; Martin, A. V.; Barty, A.; Wikfeldt, K. T.; Weiss, T. M.; Caronna, C.; Feldkamp, J.; Skinner, L. B.; Seibert, M. M.; Messerschmidt, M.; Williams, G. J.; Boutet, S.; Pettersson, L. G. M.; Bogan, M. J.; Nilsson, A. Ultrafast X−ray probing of water structure below the homogeneous ice nucleation temperature. *Nature* **2014**, *510*, 381−384.

(16) Smallenburg, F.; Filion, L.; Sciortino, F. Erasing no−man's land by thermodynamically stabilizing the liquid−liquid transition in tetrahedral particles. *Nat. Phys.* **2014**, *10*, 653−657.

(17) Wikfeldt, K. T.; Nilsson, A.; Pettersson, L. G. M. Spatially inhomogeneous bimodal inherent structure of simulated liquid water. *Phys. Chem. Chem. Phys.* **2011**, *13*, 19918−19924.

(18) Haq, S.; Hodgson, A. Multilayer Growth and Wetting of Ru(0001). *J. Phys. Chem. C* **2007**, *111*, 5946−5953.

(19) Schnur, S.; Groß, A. Properties of metal−water interfaces studied from first principles. *New J. Phys.* **2009**, *11*, 125003.

(20) Feibelman, P. J. Partial Dissociation of Water on Ru(0001). *Science* **2002**, *295*, 99−102.

(21) Møgelhøj, A.; Kelkkanen, A. K.; Wikfeldt, K. T.; Schiøtz, J.; Mortensen, J. J.; Pettersson, L. G. M.; Lundqvist, B. I.; Jacobsen, K. W.; Nilsson, A.; Nørskov, J. K. Ab Initio van der Waals Interactions in Simulations of Water Alter Structure from Mainly Tetrahedral to High−Density−Like. *J. Phys. Chem. B* **2011**, *115*, 14149−14160.

(22) Pedroza, L. S.; Poissier, A.; Fernández-Serra, M.−V. Local order of liquid water at metallic electrode surfaces. *J. Chem. Phys.* **2015**, *142*, 034706.

(23) Velasco-Velez, J. J.; Wu, C. H.; Pascal, T. A.; Wan, L. F.; Guo, J.; Prendergast, D.; Salmeron, M. Interfacial water. The structure of interfacial water on gold electrodes studied by x−ray absorption spectroscopy. *Science* **2014**, *346*, 831−814.

(24) Limmer, D. T.; Willard, A. P.; Madden, P.; Chandler, D. Hydration of metal surfaces can be dynamically heterogeneous and hydrophobic. *Proc. Natl. Acad. Sci. U. S. A.* **2013**, *110*, 4200−4205.

(25) Willard, A. P.; Limmer, D. T.; Madden, P. A.; Chandler, D. Characterizing heterogeneous dynamics at hydrated electrode surfaces. *J. Chem. Phys.* **2013**, *138*, 184702.

(26) Cao, Z. M.; Kumar, R.; Peng, Y.; Voth, G. A. Hydrated proton structure and diffusion at platinum surfaces. *J. Phys. Chem. C* **2015**, *119*, 14675−14682.

(27) Limmer, D. T.; Willard, A. P.; Madden, P. A.; Chandler, D. Water exchange at hydrated platinum electrode is rare and collective. *J. Phys. Chem. C* **2015**, *119*, 24016−24024.

(28) Limmer, D. T.; Chandler, D. The putative liquid−liquid transition is a liquid−solid transition in atomistic models of water I. *J. Chem. Phys.* **2011**, *135*, 134503.

(29) Limmer, D. T.; Chandler, D. The putative liquid−liquid transition is a liquid−solid transition in atomistic models of water II. *J. Chem. Phys.* **2013**, *138*, 214504.

(30) Watkins, M.; Pan, D.; Wang, E. G.; Michaelides, A.; VandeVondele, J.; Slater, B. Large variation of vacancy formation energies in the surface of crystalline ice. *Nat. Mater.* **2011**, *10*, 794−798.

(31) ISIS Disordered Materials Database. http://www.isis.stfc.ac.uk/groups/disordered.

(32) Chau, P. L.; Hardwick, A. J. A new order parameter for tetrahedral configurations. *Mol. Phys.* **1998**, *93*, 511−518.

(33) Major, R. C.; Houston, J. E.; McGrath, M. J.; Siepmann, J. I.; Zhu, X. Y. Viscous Water Meniscus under Nanoconfinement. *Phys. Rev. Lett.* **2006**, *96*, 177803.

(34) Raviv, U.; Laurat, P.; Klein, J. Fluidity of water confined to subnanometre films. *Nature* **2001**, *413*, 51−54.

(35) Ortiz-Young, D.; Chiu, H.−C.; Kim, S.; Voïtchovsky, K.; Riedo, E. The interplay between apparent viscosity and wettability in nanoconfined water. *Nat. Commun.* **2013**, *4*, 2482.

(36) Doyle, A. D.; Montoya, J. H.; Vojvodic, A. Improving Oxygen Electrochemistry through Nanoscopic Confinement. *ChemCatChem* **2015**, *7*, 738−742.

(37) Zimbitas, G.; Haq, S.; Hodgson, A. The structure and crystallization of thin water films on Pt(111). *J. Chem. Phys.* **2005**, *123*, 174701.

(38) Nie, S.; Feibelman, P. J.; Bartelt, N. C.; Thürmer, K. Pentagons and Heptagons in the First Water Layer on Pt(111). *Phys. Rev. Lett.* **2010**, *105*, 026102.

(39) Revilla-López, G.; López, N. A unified study for water adsorption on metals: meaningful models from structural motifs. *Phys. Chem. Chem. Phys.* **2014**, *16*, 18933−18940.

(40) Lespes, N.; Filhol, J.−S. Using the electrochemical dimension to build water/Ru(0001) phase diagram. *Surf. Sci.* **2015**, *631*, 8−16.

(41) Kim, Y.; Moon, E.−S.; Shin, S.; Kang, H. Acidic Water Monolayer on Ruthenium(0001). *Angew. Chem., Int. Ed.* **2012**, *51*, 12806−128090.

(42) Howe, R.; Whitworth, R. W. A determination of the crystal structure of ice XI. *J. Chem. Phys.* **1989**, *90*, 4450.

(43) Kresse, G.; Furthmüller, J. Efficiency of ab−initio total energy calculations for metals and semiconductors using a plane−wave basis set. *Comput. Mater. Sci.* **1996**, *6*, 15−50.

(44) Kresse, G.; Hafner, J. Ab initio molecular dynamics for liquid metals. *Phys. Rev. B: Condens. Matter Mater. Phys.* **1993**, *47*, 558.

(45) Blöchl, P. E. Projector augmented−wave method. *Phys. Rev. B: Condens. Matter Mater. Phys.* **1994**, *50*, 17953.

(46) Perdew, J. P.; Burke, K.; Ernzerhof, M. Generalized Gradient Approximation Made Simple. *Phys. Rev. Lett.* **1996**, *77*, 3865.

(47) Grimme, S.; Antony, S.; Ehrlich, S.; Krieg, H. A consistent and accurate ab initio parametrization of density functional dispersion correction (DFT−D) for the 94 elements H−Pu. *J. Chem. Phys.* **2010**, *132*, 154104.

(48) Almora-Barrios, N.; Carchini, G.; Błoński, P.; López, N. Costless Derivation of Dispersion Coefficients for Metal Surfaces. *J. Chem. Theory Comput.* **2014**, *10*, 5002−5009.

(49) Nosé, S. A unified formulation of the constant temperature molecular−dynamics methods. *J. Chem. Phys.* **1984**, *81*, 511−519.

(50) Hoover, W. G. Canonical dynamics: Equilibrium phase−space distributions. *Phys. Rev. A: At., Mol, Opt. Phys.* **1985**, *31*, 1695−1697.

(51) Kaya, S.; Schlesinger, D.; Yamamoto, S.; Newberg, J. T.; Bluhm, H.; Ogasawara, H.; Kendelewicz, T.; Brown, G. E., Jr; Pettersson, L. G. M.; Nilsson, A. Highly compressed two-dimensional form of water at ambient conditions. *Sci. Rep.* **2013**, *3*, 1074.

Solvation Effects on Methanol Decomposition on Pd(111), Pt(111), and Ru(0001)

Miquel Garcia-Ratés,*[ORCID] Rodrigo García-Muelas,[ORCID] and Núria López*[ORCID]

Institute of Chemical Research of Catalonia (ICIQ), The Barcelona Institute of Science and Technology, Avinguda dels Països Catalans 16, 43007 Tarragona, Spain

S Supporting Information

ABSTRACT: Solvation is crucial in many chemical and electrochemical processes related to alcohol conversion on metal surfaces. Particularly, understanding the dehydrogenation mechanism of methanol on solvated Pd, Pt, and Ru surfaces could allow the design of efficient methanol fuel cells. The large computational cost related to adopting an explicit solvation approach into density functional theory can be reduced drastically by using implicit solvation methods. In this study, we use our recently developed continuum solvation model (MGCM) to elucidate the minimum number of explicit water molecules to add to the solvated methanol/metal surface systems to reproduce experimental data with an optimized balance between time and reliability. Our results stress the importance of adding two explicit water molecules, especially for the case of Ru surfaces. For this later system, we provide a first insight into the decomposition mechanism of methanol using first-principles calculations. Our predictions can be then a useful reference for future studies that aim at designing more efficient heterogeneous catalysts with solvents.
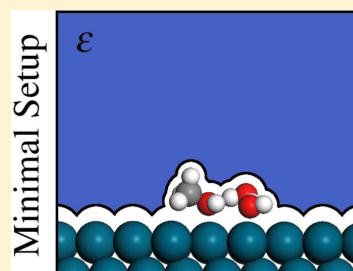
INTRODUCTION

Biomass-derived compounds have received increasing attention in recent years as an alternative source of energy to fossil fuels.[1] Commonly biomass resources contain significant amounts of water. To avoid the complexity of long carbon polyalcohols, studies have been centered in surrogates, small alcohols, that already are of technological interest. Among such compounds, methanol, the simplest alcohol, has many advantages as energy carrier due to its high hydrogen content, availability, low cost, and ease of transport and storage. The use of methanol as a fuel is based on the so-called fuel-cell technology with potential applications in portable power and electric vehicles.[2] Direct methanol fuel cells (DMFCs) are used to decompose methanol to produce electricity. On the anode side of the DMFC methanol is oxidized on a metal catalyst such as platinum (Pt), palladium (Pd), or ruthenium (Ru) in an aqueous environment.[2] Water plays then a key role on the surface chemistry in DMFCs as it interacts with the adsorbate through hydrogen bonds, short-, and long-range interactions, and it modifies the number of available active sites on the metal catalyst. Therefore, should an active and selective catalyst be designed, the effect of the environment is to be considered carefully.

Density functional theory (DFT) has been employed extensively in methanol decomposition on metal surfaces.[3] Studies of methanol adsorption on metal/vacuum and metal/water interfaces suggest that the methanol dehydrogenation pathway depends strongly on the environment. While experiments in ultrahigh vacuum (UHV) show that the adsorption of methanol on Pt and Ru surfaces starts with the O−H scission,[4,5] theoretical studies under the same conditions lead to different reaction pathways. For instance, Desai et al.[6] studied the adsorption of methanol over Pt(111) surfaces in vacuum and observed that dehydrogenation pathways starting via the activation of the C−H bond are favored. A similar pathway for methanol decomposition on Pt(111) was suggested by Greeley and Mavrikakis through microkinetic modeling based on first-principles results.[7] DFT-based results for the case of methanol adsorbed on Pd, Pt, and Ru surfaces in vacuum show that several C−H bond breakings occur before O−H scission. However, the formation of adsorbed methanol clusters is favored, and this promotes the O−H bond breaking.[8] A good agreement is found between the results obtained from experiments and theoretical studies when aqueous methanol decomposition is considered. In this case, the initial step in the reaction pathway is the C−H bond cleavage.[9−11] Neurock et al.[12] studied the dehydrogenation pathway from CH_3OH to CO on Pt(111) in the presence of explicit water molecules through DFT calculations. All dehydrogenation steps were more exothermic than in vacuum. In this case, CH_xOH intermediates are stabilized by hydrogen bonding with nearby H_2O and H_3O^+ species, and then the C−H bond cleavage is favored over the O−H bond breaking during the reaction path. Similar results were reported by Hartnig and Spohr[13] who observed that O−H bond dissociation does not occur when methanol is hydrogen-bonded to a water molecule. However,
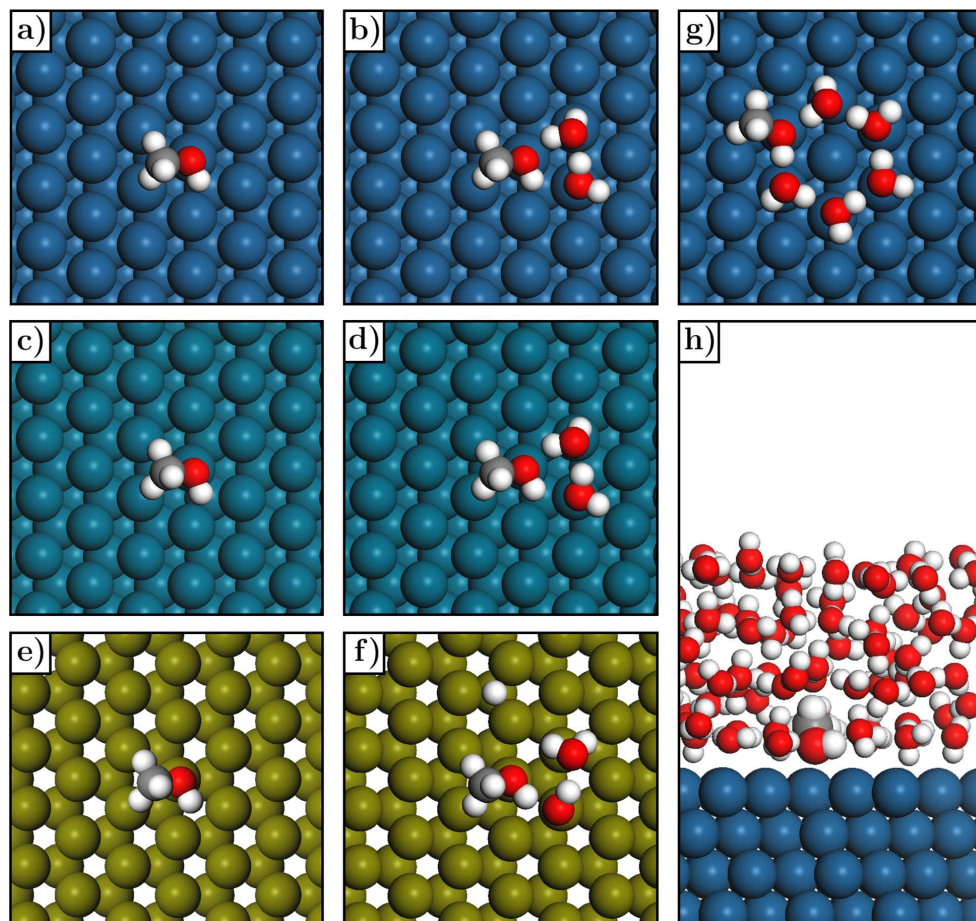
Article

Figure 1. Models employed to study the adsorption of methanol on Pt, Pd, and Ru surfaces. Left panels (a, c, e) correspond to the CS (Pt(111) top, Pd(111) middle, and Ru(0001) bottom), while central panels (b, d, f) correspond to the S2W. Right panels correspond to the S5WR (g) and S71W (h) systems. For this last system, the radii of methanol atoms have been increased to distinguish the adsorbate from water molecules. Blue, turquoise, and golden spheres stand for platinum, palladium and ruthenium atoms, respectively, while red accounts for oxygen, white for hydrogen, and gray for carbon.

these studies mainly consider explicit molecules, and long-range solvent effects were not introduced.

Considering solvation effects in first-principles calculations is, nevertheless, a delicate issue. Explicit solvent modeling involves long-time scale molecular dynamics (MD) simulations as physical quantities should be averaged to compute the thermodynamic properties of interest.[14] This results in an unaffordable computational cost for most of the systems of interest. However, the hydrogen bond stabilization of the adsorbed methanol comes mainly from the water molecules surrounding it and from those solvating the metal surface. In fact, water molecules located in the bulk, far away from the adsorption site, will have a residual effect on the methanol decomposition pathway. Thus, an alternative approach is to treat the solvent as a structureless continuum medium characterized by the value of its dielectric permittivity, while the solute and the nearby water molecules are treated through

quantum mechanics. This strategy, known as implicit solvation,[15] reduces drastically the computational cost of the calculations without affecting the accuracy of the computed physical quantities. In this context, we have recently developed a continuum solvation model into the Vienna ab Initio Simulation Package (VASP),[16] a plane-wave based electronic structure code, VASP-MGCM (VASP-Multigrid Continuum Model).[17] The model solves the electrostatic problem through a multigrid solver and has been tested for a large number of isolated and adsorbed molecules on metal surfaces with a good agreement between experimental and simulation data. The key point in this type of calculations is to determine the number of solvent molecules to add to the simulation box.[18,19] On the one hand, if no explicit solvent molecules are considered, the solute adsorption geometry can differ from the true configuration as the short-range polarization of the adsorbate is not properly described.[20] This leads to wrong estimates for thermodynamic

Article

and kinetic parameters. On the other hand, adding a large number of solvent molecules results in a high computational cost and does not necessarily improve substantially the accuracy of the results with respect to the case where we consider a few number of explicit molecules.[21] Several studies have adopted a combined explicit/implicit solvation approach to study different reactions on Pt(111) and its alloys. This is the case of the oxygen reduction reaction (ORR),[20,22,23] the adsorption of H, O, and OH,[24] and the H_2O interactions with CO and sugar alcohols.[25] Although these studies provide relevant information about the reaction mechanisms of organic molecules on Pt(111) under solvation, the suitability of the explicit/implicit solvent approach has not been extensively studied for other metal surfaces like Pd(111) or Ru(0001).

In the present work, we have studied the effect of the solvent on the decomposition of methanol to formaldeyhde on Pd(111), Pt(111), and Ru(0001) through DFT calculations. Our aim is not only to report the mechanisms of methanol dehydrogenation on metal surfaces under solvation, thus closer to the DMFC working conditions, but more importantly, to identify a minimum system setup to describe solvation effects accurately at the lowest computational cost. First of all, we demonstrate that the addition of two water molecules on the Pd and Pt surfaces permits to reproduce experimental and simulation results where the methanol C−H bond breaking is the preferred first dehydrogenation step under solvation. In addition, we report for the first time the mechanism that governs methanol dehydrogenation on Ru surfaces in an aqueous environment. This mechanism, which can only be observed when explicit water molecules are bonded to the adsorbate, consists on a proton transfer from the hydroxyl group to nearby water molecules that dissociate afterward. Experimental and computational studies involving methanol dehydrogenation on Ru(0001) have only been done in vacuum.[5,8,26,27] Our results are a step forward in describing the methanol decomposition pathway at the metal-water interface and can serve as a reference for further studies.

THEORETICAL METHODS

Simulated Systems. For each metal we consider two different situations: (1) no water molecules are added to the simulation box and (2) two water molecules are bonded to both methanol and the metal surface (see Figure 1a−f). For simplicity, we refer to these systems as CS (clean surface) and S2W (surface with two water molecules), respectively. The configuration of the two molecules for the later system is a chain so that the HOMO (basicity) of water is close enough to a water cluster value.[28] In both cases, the systems are also immersed in a continuum water medium simulated using VASP-MGCM. As the water dissociation ratio on Ru(0001) is about 40 to 50%,[29] one water molecule is dissociated on the Ru S2W (Figure 1f). For Pt, we have also studied the decomposition path of methanol when it belongs to a solvated explicit ice-like water ring as that described in ref 29 (Figure 1g), both in vacuum and under solvation. We refer to this system as S5WR (surface with a five-water ring). The S5WR configuration is present in long-time simulations of liquid water (Born−Oppenheimer molecular dynamics, BOMD, at 300 K),[29] although other less structured 7-, 6-, and 5-membered rings are also present at the interface. At the same time, we have extracted a snapshot from the BOMD in ref 29 for the system containing the Pt surface (labeled as Pt4 in that reference) solvated by 72 water molecules. We replaced a flat water

molecule by methanol, preserving the hydrogen bonds that the replaced molecule had with its neighbors. Then, the adsorbate was relaxed along its vicinal water molecules (see Figure 1 h). This system is called S71W (surface with 71 water molecules). For the S5WR, the water configuration is reminiscent of that found around the methanol molecule in the S71W. Notice that unlike a water ring model coming from ice, the S5WR presents some molecules with the dipole moment slightly tilted with respect to the Pt surface. The S5WR retains then a certain degree of liquid-like behavior in the water configuration. Both the results for the S5WR and the S71W serve as a benchmark to assess the accuracy of the two strategies described above (CS and S2W).

Computational Details. DFT calculations were performed using the Vienna ab Initio Simulation Package (VASP),[16] version 5.3.3, with the Perdew−Burke−Ernzerhof (PBE) GGA exchange-correlation functional.[30] Dispersion interactions were calculated through the semiempirical Grimme's DFT-D2 method,[31] with our reparameterized values for the metal atoms.[32] Core electrons were described using the projector augmented wave (PAW) formalism,[33] while valence electrons were represented by plane waves with a cutoff energy of 450 eV. Solvent effects were treated through the VASP-MGCM. In this case, the value of the dielectric permittivity ϵ in the space is calculated using the Fattebert and Gygi functional form:[34]

$$\epsilon(r) = \frac{\epsilon_0 - 1}{1 + (\rho_{el}(r)/\rho_0)^{2\beta}}$$

(1)

Here, ρ_{el} stands for the electronic charge density, ϵ_0 is the permittivity of the bulk phase of the solvent (78.5 for water), and ρ_0 and β are parameters controlling the shape of ϵ. The adopted values for these two parameters are $\beta = 1.7$ and $\rho_0 = 6 \times 10^{-4}$ a.u. The electronic convergence threshold was set to 10^{-5} and 10^{-6} eV for calculations involving metal surfaces and isolated molecules, respectively. In the case of gas-phase systems and the CS, the initial configurations were relaxed until forces acting on ions were lower than 30 meV/Å (15 meV/Å for solvated and unsolvated isolated molecules). In this case, a conjugate-gradient (CG) algorithm[35] was used to relax the ions into their instantaneous ground state. When explicit water molecules were adsorbed on the metal surfaces, the convergence criterion for the forces was slightly changed to 50 meV/Å and a quasi-Newton algorithm[36] was used to relax the ions for solvated systems. The choice of such algorithm was based on the fact that, when considering a CG algorithm for ion relaxation, we observed that some water molecules tended to rotate too much due to the interaction with the implicit aqueous environment. The CS and S2W metal surfaces were modeled by a four-layers $2\sqrt{3} \times 2\sqrt{3} - R30°$ slab separated by at least 13 Å of vacuum along the z-axis, with dipole corrections included along this direction. For the S5WR and the S71W, we used a $3\sqrt{3} \times 3\sqrt{3} - R30°$ reconstruction. The two topmost layers were relaxed, while the bottom ones were fixed to the bulk distances. The lattice parameters for Pd, Pt, and Ru were 3.939, 3.968, and 3.629 Å, respectively, and $[c/a]_{Ru} = 1.581$, in good agreement with the experimental values: 3.878, 3.924, and 3.615 Å, and $[c/a]_{Ru} = 1.584$.[37] The Brillouin zone was sampled by $3 \times 3 \times 1$ (CS and S2W systems) and $2 \times 2 \times 1$ (S5WR and S71W systems) Γ-centered k-points meshes constructed through the Monkhorst−Pack scheme.[38] A Gaussian smearing function with a width of 0.03 eV was used to broaden the energy levels around the Fermi level. Finally, we performed
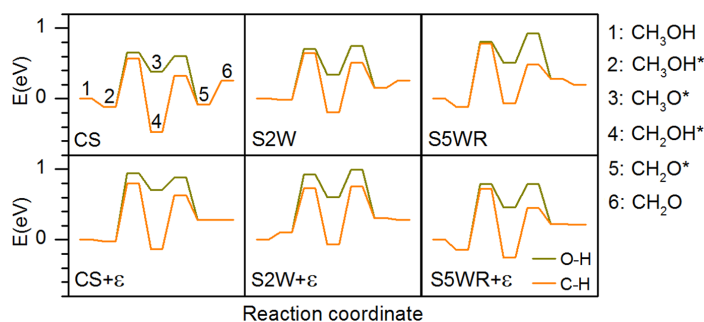
Figure 2. Reaction profiles for the dehydrogenation of methanol to CH_2O on Pt(111). ϵ stands for solvated systems. For clarity, all the intermediates are labeled.
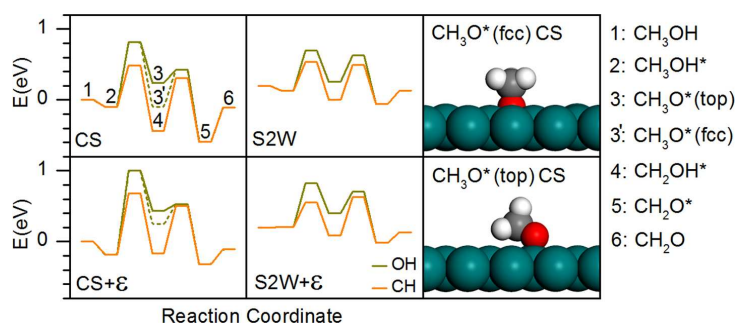

Figure 3. Reaction profiles for the dehydrogenation of methanol to CH_2O on Pd(111). The dashed line for the CS corresponds to the path starting with the O−H bond breaking but with the oxygen atom from the adsorbed methoxy tricoordinated to the Pd surface. ϵ stands for solvated systems. On the right panels we show the methoxy configurations on the CS (one of the H atoms is hidden due to the perspective); tricoordinated (top) and monocoordinated (bottom). For clarity, all the intermediates are labeled.

transition state (TS) searches through the improved dimer method (IDM).[39] A data set collection of computational results, including all the structures, is available in the ioChem-BD repository.[40,41]

■ **RESULTS AND DISCUSSION**

Pt(111). In Figure 2 we show the energy profile for methanol decomposition on Pt(111) for the different systems in vacuum and under solvation. The first step is the adsorption of methanol to the metal surface, described by the replacement energy, E_r, the energy cost of replacing a water molecule by methanol.

$$E_r^{0,\epsilon} = E_{m,s}^{0,\epsilon} + E_w^{0,\epsilon} - E_{w,s}^{0,\epsilon} - E_m^{0,\epsilon} \qquad (2)$$

Here, $E_{m,s}$ is the energy of the system with adsorbed methanol, $E_{w,s}$ stands for the same system with a water molecule located at the methanol position, while E_m and E_w are the energies of the isolated methanol and water molecules, respectively. The superscript "0" denotes vacuum, while ϵ stands for the continuum-solvated. Adsorption energies for methanol on the CS in vacuum are provided in Section S1. Except for the S5WR, where the replacement is more exothermic in solution than in vacuum, the replacement energies increase when solvating the systems. Nevertheless, the values of E_r fall in the range (−0.14,0.11) eV, making the replacement of water by methanol almost thermoneutral. We have also calculated E_r for the S71W

in vacuum. In this case, $E_r = 0.09$ eV, a value that falls in the range of the error for all our measured replacement energies.

Solvent effects are found in the first dehydrogenation step. From now on, we call ΔE_a the difference in the height of the first activation barrier between the paths involving O−H and C−H bond breaking. That is, $\Delta E_a = E_{TS}^{OH} - E_{TS}^{CH}$, with E_{TS}^{OH} and E_{TS}^{CH} standing for the first transition state energies, respectively. In the three studied systems, there is an increase in ΔE_a under solvation with respect to what we observe in vacuum. This result agrees with both experimental and simulation data for methanol decomposition on Pt(111), where hydroxymethyl (H_2COH) becomes the most stable product in liquid.[9−11] A commonly adopted explanation is that, under solvation, the methanol OH group has a larger number of water molecules around it as compared to the CH_3 group.[9] This situation reduces the probability for the binding of the OH group to the Pt surface catalytic sites and favors the C−H bond breaking. To account for this fact, it is specially important to include explicit water molecules near the OH group in order to reproduce part of its first solvation shell. This strategy, adopted in the S2W, limits the methanol OH group mobility and its further binding to the Pt surface. Increasing the number of explicit molecules further does not improve the model, as ΔE_a is very small (0.06 eV under solvation and 0.03 eV in vacuum), and thus, both C−H and O−H bond breakings are possible in contrast with the experimental observation. This result is due to the strong rigidity imposed by the S5WR model.
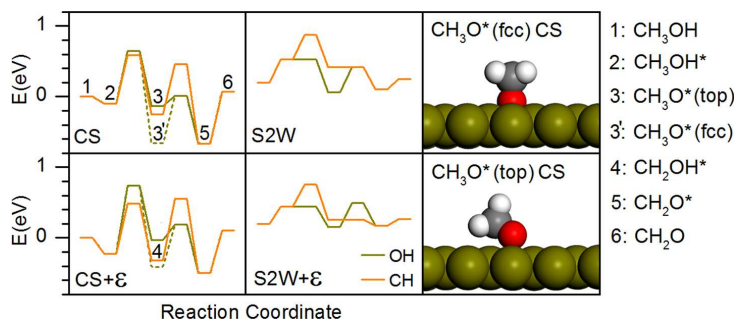
Figure 4. Reaction profiles for the dehydrogenation of methanol to CH_2O on Ru(0001). The dashed line for the CS corresponds to the path starting with the O−H bond breaking but with the oxygen atom from the adsorbed methoxy tricoordinated to the Ru atoms. ϵ stands for solvated systems. On the right panels we show the methoxy configurations on the CS (one of the H atoms is hidden due to the perspective); tricoordinated (top) and monocoordinated (bottom). For clarity, all the intermediates are labeled.
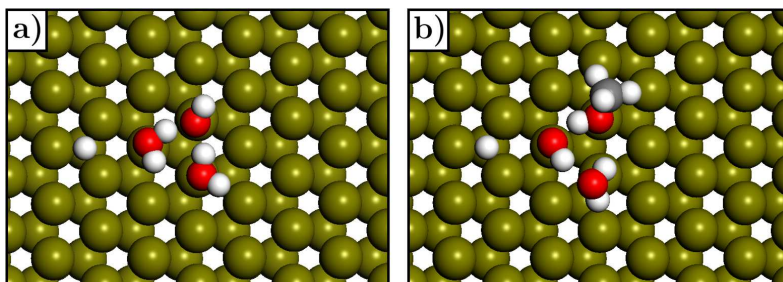

Figure 5. Adsorbate configuration for the S2W before methanol replaces a dissociated water molecule (a) and after methanol is adsorbed (b).

We have simulated a methanol trimer adsorbed on the CS to address cooperative effects. For the isolated molecules, the methanol cluster is more stable than the separated methanol molecules (both in vacuum and solvated by water). When the trimer is adsorbed on Pt, the methanol trimer is only more stable in vacuum but solvation renders separated methanol molecules more favorable (see Section S2). Therefore, O−H bond breaking cannot be favored through cooperative interactions on the surface if water is present.

The second dehydrogenation step under solvation is rather similar for the S2W and the S5WR systems. In particular, for the CH_3O dehydrogenation, the height of the barrier equals 0.17 and 0.39 eV for the CS and S2W, respectively, being this quantity for the S5WR equal to 0.33 eV. With regard to the CH_2OH dehydrogenation, both the CS and S2W yield similar results as compared to the S5WR.

Pd(111). The analysis of the energy profiles on Pd(111) yields similar results to those for the Pt surface (see Figure 3). Regarding the replacement energies, E_r^ϵ equals −0.19 and 0.01 eV for the CS and S2W, respectively, meaning that methanol adsorption is not much more preferred than desorption, even in an aqueous environment. The value of ΔE_a for the CS is the same for both solvated and unsolvated systems ($\Delta E_a = 0.33$ eV). However, ΔE_a increases by 0.16 eV for the S2W when solvating the system (from 0.24 eV in vacuum to 0.40 eV under solvation). The first activation barrier for the C−H bond breaking decreases from 0.61 eV (vacuum) to 0.53 eV (solvation). These results indicate that, like in Pt, the C−H

bond breaking becomes the preferential mechanism in aqueous environment.

With respect to the configuration of the adsorbed CH_3O there is a difference between the Pd CS and S2W (see Figure 3). For the CS, the configuration with the oxygen atom coordinated to a fcc site (tricoordinated structure) is 0.34 eV more stable in vacuum than that with the oxygen atom coordinated to a top site (monocoordinated structure, see dashed line in Figure 3). When solvating the tricoordinated geometry, the energy decreases by 0.19 eV with respect to the flat situation due to the three available hydrogen atoms that the implicit solvent has to interact with. The scenario is quite different for the S2W as the water molecules maintain the adsorbate configuration flat and close to the surface. This adsorption reordering is the most serious reason to include explicit water molecules in any calculation under solvation.

Ru(0001). Water dissociates on Ru surfaces (dissociation ratio of about 40 to 50%), which might have an effect on methanol decomposition. For instance, explicit water molecules have been taken into account to study the conversion of levulinic acid on this surface.[42,43] In Figure 4 we show the energy profile for methanol dehydrogenation on the Ru surfaces. For the CS $E_r^\epsilon = -0.22$ eV (in vacuum, $E_r^0 = -0.09$ eV). Solvating the system increases ΔE_a in 0.20 eV with respect to the vacuum situation, and therefore, the C−H bond breaking becomes the most favored methanol first decomposition mechanism. The exothermic character of the methanol O−H bond breaking depends, however, on the orientation of the C−O bond with respect to the surface plane. This issue, which

Article

is inherent to the CS, becomes more clear for the solvated system where the reaction is exothermic if the C−O bond is perpendicular to the surface plane and endothermic when the C−O bond is parallel to it. The net effect of taking the tricoordinated CH_3O structure is an increase in the height of the activation barrier for its dehydrogenation of 0.53 and 0.38 eV for the unsolvated and solvated systems, respectively.

The situation changes drastically when we add two water molecules (one dissociated) to the simulation box. On the reference S2W (that with two water molecules and an OH, see Figure 5a) the oxygen atom from the dissociated water is hydrogen-bonded at the same time to two hydrogen atoms. When methanol replaces the dissociated water, one of the remaining two water molecules becomes an OH group (see Figure 5b). Then, the global hydrogen bond network becomes slightly more distorted than for the previous situation making the methanol adsorption more endothermic than on the Pd and Pt surfaces (E_r^0 = 0.49 eV and E_r^ϵ = 0.37 eV). With regard to the methanol first dehydrogenation step, the O−H bond breaking is barrierless as the proton is transferred to the nearest water molecule (which is a dissociated water) and then the newly formed water molecule dissociates. This situation is not observed for the path involving the C−H bond breaking, where the activation barrier equals 0.52 and 0.46 eV for the unsolvated and solvated systems, respectively. These results give us some clues about the mechanism that governs methanol decomposition on Ru. This fact reinforces not only the need for the addition of two water molecules to the simulation box but also the importance of adopting a configuration such as that in Figure 5b. With regard to the CH_2OH dehydrogenation, it is also an inactivated process due to the proton transfer from the OH group to a water molecule. In this case, solvating the system involves that the surface with the adsorbed CH_2OH has a similar energy to that with the adsorbed CH_2O (0.13 eV of difference). For the CH_3O dehydrogenation, however, adding the solvent does not involve a large change in the barrier (−0.04 eV).

To compile the results, a comparison between the three surfaces can be drawn. We have found that (i) for Pd and Pt the methanol C−H bond breaks first, whereas the O−H bond breaking is the first step on Ru, (ii) the number of explicit water molecules needed is the same for all surfaces, (iii) although the S5WR ring structures are slightly more flexible than the ice-derived ones, they might still be too rigid to represent the aqueous environments found in ref 29 where 5-, 6- and 7-membered rings also appear, and (iv) the models used to study water-assisted processes on Ru need to account for the dissociation of some water molecules.

CONCLUSIONS

We have employed first-principles calculations to study the methanol dehydrogenation path to formaldehyde on Pd(111), Pt(111), and Ru(0001) under aqueous environment. In particular, we have adopted a combined explicit/implicit solvation approach. The results for the methanol dehydrogenation profiles on solvated Pd and Pt surfaces agree with experiments where the methanol C−H bond breaking is the preferred first dehydrogenation step. This situation is attributed to the fact that the methanol CH groups in solution are more exposed to the metal surface atoms than the OH group, which favors the C−H bond breaking. The calculated reaction profiles for the surface containing two explicit water molecules (S2W) qualitatively agree with those calculated for a benchmark system, the S5WR (surface with a five-water ring) where the methanol environment is close to that encountered on systems with several explicit water layers. The addition of two explicit water molecules also prevents the intermediates to adopt undesired configurations (specially for the case of the CH_3O in Pd and Ru in the CS) that result in overestimated values for the activation energies. Water dissociation on Ru(0001) makes the methanol decomposition very different from the case of Pd and Pt surfaces. The dehydrogenation of methanol on the Ru S2W occurs via a proton transfer from the methanol OH group to a nearby water molecule that dissociates afterward. This makes the methanol O−H bond breaking to become barrierless. No theoretical results exist for the dehydrogenation of methanol on solvated Ru(0001), and, therefore, the aforementioned mechanism can serve as a reference for further studies. Notice that the water dissociation at the Ru interface is crucial to address the catalytic properties of this particular surface that is extensively used, for instance, in the conversion of levulinic acid to gamma-valerolactone.[43] Our results show the need to include both implicit and explicit water molecules in the computational box and thus pave the way toward faster and more reliable simulations in catalytic and electrochemical reactions on surfaces.

ASSOCIATED CONTENT

Supporting Information

The Supporting Information is available free of charge on the ACS Publications website at DOI: 10.1021/acs.jpcc.7b05545.

In Section S1, we provide the data associated with the energy profiles for the methanol dehydrogenation, that is methanol adsorption and replacement energies, and desorption energies of formaldehyde as well as activation and reaction energies; in Section S2, we give the energies for the clustered methanol species on metal surfaces (PDF)

AUTHOR INFORMATION

Corresponding Authors
*E-mail: mgarciar@iciq.es.
*E-mail: nlopez@iciq.es. Phone: +34 977 920237. Fax: +34 977 920231.
ORCID
Miquel Garcia-Ratés: 0000-0002-6315-0845
Rodrigo García-Muelas: 0000-0002-2219-5027
Núria López: 0000-0001-9150-5941
Notes
The authors declare no competing financial interest.

ACKNOWLEDGMENTS

REFERENCES

(1) Huber, G. W.; Iborra, S.; Corma, A. Synthesis of Transportation Fuels from Biomass: Chemistry, Catalysts, and Engineering. *Chem. Rev.* **2006**, *106*, 4044−4098.
(2) Larminie, J.; Dicks, A. *Fuel Cell Systems Explained*; John Wiley & Sons: Chichester, U.K., 2003.
(3) Martin, R. M. *Electronic Structure: Basic Theory and Practical Methods*; Cambridge University Press: Cambridge, U.K., 2004.

(4) Akhter, S.; White, J. M. A Static SIMS/TPD Study of the Kinetics of Methoxy Formation and Decomposition on O/Pt(111). *Surf. Sci.* **1986**, *167*, 101−126.

(5) Barros, R.; Garcia, A.; Ilharco, L. The Decomposition Pathways of Methanol on Clean Ru(0001), Studied by Reflection-Absorption Infrared Spectroscopy (RAIRS). *J. Phys. Chem. B* **2001**, *105*, 11186−11193.

(6) Desai, S. K.; Neurock, M.; Kourtakis, K. A Periodic Density Functional Theory Study of the Dehydrogenation of Methanol over Pt(111). *J. Phys. Chem. B* **2002**, *106*, 2559−2568.

(7) Greeley, J.; Mavrikakis, M. Competitive Paths for Methanol Decomposition on Pt(111). *J. Am. Chem. Soc.* **2004**, *126*, 3910−3919.

(8) García-Muelas, R.; Li, Q.; López, N. Density Functional Theory Comparison of Methanol Decomposition and Reverse Reactions on Metal Surfaces. *ACS Catal.* **2015**, *5*, 1027−1036.

(9) Franaszczuk, K.; Herrero, E.; Zelenay, P.; Wieckowski, A.; Wang, J.; Masel, R. I. A Comparison of Electrochemical and Gas-Phase Decomposition of Methanol on Platinum Surfaces. *J. Phys. Chem.* **1992**, *96*, 8509−8516.

(10) Sakong, S.; Groß, A. The Importance of Electrochemical Environment in the Electro-Oxidation of Methanol on Pt(111). *ACS Catal.* **2016**, *6*, 5575−5586.

(11) Herron, J. A.; Morikawa, Y.; Mavrikakis, M. Ab Initio Molecular Dynamics of Solvation Effects on Reactivity at Electrified Interfaces. *Proc. Natl. Acad. Sci. U. S. A.* **2016**, *113*, E4937−E4945.

(12) Neurock, M.; Wasileski, S. A.; Mei, D. From First Principles to Catalytic Performance: Tracking Molecular Transformations. *Chem. Eng. Sci.* **2004**, *59*, 4703−4714.

(13) Hartnig, C.; Spohr, E. The Role of Water in the Initial Steps of Methanol Oxidation on Pt(111). *Chem. Phys.* **2005**, *319*, 185−191.

(14) Frenkel, D.; Smit, B. *Understanding Molecular Simulation, from Algorithms to Applications*, 2nd ed.; Academic: San Diego, CA., 1996.

(15) Tomasi, J.; Mennucci, B.; Cammi, R. Quantum Mechanical Continuum Solvation Models. *Chem. Rev.* **2005**, *105*, 2999−3093.

(16) Kresse, G.; Furthmüller, J. Efficiency of Ab-Initio Total Energy Calculations for Metals and Semiconductors Using a Plane-Wave Basis Set. *Comput. Mater. Sci.* **1996**, *6*, 15−50.

(17) Garcia-Ratés, M.; López, N. Multigrid-Based Methodology for Implicit Solvation Models in Periodic DFT. *J. Chem. Theory Comput.* **2016**, *12*, 1331−1341.

(18) Díez, J.; Gimeno, J.; Lledós, A.; Suárez, F. J.; Vicent, C. Imidazole Based Ruthenium(IV) Complexes as Highly Efficient Bifunctional Catalysts for the Redox Isomerization of Allylic Alcohols in Aqueous Medium: Water as Cooperating Ligand. *ACS Catal.* **2012**, *2*, 2087−2099.

(19) Ortuño, M. A.; Lledós, A.; Maseras, F.; Ujaque, G. The Transmetalation Process in Suzuki-Miyaura Reactions: Calculations Indicate Lower Barrier via Boronate Intermediate. *ChemCatChem* **2014**, *6*, 3132−3138.

(20) Fang, Y.-H.; Wei, G.-F.; Liu, Z.-P. Constant-Charge Reaction Theory for Potential-Dependent Reaction Kinetics at the Solid-Liquid Interface. *J. Phys. Chem. C* **2014**, *118*, 3629−3635.

(21) Zaffran, J.; Michel, C.; Delbecq, F.; Sautet, P. Towards More Accurate Prediction of Activation Energies for Polyalcohol Dehydrogenation on Transition Metal Catalysts in Water. *Catal. Sci. Technol.* **2016**, *6*, 6615−6624.

(22) Wei, G.-F.; Fang, Y.-H.; Liu, Z.-P. First Principles Tafel Kinetics for Resolving Key Parameters in Optimizing Oxygen Electrocatalytic Reduction Catalyst. *J. Phys. Chem. C* **2012**, *116*, 12696−12705.

(23) He, Z.-D.; Hanselman, S.; Chen, Y.-X.; Koper, M. T. M.; Calle-Vallejo, F. Importance of Solvation for the Accurate Prediction of Oxygen Reduction Activities of Pt-Based Electrocatalysts. *J. Phys. Chem. Lett.* **2017**, *8*, 2243−246.

(24) Sakong, S.; Naderian, M.; Mathew, K.; Hennig, R. G.; Groß, A. Density Functional Theory Study of the Electrochemical Interface between a Pt Electrode and an Aqueous Electrolyte Using an Implicit Solvent Method. *J. Chem. Phys.* **2015**, *142*, 234107.

(25) Bodenschatz, C. J.; Sarupria, S.; Getman, R. B. Molecular-Level Details about Liquid H_2O Interactions with CO and Sugar Alcohol

Adsorbates on Pt(111) Calculated Using Density Functional Theory and Molecular Dynamics. *J. Phys. Chem. C* **2015**, *119*, 13642−16351.

(26) Gazdzicki, P.; Jakob, P. Reactions of Methanol on Ru(0001). *J. Phys. Chem. C* **2010**, *114*, 2655−2663.

(27) Lu, X.; Wang, W.; Deng, Z.; Zhu, H.; Wei, S.; Ng, S. P.; Guo, W.; Wu, C. M. L. Methanol Oxidation on Ru(0001) for Direct Methanol Fuel Cells: Analysis of the Competitive Reaction Mechanism. *RSC Adv.* **2016**, *6*, 1729−1737.

(28) Bellarosa, L.; Castillo, J. M.; Vlugt, T.; Calero, S.; López, N. On the Mechanism Behind the Instability of Isoreticular Metal-Organic Frameworks (IRMOFs) in Humid Environments. *Chem. - Eur. J.* **2012**, *18*, 12260−12266.

(29) Bellarosa, L.; García-Muelas, R.; Revilla-López; López, N. Diversity at the Water-Metal Interface: Metal, Water Thickness, and Confinement Effects. *ACS Cent. Sci.* **2016**, *2*, 109−116.

(30) Perdew, J. P.; Burke, K.; Ernzerhof, M. Generalized Gradient Approximation Made Simple. *Phys. Rev. Lett.* **1996**, *77*, 3865−3868.

(31) Grimme, S. Semiempirical GGA-Type Density Functional Constructed with a Long-Range Dispersion Correction. *J. Comput. Chem.* **2006**, *27*, 1787−1799.

(32) Almora-Barrios, N.; Carchini, G.; Błoński, P.; López, N. Costless Derivation of Dispersion Coefficients for Metal Surfaces. *J. Chem. Theory Comput.* **2014**, *10*, 5002−5009.

(33) Blöchl, P. E. Projector Augmented-Wave Method. *Phys. Rev. B: Condens. Matter Mater. Phys.* **1994**, *50*, 17953−17979.

(34) Fattebert, J.-L.; Gygi, F. Density Functional Theory for Efficient Ab Initio Molecular Dynamics Simulations in Solution. *J. Comput. Chem.* **2002**, *23*, 662−666.

(35) Press, W. H.; Teukolsky, S. A.; Vetterling, W. T.; Flannery, B. P. *Numerical Recipes in Fortran 90. The Art of Parallel Scientific Computing*, 2nd ed.; Cambridge University Press: New York, 1999.

(36) Pulay, P. Convergence Acceleration of Iterative Sequences. The Case of SCF Iteration. *Chem. Phys. Lett.* **1980**, *73*, 393−398.

(37) Lide, D. R. *CRC Handbook of Chemistry and Physics*, 84th ed.; CRC Press LLC: Boca Raton, FL, 2003.

(38) Monkhorst, H. J.; Pack, J. D. Special Points for Brillouin-Zone Integrations. *Phys. Rev. B* **1976**, *13*, 5188−5192.

(39) Heyden, A.; Bell, A. T.; Keil, F. J. Efficient Methods for Finding Transition States in Chemical Reactions: Comparison of Improved Dimer Method and Partitioned Rational Function Optimization Method. *J. Chem. Phys.* **2005**, *123*, 224101.

(40) Álvarez-Moreno, M.; de Graaf, C.; López, N.; Maseras, F.; Poblet, J. M.; Bo, C. Managing the Computational Chemistry Big Data Problem: The ioChem-BD Platform. *J. Chem. Inf. Model.* **2015**, *55*, 95−103.

(41) Data-set collection of computational results, including all the structures. https://doi.org/10.19061/iochem-bd-1-39 (accessed June 8, 2017).

(42) Steinmann, S. N.; Sautet, P.; Michel, C. Solvation Free Energies for Periodic Surfaces: Comparison of Implicit and Explicit Solvation Models. *Phys. Chem. Chem. Phys.* **2016**, *18*, 31850−31861.

(43) Albani, D.; Li, Q.; Vilé, G.; Mitchell, S.; Almora-Barrios, N.; Witte, P. T.; López, N.; Pérez-Ramírez, J. Interfacial acidity in Ligand-Modified Ruthenium Nanoparticles Boosts the Performance for the Continuous Hydrogenation of Levulinic Acid to Gamma-Valerolactone. *Green Chem.* **2017**, *19*, 2361−2370.

PAPER

CrossMark
← click to updates

Glycerol oxidehydration to pyruvaldehyde over silver-based catalysts for improved lactic acid production†

G. M. Lari,[a] R. García-Muelas,[b] C. Mondelli,*[a] N. López[b] and J. Pérez-Ramírez*[a]

Sustainable technologies for the valorisation of the burgeoning amounts of glycerol (GLY) obtained as waste in the production of biodiesel are increasingly sought after. Its conversion into lactic acid (LA) is appealing due to the versatility of this platform chemical and its high added value. Here, we introduce Ag-based catalysts for the oxidehydration of GLY to pyruvaldehyde (PAl) and demonstrate the superiority of this compound in comparison to dihydroxyacetone (DHA) as the intermediate of an alternative two-step GLY-to-LA process. Evaluation of various metals and carriers identified Ag/Al_2O_3 as the best performer for PAl production. This was rationalised based on the optimal redox potential of the metal and the high concentration of Lewis-acid sites and the limited Brønsted acidity of the support. At 623 K and O_2/GLY = 0.5, a PAl yield of 80% was attained, which remained stable for 24 h. Characterisation of the used catalyst indicated that the surface of the silver nanoparticles was partially oxidised upon reaction. Density functional theory (DFT) modelling revealed that the oxidation of acetol obtained from GLY after the initial dehydration step is kinetically and thermodynamically favoured on a partially oxidised silver surface (AgO_x/Ag) compared to metallic (Ag) or fully oxidic (Ag_2O) ones. Finally, we show that PAl can be isomerised into LA and methyl lactate over Sn-containing zeolites with the same rates as DHA but at a 40 K lower temperature (343 vs. 383 K). This not only allows for energy savings but also for a remarkably increased catalyst stability.
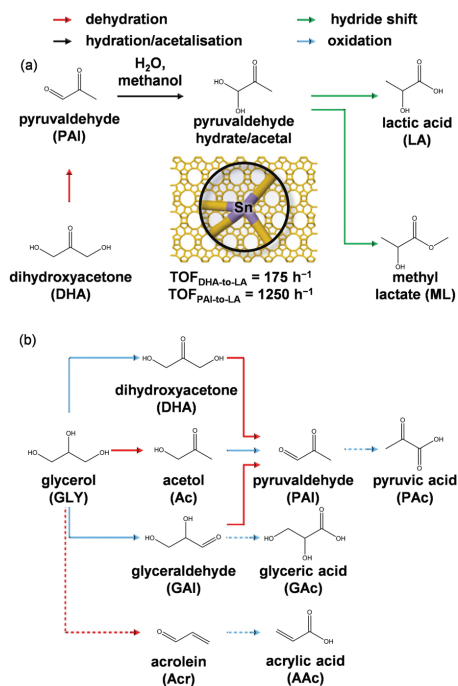
Introduction

Lactic acid (LA) has been recognised as a primary biobased platform molecule, in view of its multiple applications in the healthcare and food industries and its use in the production of acrylates and biodegradable and biocompatible polymers.[1] Especially due to the increasing prominence of polylactic acid, which is replacing polyethylene terephthalate (PET) in a growing number of uses,[2] the annual demand for LA is expected to increase to 6×10^5 ton by 2020.[3] The current man-

ufacture route, based on the fermentation of sugars, seems unable to sustain such a large market, due to its low productivity and the stoichiometric amount of gypsum generated as waste.[3] The application of electrodialysis membranes to split the salts avoiding the addition of sulphuric acid or the engineering of yeasts able to withstand solutions with lower pH have been proposed to address the latter issue,[4] but the low sugar concentration of the fermentation broth remains a limiting factor of the biocatalytic technology. For this reason, alternative pathways enabling a large-scale, economically and environmentally-friendly production of LA are demanded. One of the most promising strategies in this respect comprises the conversion of glycerol (GLY) through oxidation to dihydroxyacetone (DHA) followed by isomerisation.[5] The triol is obtained as a by-product in the preparation of biodiesel in growing amounts and its very low price justifies its purification to serve as feedstock for the preparation of added-value chemicals.[6] The conversion of glycerol into lactic acid has been conducted either in one pot over Au/CeO_2, Au–Pt/TiO_2 and Pt/Sn-MFI catalysts[7] or in two separate steps, using an enzyme or an iron-containing zeolite in the first reaction[8] and Lewis acids for the second.[9] Zeolites containing tin atoms in framework positions are superior catalysts for DHA isomerisation,[10] which involves the dehydration of DHA to pyruvaldehyde (PAl), followed by the addition of a solvent (*i.e.*, water or alcohol) molecule and a

[a]Institute for Chemical and Bioengineering, Department of Chemistry and Applied Biosciences, ETH Zurich, Vladimir-Prelog-Weg 1, CH-8093 Zurich, Switzerland. E-mail: cecilia.mondelli@chem.ethz.ch, jpr@chem.ethz.ch
[b]Institute of Chemical Research of Catalonia, ICIQ, The Barcelona Institute of Science and Technology, Av. Països Catalans 16, ES-43007 Tarragona, Spain

Scheme 1 (a) Steps involved in the liquid-phase isomerisation of DHA to LA in water or methanol and (b) reaction network envisaged for the gas-phase conversion of GLY to PAl. The dashed arrows identify competitive oxidation and dehydration pathways.

1,2-hydride shift (Scheme 1a).[11] Kinetic studies demonstrated that the overall rate is determined by the dehydration step,[11] and that the direct conversion of PAl is up to one order of magnitude faster than that of DHA under the same conditions.[12] Based on these observations, an alternative process with PAl as the intermediate would be advantageous to diminish the mass of catalyst or the temperature applied to the isomerisation step. Most importantly, milder conditions are expected to minimise one of the biggest drawbacks of the stannosilicates, *i.e.*, their fast deactivation under continuous-flow operation.[12] In this respect, it has been shown that the hydrothermal stability of zeolites increases at lower temperatures[13] and the highly oxygenated reactant and intermediates are less prone to condensation reactions leading to fouling.[14]

The selective conversion of GLY to PAl has been scarcely investigated. A patent reported the activity of transition metals, comprising vanadium, molybdenum, copper, silver and tin, supported onto an aluminosilicate.[15] Additionally, PAl has been observed as a byproduct in the liquid-phase conversion of GLY under oxidising conditions[16] and in its gas-phase oxidative upgrading to DHA or acrylic acid (AAc), respectively.[8b,17] It has been noted that the coexistence of redox and

Lewis-acid sites favours the formation of PAl by oxidation-dehydration (oxidehydration), but there is limited information on the reaction pathway (Scheme 1b) and the exact nature of the two functionalities.

Herein, we evaluate different metals and carriers used in oxidation and dehydration reactions, respectively, identifying silver supported on alumina as an efficient system for the gas-phase production of PAl from GLY. Its superiority is explained based on the optimal redox potential of the active phase and the Lewis acidity of the oxide. Additionally, we assess the impact of the reaction conditions and study the stability of the best-performing catalyst. The dehydrogenation mechanism and the chemical state of the surface are unravelled by combining DFT simulations and in-depth catalyst characterisation. Finally, the benefits of using PAl as the intermediate in the novel GLY-to-LA process are shown by confronting the long-term stability of Sn-containing zeolites in the conversion of PAl and DHA in water and methanol.

Experimental

Catalyst preparation

Supported metal catalysts. Supported catalysts containing 5 wt% of V, Ni, Fe, Sn, Cu, Ru, Ag, Pd or Pt were prepared by dry impregnation of γ-alumina (Alfa Aesar, 42 576, 99.997%, labelled as Al_2O_3-a) using NH_4VNO_3 (Fluka, >99%), $NiCl_2 \cdot 6H_2O$ (Alfa Aesar, 99.95%), $Fe(NO_3)_3 \cdot 9H_2O$ (Sigma-Aldrich, >98%), $SnSO_4$ (ABCR, 95%), $Cu(NO_3)_2 \cdot 3H_2O$ (Sigma-Aldrich, 98–103%), $RuCl_3 \cdot xH_2O$ (ABCR, 99.9%), $AgNO_3$ (ABCR, 99.9%), $Pd(NO_3)_2 \cdot xH_2O$ (ABCR, 99.9%), H_2PtCl_6 (Sigma-Aldrich, 8 wt% water solution) and $HAuCl_4 \cdot 3H_2O$ (ABCR, 99.99%) as the metal precursors. An aliquot of the salt (corresponding to 0.05 g of the metal) was dissolved in deionised water (0.50 cm³) and the solution was added to 0.95 g of the dried support. The wet powder was mixed for 5 min and freeze-dried at 3×10^{-4} bar for 16 h. Additional catalysts containing 5 wt% Ag were obtained following the same procedure using zeolites with MFI framework and a nominal Si/Al ratio of 40 (Zeolyst, CBV8014, denoted as Z40) or 940 (Tosoh Corp., HSZ-8090H0A, denoted as Z940), other γ-aluminas (Sigma-Aldrich, acidic, basic and neutral, Brokmann grade I, labelled as Al_2O_3-b, Al_2O_3-c and Al_2O_3-d, respectively), silica (Evonik, Sipernat 120), amorphous silica-alumina (Sigma-Aldrich, grade 135) and silicon carbide (Sigma-Aldrich, particle size <100 nm) as carriers. Finally, a large batch (*ca.* 50 g) of 5 wt% Ag/Al_2O_3-a was prepared by spray deposition[18] using a Büchi Mini Spray Dryer B-290. Silver nitrate (3.95 g) was dissolved in deionised water (500 cm³) under magnetic stirring at room temperature, followed by the addition of the support (47.5 g). The resulting suspension was pumped at 10 cm³ min⁻¹ into the two-fluid nozzle (1.4 mm diameter), using an air flow of 0.5 m³ h⁻¹ to form the spray. The inlet temperature was set at 493 K, the aspiration rate at 35 m³ h⁻¹ and the outlet temperature at 353 K. The dried particles were separated using a cyclone.

Tin zeolites. Z940 was used as received for post-synthetic incorporation of tin.[19] The zeolite (3.3 g) was added to an aqueous solution of NaOH (0.3 M, 100 cm^3) and SnSO$_4$ (0.04 M) and the mixture was hold at 338 K for 30 min in an Easymax™ 102 reactor system (Mettler Toledo). Thereafter, the treatment was quenched using 2 dm^3 of deionised water and the suspended material was filtered and washed until neutral pH of the filtrate was achieved. The solid obtained was ion exchanged in aqueous NH$_4$NO$_3$ (0.1 M, 6 h, 298 K, 100 cm^3 per gram of dried zeolite, 3 times), dried (338 K, 16 h) and calcined. This material was labelled as Sn-MFI. Another catalyst coded as [Sn]BEA was prepared by hydrothermal synthesis following a reported procedure.[20] Briefly, tetraethyl orthosilicate (Sigma-Aldrich, 99.9%, 30 g) and tetraethyl ammonium hydroxide (Sigma-Aldrich, 35 wt%, 33 g) were mixed for 90 min. A solution of SnCl$_4$·5H$_2$O in water (0.45 g in 2.75 cm^3) was added and the stirring was continued until complete evaporation of the ethanol formed upon hydrolysis. Then, HF (Sigma-Aldrich, 48 wt% in water, 3.2 g) was added to the clear solution under stirring, resulting in the formation of a thick gel. Thereafter, commercial zeolite beta (Tosoh Corporation, HSZ-980HOA, bulk Si/Al = 220, 0.36 g) suspended in water (0.36 g in 2.75 cm^3) was added to act as a nucleation seed and the gel was transferred into a 100 cm^3 Teflon-lined autoclave and heated at 413 K for 11 days. The [Sn]BEA solid obtained was subjected to the same filtration, calcination and ion exchange procedures as described above.

Catalyst characterisation

The metal content in the samples was determined by X-ray fluorescence (XRF) spectroscopy using an EDAX Orbis Micro-XRF analyser equipped with a Rh source operated at a voltage of 35 kV and a current of 500 µA. Powder X-ray diffraction (XRD) was performed using a PANalytical X'Pert PRO-MPD diffractometer with Ni-filtered Cu Kα radiation (λ = 0.1541 nm), acquiring data in the 5–70° 2θ range with a step size of 0.05° and a counting time of 8 s per step. N$_2$ sorption was conducted at 77 K using a Micromeritics Tristar analyser. Prior to the measurements, the samples were evacuated at 573 K and 10^{-4} bar for 3 h. Fourier transform infrared (FTIR) spectroscopy of adsorbed pyridine (Sigma-Aldrich, >99%) was carried out using a Bruker IFS66 spectrometer equipped with a liquid-N$_2$ cooled mercury cadmium telluride (MCT) detector. Sample wafers (ca. 1 cm^2, 0.02 g) were evacuated (10^{-6} bar) for 4 h at 693 K, prior to adsorption at room temperature. Gaseous and weakly adsorbed molecules were subsequently removed by evacuation at 373 K (for selected samples) and at 473 K for 30 min. Spectra were recorded in the range of 650–4000 cm^{-1} with a resolution of 4 cm^{-1} and co-addition of 32 scans. The concentration of Brønsted- and Lewis-acid sites was calculated from the area of the pyridine bands at 1545 and 1454 cm^{-1}, respectively, using their corresponding extinction coefficients $\varepsilon_{Brønsted}$ = 1.67 and ε_{Lewis} = 2.94 cm µmol^{-1}. Temperature-programmed reduction with hydrogen (H$_2$-TPR) was performed using a Micromeritics Autochem II 2920 unit connected to a MKS Cirrus 2 quadrupole mass spectrometer. The samples (0.1 g) were pre-treated in He flow (20 cm^3 min^{-1}) at

423 K for 1 h, cooled to 308 K and finally heated up to 1273 K (10 K min^{-1}) while monitoring the consumption of H$_2$ and the formation of H$_2$O. Quantification was achieved by integration of the area of the reduction peaks, using the results obtained in the H$_2$-TPR of known amounts of CuO for calibration. Thermogravimetric analysis (TGA) of the used catalysts was conducted using a Mettler Toledo TGA/DSC1 instrument. The samples (0.015 g) were heated in the range of 323–1023 K (10 K min^{-1}) under an air flow (40 cm^3 min^{-1}). The weight loss between 523–1023 K was ascribed to the removal of carbonaceous deposits. X-ray photoelectron spectroscopy (XPS) was carried out under UHV (10^{-8} mbar) using a VG Thermo Escalab 220i-XL spectrometer equipped with a high-intensity twin anode (Al Kα radiation). In the case of the used Ag/Al$_2$O$_3$-a sample, the measurement was repeated after sputtering with 4 kV Ar$^+$ ions rastered over a 2 × 2 mm area. The spectra were charge-corrected with respect to the Al 2p signal at 74.0 eV. TEM images were acquired using an FEI Talos instrument operated at 200 kV. Powdered samples were deposited on Mo-grids as such.

Catalyst testing

Gas-phase conversion of GLY to PAl. The oxidehydration of GLY to PAl was studied at ambient pressure in a continuous-flow fixed-bed reactor (Scheme 2a) comprising: (i) mass flow controllers for feeding N$_2$ (PanGas, 99.999%), H$_2$ (PanGas, 99.999%) and O$_2$ (PanGas, 99.995%), (ii) a syringe pump for feeding an aqueous GLY (Sigma-Aldrich, 99%) solution, (iii) a tubular quartz micro-reactor (i.d. = 6 mm) heated in an oven, (iv) a liquid-gas separator immersed in an ice bath and (v) a bag for the collection of gaseous samples. The supported metal catalysts (0.1 g, particle size = 0.2–0.4 mm) were loaded into the reactor, which was then filled with 2-mm glass spheres in order to facilitate the evaporation of the liquid feed. The system was heated at the reaction temperature (623 K) in an N$_2$ flow (100 cm^3 min^{-1}) and allowed to equilibrate for 30 min. Thereafter, the gas composition was changed to 20 vol% H$_2$/N$_2$ (100 cm^3 min^{-1}) for 60 min to reduce the metal. Finally, O$_2$/N$_2$ (typically 1.5 vol%, 100 cm^3 min^{-1}) was admitted along with a 10 wt% aqueous GLY solution (0.1 cm^3 min^{-1}). Liquid samples were periodically collected at the reactor outlet and analysed by high-performance liquid chromatography (HPLC) using a Merk LaChrome system equipped with a HPX-87H column kept at 308 K and refraction index and UV-Vis detectors. A 0.005 M aqueous H$_2$SO$_4$ solution flowing at 0.600 cm^3 min^{-1} was used as the eluent. Calibration curves were measured in the 0.1–10 wt% range using GLY (Sigma-Aldrich, 99%), Ac (Alfa Aesar, 95%), PAl (Acros Organics, 40 wt% aqueous solution), PAc (ABCR, 98%), Acr (Fluka, >95%), AAc (Acros Organics, 99.5%), DHA (Merck, >98%), GAl (Sigma-Aldrich, >90%) and GAc (Acros Organics, >99.7%). CO and CO$_2$ in the gas samples were analysed by gas chromatography using a HP5890 unit equipped with a gas-sampling valve, a Restek-Shin Carbon ST80/100 column and a thermal conductivity detector. Helium was used as the carrier gas. The concentrations of the carbon oxides were determined from their absolute peak areas using calibration curves measured in the

Green Chemistry
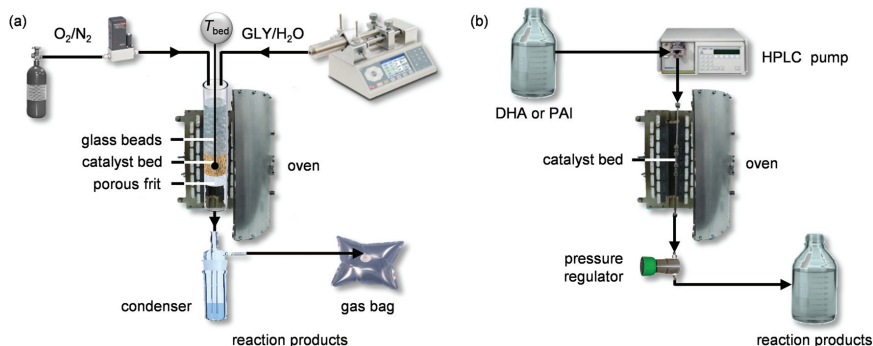
Scheme 2 Reactor setups used for (a) the continuous gas-phase conversion of GLY into PAl and (b) the continuous liquid-phase conversion of DHA and PAl into LA.

0–10 wt% range. The conversion of GLY (X_{GLY}) and selectivity to the product i (S_i) were calculated as:

$$X_{GLY} = 1 - (n_{GLY,out}/n_{GLY,in})$$

$$S_i = n_{i,out}/(n_{GLY,in} - n_{GLY,out})$$

where n refers to the moles of GLY or compound i and in/out to the reactor inlet/outlet. The carbon balance was obtained as the ratio between the moles of carbon in the liquid and gaseous products and the moles of carbon fed. The experimental error, determined by three repetitions of the same catalytic run, was within 5%. No GLY conversion was observed in blank tests conducted with only quartz particles and the glass beads loaded into the reactor.

Liquid-phase conversion of DHA and PAl to LA or ML. Batch catalytic experiments for the conversion of DHA or PAl into LA were carried out under autogenous pressure in 15 cm^3 thick-walled glass vials (Ace, pressure tubes, front seal) dipped in an oil bath heated at 333–423 K. The vials were loaded with ca. 10 cm^3 of a 0.33 M aqueous DHA solution (Merk, 98%) or PAl (Acros Organics, 40 wt% in water). Then, Sn-MFI (ca. 0.01 g) was added to achieve a substrate/tin molar ratio of 1000. The mixture was allowed to react under vigorous stirring for 15 min. Thereafter, the reactions were quenched using an ice bath and the catalysts were removed by means of a Chromafil Xtra 0.25 μm syringe filter. The continuous conversion of DHA and PAl into LA or ML was studied in a homemade continuous-flow reactor setup (Scheme 2b) comprising (i) an HPLC pump (Gilson-306), (ii) a stainless-steel tubular reactor with a pre-column (Swagelok SS-T4-S-035, i.d. = 4.6 mm), both heated in a tubular oven, (iii) a backpressure regulator (Swagelok, LH2981001) and (iv) an automatic sampler. The reactor was loaded with the Sn-containing zeolite catalysts (0.10 g) diluted with quartz (1 g, particle size = 0.25–0.36 mm) and a liquid feed (0.2 cm^3 min^{-1}) was admitted which contained the substrate (0.33 M) dissolved in water or methanol. Thereafter, the system was pressurised to 20 bar and heated to 383 K or 343 K

in the case of the conversion of DHA or PAl, respectively. Samples were periodically collected at the outlet of the reactor and analysed by HPLC using the same instrument and method as described for the analysis of the condensate obtained from the conversion of GLY. An additional calibration curve was measured in the 0.1–10 wt% range for L-lactic acid (ABCR, 98%). For the reactions performed in methanol, the amount of ML produced was determined using a gas chromatograph (HP 6890) equipped with an HP-5 capillary column and a flame ionisation detector. Quantification was accomplished by integration of its peak using 2,2,4-trimethylpentane (Fluka, 99.5%) as the internal standard. Conversion and selectivity data were calculated as mentioned above.

Computational details

Simulations were conducted using the Vienna *Ab-initio* Simulation Package (VASP)[21] and the RPBE functional.[22] Core electrons were described by projector augmented wave (PAW) pseudopotentials,[23] while valence electrons by a kinetic energy cutoff of 450 eV. Although its true structure has been debated for long,[24] experimental observations herein gathered indicate that silver forms a partially oxidised ultrathin film in O_2-rich environments that is commensurate with the p(4 × 4) Ag(111) unit cell. Therefore, three different models were used to describe the silver catalyst to account for poor, medium and rich oxygen conditions, respectively (Fig. 1). Metallic silver, which dominates at low O_2/GLY ratios, was represented by
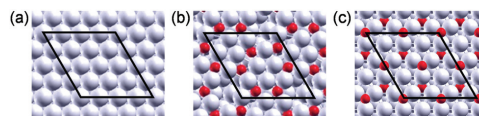

Fig. 1 Representation of the three (111) surfaces used as the models for (a) metallic Ag, (b) the partially oxidised metal AgO$_x$/Ag and (c) the bulk oxide Ag$_2$O.

Paper

Green Chemistry

4 layers of a clean 4 × 4 Ag(111) surface. For intermediate O_2/GLY ratios (~0.5), the p(4 × 4) model reported elsewhere[24b] was used. This can be generated from metallic Ag(111) by removing 4 metal atoms and adding 6 oxygen atoms to the topmost layer. The lattice parameter of the bulk metal was 4.22 Å, in good agreement with the experimental value of 4.09 Å.[25] Thus, both metallic and oxygen-covered silver surfaces have a length of 11.94 Å. Finally, for high O_2/GLY ratios, the p(2 × 2) Ag_2O(111) surface was used. Here, the on-surface distance between the cells is 13.92 Å, very similar to the one of Ag(111). For completeness, a model comprising a silver oxide layer epitaxially-grown on metallic silver, Ag_2O/Ag(111), was also investigated. Details to this model are provided in the ESI.† For all of the surfaces, the two topmost layers were relaxed while keeping the two bottom ones fixed to the bulk distances. The density of states for the clean surfaces is shown in Fig. S1.†

The Brillouin zone was sampled by a 3 × 3 × 1 Γ-centred k-points mesh generated through the Monkhorst–Pack method.[26] To avoid spurious interactions between the periodic images, a vacuum region between the slabs of 15 Å and dipole correction along z were included.[27] To find the transition states, the climbing image nudged elastic band (CI-NEB) method was employed.[28] The optimisation thresholds of 10^{-5} and 10^{-3} eV were applied for electronic and ionic relaxations, respectively. The assessment of the minima and transition states was performed by diagonalising the numerical Hessian matrix obtained by ±0.02 Å displacements. In the calculation of frequencies, the surface atoms were kept frozen, except for the oxygen atoms on AgO_x/Ag or Ag_2O that were part of the reaction. All of the DFT energies reported along the manuscript include zero-point energies.

Results and discussion

Catalytic oxidehydration of GLY to PAl

Evaluation of alumina-supported metal catalysts. A series of alumina-supported metal catalysts were prepared to assess the role of the metal in the conversion of GLY into PAl. The metals comprised V, Ni, Fe, Sn, Cu, Ru, Ag, Pd, Pt and Au and were selected among noble and non-noble transition metals based

on their reported catalytic activity in the dehydrogenation of alcohols. They are characterised by different redox potentials, spanning from −1.13 to 1.68 V, relatively to the semi-reactions reported in Table 1.[25] The metal content in the final materials was similar and was comprised between 4.4 and 5.1 wt% in all cases except for Ni and Sn. For these, the loading was limited to 3.1 and 1.9 wt%, respectively, due to the poor water solubility of the precursors. The choice of the alumina carrier was based on literature reports indicating that the reaction proceeds through the dehydration of GLY to Ac, followed by its dehydrogenation, and that the first reaction is catalysed by Lewis-acid sites.[3] Indeed, testing of the bare support yielded a GLY conversion of 53% with high Ac selectivity (85%, Table S1†). The most prominent by-product was Acr. The impregnation of the support with the metal precursors led to only minor modification in the surface area and did not significantly alter its Lewis acidity. In contrast, its mild Brønsted acidity (Table 1) generally decreased, likely due to the replacement of protons at ion-exchange positions with the metal cations, except for the Cu-, Ru- and Pd-based catalysts. For these, a slight increase was noticed, which could be associated with the higher electronegativity of the metals and thus with the stronger acidic nature of H atoms of hydroxyl groups.

Fig. 2a shows the catalytic data collected upon testing of the catalysts in the gas-phase oxidehydration of GLY at 623 K. With the exception of the Pt- and Au-based samples, all of the materials attained a high GLY conversion level. This suggests that a certain degree of oxidation of the metal is advantageous, which cannot be achieved with the most noble metals. The product distribution, evidencing a low Ac selectivity at high PAl yields and *vice versa*, is in line with the two-step reaction path proposed in Scheme 1b. Only minor amounts of DHA (<1%), Gal (<1%) and GAc (<2%) were detected (Table S1†), indicating that the direct dehydrogenation of the hydroxyl groups of GLY is hindered under these conditions. Indeed, we have recently reported the oxidation of GLY to DHA to happen at much higher O_2/GLY ratios over steamed iron-containing silicalite featuring negligible acidity.[8b] The competitive dehydration reaction leading to Acr, which can be further converted into AAc under oxidising conditions, was relevant only in the case of Sn-, Cu- and Ru-containing materials. This was

Table 1 Characterisation data for the alumina-supported metal catalysts

Catalyst	Metal content[a] (wt%)	S_{BET}[b] (m^2 g^{-1})	V_{pore}[c] (cm^3 g^{-1})	C_{Lewis}[d] (µmol g^{-1})	$C_{Brønsted}$[d] (µmol g^{-1})	E_h[e] (V)	Semi-reaction
V/Al_2O_3-a	4.9	74	0.39	65	8	−1.13	$V^{2+} + 2e^- \rightarrow V$
Ni/Al_2O_3-a	3.1	76	0.45	61	7	−0.72	$Ni^{2+} + 2e^- \rightarrow Ni$
Fe/Al_2O_3-a	4.8	78	0.42	72	3	−0.44	$Fe^{2+} + 2e^- \rightarrow Fe$
Sn/Al_2O_3-a	1.9	78	0.44	80	4	−0.14	$Sn^{2+} + 2e^- \rightarrow Sn$
Cu/Al_2O_3-a	4.5	81	0.38	68	18	0.34	$Cu^{2+} + 2e^- \rightarrow Cu$
Ru/Al_2O_3-a	5.1	72	0.40	76	16	0.70	$Ru^{4+} + 4e^- \rightarrow Ru$
Ag/Al_2O_3-a	4.8	74	0.45	72	8	0.80	$Ag^+ + e^- \rightarrow Ag$
Pd/Al_2O_3-a	5.0	79	0.45	70	21	0.90	$Ru^{4+} + 4e^- \rightarrow Sn$
Pt/Al_2O_3-a	4.1	72	0.35	58	26	1.20	$Pd^{2+} + 2e^- \rightarrow Pd$
Au/Al_2O_3-a	4.4	80	0.46	69	4	1.83	$Au^+ + e^- \rightarrow Au$

[a] XRF spectroscopy. [b] BET method. [c] Volume adsorbed at p/p_0 = 0.99. [d] FTIR spectroscopy of adsorbed pyridine, after desorption at 473 K. [e] Redox potential of the semi-reaction reported in the column on the right.[28]
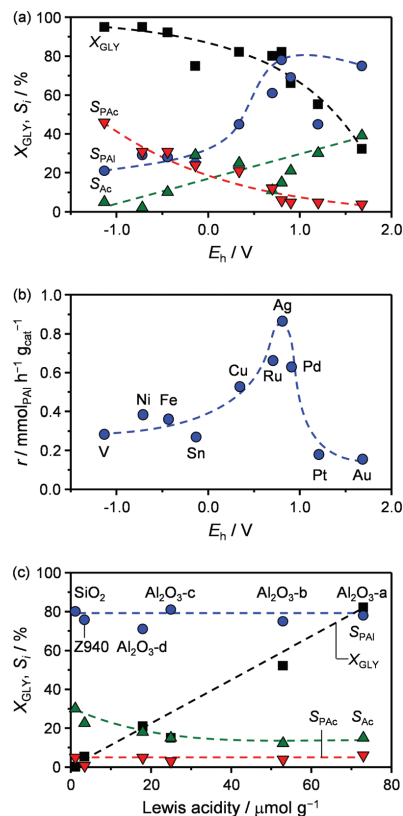
221

Paper

Fig. 2 (a) GLY conversion and selectivities to Ac, PAl and PAc as a function of the metal reduction potential for alumina-supported catalysts and (b) the corresponding PAl formation rate. (c) Reaction performance *vs.* the Lewis-acid sites concentration for alumina-, Z940- and SiO_2-supported silver catalysts. Reaction conditions: T = 623 K, P = 1 bar, C_{GLY} = 10 wt%, LHSV = 6 h^{-1} and O_2/GLY = 0.5.

explained by their comparatively high concentration of Brønsted acid sites, which are well-known active centres for the selective formation of this molecule from GLY. Pt- and Pd-containing solids, which evidenced moderate acidity upon pyridine adsorption did not show this behaviour likely because of their fully reduced status under the reaction conditions and the consequent absence of hydroxyl groups on their surface. Overall, the selectivity to the dehydration product (Ac) was higher for those materials containing a more noble metal. Assuming that GLY dehydration mostly takes place on the support and the Ac dehydrogenation is catalysed by the metal, this implies a lower activity of these metals in the dehydrogenation step. On the other hand, over-oxidation of PAl to PAc was favoured on non-noble metals. Furthermore, up to 8% of the GLY fed was converted into CO and CO_2. Overall, the Ag-based catalyst was superior to the other systems due to a good balance between activity and selectivity to PAl. This is visualised in Fig. 2b, which highlights a maximum for the PAl yield (80%) over this material. Notably, this yield matches the state-of-the-art data claimed in a patent over another Ag-based solid.[15] Accordingly, this catalyst was chosen for further studies.

Support selection for silver catalysts. A series of silver catalysts was prepared using supports with distinct acid–base properties (Table S2†), to explore whether the catalyst activity could be further enhanced by optimising the first step. The carriers comprised 3 additional aluminas, leading to solids featuring different Lewis acidity, 2 zeolites with MFI framework topology and a Si/Al ratio of *ca.* 40 or 940 as well as amorphous silica and silica-alumina, generating catalysts with very diverse Brønsted and Lewis acidity (Table 2). The specific surface area of the carriers was in line with that generally reported for these materials and was not substantially altered by the deposition of the silver phase, suggesting a good metal dispersion. An increased Lewis-acidic character was shown to be beneficial to raise the conversion of the substrate while keeping a high selectivity (Fig. 2c). Indeed, for all the alumina-supported samples a linear conversion-*vs.*-Lewis acidity trend was observed. The strength of the Lewis-acid sites appeared to play no significant role, since it varied significantly among materials displaying a similar selectivity (Table 2). Brønsted-acid sites proved extremely detrimental for the selectivity of

Table 2 Characterisation data for the Ag-based catalysts

Support	Ag^a (wt%)	S_{BET}^b (m^2 g^{-1})	V_{pore}^c (cm^3 g^{-1})	C_{Lewis}^d (μmol g^{-1})	$C_{Brønsted}^d$ (μmol g^{-1})	Lewis sites strength^e	Brønsted sites strength^e
Ag/Al_2O_3-a	4.8	74	0.45	72	8	0.91	0.45
Ag/Al_2O_3-b	4.8	70	0.38	53	2	0.86	0.52
Ag/Al_2O_3-c	4.9	73	0.51	25	0	0.60	—
Ag/Al_2O_3-d	4.8	76	0.56	18	0	0.75	—
Ag/SiO_2	4.9	121	0.35	1	0	1.00	—
Ag/ASA	5.1	80	0.61	51	54	0.41	0.88
Ag/Z940	4.7	325	0.19	21	0	0.80	—
Ag/Z40	5.0	403	0.21	89	151	0.57	0.79

^{a} XRF spectroscopy. ^{b} BET method. ^{c} Volume adsorbed at p/p_0 = 0.99. ^{d} FTIR spectroscopy of adsorbed pyridine, after desorption at 473 K. ^{e} Defined as the ratio between the sites probed by pyridine after desorption at 473 and at 373 K.

the reaction (Fig. S2†). While promoting a high GLY conversion, the strongly Brønsted-acidic Z40 and ASA support limited the formation of the product of interest since they favoured the dehydration of GLY to Acr (Table S1†). Based on these results, a bigger batch of 5 wt% Ag/Al$_2$O$_3$-a was prepared to enable an in-depth characterisation and testing at variable reaction conditions. Spray deposition was used as a synthesis method instead of impregnation due to the higher reproducibility of the properties of the solids obtained by this technique.[19] The catalyst showed the same catalytic performance as that obtained by impregnation. The XRD pattern of the solid in as-prepared form evidenced, after subtraction of the diffractogram of the bare support, weak reflections specific to Ag(ı) oxide (Fig. 3a). After activation of this material by reduction in diluted hydrogen, the diffraction lines of Ag$_2$O disappeared and two reflections appeared at 38 and 64 2θ, which are attributed to metallic silver nanoparticles of about 13 nm diameter. H$_2$-TPR analysis confirmed the stoichiometry of the silver oxide in the freshly-synthesised sample (Fig. 3b). After activation, negligible hydrogen consumption was measured, indicating the complete reduction to the metallic state. Transmission electron micrographs (Fig. 4a and b) revealed that the Ag$_2$O particles were very small (ca. 5 nm) and that the metallic phase featured larger aggregates (ca. 12 nm). The latter evidence is in agreement with the XRD data and indicates that clustering happened upon reduction (Fig. 3a). Finally, the nature of the metal surface was investigated by XPS (Fig. 3c). A signal centred at 368.2 eV was observed for the as-prepared sample, which is attributed to the 3d transition of Ag(ı) species.[29] After reduction of the catalyst, the position of the 3d signal shifted to 367.2 eV, as expected for metallic silver. This difference is also in good agreement with the data calculated by DFT (Table S3†), which predicted that the signal of oxidic silver would appear at a 0.7 eV higher binding energy than that of metallic silver.

Impact of the reaction conditions for Ag/Al$_2$O$_3$-a. The dependence of the reaction performance on the temperature and on the O$_2$-GLY ratio was studied in the 573–673 K and 0–1.5 ranges, respectively, using the 5 wt% Ag/Al$_2$O$_3$-a catalyst prepared by spray deposition. As expected, the conversion increased at higher temperatures (Fig. 5a). The selectivity to PAl was preserved until 623 K. Above this temperature, the over-oxidation to PAc increased. This effect is in line with the fact that the oxidation of the aldehyde also happens homogeneously following a non-catalytic radical pathway, the rate of which strongly depends on temperature.[30] In the absence of oxygen, Ac was the most prominent product (Fig. 5b) and the Acr yield was comparable to that obtained in a blank run with the bare support. This indicates that the rate of dehydrogenation is negligible if O$_2$ is not supplied. As detailed below, it additionally hints the inactivity of the metal in its reduced state or the necessity of reducing the surface coverage of the hydrogen abstracted from the substrate using an oxidant. The PAl yield steeply increased upon addition of O$_2$ reaching ca. 80% at O$_2$/GLY = 0.5, i.e., the stoichiometric ratio. Above this value, it diminished due to the more pronounced over-oxidation.

The stability of the catalyst was tested at the optimal temperature and O$_2$/GLY ratio in a 24 h run (Fig. 5c). The PAl yield decreased by only ca. 10% in this test highlighting the robustness of the material. This minor loss of performance was ascribed to the deposition of carbonaceous species (4.8 wt% C on the used catalyst) and a slight sintering of the silver particles from ca. 12 to 15 nm (Fig. 4c). It should be noted that a catalyst featuring a distinct Brønsted acidity would undergo rapid deactivation by fouling due to the promoted formation of dehydration and condensation products.

DFT simulations on Ac dehydrogenation to PAl

Since the catalyst testing evidenced a strong influence of the addition of oxygen on the oxidehydration of GLY, the oxidative conversion of Ac to PAl was investigated in greater detail by DFT. The reaction occurs as described hereon. Firstly, Ac adsorbs on the surface (1), which abstracts an H atom cleaving
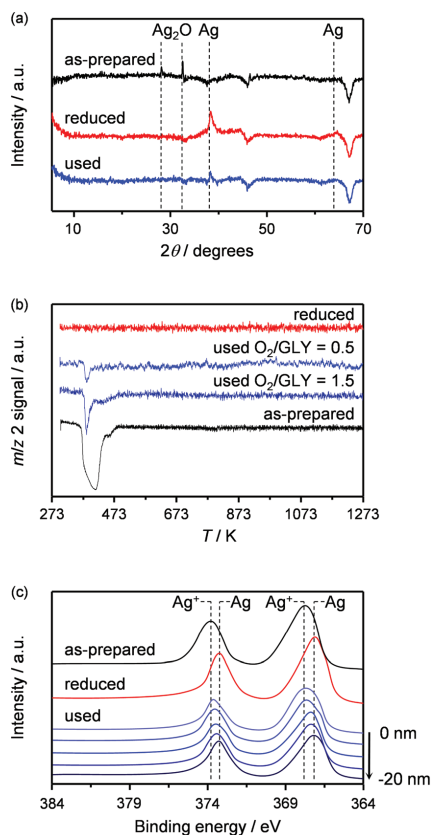

Fig. 3 Characterisation of the as-prepared, activated and used Ag/Al$_2$O$_3$-a catalyst by (a) XRD, (b) H$_2$-TPR and (c) XPS.
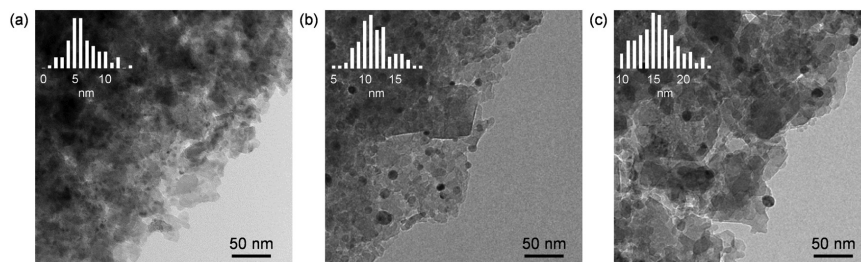
Green Chemistry

Paper

Fig. 4 TEM micrographs for the (a) as-prepared, (b) activated and (c) used Ag/Al$_2$O$_3$-a catalyst. The particle size distributions of the Ag-based phase are reported in the insets.
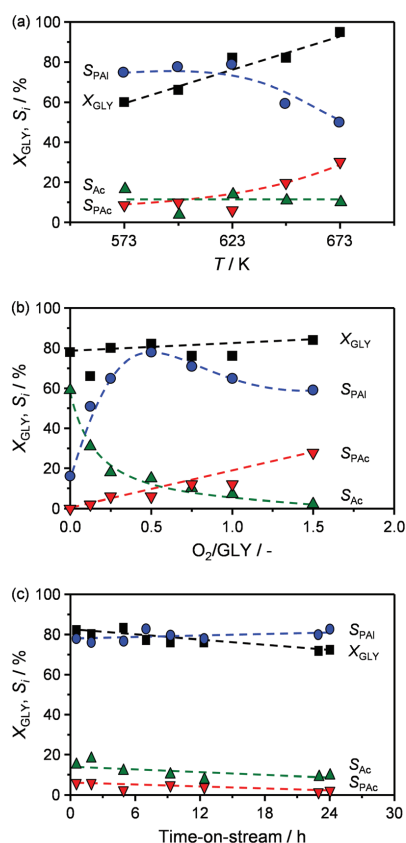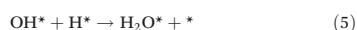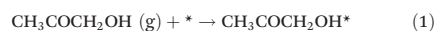

Fig. 5 GLY conversion and product selectivity over Ag/Al$_2$O$_3$-a as a function of (a) the temperature, (b) the O$_2$/GLY ratio and (c) the time on stream. Reaction conditions: $T = 623$ K, $P = 1$ bar, $C_{GLY} = 10$ wt%, LHSV $= 6$ h^{-1} and O$_2$/GLY = 0.5.

the more labile O–H bond (2).[31] The latter is performed by an Ag atom on a metallic surface or by an O atom in the case of AgO$_x$/Ag and Ag$_2$O. Then, the vicinal C–H bond is broken (3), forming adsorbed PAl. The reaction proceeds with the desorption of PAl (4). When oxygen is present on the surface, catalyst regeneration occurs through the formation of water by combination of two hydroxyl groups (5). The subsequent desorption of water creates an oxygen vacancy (6), that is healed by the adsorption of an oxygen molecule (7). Albeit comprising multiple steps, the latter is represented as an elementary step for the sake of clarity.

$$CH_3COCH_2OH \text{ (g)} + * \rightarrow CH_3COCH_2OH* \quad (1)$$

$$CH_3COCH_2OH* + * \rightarrow CH_3COCH_2O* + H* \quad (2)$$

$$CH_3COCH_2O* + * \rightarrow CH_3COCHO* + H* \quad (3)$$

$$CH_3COCHO* \rightarrow CH_3COCHO \text{ (g)} + * \quad (4)$$

$$OH* + H* \rightarrow H_2O* + * \quad (5)$$

$$H_2O* \rightarrow H_2O \text{ (g)} + * \quad (6)$$

$$\frac{1}{2}O_2 \text{ (g)} + * \rightarrow O* \quad (7)$$

The energy profiles corresponding to the steps (1)–(4) are shown in Fig. 6, while those relative to steps (5)–(7) are depicted in Fig. S3.† On pure Ag, the adsorption of Ac is endothermic and the barrier for step (2) is higher than on the other two model surfaces, indicating that it shall proceed with very low rates. The second dehydrogenation (3) occurs simultaneously with PAl desorption (4). On Ag$_2$O, the adsorption of Ac is more exothermic than on the other systems (1), indicating that the bulk oxide traps Ac more effectively. The first dehydrogenation (2) is less energy demanding than for pure Ag and the second dehydrogenation (3) proceeds rapidly and is followed by the exothermic desorption of the desired product PAl. However, water formation (5) is relatively difficult, thus hindering the regeneration of the catalyst. On AgO$_x$/Ag, the low reaction and activation energies of step (2) suggest that CH$_3$COCH$_2$O* is in equilibrium with adsorbed Ac. Reaction (3) has a low activation energy and is very exothermic. Since step
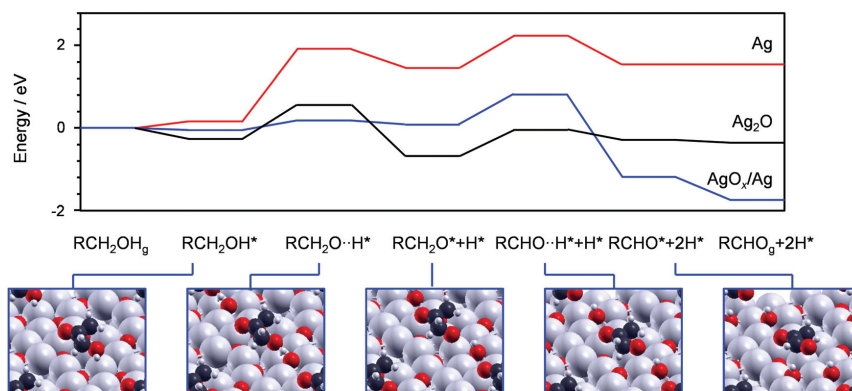
Paper

Fig. 6 Energy profiles for the dehydrogenation of Ac to PAl and the corresponding structures calculated over the AgO$_x$/Ag surface.

(7) is less energy demanding, the surface will regenerate faster than in the case of bulk Ag$_2$O. For the oxidic surface and the bulk oxide, PAl desorption is always exothermic, thus preventing the on-surface over-oxidation to PAc. It should be noted that step (2) is an acid–base reaction that could also be catalysed by the support. Spillover of the oxygenate fragment to the metal phase would enable the occurrence of the subsequent steps (3)–(7). However, control experiments with a SiC-supported Ag catalyst excluded the participation of the alumina carrier in the abstraction of the first H atom (Table S4†). The results obtained over the Ag$_2$O/Ag surface (Fig. S4 and S5†) are close to those described for the bulk Ag$_2$O system and are discussed in the ESI.†

Based on the analysis of the energy diagrams, the high PAl yield found at O$_2$/GLY = 0.5 is explained by its quick elimination from the surface and the easy catalyst regeneration, while the low PAl yields measured for low and high O$_2$/GLY ratios are due to a very slow C–H stripping and a hindered regeneration of the metal sites, which remain hydroxylated, respectively. These findings hence rationalise the volcano-shape observed in Fig. 5b.

Characterisation data for the Ag/Al$_2$O$_3$-a catalyst indicate the surface oxidation of the metal nanoparticles after use under the optimised conditions. This corresponds to the most active surface (AgO$_x$/Ag) analysed for the reaction. Indeed, XRD (Fig. 3a) evidenced a weakening and sharpening of the diffraction peaks attributed to metallic silver, pointing to the formation of bigger particles and of a secondary Ag-based phase, which remained undetected possibly due to the its limited amount and/or high dispersion. H$_2$-TPR analysis (Fig. 3b) showed a reduction peak centred at *ca.* 523 K, indicating that *ca.* 13% of the metal was oxidised to Ag(I) oxide. The location of this phase was investigated through XPS by measuring spectra after removing a progressively thicker layer of material from the surface by sputtering with Ar$^+$ (Fig. 3c). The 3d signal of silver appeared at 368.0 eV in the spectrum of the used untreated sample and stepwise shifted to 367.2 eV in those

after irradiation with the ion beam. This finding implies the formation of an oxidised silver shell around a metallic core upon reaction. Since the oxygen-to-silver ratio at the surface was lower than that of Ag$_2$O, as indicated by the slightly shifted XPS peak, silver might not be fully oxidised to Ag(I) in this outer layer. The partial oxidation of the Ag phase upon reaction was confirmed by H$_2$-TPR analysis of another sample, *i.e.*, Ag/Al$_2$O$_3$-d (15%, Fig. S6†). Additionally, characterisation of the Ag/Al$_2$O$_3$-a catalyst used at O$_2$/GLY = 1.5 by the same technique revealed a 2.5-times greater extent of oxidation of silver (32%, Fig. 3b), highlighting the sensitivity of the active phase to the oxygen feed content. The change in oxidation state of the surface silver atoms is analogous to that observed for Ru-based catalysts applied in the transfer hydrogenation of furfural to 2-methylfurane, where the active phase has been reported to include both oxidic and metallic species. The similarity of the two systems is attributed to the similar E_h values of the two metals (Fig. 2b).[32] It should also be noticed that the partial oxygen pressures and temperatures employed in the reaction herein studied are similar to those commonly applied in ethylene epoxidation.[24,33] This transformation com-
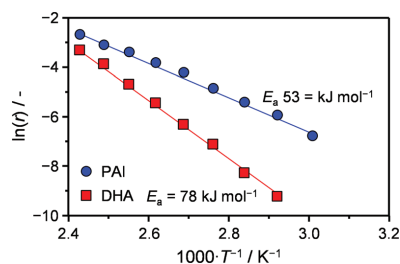

Fig. 7 Rate of LA formation from DHA and PAl over Sn-MFI in water. Reaction conditions: $C_{DHA, PAl}$ = 0.33 M and DHA, PAl/Sn = 1000.

Green Chemistry   Paper
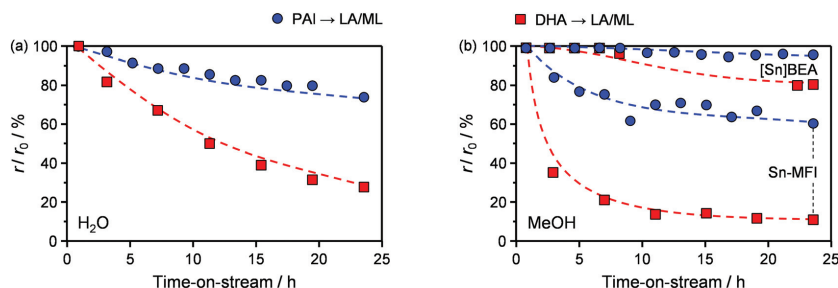

Fig. 8 (a) Percentage of the initial rate of LA formation over Sn-MFI in water and (b) of ML formation over Sn-MFI and [Sn]BEA in methanol. Reaction conditions: T_{DHA} = 383 K, T_{PAl} = 343 K, P = 20 bar, $C_{DHA, PAl}$ = 0.33 M, LHSV = 120 h^{-1}.

Continuous liquid-phase conversion of PAl to LA

The rate of formation of LA and methyl lactate (ML) from DHA over Sn-containing Lewis-acid zeolites has been reported to be limited by the dehydration of the ketone to PAl (Scheme 1a).[12] Therefore, the use of the latter as a substrate would enable the same productivity at reduced operation temperatures, thus decreasing the energy demand of the process. Additionally, it is expected that temperature-dependent deactivation processes, including fouling and hydrothermal modifications of the zeolite, would be hindered, lowering the catalyst consumption and the operating costs. To confirm the advantages of the use of PAl as an alternative substrate to DHA for the production of LA and methyl lactate (ML), the state-of-the-art [Sn]BEA zeolite as well as a Sn-MFI material prepared by alkaline-assisted stannation were evaluated in the two reactions. The latter catalyst was selected in view of the rapidity and scalability of its preparation which contrast the limited industrial amenability of the synthesis of the former material.[19] The crystallinity, textural properties and the coordination of the tin sites, probed by diffuse reflectance UV-Vis and acetonitrile-FTIR spectroscopies (Table S5 and Fig. S7†), of the stannosilicates were in good agreement with previous data published for these materials.[12] At first, Sn-MFI was tested in the conversion of DHA and PAl in batch experiments at different temperatures in order to choose conditions suitable to compare initial turnover frequencies for the two substrates. The results (Fig. 7) indicate that the rate of LA formation from DHA at 383 K, a typical temperature for this reaction, could be matched using PAl at only 343 K. Hence, continuous experiments were performed at these two temperatures. When Sn-MFI was operated in water (Fig. 8a) in a 24 h test, the loss of LA yield was limited to only 23% in the case of PAl, as opposed to 75% when the reaction was performed using DHA. An even more pronounced difference in the deactivation pattern was noticed when methanol was used as the solvent (Fig. 8b). We have previously observed that, for the

alcohol-based conversion of DHA, the 10-membered ring MFI zeolites suffer from much faster coking with respect to BEA zeolites featuring the larger 12-membered rings, which renders the catalyst almost inactive after 12 h on stream. Remarkably, at the lower temperature employed for the conversion of PAl, more than 40% of the initial activity of Sn-MFI was retained after use for 24 h. An appreciable gain in stability was observed also in the case of [Sn]BEA.

Conclusions

In this study, we uncovered silver supported on alumina as a highly efficient catalyst for the oxidehydration of waste glycerol to pyruvaldehyde and the advantages of using this compound instead of dihydroxyacetone for the sustainable manufacture of lactic acid and methyl lactate. Silver was chosen amongst other transition metals thanks to its optimal reduction potential, which enabled high activity and selectivity. In contrast, metals with a more noble character were less active and those with a higher tendency to oxidise favoured the further oxidation of the product. A maximal pyruvaldehyde yield of ca. 65% was attained, which remained stable over 24 h on stream. Characterisation of the used catalyst evidenced the formation of an oxide layer at the surface of the metal nanoparticles, which was demonstrated by DFT to be the active surface for the dehydrogenation of the acetol molecule obtained by dehydration of glycerol. In fact, the reaction was found to be thermodynamically limited on metallic silver and kinetically hindered on a pure oxide phase, due to the higher activation energy of the proton abstraction and the more difficult regeneration of the oxidic sites. Finally, we confronted the use of pyruvaldehyde and dihydroxyacetone for the preparation of lactic acid and methyl lactate over tin zeolites. Remarkably, with the former substrate it was possible to achieve comparable rates at a 40 K lower reaction temperature, greatly reducing the deactivation of the stannosilicates. Accordingly, a glycerol to lactic acid process featuring pyruvaldehyde as intermediate is expected to bring substantial environmental and economic benefits compared to the best process currently envi-

Paper

saged for the valorisation of this feedstock, which is based on the exploitation of dihydroxyacetone.

Acknowledgements

References

1 (*a*) T. Werpy and G. R. Petersen, *Top Value Added Chemicals from Biomass: Vol. I - Results of Screening for Potential Candidates from Sugars and Synthesis Gas*, US DOE, 2004; (*b*) J. J. Bozell and G. R. Petersen, *Green Chem.*, 2010, **12**, 539–554; (*c*) R. E. Drumright, P. R. Gruber and D. E. Henton, *Adv. Mater.*, 2000, **12**, 1841–1846; (*d*) S. Cohen, T. Yoshioka, M. Lucarelli, L. Hwang and R. Langer, *Pharm. Res.*, 1991, **8**, 713–720; (*e*) J. C. Serrano-Ruiz, A. Pineda, A. M. Balu, R. Luque, J. M. Campelo, A. A. Romero and J. M. Ramos-Fernández, *Catal. Today*, 2012, **195**, 162–168.

2 J. Lunt, *Polym. Degrad. Stab.*, 1998, **59**, 145–152.

3 M. Dusselier, P. Van Wouwe, A. Dewaele, E. Makshina and B. F. Sels, *Energy Environ. Sci.*, 2013, **6**, 1415–1442.

4 (*a*) R. Datta and M. Henry, *J. Chem. Technol. Biotechnol.*, 2006, **81**, 1119–1129; (*b*) Y.-J. Wee, J.-N. Kim and H.-W. Ryu, *Food Technol. Biotechnol.*, 2006, **44**, 163–172; (*c*) M. Singhvi, G. Gurjar, V. Gupta, D. Gokhale, *et al.*, *RSC Adv.*, 2015, **5**, 2024.

5 D. T. Johnson and K. A. Taconi, *Environ. Prog.*, 2007, **26**, 338–348.

6 R. Ciriminna, C. Della Pina, M. Rossi and M. Pagliaro, *Eur. J. Lipid Sci. Technol.*, 2014, **116**, 1432–1439.

7 (*a*) P. Lakshmanan, P. P. Upare, N.-T. Le, Y. K. Hwang, D. W. Hwang, U.-H. Lee, H. R. Kim and J.-S. Chang, *Appl. Catal., A*, 2013, **468**, 260–268; (*b*) Y. Shen, S. Zhang, H. Li, Y. Ren and H. Liu, *Chem. – Eur. J.*, 2010, **16**, 7368–7371; (*c*) H. J. Cho, C.-C. Chang and W. Fan, *Green Chem.*, 2014, **16**, 3428–3433.

8 (*a*) D. Hekmat, R. Bauer and J. Fricke, *Bioprocess Biosyst. Eng.*, 2003, **26**, 109–116; (*b*) G. M. Lari, C. Mondelli and J. Pérez-Ramírez, *ACS Catal.*, 2015, **5**, 1453–1461.

9 P. Y. Dapsens, C. Mondelli and J. Pérez-Ramírez, *Chem. Soc. Rev.*, 2015, **44**, 7025–7043.

10 C. M. Osmundsen, M. S. Holm, S. Dahl and E. Taarning, *Proc. R. Soc. London, Ser. A*, 2012, **468**, 2000–2016.

11 F. de Clippel, M. Dusselier, R. Van Rompaey, P. Vanelderen, J. Dijkmans, E. Makshina, L. Giebeler, S. Oswald, G. V. Baron, J. F. M. Denayer, P. P. Pescarmona, P. A. Jacobs and B. F. Sels, *J. Am. Chem. Soc.*, 2012, **134**, 10089–10101.

12 G. M. Lari, P. Y. Dapsens, D. Scholz, S. Mitchell, C. Mondelli and J. Pérez-Ramírez, *Green Chem.*, 2016, **18**, 1249–1260.

13 R. M. Ravenelle, F. Schuessler, A. D'Amico, N. Danilina, J. A. van Bokhoven, J. A. Lercher, C. W. Jones and C. Sievers, *J. Phys. Chem. C*, 2010, **114**, 19582–19595.

14 P. T. Williams and S. Besler, *Renewable Energy*, 1996, **7**, 233–250.

15 H. Baltes and E. I. Leupold, *US Pat* 4302609, 1981.

16 R. K. Pazhavelikkakath Purushothaman, J. van Haveren, I. Melián-Cabrera, E. R. H. van Eck and H. J. Heeres, *ChemSusChem*, 2014, **7**, 1140–1147.

17 F. Auneau, S. Noël, G. Aubert, M. Besson, L. Djakovitch and C. Pinel, *Catal. Commun.*, 2011, **16**, 144–149.

18 A. H. Øygarden, J. Pérez-Ramírez, D. Waller, K. Schöffel and D. Brackenbury, *WO* 2004/110622, 2004.

19 P. Y. Dapsens, C. Mondelli, J. Jagielski, R. Hauert and J. Pérez-Ramírez, *Catal. Sci. Technol.*, 2014, **4**, 2302–2311.

20 S. Valencia and A. Corma, *US Pat* 5968473, 1999.

21 (*a*) G. Kresse and J. Furthmüller, *Comput. Mater. Sci.*, 1996, **6**, 15–50; (*b*) G. Kresse and J. Furthmüller, *Phys. Rev. B: Condens. Matter*, 1996, **54**, 11169–11186.

22 B. Hammer, L. B. Hansen and J. K. Nørskov, *Phys. Rev. B: Condens. Matter*, 1999, **59**, 7413–7421.

23 (*a*) P. E. Blöchl, *Phys. Rev. B: Condens. Matter*, 1994, **50**, 17953; (*b*) G. Kresse and J. Joubert, *Phys. Rev. B: Condens. Matter*, 1999, **59**, 1758.

24 (*a*) M. Schmid, A. Reicho, A. Stierle, I. Costina, J. Klikovits, P. Kostelnik, O. Dubay, G. Kresse, J. Gustafson, E. Lundgren, J. N. Andersen, H. Dosch and P. Varga, *Phys. Rev. Lett.*, 2006, **96**, 146102; (*b*) J. Schnadt, A. Michaelides, J. Knudsen, R. T. Vang, K. Reuter, E. Lægsgaard, M. Scheffler and F. Besenbacher, *Phys. Rev. Lett.*, 2006, **96**, 146101.

25 W. M. Haynes, *CRC Handbook of Chemistry and Physics*, CRC Press, Boca Raton, 96th edn, 2015.

26 H. J. Monkhorst and J. D. Pack, *Phys. Rev. B: Solid State*, 1976, **13**, 5188–5192.

27 G. Makov and M. C. Payne, *Phys. Rev. B: Condens. Matter*, 1995, **51**, 4014–4022.

28 (*a*) G. Henkelman and H. Jónsson, *J. Chem. Phys.*, 2000, **113**, 9978–9985; (*b*) G. Henkelman, B. P. Uberuaga and H. Jónsson, *J. Chem. Phys.*, 2000, **113**, 9901–9904.

29 (*a*) A. M. Ferraria, A. P. Carapeto and A. M. Botelho do Rego, *Vacuum*, 2012, **86**, 1988–1991; (*b*) S. W. Gaarenstroom and N. Winograd, *J. Chem. Phys.*, 1977, **67**, 3500–3506.

30 M. Besson and P. Gallezot, *Catal. Today*, 2000, **57**, 127–141.

31 Y. Kwon, S. C. S. Lai, P. Rodriguez and M. T. M. Koper, *J. Am. Chem. Soc.*, 2011, **133**, 6914–6917.

32 M. J. Gilkey, P. Panagiotopoulou, A. V. Mironenko, G. R. Jenness, D. G. Vlachos and B. Xu, *ACS Catal.*, 2015, **5**, 3988–3994.

33 J. P. Dever, K. F. George, W. C. Hoffman and H. Soo, Ethylene Oxide, in *Kirk-Othmer Encyclopedia of Chemical Technology*, John Wiley & Sons, Inc., Hoboken, 2004, pp. 632–673.